

The Pennsylvania State University

The Graduate School

Materials Science and Engineering

GROWTH AND PROPERTIES OF ANODIC OXIDE FILMS ON PLATINUM

A Thesis in

Materials Science and Engineering

by

Adan Sun

© 2006 Adan Sun

Submitted in Partial Fulfillment
of the Requirements
for the Degree of

Doctor of Philosophy

August 2006

The thesis of Adan Sun was reviewed and approved* by the following:

| | |
|--------------------|--|
| Professor's Name | Digby D. Macdonald |
| Title(s) | Distinguished Professor of Materials Science and Engineering |
| Thesis Advisor | Digby D. Macdonald |
| Chair of Committee | Digby D. Macdonald |

| | |
|------------------|---|
| Professor's Name | Thomas E. Mallouk |
| Title(s) | Dupont Professor of Materials Chemistry and Physics |

| | |
|------------------|--|
| Professor's Name | Christopher Muhlstein |
| Title(s) | Assistant Professor of Materials Science and Engineering |

| | |
|------------------|--|
| Professor's Name | Joan M. Redwing |
| Title(s) | Associate Professor of Materials Science and Engineering |

| | |
|------------------------|---|
| Department Head's Name | Gary L. Messing |
| Title(s) | Distinguished Professor of Ceramic Science and Engineering |
| Administrative Title | Head of the Department of Materials Science and Engineering |

*Signatures are on file in the Graduate School

ABSTRACT

Electrocatalysts supporting the oxygen electrode reaction are commonly covered with thin oxide films that may have a profound influence over the kinetics of the reaction. Little is currently known about the role of oxide films in electrocatalysts, particularly with regard to the role of the defect structure. In this work, the physical and defect structures of the oxide film that forms on platinum in acid and alkaline solutions under steady state conditions has been investigated using Electrochemical Impedance Spectroscopy (EIS) and ARXPS (Angle-Resolved X-Ray Photoelectron Spectroscopy). Mott-Schottky analysis shows that the film in both acid and alkaline solutions is n-type, indicating that the defects in the film are either platinum interstitials or oxygen vacancies, or both. ARXPS analysis of films formed in acid solution shows that, for potentials between 1.0 and 1.3 V_{SHE} , a single-layer film develops, with the principal oxidation state for Pt (in the film) being +2. However, a bi-layer structure was observed for films formed at potentials greater than 1.3 V_{SHE} and ARXPS analysis shows that these bi-layer films comprise an inner layer containing Pt(II) and an outer layer containing Pt(IV). Optimization of the Point Defect Model on the EIS data obtained in acid solution yields values for various kinetic parameters that are then used to predict the steady state thickness and current. Good agreement with experiment is obtained.

The kinetics of growth of the oxide film on platinum has been studied in alkaline solution as a function of pH. The experimental data confirm the existence of steady states in the current and thickness. Both transient and steady state currents are found to increase with pH. The donor density in the film calculated according to Mott-Schottky

analysis increases with pH. Diagnostic criteria for the dependence of the steady state current and thickness on applied potential and pH are derived from the PDM, in which the principal point defects in the barrier layer are postulated to be cation interstitials and oxygen vacancies, thereby accounting for the n-type electronic character. The steady state thickness is then predicted to vary linearly with the applied potential and pH. These predictions are in good agreement with the experimental findings. The PDM also predicts a linear relationship between the logarithm of steady state current and applied formation potential with a non-zero slope, but only if $\Gamma \neq \chi$. If $\Gamma = \chi$ and the film is n-type, then $\ln(I_{ss})$ is predicted to be independent of the applied voltage. The experimentally observed diagnostic criteria derived from the PDM are employed as the constraints in the optimization of the PDM on EIS data obtained in alkaline solutions. Good agreement between the experimental data and the calculated data is observed.

TABLE OF CONTENTS

| | |
|---|------|
| LIST OF FIGURES | vii |
| LIST OF TABLES | xi |
| ACKNOWLEDGEMENTS | 15 |
| LIST OF THE PRINCIPAL SYMBOLS..... | xiii |
| Chapter 1 INTRODUCTION..... | 1 |
| Chapter 2 BACKGROUND..... | 4 |
| 2.1 Characteristic of Oxide Films on Platinum under Transient Conditions..... | 5 |
| 2.2 Steady State Growth of Oxide Film..... | 9 |
| 2.3 Solid State Properties..... | 15 |
| 2.4 Composition, Microstructure and Morphology | 20 |
| 2.4.1 Composition | 20 |
| 2.4.2 Microstructure | 22 |
| 2.4.3 Morphology | 23 |
| 2.5 Growth Mechanism | 24 |
| 2.5.1 Place Exchange Model | 24 |
| 2.5.2 High Field Model | 26 |
| 2.5.3 Nucleation and Growth Model | 28 |
| 2.5.4 Point Defect Model..... | 31 |
| 2.5.5 Summary..... | 36 |
| References..... | 37 |
| Chapter 3 EXPERIMENTAL | 43 |
| Chapter 4 GROWTH AND PROPERTIES OF OXIDE FILMS ON PLATINUM ... | 46 |
| 4.1 Transient Growth of Platinum Oxide Film..... | 46 |
| 4.2 Steady State Growth of Platinum Oxide Film | 49 |
| 4.3 Electronic Properties..... | 57 |
| 4.4 Compositions of Platinum Oxide Film | 67 |
| 4.5 Summary..... | 72 |
| References..... | 72 |

| | |
|--|-----|
| Chapter 5 GROWTH MECHANISM OF PLATINUM OXIDE FILM | 75 |
| 5.1 Interfacial Impedance Due to the Generation and Annihilation of Defects at the Interfaces and Dissolution of the Film..... | 80 |
| 5.2 Warburg Impedance Due to Transport of Defects in the Film | 88 |
| 5.3 Summary..... | 108 |
| References..... | 109 |
| Chapter 6 PH DEPENDENCE IN ALKALINE SOLUTIONS..... | 112 |
| 6.1 Electrochemical Properties | 112 |
| 6.2 Diagnostic Criteria of the PDM..... | 124 |
| 6.3 Optimization of the PDM on EIS Data as a Function of pH | 138 |
| 6.4 Summary..... | 148 |
| References..... | 149 |
| Chapter 7 CONCLUSIONS AND FUTURE WORK | 151 |
| 7.1 Conclusions..... | 151 |
| 7.2 Future Work..... | 154 |
| Appendix A AN ELECTROCHEMICAL IMPEDANCE STUDY OF ALLOY- 22 IN NACL BRINE AT ELEVATED TEMPERATURE: II REACTION MECHANISM ANALYSIS | 156 |
| Appendix B GENENERAL CORROSION OF ALLOY 22: EXPERIMENTAL DETERMINATION OF MODEL PARAMETERS FROM ELECTROCHEMICAL IMPEDANCE SPECTROSCOPY DATA... | 197 |

LIST OF FIGURES

| | |
|--|----|
| Figure 2-1: Cyclic voltammograms for platinum in 0.5M H ₂ SO ₄ at a voltage sweep rate of 50 mV/s (T = 20±2°C). Working electrode surface area = 0.32 cm ² . | 6 |
| Figure 2-2: Variation of Current density for platinum in 0.1M KOH with time at a constant oxide formation potential. The current density becomes constant after at least 12 hours indicating that the system is at steady state. | 11 |
| Figure 2-3: Current vs. voltage curve showing pseudo-linearity | 13 |
| Figure 2-4: Schematic of physicochemical processes that are envisioned to occur within the barrier oxide (MO _{x/2}) layer on passive platinum, according to the Point Defect Model. m = metal atom; V_M^{\bullet} = cation vacancy; v_m = metal vacancy in metal lattice; M_M = metal cation in a normal cation position in the barrier layer; M^{r+} = metal cation in the solution phase (outer layer); V_o^{\bullet} = oxygen vacancy; O_o = oxygen ion in an anion site in the barrier layer | 13 |
| Figure 3-1: Diagram of electrochemical cell used in the work | 43 |
| Figure 4-1: Cyclic voltammograms for platinum in 0.5M H ₂ SO ₄ at a voltage sweep rate of 50 mV/s (T = 20±2°C). Working electrode surface area = 0.32 cm ² . | 48 |
| Figure 4-2: Steady state current density for platinum in 0.5M H ₂ SO ₄ as a function of oxide formation potential, measured in both the ascending and descending potential directions. The lack of hysteresis indicates that the system is at steady state. | 50 |
| Figure 4-3: Nyquist plots for platinum in 0.5M H ₂ SO ₄ measured at different oxide formation potentials. | 51 |
| Figure 4-4: Nyquist and Bode plots for platinum at a potential of 1.24V _{SHE} , measured sequentially at descending (“down”) and ascending (“up”) frequencies. The lack of significant hysteresis indicates that the system is at steady state. | 53 |
| Figure 4-5: K-K transforms of EIS data for platinum in 0.5M H ₂ SO ₄ at a potential 1.24V _{SHE} . The good agreement between the transformed and experimental data demonstrates that the system conforms to the constraints of Linear Systems Theory | 56 |

| | |
|--|----|
| Figure 4-6: Mott-Schottky plot for platinum passivated at a formation potential of 1.39V _{SHE} in 0.5M H ₂ SO ₄ solution for 24 hours. The impedance was measured at a frequency 10k Hz while sweeping the potential in the negative direction from the formation potential at a voltage scan rate of 100mV/s..... | 59 |
| Figure 4-7: Mott-Schottky plots for platinum at different oxide formation potentials in 0.5M H ₂ SO ₄ solution after polarization for 24 hours. The impedance was measured at a frequency 10k Hz while sweeping the potential in the negative direction from the formation potential at a voltage scan rate of 100mV/s..... | 61 |
| Figure 4-8: Donor density at 20°C calculated from the Mott-Schottky plots as a function of formation potential. | 62 |
| Figure 4-9: Steady-state Mott-Schottky plot for platinum constructed from the capacitance data measured at 1194 Hz in 0.5M H ₂ SO ₄ solution at T=20°C after polarization for 24 hours at each voltage. Sinusoidal amplitude =10mV (peak-to peak). | 63 |
| Figure 4-10: Mott-Schottky plots for platinum at 1.39 V _{SHE} in 0.5 M H ₂ SO ₄ solution after polarization for 24 hours as a function of frequency. The impedance was measured at frequencies of 1 kHz, 5 kHz, and 10 kHz, while sweeping the potential in the negative direction from the formation potential at a voltage scan rate of 100 mV/s. | 66 |
| Figure 4-11: ARXPS spectra of the Pt4f regions recorded at two different takeoff angles for Pt surfaces passivated in 0.5M H ₂ SO ₄ for 24 hours at different potentials. | 70 |
| Figure 5-1: Schematic of physicochemical processes that are envisioned to occur within the barrier oxide (PtO _{x/2}) layer on passive platinum, according to the truncated Point Defect Model. $Pt \equiv$ platinum atom; $Pt_i^{z*} \equiv$ interstitial platinum cation; $v_{Pt} \equiv$ platinum vacancy in Pt metal substrate; $Pt_{Pt} \equiv$ platinum cation in a normal cation position in the barrier layer; $Pt^{F+} \equiv$ platinum cation in the solution phase (outer layer); $V_O^- \equiv$ oxygen vacancy; $O_O \equiv$ oxygen ion in a normal anion site in the barrier layer. | 76 |
| Figure 5-2: Impedance array describing the total impedance of passive platinum..... | 77 |
| Figure 5-3: Nyquist and Bode plots of impedance data for Pt in 0.5 M H ₂ SO ₄ at applied voltages of 1.19 V _{SHE} , 1.24 V _{SHE} , 1.29 V _{SHE} , 1.34 V _{SHE} , and 1.39 V _{SHE} | 97 |

| | |
|--|-----|
| Figure 5-4: Calculated and experimental steady state current density as a function of oxide formation potential. The simulated data were calculated using Equation 5.36 and the mean parameter values summarized in Table 5-2. | 102 |
| Figure 5-5: Calculated steady state current density due to the movement of platinum interstitials and oxygen vacancies as a function of oxide formation potential. The simulated data were calculated using Equation 5.36 and the mean parameter values summarized in Table 5-2. | 103 |
| Figure 5-6: Calculated steady state barrier layer thickness from the optimization of the PDM on impedance data compared with the thickness measured by Bockris [10] using ellipsometry and by the present authors using potentiodynamic cathodic reduction at a voltage scan rate 5 mV/s. | 105 |
| Figure 5-7: Unit cell of PtO with $a = b = 0.304\text{nm}$ and $c = 0.534\text{nm}$. It is proposed that the barrier layer comprises the unit cell in nanocrystalline domains with the c-axis perpendicular to the metal surface. ... | 107 |
| Figure 6-1: Cyclic voltammograms of platinum in KOH solutions with 0.01M, 0.1M, and 1M. | 113 |
| Figure 6-2: Mott-Schottky plots of platinum oxide film formed in 0.01M KOH solution as a function of film formation potential. | 115 |
| Figure 6-3: Mott-Schottky plots of platinum oxide film formed in 0.1M KOH solution as a function of film formation potential. | 116 |
| Figure 6-4: Mott-Schottky plots of platinum oxide film formed in 1M KOH solution as a function of film formation potential. | 117 |
| Figure 6-5: Mott-Schottky plots of platinum oxide film formed at potential $0.44V_{\text{SHE}}$ in 1M KOH solution as a function of sweep frequencies. | 118 |
| Figure 6-6: Mott-Schottky plots of platinum at oxide formation potential $0.44V_{\text{SHE}}$ as a function of pH, sweep rate is 100mV/s. | 119 |
| Figure 6-7: Donor concentrations of oxide films calculated according to Mott-Schottky method as function of pH. | 120 |
| Figure 6-8: Electrochemical impedance spectroscopy data of platinum oxide film in KOH solution of 0.01M, 0.1M, and 1M. | 121 |

| | |
|--|-----|
| Figure 6-9: Experimental for the reduction in thickness of the passive film on platinum as a function of pH upon stepping the potential from the high to low values. | 123 |
| Figure 6-10: Schematic of physicochemical processes that are envisioned to occur within the barrier oxide ($\text{MO}_{x/2}$) layer on passive metal, according to the Point Defect Model. $m \equiv$ metal atom; $V_M^{\times\cdot} \equiv$ cation vacancy; $M_i^{\times\cdot} \equiv$ interstitial cation; $v_m \equiv$ metal vacancy in metal substrate; $M_M \equiv$ metal cation in a normal cation position in the barrier layer; $M^{\Gamma+} \equiv$ metal cation in the solution phase (outer layer); $V_O^{\cdot\cdot} \equiv$ oxygen vacancy; $O_O \equiv$ oxygen ion in a normal anion site in the barrier layer. | 127 |
| Figure 6-11: Dependence of the steady state current density on applied potential and pH. | 133 |
| Figure 6-12: Dependence of steady state thickness of the platinum oxide film as a function of applied voltage and pH. The film thickness is obtained from capacitance by assuming that the oxide is the dielectric of a parallel plate capacitor with a leak resistance in analyzing EIS data measured at each formation potential. | 135 |
| Figure 6-13: Dependence of the steady state current on pH for platinum in KOH solution. | 136 |
| Figure 6-14: Dependence of the steady state thickness on pH for platinum oxide. | 137 |
| Figure 6-15: Nyquist and Bode plots of impedance data for Pt in 0.01M KOH at applied voltages of 0.34 V_{SHE} | 139 |
| Figure 6-16: Nyquist and Bode plots of impedance data for Pt in 0.1M KOH at applied voltages of 0.34 V_{SHE} | 140 |
| Figure 6-17: Nyquist and Bode plots of impedance data for Pt in 1M KOH at applied voltages of 0.34 V_{SHE} | 141 |
| Figure 6-18: Dependence of steady state current on pH for platinum in KOH solution. | 146 |
| Figure 6-19: Dependence of steady state current due to the transport of platinum interstitials and oxygen vacancies, respectively, on pH for Pt in KOH solutions. | 147 |
| Figure 6-20: Dependence of steady state thickness on pH for platinum in KOH solution. | 148 |

LIST OF TABLES

| | |
|---|-----|
| Table 2-1: Comparison of conditions of Mott-Schottky theory and electrochemical experiment | 20 |
| Table 2-2: Diagnostic criteria derived from Equation 2.21 and Equation 2.22 | 34 |
| Table 2-3: Rate laws of passive film growth models..... | 37 |
| Table 4-1: Atomic concentrations from Pt4f recorded at two different takeoff (T/O) angles for Pt surfaces passivated in 0.5M H ₂ SO ₄ at the indicated film formation potentials for 24 hours..... | 71 |
| Table 5-1: Rate constants $k_i = k_i^0 e^{a_i V} e^{-b_i L}$ for five interfacial reactions in terms of the Point Defect Model. | 88 |
| Table 5-2: Parameter values from optimization of the Point Defect Model on the experimental impedance data for platinum in deaerated H ₂ SO ₄ (0.5M, pH = 0.2) solution at 20°C as a function of applied potential..... | 99 |
| Table 6-1: Rate constants $k_i = k_i^0 e^{a_i V} e^{-b_i L}$ for the interfacial defect generation and annihilation reactions employed in the Point Defect Model..... | 126 |
| Table 6-2: Definition of the standard rate constants for the interfacial defect generation and annihilation reactions employed in the Point Defect Model..... | 128 |
| Table 6-3: Diagnostic criteria for determining the conductive nature of the barrier layer ($\Gamma=\chi$). | 132 |
| Table 6-4: Parameter values from optimization of the Point Defect Model on the experimental impedance data for platinum formed at 0.34V _{SHE} in deaerated KOH solutions at 20°C as a function of pH..... | 144 |

LIST OF THE PRINCIPAL SYMBOLS

| | |
|-------------|--|
| A | surface area of the electrode |
| C | interfacial capacitance |
| C_{dl} | Helmholtz double layer capacitance |
| C_g | geometric capacitance of the film, $C_g = \hat{\epsilon}\epsilon_0 / L$ |
| C_{sc} | space charge capacitance |
| C_{ss} | surface state capacitance |
| C_{H^+} | hydrogen ion concentration in the solution at the film/solution interface |
| $C_{H^+}^0$ | standard state hydrogen ion concentration, defined as being 1.0mol/l |
| C_i | concentration of metal interstitials |
| C_O | concentration of oxygen vancancies |
| D | diffusivity |
| F | Faraday's constant |
| I_{ss} | steady state current density |
| $J_i^{m/f}$ | flux of platinum interstitials through the metal/film interface |
| $J_i^{f/s}$ | flux of platinum interstitials through the film/solution interface |
| $J_O^{m/f}$ | flux of platinum interstitials through the metal/film interface |
| J_O | flux of oxygen vacancies within the barrier layer |
| k | Boltzman constant |
| k_i | rate constants for the i elementary interfacial reactions |
| k_i^0 | rate constants independent of potential and thickness for the i elementary interfacial reactions |

| | |
|------------|--|
| k_i^{00} | standard rate constant independent of potential, thickness and pH for the i elementary interfacial reactions |
| L_{Db} | Debye length |
| L | thickness of the oxide film |
| n | the kinetic order of the film dissolution reaction with respect to C_{H^+} |
| N_D | donor density |
| N_A | acceptor density |
| N_V | Avagadro's number |
| Q | charge density |
| $R_{e,h}$ | electronic resistance due to the transport of electrons and holes through the film |
| R_s | solution resistance |
| RHE | reversible hydrogen electrode |
| SHE | Standard hydrogen electrode |
| t | time |
| V | potential |
| Z'' | imaginary component of the impedance |
| Z_T | total impedance for the film growth |
| Z_f | impedances due to the interfacial reactions |
| Z_w | impedances due to the transport of ionic defects |
| $Z_{R/O}$ | the redox reaction impedance that occurs at the film/solution interface |
| Z_O | Warburg impedance due to the transport of oxygen vacancies in the film |
| Z_i | Warburg impedance due to the transport of platinum interstitials in the film |

| | |
|------------------|--|
| α | polarizability of the barrier layer/outer layer (solution) interface |
| α_i | transfer coefficients, subscript i represents the i elementary interfacial reactions |
| β | dependence of the potential drop across the same interface on pH |
| χ | oxidation state of platinum in the barrier layer in the passive state |
| $\hat{\epsilon}$ | dielectric constant of the oxide |
| ε | electric field strength |
| $\phi_{f s}^0$ | value of $\phi_{f s}$ in the standard state |
| η | overpotential |
| σ_w | Warburg coefficient |
| Γ | oxidation state of platinum in solution in the passive range |
| ν | voltage scan rate in the cyclic voltammetry |
| Ω | molar volume per cation of the barrier layer |

ACKNOWLEDGEMENTS

I can not adequately express gratitude to my advisor, Dr. Macdonald, whose guidance, encouragement and support played the greatest role in sustaining me through the challenge of this dissertation work. The Pennsylvania State University has my appreciation for providing an atmosphere conducive to finishing this work.

I want to thank all my colleagues in the group for their tremendous cooperation and help. Special thanks to Brian, Zijie, and Yingzi. Their support accompanied me through this whole dissertation work.

Finally, I would like to thank my families, my husband Zhiqiang and my son Evan. I thank them for encouraging and supporting me with their endless love and patience.

Chapter 1

INTRODUCTION

As a noble metal, platinum is often considered as being “inert”, and is thus frequently used as a catalyst for hydrogen and small organic molecule oxidation, as well as for oxygen reduction in the fuel cells. However, it has been found that platinum is passivated at fuel cell cathodic operating potentials of about 0.8V vs. RHE (Reversible Hydrogen Electrode) in acid solution, and that the rate of oxygen reduction is significantly lower on the passive film covered platinum surface than on a film-free surface.

It has been known for many decades that the oxide films present on metals play critical roles in determining the rates of redox reactions at the surfaces, since charge carriers must transit the oxide for the reaction to occur. Thus, the film acts as a barrier through which charge carriers must quantum mechanically tunnel and the extreme dependence of the tunneling constant on the film thickness is such that films of only a few monolayers thickness may substantially inhibit the reaction. On the other hand, there exists the possibility that crystallographic defects in the surface of the oxide film (e.g., surface oxygen vacancies) may act as reaction sites in the catalytic sense and hence act to enhance the reaction rate. Little progress is likely to be made in designing new electrocatalysts at the fundamental level until these factors are understood.

The present dissertation is tightly focused on characterization of the passive state on Pt under oxygen reduction reaction conditions, in order to develop viable model for

electron transfer and hence to establish theory-based rules for designing new electrocatalysts.

In this work, we :

- 1) Studied the transient and steady state growth of the oxide film on Pt by electrochemical methods, such as cyclic voltammetry, potentiostatic polarization, and electrochemical impedance spectroscopy (EIS)
- 2) Defined the electronic properties of the oxide film on Pt. Since a large number of defects exist in the barrier oxide layer, it is possible that these defects might be involved catalytically in the oxygen reduction reaction. The identity of the principal defects is determined from the diagnostic criteria afforded by the Point Defect Model (PDM) [1] and from Mott-Schottky analysis.
- 3) Determined the physical structure and film thickness of the oxide film by X-ray Photoelectron Spectroscopy and Ellipsometry, respectively.
- 4) Further develop the Point Defect Model for describing nano scale oxide films on metal surfaces as a function of formation conditions (temperature, pH etc.) by the analysis of EIS data.

The material presented in this thesis is divided into 7 chapters. The research objectives and thesis arrangements are presented in Chapter 1. Chapter 2 serves as a general introduction to the properties and growth mechanisms of the oxide film on platinum and is intended to provide sufficient background information to permit an intelligible appreciation of the material that is developed in later chapters. Experimental techniques are discussed in Chapter 3, in particular the electrochemical impedance

spectroscopy and capacitance measurements. Chapter 4 contains a detailed characterization of oxide film on platinum under transient and steady state conditions in acid solution by electrochemical techniques (EIS, potentiostatic polarization, and cyclic voltammetry) and by physical characterization methods (XPS, ellipsometry). This material provides experimental verification of the growth mechanism described in Chapter 5. Chapter 5 examines the EIS data obtained under steady state conditions for oxide film growth as interpreted using the PDM, and extracts values for various parameters (including kinetic parameters for the generation and annihilation of point defects within the barrier layer) in the model that predict the steady state thickness and current. Chapter 6 is devoted to the study of kinetics of growth of oxide films on platinum in alkaline solution as a function of pH. The new diagnostic criteria are derived for the model that includes the production and annihilation of metal interstitials at the interfaces. Conclusions and recommendations for future work are presented in Chapter 7.

References:

- [1] D.D. Macdonald, J. Electrochem. Soc., 139 (1992) 3434.

Chapter 2

BACKGROUND

During the past decade, the interest in developing the fuel cell, especially the Proton Exchange Membrane Fuel Cell (PEMFC), for generating clean and efficient power for the automotive industry has increased dramatically. One of the prime factors, which will decide the future of this technology, lies in the advancement of electrocatalysis science and technology for both anode and cathode [poor oxygen reduction reaction (ORR) kinetics] electrode processes.

Although a great deal of effort has been invested over many decades in studying the kinetics of the oxygen reduction reaction on platinum and other noble metals, the reaction mechanism and the role of surface oxide films on the electrocatalytic properties of the substrate remain controversial. Of particular importance is the lack of emphasis in current models on the properties of the passive oxide film, particularly on the crystallographic and electronic defect structures. It has been known for many decades that the oxide films present on metals play critical roles in determining the rates of redox reactions at the surfaces since charge carriers must transit the oxide for the reaction to occur. Thus, the film acts as a barrier through which charge carriers must quantum mechanically tunnel. The extreme dependence of the tunneling constant on the film thickness is such that films of only a few monolayer thickness may substantially inhibit the reaction. On the other hand, there exists the possibility that crystallographic defects in the surface of the oxide film (e.g., surface oxygen vacancies) may act as reaction sites

in the catalytic sense and hence act to enhance the reaction rate. Little progress is likely to be made in designing new electrocatalysts at the fundamental level until these factors are understood.

2.1 Characteristic of Oxide Films on Platinum under Transient Conditions

As a very powerful transient technique, cyclic voltammetry has been widely applied for acquiring qualitative information about electrochemical reactions. The power of this technique results from its ability to examine both the thermodynamic and kinetic aspects of electrochemical surface processes (i.e., the redox potentials, the stability of the different oxidation states, and adsorption processes). In cyclic voltammetry, the potential is scanned linearly over a working electrode by using a triangular potential waveform. During the potential sweep, the potentiostat measures the current resulting from the applied potential. The resulting plot of current vs. potential is termed a cyclic voltammogram.

The cyclic voltammogram of platinum in acid solutions (Figure 2-1) has been extensively investigated due to its “model” surface for studies of hydrogen chemisorption, and electrocatalysis in electrochemical surface science [1]. As Figure 2-1 shows, the voltammogram of platinum may be divided into 3 regions, hydrogen region, double layer capacitance region, and oxide region. In the hydrogen region, the symmetrical peaks in both the anodic and cathodic directions indicate that the adsorption of hydrogen on platinum is reversible. The quantity of the hydrogen adsorbed at a potential considerably anodic to the reversible hydrogen potential could be determined by integrating the charge

passed in reaching that potential. The real surface area of the platinum electrode can thus be determined according to the quantity of charge corresponding to the saturation hydrogen coverage by assuming that each surface platinum atom is associated with one chemisorbed hydrogen atom. The characteristic of hydrogen adsorption also provide a good test of the cleanliness of the system; such as a blurring of the details in the hydrogen region due to the existence of impurities.

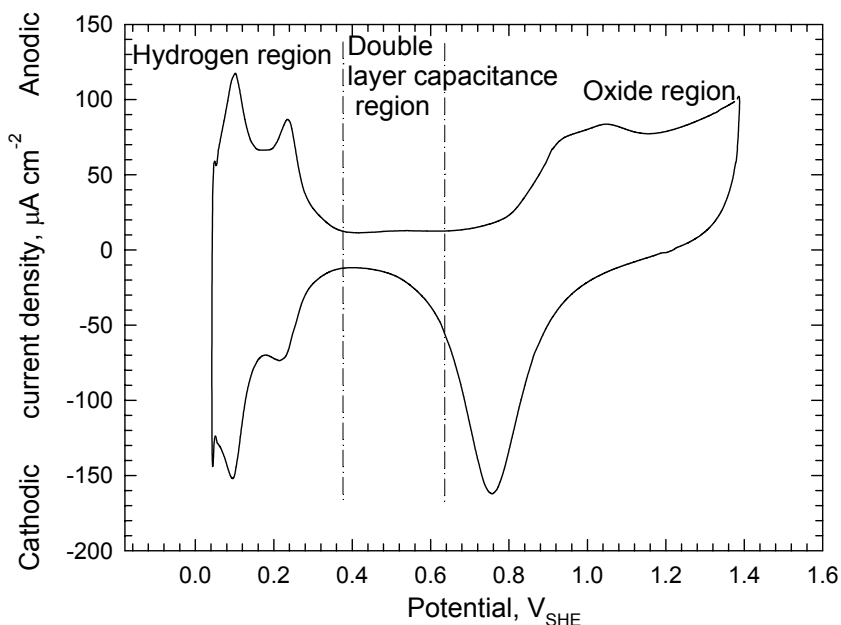


Figure 2-1: Cyclic voltammograms for platinum in 0.5M H₂SO₄ at a voltage sweep rate of 50 mV/s ($T = 20 \pm 2^\circ\text{C}$). Working electrode surface area = 0.32 cm².

Many aspects of the platinum oxide formation process have been studied by cyclic voltammetry, e.g., the irreversibility of oxide formation and imbalance between charge for oxide formation and reduction after double layer capacitance correction. Rand and Woods [2] noted that if the curve of charge imbalance as a function of anodic potential limit is extrapolated to zero, then the corresponding potential value at zero charge

imbalances is consistent with the standard potentials of the metal/metal-ion couples. Therefore, they concluded that the charge imbalance occurs due to the metal dissolution during the anodic process. Since the standard potential corresponds to the bulk Gibbs energy, this result provides a thermodynamic support that the oxide on platinum is a phase oxide.

The structure of the oxide film on Pt has been substantially investigated using cyclic voltammetry. For example, Shibata [3] studied the formation and reduction of the anodic oxide film on platinum and suggested that the oxide film comprises two layers, a thin, monolayer (referred to as the α -oxide) and a thick, quasi-3-D layer (referred to as the β -oxide), with the latter forming at higher potentials. It has also been suggested that a thicker oxide layer grows between the platinum metal substrate and the monolayer. However, Gottesfeld et al. [4] later found that the growth of the thick layer of β -oxide has an effect on the oxygen evolution reaction. They concluded that the thick oxide layer must be the outer layer. i.e., a structure of Pt/thin film (α -oxide)/thicker film (β -oxide)/solution is present. Conway et al. [5] used cyclic voltammetry to indicate that a “monolayer oxide” lies beneath the thick film and that the formation and reduction process of this monolayer is independent of the growth of the thick film. Their studies also showed that the thick, outer film is microscopically porous and enables the 2-D inner oxide film to be regenerated beneath it as though the outer layer does not exist. This bilayer structure is an integral part of the Point Defect Model (PDM) [6]. This model proposes that the inner (barrier) layer forms directly from the metal via the generation and annihilation of oxygen vacancies at the metal/barrier layer interface and at the barrier

layer/outer layer interface. The model also proposes that the outer layer forms by hydrolysis and precipitation of cations transmitted through the barrier layer or by restructuring of the outer surface of the inner layer.

As the oxide formation on platinum is a relatively slow process and hence the oxide formation is dependent on both potential and time [7], Vetter and Schultze [8] measured that the dependence of oxide formation on potential and time. They found that the thicknesses obtained by integrating the charge passed in reaching a given potential increases linearly with the potentials and increases logarithmically with time. In another study, Conway and Jerkiewicz [9] explored anodic oxide growth on a platinum single crystal surfaces (100 and 111) and polycrystalline platinum in acidic solutions at 25°C. The thickness of both the thin inner layer and the thick outer layer was also found to increase logarithmically with time. Furthermore, some observations reported by Biegler and Woods [10] and Biegler et al. [11] showed that the film growth on platinum surface reaches a limit as the potential increases. Biegler et. al. [11] attributed the discrepancies between their observations and other authors' work to the difference in experimental conditions. They suggest that the formation potential used by other investigators is not high enough to reach the point where the film growth is limited. In their study, the oxide is considered to be composed of one single oxide species. The same phenomenon was also noted by Conway et al. [12] in considering the structure of the platinum oxide layer. The reduction peak corresponding to the inner layer of the platinum oxide was found to remain constant at a value of $880 \mu\text{C cm}^{-2}$, and to be independent of the increasing quantities of oxide in the outer layer. Conway et. al. thus concluded that only the inner layer reaches a limit

as the potential increases while the outer layer continuously grows without reaching any limit.

A large amount of work, using mostly cyclic voltammetry, has been reported in which various oxidation/reduction peaks in the i - V profiles have been resolved to indicate the composition and mechanism of electrochemical formation and reduction of platinum oxide films. However, cyclic voltammetry does not readily provide information concerning the crystallographic and electronic defects in the oxide film under steady state conditions and it is currently unable to provide detailed kinetic data for the complex heterogeneous reactions interacting with mass transport.

2.2 Steady State Growth of Oxide Film

Information obtained at constant potential allows the effects of potential and time to be investigated separately. Steady state is usually defined as the state of a system in which the conditions do not change over time. A large number of electrochemists claimed that their passive systems attain steady state after maintaining a given potential for a short time, e.g. 10 seconds, 20 minutes, 1 or 2 hours. However, as shown in Figure 2-2, the current density only remains constant with time at a given passive potential after at least 12 hours. Therefore, the steady state condition should be tested when any techniques based on this condition are applied to a system. Macdonald et al. [13, 14] have suggested several methods for testing stability of the system. One method is to measure the current in the positive (“up”) and negative (“down”) potential step directions for the potentiostatic experiments; a lack of hysteresis demonstrates that the

system is at a steady state during the measurements. Electrochemical Impedance Spectroscopy (EIS) as a technique for obtaining information from a linear system requires that the system must be stable to ensure that the data are valid. Because a steady state interface should afford the same response regardless of whether the measurements are made in the forward or reverse frequency sweep directions, the impedance plots should be in good agreement when the frequency is scanned (stepped) from low to high values and then immediately stepped in the reverse direction. Kramers-Kronig transforms were also modified and employed first by Macdonald et al. [15] to examine the impedance system with respect to the linearity, causality, and stability constraints of Linear Systems Theory. By transforming the real axis into the imaginary axis and the imaginary axis into the real axis and then comparing the transformed quantities with the respective experimental data, the system is tested for the stability.

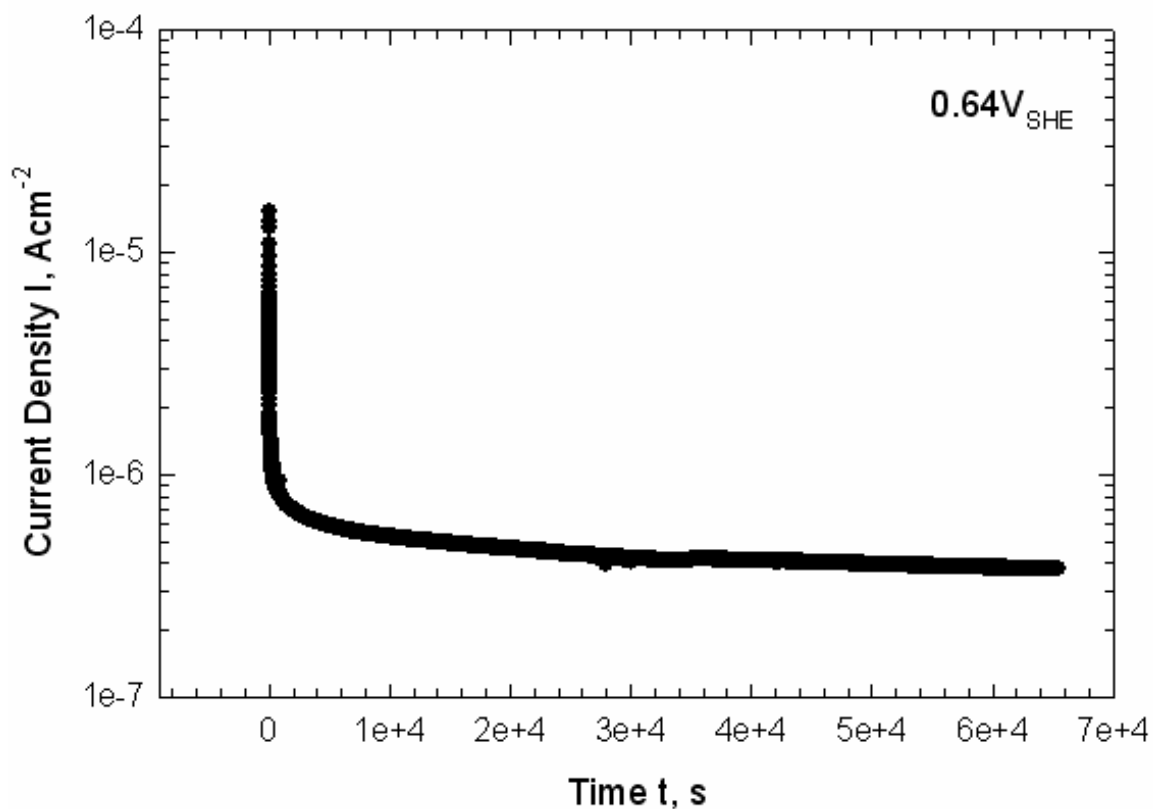


Figure 2-2: Variation of Current density for platinum in 0.1M KOH with time at a constant oxide formation potential. The current density becomes constant after at least 12 hours indicating that the system is at steady state.

As a powerful technique for *in situ* characterization of electrochemical surface systems, EIS has become very popular in investigating the mechanisms of electrochemical interface reaction, and evaluating the behavior of material in corrosive environments. The advantages of this technique are many. First, the linearity, stability, and causality requirements of the technique enable the results to be readily interpreted by linear system theory. Secondly, the integration over many cycles enhances the signal to noise ratio so that the experimental efficiency is very high. In addition, the experimental bias errors are allowed to be tested by Kramers-Kronig relations. A brief review of the

basic electrochemical theoretical basis for EIS follows for additional background information.

It has been observed for a hundred years that the current varies exponentially with the overpotential for charge transfer reactions occurring at interfaces under activation control [16]. This relationship discovered empirically is the foundation of electrochemical kinetics and referred to as the Tafel equation (Equation **2.1**) .

$$i = i_0 \left(e^{-\alpha n \eta F / RT} \right) \quad (2.1)$$

In Equation **2.1**, i is the current density, i_0 is the exchange current density corresponding to $\eta=0$, η is the overpotential ($\eta = E - E^e$), E is the applied potential, E^e is the equilibrium potential, α is the transfer coefficient, n is the charge number, F is Faraday's constant, R is the universal gas constant, T is the Kelvin temperature.

A linear form of Equation **2.1** arises for sufficiently small η values when e^x is approximated as $1+x$ when x is sufficiently small. Equation **2.1** can then be written:

$$i = i_0 (-nf\eta) \quad (2.2)$$

which shows that the net current is linearly proportional to the overpotential in a narrow potential range near the equilibrium potential of the system. The ratio of η/I has dimensions of resistance and is often called the charge transfer resistance [7].

This linear relationship of current-overpotential is the theoretical basis of the EIS technique. As Figure **2-3** shows [17], the system is pseudo-linear if a very small AC potential (5-10mV) is applied to the system with respect to a constant DC potential under steady state conditions. Electrochemical impedance is thus measured by applying an AC

potential to an electrochemical interface and measuring the current response as the excitation frequency changes. In a linear system, the current response to a sinusoidal potential will be a sinusoid at the same frequency but shifted in phase. An expression analogous to Ohm's law for calculating the impedance of the system is then:

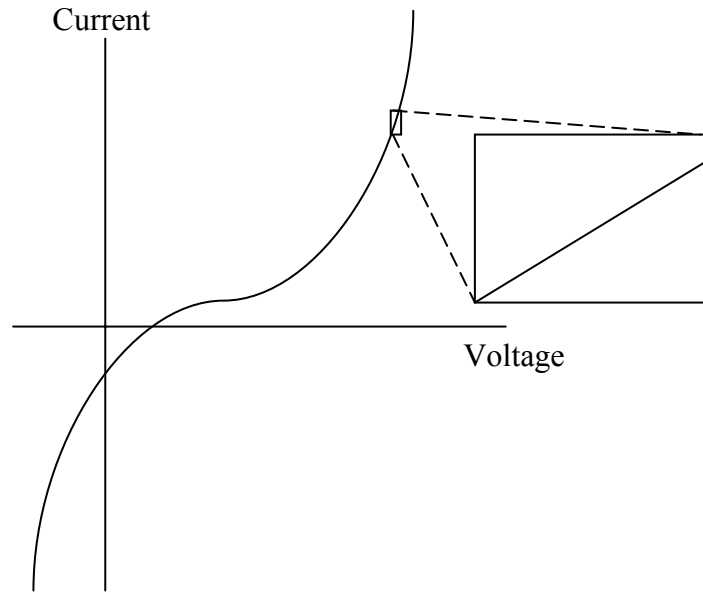


Figure 2-3: Current vs. voltage curve showing pseudo-linearity

$$Z = \frac{E_t}{I_t} = \frac{E_0 \sin(\omega t)}{I_0 \sin(\omega t + \phi)} = Z_0 \frac{\sin(\omega t)}{\sin(\omega t + \phi)} \quad (2.3)$$

The impedance equations describing these processes are often more simple to solve in frequency space (Laplace or Fourier) than in temporal space. Thus, the impedance equations in the time domain are transformed to Fourier domain in order to solve the problem. The solutions are then transformed back to real-time space. The Fourier domain impedance is expressed as a complex number, $Z(\omega)$,

$$Z(\omega) = Z_0 \exp(j\phi) = Z_0 (\cos \phi + j \sin \phi) \quad (2.4)$$

where Z_0 is the magnitude of the impedance $Z_0 = \sqrt{Z'^2 + Z''^2}$, and ϕ is the phase angle $\tan \phi = -Z'' / Z'$. Equation 2.4 leads directly to the two common forms for displaying impedance data: the Nyquist plot (Z' vs. Z'') and the Bode plot ($\log Z_0$ and ϕ vs. $\log \omega$).

The interpretation of the EIS data is usually categorized into two approaches: 1) analogs, and 2) physical models. Models based on electrical circuit analogs to the data are widely applied in the industrial environment. The electrical elements, such as capacitor, resistor, and inductors, are assigned to the experimental phenomena, and the impedance locus is then reproduced. The polarization resistance, charge transfer resistance, or double layer capacitance etc. as the model parameter is thus extracted from the regression of equivalent electrical circuit model. It must be noted that the equivalent electrical circuit for the system is not unique and there may be other analogs that represent the data equally well within the accuracy of the data. Therefore, the physics of the system can not be described accurately according to the analogs. It's also not possible to demonstrate compliance of the system with linear systems theory with inaccuracy in the physics. A second approach is to develop the models based on charge transfer reactions that occur at the interfaces. The kinetic equations are solved in terms of frequency dispersion of the impedance and the kinetic parameters from the optimization to the experimental results are obtained. Several groups [6, 18, 19] have been developing the reaction mechanism model using EIS. For example, an impedance model based on PDM has been used to describe the passive film growth. Priyantha et al. [20] have successfully applied EIS to

study the passive film on Alloy-22 in NaCl solution and have extracted kinetic parameters for the multi-step reaction mechanisms.

Few investigations of platinum anodic oxide film using EIS are in the literature. Harrington et al. [21, 22] claim that the EIS is not qualified for studying anodic oxide film formation on Pt because the oxide growth follows the logarithmic rate law, which implies that the oxide continues growing at a constant potential without achieving steady state. The ac voltammetry data of platinum oxide formation were thus collected for one frequency per sweep cycle and the frequency dispersions were analyzed to extract the rate constants using the impedance plane. However, as we have stated above, the film will not grow infinitely and steady state must be achieved for film growth at a constant potential. In addition, the test for K-K consistency of Harrington's impedance results [22] shows that the impedance data at low frequencies (1Hz to 100Hz) have large system deviations. Harrington explained that these are due to the lack of lower frequency data. However, this could also be accounted for by the instability of the system caused by the measurement technique. Some EIS work which is related to platinum oxide has been reported by Glarum [23] and Conway [24] et. al. Formation of oxides in their study does not reach steady state and the analysis of EIS data are qualitative and does not provide kinetic information of oxide formation.

2.3 Solid State Properties

Solid state properties for thin oxides tend to be incomplete. Little work has been published on oxides of the noble metals such that the main purpose of this section is to

review the properties obtained from the appropriate techniques; such as the photoelectrochemical technique and capacity measurements.

As Stimming described [25], a photoelectrochemical reaction on a passive metal electrode can simply be either the current change at constant potential or a potential change at constant current from an electrochemical reaction at the electrode/electrolyte interface when a certain range of light is absorbed by the passive film. Depending on the properties of the passive film with respect to its conduction type, different energetic conditions can be distinguished for an n-type or p-type semiconductor or an insulating film. The flatband potential could be obtained from the extrapolation of potential dependence of the photocurrent and can be compared with values obtained from capacity measurements.

There have been several studies on the photoelectrochemical behavior of anodic platinum oxide film. Rudge et al. [26] reported that small anodic photocurrents were detected in the potential region that permits formation of the thin oxide, and with the formation of the thick oxide the photocurrent transient becomes cathodic. The same result has also been observed by Vinnikov et al. [27] and interpreted as a characteristic of n type semiconductors for thin oxide and p-type for thick oxide. Felske and Plieth [28] investigated the thin oxide layer using pulsed laser irradiation in stead of traditional continuous light and observed an anodic current for this thin oxide.

Little is known about the charge distribution in the anodic platinum oxide film. Capacitance measurements, the potential dependence of film capacity analyzed by Mott-Schottky methods, are a good means to determine the charge distribution in the passive

film. The electronic properties of the film are thus obtained; such as defect concentration, the flatband potential, and the electronic type.

The classical Mott-Schottky equations [29] are derived for the space charge layer from the Poisson equation:

$$dV/dx = \rho / \varepsilon \varepsilon_0 \quad (2.5)$$

we then have,

$$d^2V/dx^2 = -(N_{sc} e / \varepsilon \varepsilon_0) [\exp(-eV / kT) - 1] \quad (2.6)$$

The linear relation between the inverse square of the space charge capacity and the applied potential is then found and written as follows

$$\frac{1}{C_{sc}^2} = \frac{2}{\varepsilon \varepsilon_0 e N_A A^2} \left(V - V_{fb} - \frac{kT}{e} \right) \quad \text{n-type} \quad (2.7)$$

$$\frac{1}{C_{sc}^2} = \frac{-2}{\varepsilon \varepsilon_0 e N_A A^2} \left(V - V_{fb} - \frac{kT}{e} \right) \quad \text{p-type} \quad (2.8)$$

where ε is the dielectric constant of the oxide, A is the surface area of the interface, and ε_0 is the vacuum permittivity. C_{sc} is the space charge capacitance of the semiconductor. e is the charge of the electron (1.6×10^{-19} C), N_D and N_A are the donor density and acceptor density (cm^{-3}), respectively, and V_{fb} is the flat band potential (V vs. SHE). Thus the impedance is measured at a high frequency (on the order of kHz) in which the response is only electronic due to negligible ionic conductivity and the result is analyzed in terms of

the equivalent circuit of a series combination of a resistor and a capacitance. The capacitance is then calculated from the imaginary component of the impedance using the relationship $Z'' = 1/2\pi fC$.

Although Mott-Schottky equations are derived for a single type semiconductor, the pn junction capacitance has a similar dependence on the applied potential. For one-sided junction such as a p^+n junction the main defect density can also be calculated according to Mott-Schottky equations. The passive film is often described as a inverse pn junction by a model [6, 30] in which defects in the film are the main charge carriers for passive film growth. The Mott-Schottky method is thus appropriate to be applied to study the electronic properties of the film. The PDM describes that the electronic structure appears to correspond to that of an n-i-p junction [31]. The electronic structure appears to resemble that of a classical tunnel junction, that is obtained by interfacing two heavily doped n and p type materials. These junctions have two important properties as far as passive films are concerned [16]; (i) the depletion region is very thin (typically 0.5-2 nm), depending on dopant concentration and hence can be accommodated within the known thickness of the barrier film, and (ii) the electric field strength is constant due to Esaki tunneling. As the voltage applied across the film is varied, the width of the depletion region rather than the electric field strength changes. Assuming that the depletion region occupies the entire barrier film thickness, the variation in the width of the depletion region with applied voltage is expected to correspond closely with the change in the thickness of the barrier film.

Linear Mott-Schottky plots are often observed, but at times experimental results show a deviation from the ideal Mott-Schottky behavior. One question that merits

consideration is, “Is the theory in confluence with experiment?”. As stated by Morrison [29], there are several contributions to the capacity at a semiconductor (passive film)/solution interface. The measured interfacial capacitance is estimated as follows:

$$C^{-1} = (C_{sc} + C_{ss})^{-1} + C_H^{-1} \quad (2.9)$$

where C_{sc} is the space charge capacitance, C_{ss} is the surface state capacitance, and C_H is the Helmholtz double layer capacitance. In order to simplify the above equation to $C^{-1} = C_{sc}^{-1}$, the classical Mott-Schottky theory includes several assumptions. For example, the surface states is assumed. In addition, the double layer capacitance is assumed to be much greater than the space charge capacitance in the film (barrier layer). However, as has been shown in many studies, including this work, the anodic oxide film formed on platinum in the oxygen reduction region is only a few monolayers thick. The Debye length is of the same order as the thickness of the depletion layer, thereby negating the assumption that the dimension is infinite in the through-thickness direction. Thus, the assumption that the potential approaches the bulk value asymptotically is not valid. Also, slow transfer of the electrons to/from surface states due to an insufficiently high sweep frequency applied during the experimental measurements of the capacitance may cause the surface state capacitance C_{ss} not to be negligible compared with C_{sc} . This may then give rise to a frequency-dependence of the capacitance in the Mott-Schottky plots. Table 2-1 lists several of the conditions that will not be sufficiently fulfilled in electrochemical experiments [32].

Table 2-1: Comparison of conditions of Mott-Schottky theory and electrochemical experiment

| | Theory | Electrochemical Experiments |
|-----------------------------------|--|--|
| 1)Capacitance | Space charge capacitance | Interfacial capacitance |
| 2)Junction type | Abrupt junction | Exponentially graded |
| 3)Spatial distribution of defects | Uniform | Non-uniform distribution is possible due to a pretreatment of sample |
| 4)Dielectric constant | Independent of frequency | Dependent of frequency |
| 5)Surface states | Not present | present |
| 6)Interface dimension | Plannar and two-dimensionally infinite | Electrode defects and two-dimensionally finite |
| 7)Electrolyte resistance | Not present | Present |

Therefore, the application of Mott-Schottky theory in electrochemical experimentation to study the electronic properties of passive film should be regarded as being only semi-quantitative. Other techniques such as photoelectrochemical experiments and chemical analysis technique should be combined with capacitance measurements in order to describe precisely the solid state properties of a passive film.

2.4 Composition, Microstructure and Morphology

2.4.1 Composition

Controversy remains concerning the composition of the anodic oxide film formed on platinum. Determining the composition as a function of various independent variables is currently an active research area in this field. In attempts to clarify the chemical

composition of the oxide layer(s), various surface structural and analytical methods have been used to characterize the interface. Conway [1] suggests that, upon the basis of linear potential sweep voltammetry, film formation results in the storage of a charge of 1800 $\mu\text{C}/\text{cm}^2$, corresponding to the formation of two monolayers of inner “PtO” (880 μC per cm^2) and one monolayer of outer “PtO₂” (another 880 μC per cm^2). Therefore, the thick Pt(IV) oxide resides on top of the thin Pt(II) oxide. A number of surface characterization techniques have been employed to identify the composition of the anodic oxide film at platinum.

The most direct way of deducing the chemical identity is by X-ray photoelectron spectroscopy (XPS). The XPS measurement involves the ejection of core electrons from an atom by irradiation with soft X-rays followed by energy analysis of the photoelectrons. The resulting core electron binding energies are a function of the oxidation state of the emitting atom. Thereby, XPS is able to provide information about the oxidation state of the atom undergoing photo emission. Only photoelectrons emitted from the first several atomic layers of the sample escape without losing most of their energy as a result of collisions with the atomic lattice. Therefore, XPS is a surface technique that routinely analyzes approximately 0 to 50 angstroms of the sample. XPS thus is applied widely in the study of the chemistry of metal surfaces.

The postulated composition, as determined by XPS [33-35], for the α -oxide (barrier layer) and β -oxide (outer layer), includes components of PtO, PtO₂, Pt(OH)₂ and Pt(OH)₄. The degree of hydration of the species is difficult to identify using exclusively XPS due to the existence of carbon on the surface which produce C-O and C=O bonding species thus disturbing the analysis of O-1s spectra. Birss et al. [36-38] utilized an

electrochemical quartz-crystal microbalance (EQCM) to show that the thin film on Pt is anhydrous in nature (PtO). This has also been proved recently by Jerkiewicz et al. [39] using combined EQCM and AES.

It is also noteworthy that some deviation from stoichiometry will exist in the anodic oxide film due to the semiconductor character of the film. As we have discussed in section 2.3, the thin platinum oxide shows semiconductive character. Therefore, for an n type oxide, the oxide can be represented by $M_{1-x}O_{1+y}$.

2.4.2 Microstructure

The structure order of anodic platinum oxide formed at potentials before the onset of oxygen evolution remains a subject of controversy even though the surface structure changes at Pt during oxide film formation and reduction have been extensively investigated [40-44]. STM work coupled with cyclic voltammetry by Itaya et al. [43] suggests that if thin oxide film is formed on an electrochemically inactivated surface of single crystal platinum, the structure order of the single crystal surface will be maintained. It is claimed by Ross et al. [40, 41] that the thin oxide on platinum is amorphous according to the invisible LEED spots for the film formed at $1.7V_{RHE}$. They also attributed the attenuated LEED spots for film formed between $1.2-1.7V_{RHE}$ to the partial oxidation of the surface. However as our results and other researchers' work show, the oxide film formed at a potential over $1.4V_{SHE}$ has two different structures corresponding to the two chemical layers of the oxide film. The hydroxide outer layer [36, 37] usually

has a granular and amorphous structure due to the incorporation of water molecules [45]. The lack of crystalline order of the oxide film could thus be assigned to the formation of a hydroxide outer layer.

2.4.3 Morphology

The morphology of electrochemically activated platinum surfaces has been investigated by both *ex situ* [46] and *in situ* STM [47, 48]. *Ex situ* STM by Vazquez et al. [46] reports that rough structures (~ 50 Å), that are caused by defects produced in the mechanical polishing stages, were frequently observed on polished Pt surfaces. Comparison of platinum electrode surfaces morphologies before and after electroactivation shows a significant change of the surface structure. Itaya and coworkers [48] found that the atomic flat surface before electroactivation changes to diatomic height islands after electroactivation. A microscopic model could thus be developed to describe the film growth according to the work by STM.

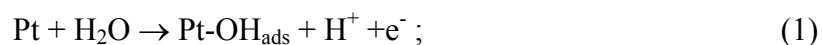
Although much work has been published on the study of the surface structure changes and morphology of the electroactivated platinum electrode surface, the amount of published information on the structure order and morphology of platinum oxide film formed on unelectroactivated surface is severely insufficient. These properties of the platinum oxide film need to be further explored by *in situ* observation in solution by STM and LEED etc.

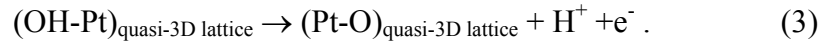
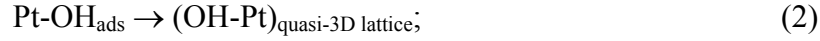
2.5 Growth Mechanism

Due to its noble metal property, no dissolution product exists on the platinum electrode surface before anodic oxidation. Platinum thus becomes an ideal metal for investigating the process of oxide formation from its initiation, through monolayer, to growth of the thick multilayer oxide. A few models have been proposed previously to describe anodic oxide film growth at the platinum electrode. However, due to controversy regarding the rate determining step in each model, no consensus exists about the kinetics of film growth on platinum. Here we briefly review the Place Exchange Model (PEM), the High Field Model (HFM), and the Nucleation and Growth Model (NGM). The PDM will be reviewed in detail since this model is applied in our current work to account for the passivity of platinum.

2.5.1 Place Exchange Model

The Place Exchange Model (PEM) is the most well known mechanism for describing the initial growth of platinum oxide. It was first proposed by Trapnell et al. [49] to account for the initial oxidation of metals. Sato and Cohen [50] then derived a mathematical expression for the rate of film growth on iron by considering the transfer probability of oxygen from the OH^- to the oxide and the activation energy for an equivalent ion pair exchange. They did not treat the kinetic of film growth. Reddy et al. [51] suggested the following formation path for thin platinum oxide in aqueous H_2SO_4 and derived a direct logarithmic rate law of film growth at platinum.





where reaction (1) refers to the oxidation of H₂O molecules with the formation of an adsorbed hydroxyl group, reaction (2) represents the interfacial place exchange between OH_{ads} and surface platinum atoms that leads to formation of a quasi-3D lattice, a rate determining step, and reaction (3) stands for the subsequent oxidation of Pt within the quasi-3D lattice resulting in the departure of H⁺. The reaction rate is thus written in terms of Tempkin theory by

$$\frac{dq_{ox}}{dt} = nk \exp[(1 - \beta)VF / RT] \exp(-aq_{ox}) \quad (2.10)$$

The integration of Equation 2.10 yields

$$aq_{ox} = \text{const} + [(1 - \beta)VF / RT] + \ln t \quad (2.11)$$

which is consistent with the experimental observations.

Conway et. al. [52, 53] further explored the formation mechanism by cyclic voltammetry etc, and categorized the above reactions into two potential regions. Reaction (1) is ascribed to reversible physical adsorption of OH⁻ at the electrode surface and the sequential formation of several surface compounds such as Pt₄OH, Pt₃OH, and Pt₂OH in the 0.85-1.10V potential region. Reaction (2) and (3) occur in the potential region (1.10-1.40 V) in which place exchange occurs and 2-D phase oxide is formed. The rate of film growth developed on the basis of adsorption theory was then applied to produce the transient *i-V* profile. This shows that the adsorption theory is in pretty good agreement with the experimental results below 1.2V, but as potential increases, the deviation from

the experimental results also increases. They suggest that this is due to the initial stage of oxide formation being reversible adsorption, in agreement with adsorption theory, and as the potential moves into the phase oxide formation region a place exchange mechanism becomes dominant.

Work by Birss [36] and Jerkiewicz et al. [39] using an electrochemical quartz-crystal nanobalance indicates that the OH group is not involved in the oxide formation as an intermediate. Jerkiewicz [39] thus modified the mechanism suggested by Conway [52, 53] and proposed a two electron reaction mechanism in which the O_{chem} adatom acts as an intermediate and the lateral repulsion between the Pt-O dipoles promotes the place exchange between the first half monolayer O_{chem} and the surface platinum atom. Harrington [54] developed a noteworthy model in which the OH group is also omitted and the Pt-Pt bonding break is the rate limiting step. The surface reconstruction observed by CV, STM, and LEED etc. after a few cyclic sweeps is thus accounted for by the model.

2.5.2 High Field Model

After Mott first proposed a passive film formation theory, Cabrera and Mott [55] presented a detailed ionic conduction model for the formation of very thin films. In this model, they assumed that the film is formed due to the transport of cations, assisted by a high field existing in the film, through the film to the film/solution interface in which they react with the electrolyte. The rate determining step is thus the injection of metal cations from the metal into the film. The reaction rate is then

$$dL / dt = u \exp\left(\frac{qa'}{kT} \varepsilon\right) = u \exp\left(\frac{qa' V}{kT L}\right) \quad (2.12)$$

where $\varepsilon = V/L$, ε being the electric field strength, V being the potential difference between the metal and the electrolyte, which is constant through the film and independent of the film thickness.

By neglecting the higher order terms in $2LkT/qa\phi_f$, an approximate integration of Equation 2.12 yields an inverse logarithmic law (Equation 2.13).

$$1/L = A - B \ln t \quad (2.13)$$

Ord and Ho [56] first tested the validity of a high field model on the formation of platinum oxide film. As Equation 2.12 indicates, the logarithm of current density is proportional to the field strength. The Tafel slope is hence proportional to the thickness since the potential is assumed to be constant and thus is independent of thickness according to the model. A linear relationship between Tafel slope and formation potential was then observed from the ellipsometry experiments although the analysis approach is questionable [56]. In the same time period Vetter and Schultze [57] proposed a similar high field ion conduction mechanism for thin film growth at platinum with a similar mathematical description of reaction rate and growth law. A detailed and specific description of the physical process of film growth is suggested by Vetter and Schultze. In their model, a place exchange reaction of platinum ions is assumed to occur at the metal/film interface and to produce the oxygen vacancies. These vacancies migrate through the film in the electric field to the film/solution interface and are filled with adsorbed oxygen ions at the interface. The platinum interstitials are simultaneously

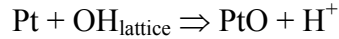
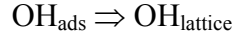
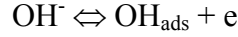
produced at the metal/film interface during the place exchange reaction and migrate in the same direction of migration as the oxygen vacancies to the film/solution interface. At the interface, the interstitials and the oxygen ions form a neutral oxide. As similar physical growth process has also been described in more detail by Macdonald [6, 58] in PDM as a function of the inverse direction of film growth. This is supported by a large volume of experimental work.

Damjanovic et al. [59-62] investigated the anodic film formation on platinum under various conditions, such as pH and temperature, following the theory of Cabrera-Mott [55]. From a pH dependence study, they found that the exchange current density is dependent on pH in alkaline solution. This is not expected for the model of high field assisted formation of films either with the step at the metal/oxide interface or step within the film as the rate determining step. Thus it is concluded that r.d.s. is actually a process at the oxide/solution interface with OH^- and H_2O as reaction species in alkaline solution and acid solution, respectively. However as Macdonald [6, 58] and other researchers remark, the dissolution of the film is present at the film/solution interface, which makes the above assumption, the emission of anions from the solution into the film as the rate determining step, impossible.

2.5.3 Nucleation and Growth Model

Nucleation and growth of a new phase on a surface under controlled potential conditions has been extensively studied by Fleischmann et al. [63]. It is assumed that nuclei form at discrete centers and grow laterally across the surface when a controlled

potential is applied. The following paths for the initial stages of film growth on platinum written by the author are therefore assumed according to Fleischman's electrocrystallization theory.



Total electrochemical free energy of a nucleus is dependent on contributions from the electrochemical potential and the area of the nucleus. Thus, the rate constant of nucleation is written as [63]

$$I_n \approx Z \left\{ \frac{(n\eta\varepsilon)^3}{4\pi^2 kTM\sigma^2 fQ} \right\}^{1/2} \exp\left(-\frac{\pi M\sigma^2 fQ}{n\eta\varepsilon kT}\right) \quad (2.14)$$

Gilroy [64] observed from his experimentation on platinum oxide formation in the range of 1.0-1.6V_{SHE} that dQ/dlogt linearly increased with increasing potential. This can not be accounted for by any of the above mechanisms. Gilroy then derived a new reaction rate (Equation 2.15) following Fleischmann's electrocrystallization theory with the assumption that nucleation is the rate determining step for anodic film growth on platinum.

$$\frac{dQ}{dt} = Z^{**} (\eta/Q^{1/3})^{1/2} \exp\left(-\frac{Q}{C\eta}\right) \quad (2.15)$$

$$\text{with } C = 3n\varepsilon/\pi M\sigma^2 f kT$$

Integration of Equation 2.15 under constant potential yields the growth law. With the assumption that the magnitude of logQ is small compared with that of Q itself, this

growth law is then consistent with the experimental observations by Gilroy. Therefore a direct logarithmic law is followed for platinum film formation when the slope continuously increase with increasing potentials.

$$\frac{Q}{C\eta} + \left(\frac{1}{6}\right)\log Q = \log t + \log A \quad (2.16)$$

with $A = Z^{**}/C\eta^{1/2}$.

However, some criticism on the validity of this nucleation and growth model on platinum oxide formation have been noted by Conway et al.[65]. Their experimental results show that the dependence of the slope of $d\log Q/dt$ on the potentials is only observed at higher potentials ($>1.7V_{\text{SHE}}$). They did not observe the characteristics of a nucleation-growth process. They did not observe a temporary increase in current upon reversal of the direction of sweep from their anodic voltammograms either.

Finally as seen from the above review, the anodic film growth kinetics on platinum has been accounted for by either the direct logarithmic law or the inverse logarithmic law. The thickness hence increases to infinity with time in both logarithmic laws. This is impossible in real experiments in which the film always grows to a finite value. It has been mentioned in Section 2.2 that extensive experimental work has shown that the film thickness and current reach a steady state after an effectively infinite time. However, none of above models has predicted the existence of a steady state film thickness and current. The dissolution of the film at the film/solution interface is not considered either even though it is a required process for the steady state condition. Addressing these contradictions, the Point Defect Model has been proposed since the 1980's by Macdonald et. al.

2.5.4 Point Defect Model

Point Defect Model was first presented by Chao and Macdonald et al. [66, 67] In this original model it is assumed that; 1) the film is highly defective, 2) a continuous film is formed when a potential at the passive range is applied, 3) charge carriers are in equilibrium, 4) since both interfaces at metal/film and film/solution are polarizable, the potential differences at these interfaces are dependent on the externally applied potential and pH, the electric field strength in the film is thus independent of external potential and thickness due to Esaki tunneling, and 5) the electric field strength is homogenous through the film and high in the order of 10^6 V/cm. The rate determining step is then the transport of oxygen vacancies through the film, which causes the film growth into the metal. The reaction rate is thus written according to the transport of oxygen vacancies across the film by assuming that the metal/film and film/solution interfaces are in electrochemical equilibrium (Equation 2.17).

$$\frac{dL}{dt} = \frac{A \exp(BV)}{\exp(2KL) - 1} \quad (2.17)$$

The impedance characteristic of passive films is explained from Warburg impedance by the transport of oxygen vacancies across the film. The model predicts that the product of the steady state passive current density and the Warburg coefficient is independent of applied potential and thickness due to the existence of a constant field strength across the film.

However in this initial PDM model, only the ionic and electronic transport is considered. The interfacial charge transfer reactions are not distinguished with regard to

their impact on boundary position. Similar to other models discussed above, this original PDM model does not count the dissolution of the barrier in the film growth either, and thus can not describe the steady state passive films. Macdonald et al. [68] thus modified the original model so that the dissolution of the barrier at the film/solution interface is included into the model and the interfacial reactions (2) and (5) (Figure 2-4) are the rate determining steps. A schematic of the physico-chemical processes that occur within the film is drawn in the Figure 2-4. During the film growth, the cation vacancy is formed at the film/solution interface, migrates through the film under the high electric field, and then is occupied at the metal/film interface by the metal ion that is ejected from the metal substrate. During this process, there is no new lattice produced. The reactions (1) and (3) are thus lattice conservative. In reaction (2), the ejected metal ion from the metal substrate occupies the cation vacancy of Schottky defects. Therefore a new lattice of oxygen vacancy is formed. The film then grows into the metal. The newly formed oxygen vacancy migrates under the high field through the film to the film/solution interface, where the adsorbed oxygen ion from the solution occupies the oxygen vacancy [reaction (4)]. Reaction (4) is thus a pure chemical reaction and lattice conservative. Reaction (5) describes the destruction of the film, thus is apparently not conservative. The dissolved metal ions in reaction (3), and (5) will partly precipitate back to the film surface during the film growth, and will form the outer layer together with the oxygen ions produced in reaction (4). The formation of the outer layer of the film is thus independent of potential as both the precipitation of metal ions from solution and the formation of oxygen ions are chemical reactions.

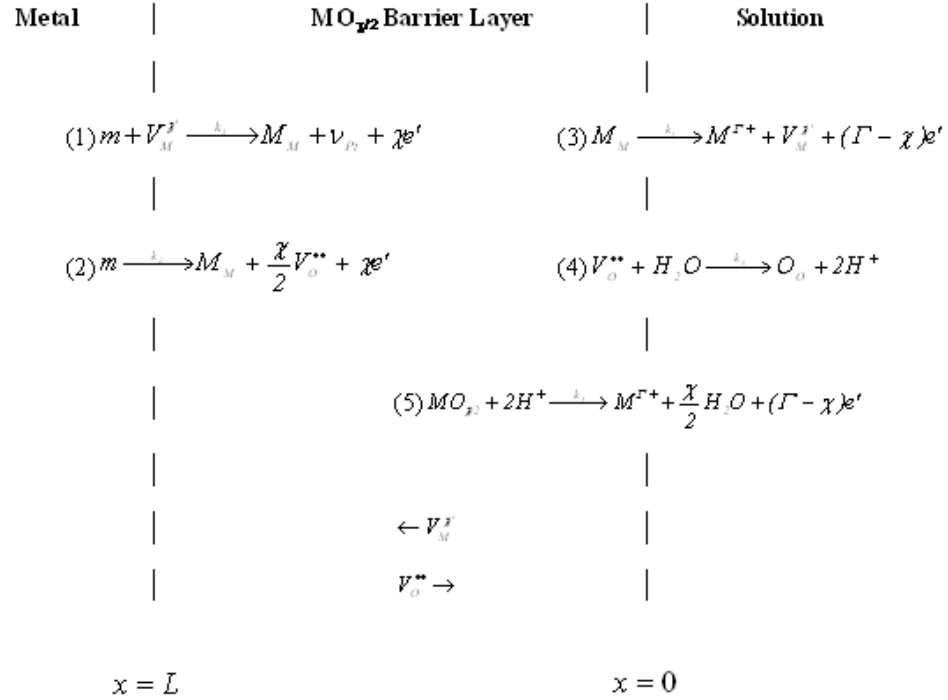


Figure 2-4: Schematic of physicochemical processes that are envisioned to occur within the barrier oxide (MO_{x/2}) layer on passive platinum, according to the Point Defect Model. $m \equiv$ metal atom; $V_M^{\cdot\cdot} \equiv$ cation vacancy; $\nu_m \equiv$ metal vacancy in metal lattice; $M_M \equiv$ metal cation in a normal cation position in the barrier layer; $M^{T+} \equiv$ metal cation in the solution phase (outer layer); $V_O^{\cdot\cdot} \equiv$ oxygen vacancy; $O_O \equiv$ oxygen ion in an anion site in the barrier layer.

A steady state is thus obtained when the rates of reaction (2) and (5) are equal as written bellow;

$$-\frac{2}{\chi} J_o^{m/f} = k_5 C_{H^+}^n \quad (2.18)$$

where $J_O^{m/f}$ is the flux of anion vacancies at the metal/film interface due to reaction (3), and the right term in Equation **2.18** is the rate of reaction (5). The steady state current density and the steady state thickness are expressed as

$$L_{ss} = \frac{I}{\varepsilon} \left[I - \alpha - \frac{\alpha\alpha_s}{\alpha_2} \left(\frac{\Gamma}{\chi} - I \right) \right] V + \frac{I}{\varepsilon} \left\{ \frac{2.303n}{\alpha_2 K} - \beta \left[\frac{\alpha_s}{\alpha_2} \left(\frac{\Gamma}{\chi} - I \right) + I \right] \right\} pH + \frac{I}{\alpha_2 K} \ln \left(\frac{k_2^0}{k_s^0} \right) \quad (2.19)$$

$$I_{ss} = IF \left[k_3^0 e^{\alpha_3 \alpha \gamma V} e^{\alpha_3 \beta \gamma pH} + k_s^0 e^{\alpha_s \alpha (\Gamma - \chi) \gamma V} e^{\beta \alpha_s (\Gamma - \chi) \gamma pH} C_{H^+}^n \right] \quad (2.20)$$

The dependencies of L_{ss} and I_{ss} on the applied voltage, $C_M^{\Gamma+}$ and pH provide the diagnostic criteria that may be used to identify the charge carrier in the film and thus the electronic character of the film (n-type or p-type), and to indicate the kinetic nature of the interfacial reactions. The diagnostic criteria [68] are summarized in Table **2-2**.

Table **2-2**: Diagnostic criteria derived from Equation **2.19** and Equation **2.20**.

| Criterion | Cation transmission | Anion transmission |
|--|--|--|
| $(\partial L_{ss} / \partial V)_{pH, C_M^{\Gamma+}}$ | $[I - \alpha - \alpha\alpha_s (\Gamma / \chi - I) / \alpha_2] / \varepsilon$ | $[I - \alpha - \alpha\alpha_s (\Gamma / \chi - I) / \alpha_2] / \varepsilon$ |
| $(\partial L_{ss} / \partial pH)_{V, C_M^{\Gamma+}}$ | $[2.303n / \alpha_2 \chi \gamma - \beta (\alpha_s (\Gamma - \chi) / \alpha_2 \chi) + I] / \varepsilon$ | $[2.303n / \alpha_2 \chi \gamma - \beta (\alpha_s (\Gamma - \chi) / \alpha_2 \chi) + I] / \varepsilon$ |
| $(\partial L_{ss} / \partial \ln C_M^{\Gamma+})_{V, pH}$ | 0 | 0 |
| $(\partial \ln I_{ss} / \partial V)_{pH, C_M^{\Gamma+}}$ | $\alpha_3 \alpha \gamma$ | $\alpha\alpha_s (\Gamma - \chi) \gamma$ |
| $(\partial \ln I_{ss} / \partial pH)_{V, C_M^{\Gamma+}}$ | $\alpha_3 \beta \gamma$ | $\beta \alpha_s (\Gamma - \chi) \gamma - 2.303n$ |
| $(\partial \ln I_{ss} / \partial \ln C_M^{\Gamma+})_{V, pH}$ | 0 | 0 |

Therefore, if the cation vacancies are the dominant defects, then the barrier layer demonstrates p-type electronic character when the cation vacancies are electron acceptors, and n-type doping when the anion vacancies are electron donors. These criteria have been applied to explore a large number of passive metal systems and the results are consistent with those investigated with other techniques such as capacitance measurements analyzed in terms of Mott-Schottky method and photoelectrochemistry. The impedance model of thin passive films according to the PDM was also modified by adding the dissolution of the film at the film/solution interface into the model. Optimization of the PDM to the experimental impedance data was executed by regarding various model parameters as variables. These parameters included the interfacial rate constants and transfer coefficients, the electric field strength, and the vacancy diffusivities. Good agreement between experimental and calculated data has been observed in Ni [69] and W [70]. Recently, the formation and destruction of metal interstitials at interfaces have been included in the model, and a truncated impedance model (n-type doping film), in which the formation and annihilation of cation vacancies are not included, has been applied to study the passive films in Alloy 22 [71, 72].

According to the PDM [73] with 7 interfacial reactions, the rate of change in the thickness of a barrier layer passive film can be written in the form;

$$\frac{dL}{dt} = a.e^{-bL} - c \quad (2.21)$$

where $a = \Omega k_3^0 e^{\alpha_3(1-\alpha)\chi\gamma V} e^{-\alpha_3\chi\beta\gamma pH}$, $b = \alpha_3\chi\epsilon\gamma$, $c = \Omega k_7 (C_{H^+} / C_{H^+}^0)^n$.

Equation 2.21 is readily integrated to yield the transient film thickness as;

$$L(t) = L_0 + \left(\frac{1}{b}\right) \ln \left[\left(\frac{a'}{c}\right) e^{-bL_0} (e^{bct} - 1) + 1 \right] - ct \quad (2.22)$$

where the constants and parameters are as given above, except that c is the dissolution rate at voltage $V + \Delta V$. Note that $a' = k_3^0 e^{\alpha_3(1-\alpha)\gamma(V+\Delta V)} e^{-\alpha_3\beta\eta pH}$. Examination of Equation 2.22 shows that the transient in film thickness is a combination of a linear relationship and a logarithmic function. If the rate of dissolution of the passive film [c in Equation 2.22] is sufficiently small that $e^{bct} \approx 1 + bct$ and ct is much less than the second term in Equation 2.22, then the rate law reduces to Equation 2.23.

$$L(t) = L_0 + \left(\frac{1}{b}\right) \ln [1 + a'be^{-bL_0}t] \quad (2.23)$$

where the parameters are as defined above. If $a'be^{-bL_0}t \gg 1$, Equation (2.23) collapses into the classical direct logarithmic relationship.

2.5.5 Summary

In summary, each model yields a rate law with the correct functional form for the growth term with respect to the dependence on film thickness as noted from Table 2-3. However, only one model, PDM, incorporates film dissolution leading to a rate law containing only a single term. If dissolution does not occur, the oxide film should grow to infinite thickness instead of reaching steady state. This would be contrary to experimental findings as reported in this thesis. The rate law of the HFM predicts that the

film growth rate must be initially infinite, which is non-physical. Therefore, of the mechanisms summarized in Table 2-3, only the PDM accounts for the existence of steady states in the film thickness and current and hence correctly describes the physics of oxide film growth. However, it is emphasized that, if the dissolution of the film is incorporated into the other models (but not on an *ad hoc* basis), the modified rate laws of these models, except for the HFM, would give the same expression for the rate law as does the PDM.

Table 2-3: Rate laws of passive film growth models.

| Model | Rate Law | Steady State Thickness | $\left(\frac{dL}{dt}\right)_{L \rightarrow 0}$ |
|---|--|------------------------|--|
| PDM [6, 30, 71] (Point Defect Model) | $\left(\frac{dL}{dt}\right) = Ae^{aV-bL} - C$ | Finite | A-C |
| PEM [36, 39, 74, 75] (Place Exchange Model) | $\left(\frac{dL}{dt}\right) = A'e^{a'V-b'L}$ | ∞ | A' |
| HFM [76, 77] (High Field Model) | $\left(\frac{dL}{dt}\right) = A''e^{b''V/L}$ | ∞ | ∞ |
| NGM [64] (Nucleation and Growth Model) | $\left(\frac{dL}{dt}\right) = A'''e^{-L/\eta}$ | ∞ | A''' |

REFERENCES

- [1] B.E. Conway, Prog. Surf. Sci., 49 (1995) 331.
- [2] D.A.J. Rand and R. Woods, J. Electroanal. Chem., 35 (1972) 209.
- [3] S. Shibata, J. Electroanal. Chem., 89 (1977) 37.

- [4] S. Gottesfeld, *Electroanalytical Chemistry: A Series of Advances*. Ed. A.J. Bard. New York: M. Dekker, 1989.
- [5] B.E. Conway, G. Tremiliosi-filho, and G. Jerkiewicz, *J. Electroanal. Chem.*, 297 (1991) 435.
- [6] D.D. Macdonald, *J. Electrochem. Soc.*, 139 (1992) 3434.
- [7] A.J. Bard, *Electroanalytical Chemistry*. Vol. 9. Marcel Dekker: New York, 1976.
- [8] K.J. Vetter and J.W. Schultze, *J. Electroanal. Chem.*, 34 (1972) 131.
- [9] B.E. Conway and G. Jerkiewicz, *J. Electroanal. Chem.*, 339 (1992) 123.
- [10] T. Biegler and R. Woods, *J. Electroanal. Chem.*, 20 (1969) 73.
- [11] T. Biegler, D.A.J. Rand, and R. Woods, *J. Electroanal. Chem.*, 29 (1971) 269.
- [12] B.E. Conway and G. Jerkiewicz, *J. Electroanal. Chem.*, 334 (1992) 359.
- [13] A. Sun, J. Franc, and D.D. Macdonald, accepted to *Journal of Electrochemical Society*, (2005)
- [14] D.D. Macdonald and M. Urquidi-Macdonald, *J. Electrochem. Soc.*, 132 (1985) 231.
- [15] M. Urquidi-Macdonald, S. Real, and D.D. Macdonald, *J. Electrochem. Soc.*, 133 (1986) 2018.
- [16] M.N. Kamrun, J. Bao, and D.D. Macdonald, *Corros. Sci.*, Special Issue Commemorating the Development of Tafel's Law, 47 (2005) 3111.
- [17] *Electrochemical Impedance Spectroscopy Primer*, www.gamry.com
- [18] M. Bojinov, S. Cattarin, M. Musiani, and E. Tribollet, *Electrochim. Acta*, 48 (2003) 4107.

- [19] C. Gabrielli, Identification of Electrochemical Processes by Frequency Response Analysis, Technical Report No. 004/83, Solartron Instruments, Farmborough, UK, (1984).
- [20] N. Priyantha, P. Jayaweera, D.D. Macdonald, and A. Sun, *J. Electroanal. Chem.*, 572 (2004) 409.
- [21] D.A. Harrington, *J. Electroanal. Chem.*, 355 (1993) 21.
- [22] M.E. Van Der Geest, N.J. Dangerfield, and D.A. Harrington, *J. Electroanal. Chem.*, 420 (1997) 89.
- [23] S.H. Glarum and J.H. Marshall, *J. Electrochem. Soc.*, 126 (1979) 424.
- [24] W.G. Pell, A. Zolfaghari, and B.E. Conway, *J. Electroanal. Chem.*, 532 (2002) 13.
- [25] U. Stimming, *Electrochim. Acta*, 31 (1986) 415.
- [26] A.J. Rudge, L.M. Peter, G.A. Hards, and R.J. Potter, *J. Electroanal. Chem.*, 366 (1994) 253.
- [27] Y.Y. Vinnikov, V.A. Shepelin, and V.I. Veselovskii, *Sov. Electrochem.*, 9 (1973) 1469.
- [28] A. Felske and W.J. Plieth, *J. Opt. Soc. Am. B*, 3 (1986) 815.
- [29] S.R. Morrison, *Electrochemistry at Semiconductor and Oxidized Metal Electrodes*, Plenum Press, New York and London, 1980.
- [30] D.D. Macdonald, *Pure Appl. Chem.*, 71 (1999) 951.
- [31] D.D. Macdonald and S.I. Smedley, *Electrochim. Acta*, 35 (1990) 1949.
- [32] F. Cardon and W.P. Gomes, *J. Phys. D: Appl. Phys.*, 11 (1978) L63.
- [33] K.S. Kim, N. Winograd, and R.E. Davis, *J. Am. Chem. Soc.*, 93 (1971) 6296.
- [34] M. Peuckert and H.P. Bonzel, *Sur. Sci.*, 145 (1984) 239.

- [35] J.S. Hammond and N. Winograd, *J. Electroanal. Chem.*, 78 (1977) 55.
- [36] V.I. Birss, M. Chang, and J. Segal, *J. Electroanal. Chem.*, 355 (1993) 181.
- [37] S.J. Xia and V.I. Birss, *Electrochim. Acta*, 44 (1998) 467.
- [38] S.J. Xia and V.I. Birss, *Electrochim. Acta*, 45 (2000) 3659.
- [39] G. Jerkiewicz, G. Vatankhah, J. Lessard, M.P. Soriaga, and Y.S. Park, *Electrochim. Acta*, 49 (2004) 1451.
- [40] F.T. Wagner and P.N. Ross Jr., *Surf. Sci.*, 160 (1985) 305.
- [41] F.T. Wagner and P.N. Ross Jr., *J. Electroanal. Chem.*, 150 (1983) 141.
- [42] Z. Nagy and H. You, *Electrochim. Acta*, 47 (2002) 3037.
- [43] K. Itaya, S. Sugawara, K. Sashikata, and N. Furuya, *J. Vac. Sci. Technol. A*, 8 (1990) 515.
- [44] F. Di Quarto, S. Piazza, C. Sunseri, M. Yang, and S.-M. Cai, *Electrochim. Acta*, 41 (1996) 2511.
- [45] J. Kunze, V. Maurice, L.H. Klein, H.-H. Strehblow, and P. Marcus, *Corr. Sci.*, 46 (2004) 245.
- [46] L. Vazquez, J. Gomez, A.M. Baro, N. Garcia, M.L. Marcos, J. Gonzalez Velasco, J.M. Vara, A.J. Arvia, J. Presa, A. Garcia, and M. Aguilar, *J. Am. Chem. Soc.*, 109 (1987) 1730.
- [47] K. Itaya, S. Sugawara, and K. Higaki, *J. phys. chem.*, 92 (1988) 6714.
- [48] K. Itaya, S. Sugawara, K. Sashikata, and N. Furuya, *J. Vac. Sci. Technol. A*, 8 (1990) 515.
- [49] A.H. Lanyon and B.M.W. Trapnell, *Proc. Roy. Soc.*, A227 (1955) 387.
- [50] N. Sato and M. Cohen, *J. Electrochem. Soc.*, 111 (1964) 512.

- [51] A.K.N. Reddy, M.A. Genshaw, and J.O.M. Bockris, *J. Chem. Phys.*, 15 (1968) 671.
- [52] P. Stonehart, H.A. Kozłowska, and B.E. Conway, *Proc. Roy. Soc.*, A310 (1969) 541.
- [53] H. Angerstein-Kozłowska, B.E. Conway, and W.B.A. Sharp, *J. Electroanal. Chem.*, 43 (1973) 9.
- [54] D.A. Harrington, *J. Electroanal. Chem.*, 420 (1997) 101.
- [55] N. Cabrera and N.F. Mott, *Rep. Prog. Phys.*, 12 (1949) 163.
- [56] J.L. Ord and F.C. Ho, *J. Electrochem. Soc.*, 118 (1971) 46.
- [57] K.J. Vetter and J.W. Schultze, *J. Electroanal. Chem.*, 34 (1972) 131.
- [58] D.D. Macdonald, *Pure Applied chemistry*, 71 (1999) 951.
- [59] A. Damjanovic, L.S.R. Yeh, and J.F. Wolf, *J. Electrochem. Soc.*, 127 (1980) 874.
- [60] A. Damjanovic and L.S.R. Yeh, *J. Electrochem. Soc.*, 125 (1978) C124.
- [61] A. Damjanovic, A.T. Ward, B. Ulrick, and M. Ojea, *J. Electrochem. Soc.*, 122 (1975) 471.
- [62] A. Damjanovic, L.S.R. Yeh, and J.F. Wolf, *J. Electrochem. Soc.*, 129 (1982) 55.
- [63] M. Fleischmann and H.R. Thirsk, *Metal deposition and electrocrystallization*, in *Advances in Electrochemistry and Electrochemical Engineering*, P. Delahay, Editor. John Wiley & Sons, Inc.: New York. London. p. 123. 1963.
- [64] D. Gilroy, *J. Electroanal. Chem.*, 71 (1976) 257.
- [65] B.E. Conway, B. Barnett, H. Angerstein-Kozłowska, and B.V. Tilak, *J. Chem. Phys.*, 93 (1990) 8361.

- [66] C.Y. Chao, L.F. Lin, and D.D. Macdonald, *J. Electroanal. Chem.*, 128 (1981) 1187.
- [67] C.Y. Chao, L.F. Lin, and D.D. Macdonald, *J. Electrochem. Soc.*, 129 (1982) 1874.
- [68] D.D. Macdonald, S.R. Biaggio, and H. Song, *J. Electroanal. Chem.*, 139 (1992) 170.
- [69] E. Sikora and D.D. Macdonald, *Electrochim. Acta*, 48 (2002) 69.
- [70] J. Sikora, E. Sikora, and D.D. Macdonald, *Electrochim. Acta*, 45 (2000) 1875.
- [71] D.D. Macdonald, A. Sun, N. Priyantha, and P. Jayaweera, *J. Electroanal. Chem.*, 572 (2004) 421.
- [72] D.D. Macdonald and A. Sun, *Electrochim. Acta*, 51 (2006) 1767.
- [73] D.D. Macdonald, M.A. Rifaie, and G.R. Engelhardt, *J. Electrochem. Soc.*, 148 (2001) B343.
- [74] N. Sato and M. Cohen, *J. Electrochem. Soc.*, 111 (1964) 512.
- [75] H. Angerstein-Kozłowska, B.E. Conway, and W.B.A. Sharp, *J. Electroanal. Chem.*, 13 (1973) 9.
- [76] L. Young, *Anodic Oxide Films*, Academic Press, NY, 1963.
- [77] A. Damjanovic, L.S.R. Yeh, and J.F. Wolf, *J. Electrochem. Soc.*, 127 (1980) 874.

Chapter 3

EXPERIMENTAL

All electrochemical studies were carried out in a three-electrode glass electrochemical cell (Figure 3-1). The counter electrode was a Pt wire that was located in a separate compartment connected with the working electrode compartment via a frit. All potentials were measured against a Saturated Calomel Electrode (SCE) that was connected to the cell via a Luggin probe. The potentials have been converted to the Standard Hydrogen Electrode (SHE) scale by adding 0.24V to the measured values.

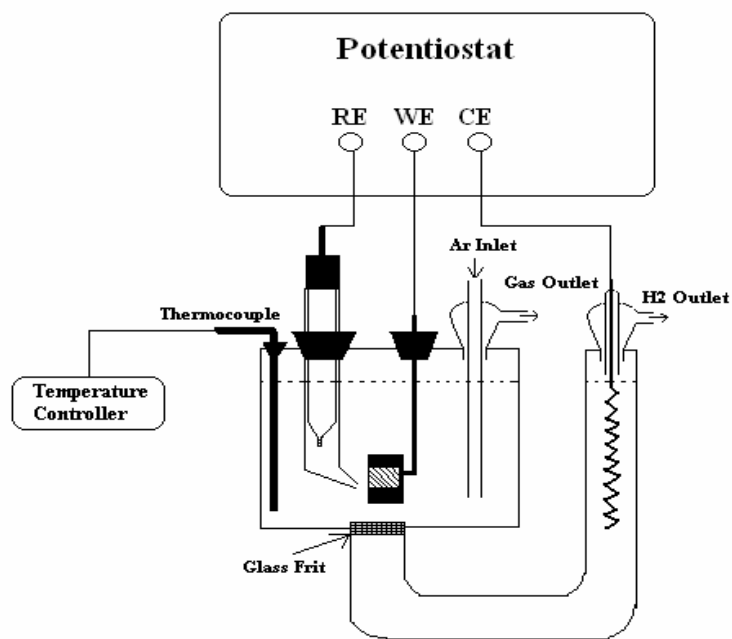


Figure 3-1: Diagram of electrochemical cell used in the work.

The working electrode was a pure platinum rod (Alfa, 99.99%), which was embedded in two-component epoxy resin. The working surface, of geometric area 0.32cm^2 , was abraded with 800 and 1200 grit SiC paper, polished with $3\text{ }\mu\text{m}$ diamond suspension (Leco), $1\text{ }\mu\text{m}$, $0.3\text{ }\mu\text{m}$, $0.05\text{ }\mu\text{m}$ Al_2O_3 powder and rinsed by D.I water ($R = 18.2\text{ M}\Omega\cdot\text{cm}$). All experiments were performed at ambient temperature ($20 \pm 2^\circ\text{C}$) in $0.5\text{M H}_2\text{SO}_4$ solution. The solution was deaerated with ultra pure Ar gas during the experiments.

Electrochemical experiments were performed using a Solartron Model 1286 Electrochemical Interface. The electrochemical impedance data were recorded with a Solartron Model 1250 Frequency Response Analyzer (FRA), using a peak-to-peak excitation voltage of 10 mV and an applied frequency ranging from 50kHz to 0.03Hz . The capacitance of the interface was measured at frequencies of 10kHz , 5kHz , and 1kHz while the potential was being swept in the negative direction from the oxide formation potential. The voltage scan rate employed was 100mV/s . This procedure was adopted, because the dopant density in the barrier layer of a passive film is predicted and found [78] to be a function of voltage, in contrast to the assumption of Mott-Schottky theory [29]. By sweeping the potential in the negative direction from the formation voltage at a sufficiently high rate, the dopant profile formed in the barrier layer at that voltage is effectively “frozen-in” while the electronic structure responds to the linearly varying potential in a quasi-equilibrium manner.

The film thickness estimated from capacitance measurement was measured at frequencies higher than 1 KHz where the electrochemical impedance displays an almost purely capacitive frequency response. The imaginary component of the electrochemical

impedance is then converted to the capacitance in terms of a series of RC equivalent circuit. The steady state thickness is thus expressed as

$$L_{ss} = \frac{\epsilon_0 \hat{\epsilon} A}{C}$$

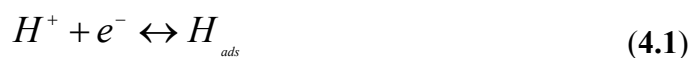
Angle-resolved XPS analyses were performed with a Kratos Analytical Axis Ultra Spectrometer, using an Al K- α X-ray source. Characterization of the oxide films was performed by means of angle-resolved measurements, which were performed at takeoff angles of 90° and 25° (angle of surface with respect to the direction of the analyzer). Oxides were first grown at different formation potentials for 24 hours, and then rinsed with D.I. water and dried in air. The samples were then transferred to the sample introduction compartment of the XPS spectrometer. A survey spectrum was first recorded to identify all elements present in the surface, then high resolution spectra of the following regions were recorded: Pt-4f, O-1s, and C-1s.

Chapter 4

GROWTH AND PROPERTIES OF OXIDE FILMS ON PLATINUM

4.1 Transient Growth of Platinum Oxide Film

The kinetics of oxide film growth on Pt was first studied by using cyclic voltammetry. Figure 4-1 shows a typical cyclic voltammogram measured by cycling the potential between $0.05V_{\text{SHE}}$ and $1.39V_{\text{SHE}}$ at ambient temperature ($20 \pm 2^\circ\text{C}$) in 0.5M H_2SO_4 solution at 50mV/s . The reduction peak centered initially at $0.63V_{\text{SHE}}$ reflects the reduction of the α -oxide film, which is consistent with data reported in the literature [1-3]. The two anodic peaks at lower potentials correspond to the desorption of hydrogen; the two cathodic peaks at the same potentials correspond to electrochemical adsorption of hydrogen onto the polycrystalline surface. The symmetry of the anodic and cathodic peaks demonstrates the reversibility of hydrogen atom adsorption/desorption process [Equation 4.1] on platinum, while the existence of two peaks indicates the presence of two, distinct adsorption sites (note that the adsorption sites may correspond to different crystallographic planes on the polycrystalline surface). As many as three peaks have been resolved in other studies and it is suspected that additional peaks, corresponding to still more distinct adsorption sites, may be “buried” in the voltammogram in the hydrogen adsorption/desorption region.



As seen from Figure 4-1, the formation of the “ α -oxide” occurs at potentials starting from around 0.8 V_{SHE} and extending to oxygen evolution, which occurs at a potential greater than 1.39 V_{SHE}. Within this range, the current attains a plateau between ca. 1.0V_{SHE} to 1.39V_{SHE}. Since $Q = \int_0^t i dt = \int_{V_0}^V \frac{i}{\nu} dV$, where ν is the voltage scan rate used in the cyclic voltammetry, the charge densities Q_a for anodic oxide film formation and Q_c for cathodic reduction were calculated from the areas under the anodic oxide formation potential region and under the cathodic peak. A double layer correction was made by subtracting the value of the current in the double layer region. A value of 772 $\mu\text{C}/\text{cm}^2$ for Q_c is obtained from the corrected cathodic reduction peak, which is less than the 880 $\mu\text{C}/\text{cm}^2$ suggested by Conway et al [2-4] for the formation of two equivalent monolayers of PtO. Previous work by Kozłowska et al [5] states that, in properly purified solutions, Q_a is exactly equal to Q_c below 1.2V_{SHE}. The ratio of Q_a to Q_c from the current experimental work is 1.37, which is greater than 1, suggesting that dissolution plays a significant role in determining the amount of charge retained at the surface upon entering the reduction sweep. Note that, in the current work, the potential was anodically swept to 1.39V vs. SHE, at which little evidence of oxygen evolution was obtained. Therefore, we conclude that the observed discrepancy in charge probably arises from significant anodic dissolution of oxide film [5, 6].

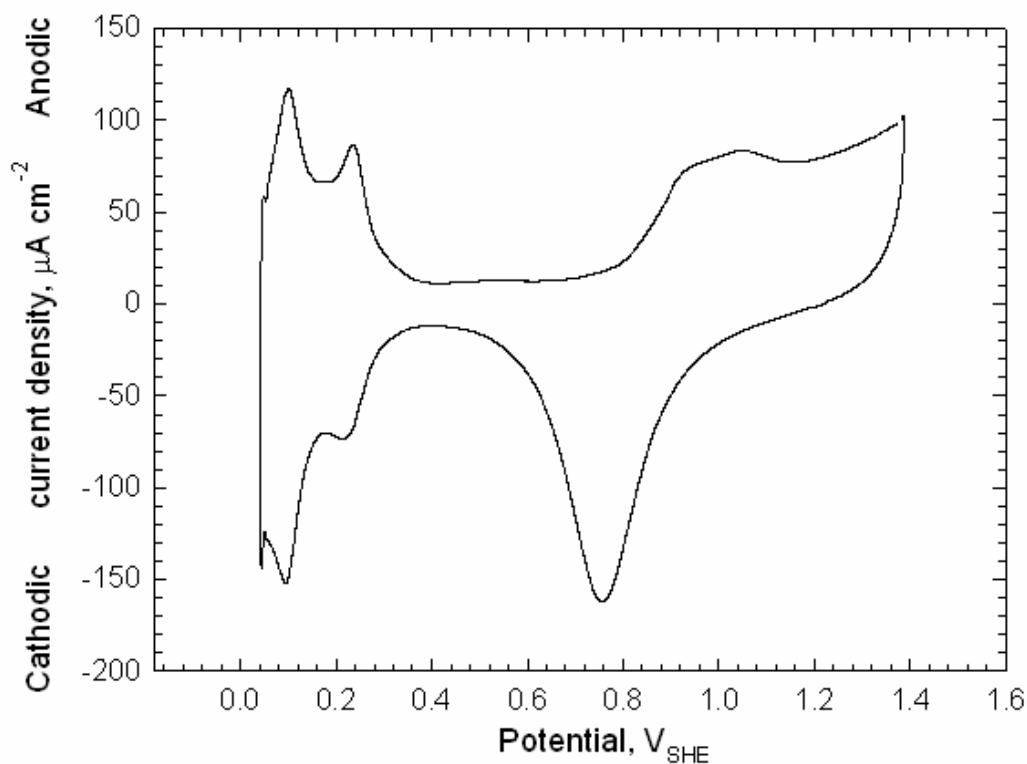


Figure 4-1: Cyclic voltammograms for platinum in 0.5M H₂SO₄ at a voltage sweep rate of 50 mV/s ($T = 20 \pm 2^\circ\text{C}$). Working electrode surface area = 0.32 cm².

A large amount of work, using mostly cyclic voltammetry, has been reported in which various oxidation/reduction peaks in the i - V profiles have been resolved to indicate the composition and mechanism of electrochemical formation and reduction of platinum oxide films. However, cyclic voltammetry does not readily provide information concerning the crystallographic and electronic defects in the oxide film under steady state conditions and it is currently unable to provide detailed kinetic data for the reactions involved.

4.2 Steady State Growth of Platinum Oxide Film

Potentiostatic experiments were performed to grow the oxide film until it had reached the steady state (after 24 hours). Figure 4-2 shows that the logarithm of the steady state current density remains constant as a function of formation potential, which is consistent with the diagnostic criteria set forth by the PDM [7] for an n-type semiconducting oxide film. Note that the steady state condition was tested by measuring the current in the positive-going (“up”) and negative-going (“down”) directions; the lack of hysteresis demonstrates that the system was indeed at a steady state during the measurements. The fact that a steady state exists provides irrefutable proof that dissolution of the barrier layer takes place and that the rate law for barrier layer formation must contain a dissolution component. The n-type electronic characteristic of the oxide film is also shown by Mott-Schottky analysis of capacitance measurements discussed later in this paper.

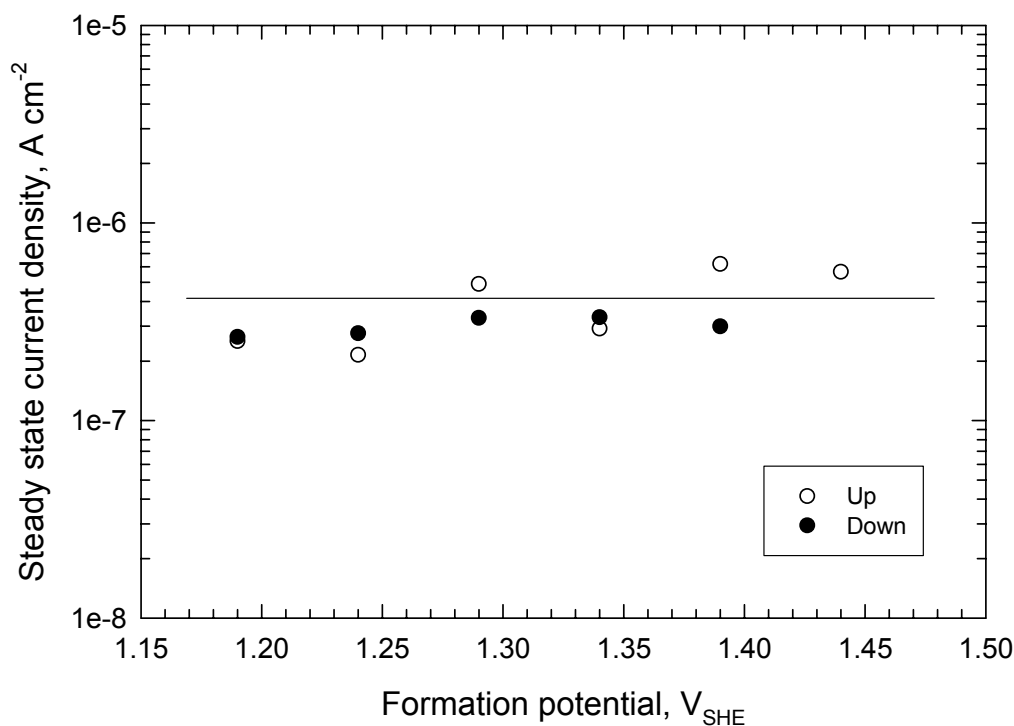


Figure 4-2: Steady state current density for platinum in 0.5M H_2SO_4 as a function of oxide formation potential, measured in both the ascending and descending potential directions. The lack of hysteresis indicates that the system is at steady state.

Electrochemical Impedance Spectroscopy (EIS) data for the oxide film on Pt under steady state conditions were measured as a function of formation potential across the passive range (Figure 4-3). The experimental impedance spectra are plotted in the form of Nyquist plots, in which the imaginary component of the impedance is plotted against the real component for decreasing frequencies. As noted in Figure 4-3, the complex plane plot in the high frequency range is almost a straight line, independent of the formation voltage, which is in agreement with the predictions of PDM [7]. In terms of the postulates of PDM, the electric field strength is assumed to be independent of the formation potential due to field buffering by Esaki tunneling and, since the transport of

the defects across the barrier layer is driven primarily by the electric field strength, it follows that the impedance should be insensitive to the film formation potential, as observed [8].

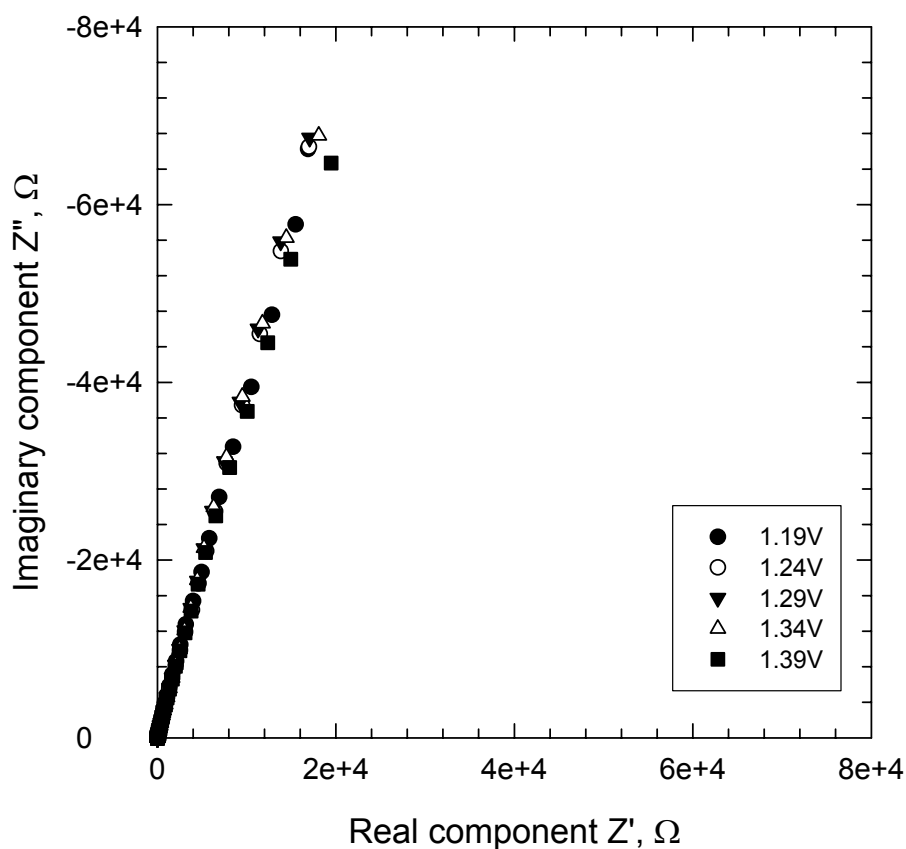
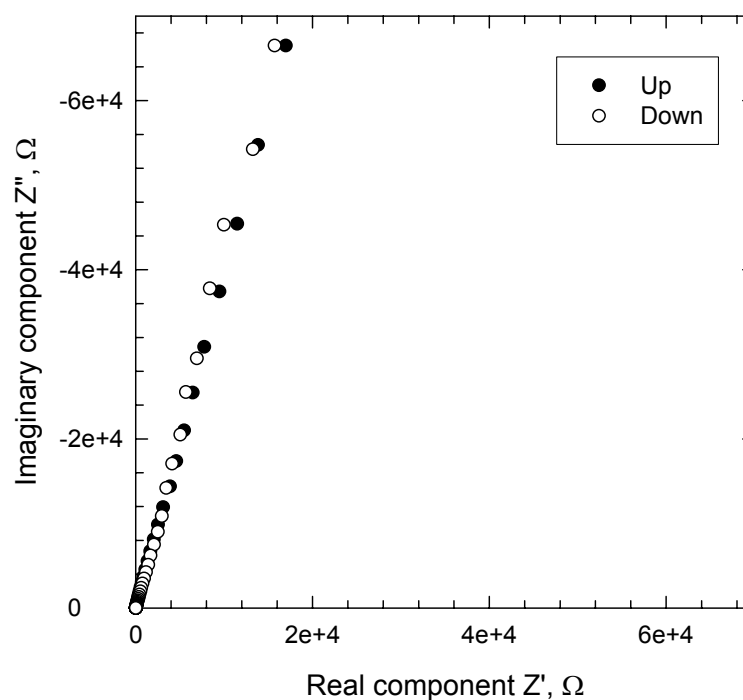


Figure 4-3: Nyquist plots for platinum in 0.5M H_2SO_4 measured at different oxide formation potentials.

Since the stability of the system during EIS measurement is critical for ensuring that the data are valid, certain precautions were taken to ensure that the system conformed to the constraints of Linear Systems Theory (LST). Because a steady state

interface should afford the same response regardless of whether the measurements are made in the forward or reverse frequency sweep directions, the frequency was scanned (stepped) from low to high frequency and then immediately scanned in the reverse direction. Figure 4-54 reveals that both the Nyquist plot and the Bode plot are in good agreement, regardless of the direction of frequency scans.



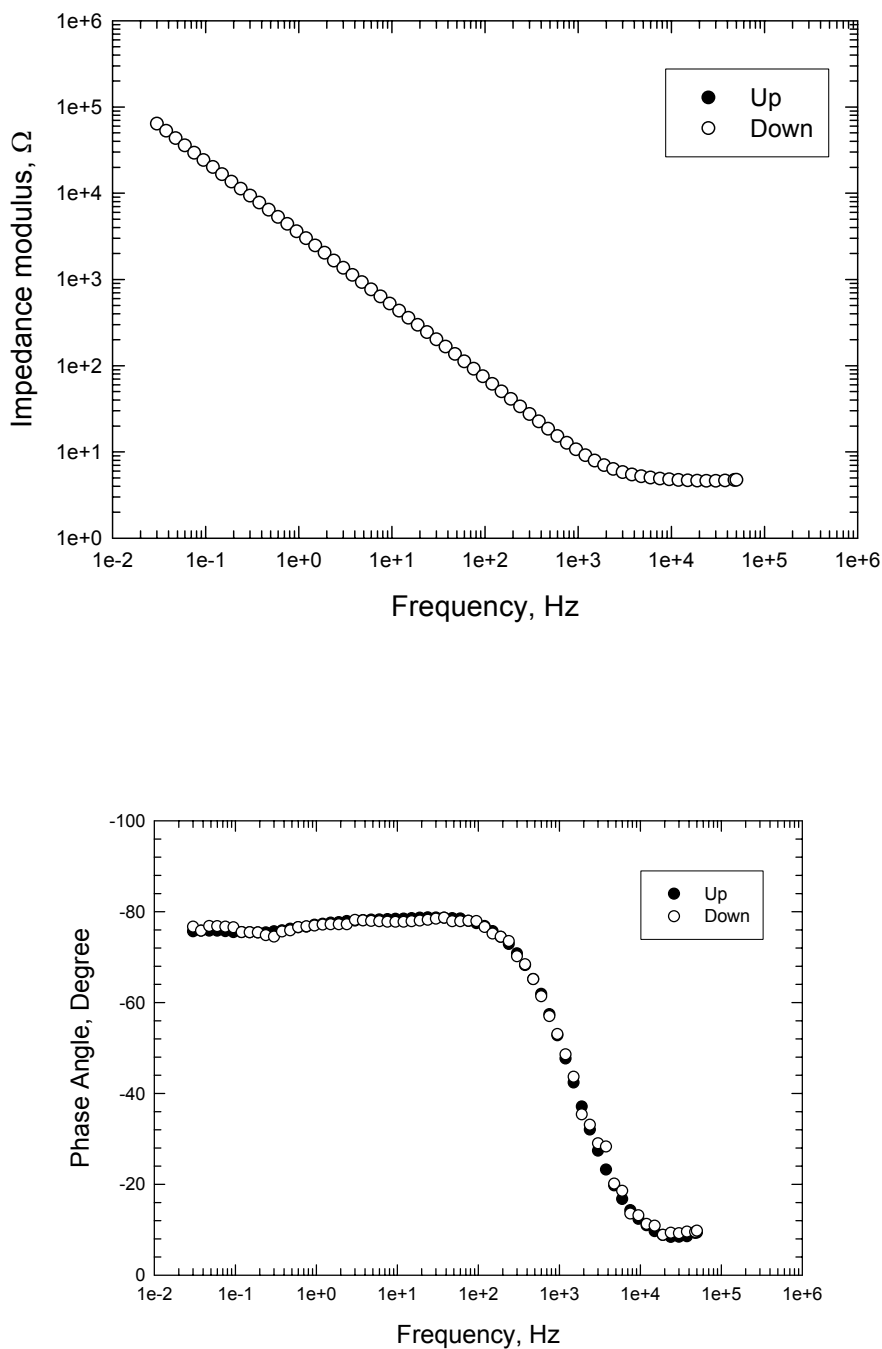


Figure 4-4: Nyquist and Bode plots for platinum at a potential of 1.24V_{SHE}, measured sequentially at descending (“down”) and ascending (“up”) frequencies. The lack of significant hysteresis indicates that the system is at steady state.

Kramers-Kronig transforms were also employed to examine the system with respect to the linearity, causality, and stability constraints of Linear Systems Theory. The K-K transforms were first introduced by Kronig [9] and Kramers [10] about eighty years ago. These relations, developed for the field of optics, establish a connection between the real and imaginary parts of complex physical quantities for linear, stable, and causal systems. Based on the assumption that four physical conditions of causality, stability, linearity, and finiteness are fulfilled, the derivations of the K-K relations are purely mathematical results and do not reflect any physical property or condition of the system. Thus, only the experimental data satisfying the above four conditions can be used to describe the properties of the systems in terms of linear systems theory. In the case of electrochemical impedance spectroscopy, Macdonald and Urquidi-Macdonald [11, 12] derived the mathematical relations transforming the real part of impedance into the imaginary part of impedance and *vice versa*. They explored iron in 1M H₂SO₄ at the open circuit for the sensitivity of the K-K transforms to violation of the linearity and stability constraints by imposing non-linearity and instability on the system via external perturbations. The results show that the K-K transforms are strongly sensitive to violation of the stability condition of the system. Clearly, the K-K transforms represent a powerful means of detecting violation of these critical constraints in EIS. Here, we applied the K-K relations to experimental impedance data for passive platinum, by transforming the real axis into the imaginary axis and the imaginary axis into the real axis and then comparing the transformed quantities with the respective experimental data. Figure 4-5 shows that the impedance data correctly transform according to the integral K-

K transforms, demonstrating that the system satisfies the constraints of Linear Systems Theory (LST). The small discrepancy between the transformed real component (to yield the imaginary component) and the experimental imaginary component at the upper extremes of frequency shown in the lower plot in Figure 4-5 is due to the well-known “tails” problem [11, 12], resulting from the fact that the impedance data are not measured over an infinite range of frequency.

The steady state film thickness was also measured by growing the film at a fixed potential for 24 hours and then reducing the film by applying a very slow, negative-going voltage scan (5 mVs^{-1}). The corresponding cathodic reduction charge was then calculated after applying the double layer charging correction. Conway et al. [4] have stated that the charge associated with the formation/reduction of a continuous, two-monolayer film under ideal conditions should be $880 \text{ } \mu\text{C cm}^{-2}$. It is also known that PtO has a bimolecular tetragonal unit cell with $c = 0.534 \text{ nm}$ [13, 14]. The film thickness could thus be obtained in terms of $L = (Q/880) * C$, where Q is the charge corresponding to cathodic reduction of the oxide film after double layer capacitance correction and C is the specific capacitance (F/cm^2). The measured thickness here is plotted together with the thickness obtained from theoretical calculation using the parameter values determined from the PDM (see Figure 5-6). As is noted, the measured thickness is a little larger than that calculated from the PDM optimization, but the anodizing constants ($\partial L_{ss} / \partial V$) is virtually the same.

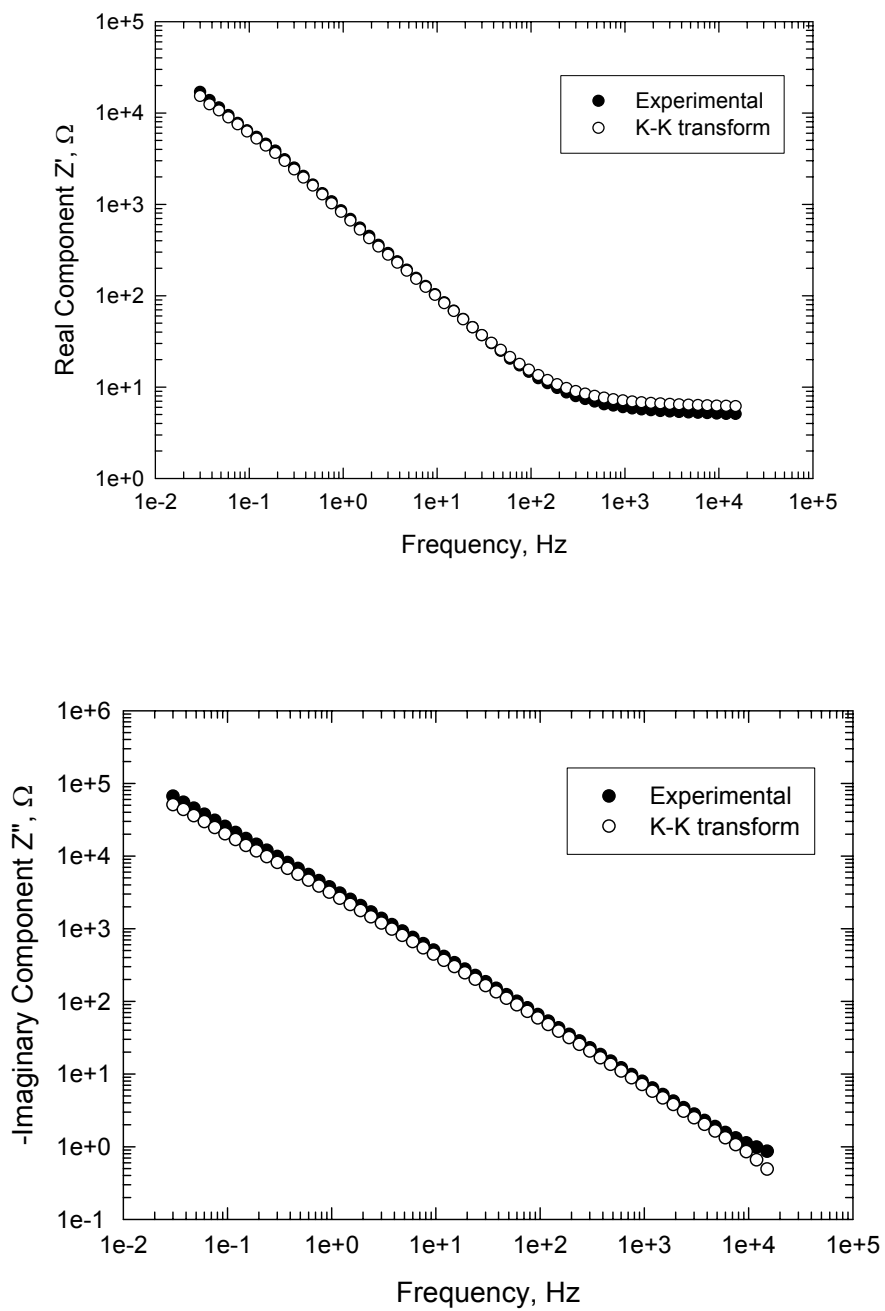


Figure 4-5: K-K transforms of EIS data for platinum in 0.5M H_2SO_4 at a potential 1.24V_{SHE}. The good agreement between the transformed and experimental data demonstrates that the system conforms to the constraints of Linear Systems Theory.

4.3 Electronic Properties

An understanding of local structural and electronic properties of the platinum oxide film is vital in exploring the catalytic mechanism of the Oxygen Electrode Reaction (OER). Since a large number of defects exist in the barrier oxide layer, it is possible that these defects might be involved in the catalytic process during the oxygen electrode reaction. Thus, the involvement of surface defects in gas-phase reactions, as reactants and catalytic reaction sites, is firmly established [15-17] and it would be remarkable if they were not also involved in condensed phase reactions, including electrochemical reactions on passive surfaces, yet we can find no reference to this possibility in the electrocatalytic literature. Recent work in this laboratory [18] has shown that the rate of reduction of oxygen on passive titanium is a sensitive function of the concentration of oxygen vacancies in the film, but we do not yet know whether the vacancies act as catalytic reactants or as quantum wells in indirect tunneling of charge carriers across the film.

Mott-Schottky analysis, based upon capacitance measurements, has been employed in the present work to determine certain fundamental parameters of the oxide, such as the electronic type, the effective donor or acceptor density (N_D or N_A), and the flat band potential. The basic equations of Mott-Schottky analysis are

$$\frac{1}{C_{sc}^2} = \frac{2}{\epsilon\epsilon_0 e N_A A^2} \left(V - V_{fb} - \frac{kT}{e} \right) \quad \text{n-type} \quad (4.2)$$

and

$$\frac{1}{C_{sc}^2} = \frac{-2}{\epsilon\epsilon_0 e N_A A^2} \left(V - V_{fb} - \frac{kT}{e} \right) \quad \text{p-type} \quad (4.3)$$

where $\hat{\epsilon}$ is the dielectric constant of the oxide, A is the surface area of the interface (cm^2), ϵ_0 is the vacuum permittivity, q is the charge of the electron ($1.6 \times 10^{-19} \text{C}$), N_D and N_A are the donor density and acceptor density ($\#/\text{cm}^3$), respectively, and V_{fb} is the flatband potential (V vs. SHE). The interfacial capacitance, C is obtained from $C = -1/\omega Z''$, where Z'' is the imaginary component of the impedance and $\omega = 2\pi f$ is the angular frequency. Assuming that the capacitance of the double layer at the oxide/electrolyte interface is much larger than the space charge capacitance in the film, the measured capacitance, C , is equal to the space charge capacitance, C_{sc} at high frequency ($f > 1 \text{kHz}$). In the Mott-Schottky analyses reported here, the specimen was first passivated for 24 hours at the desired formation potential, in order to reach to steady state, and the impedance was then measured at a fixed high frequency as the potential was swept to the negative direction at a sufficiently high voltage scan rate that the properties of the film did not change; that is, the thickness of the passive film and the vacancy structure and concentration are “frozen” during the time of acquisition of the impedance versus voltage data that are required for the analyses [19]. The rationale for performing Mott-Schottky analyses in this manner is that the concentrations of donors and acceptors in the film (cation vacancies for p-type films and oxygen vacancies and/or cation

interstitials for n-type films) are potential dependent and hence may contribute to any non-linearity in C^{-2} versus V . Once the impedance data had been acquired, the capacitance was calculated from the imaginary component.

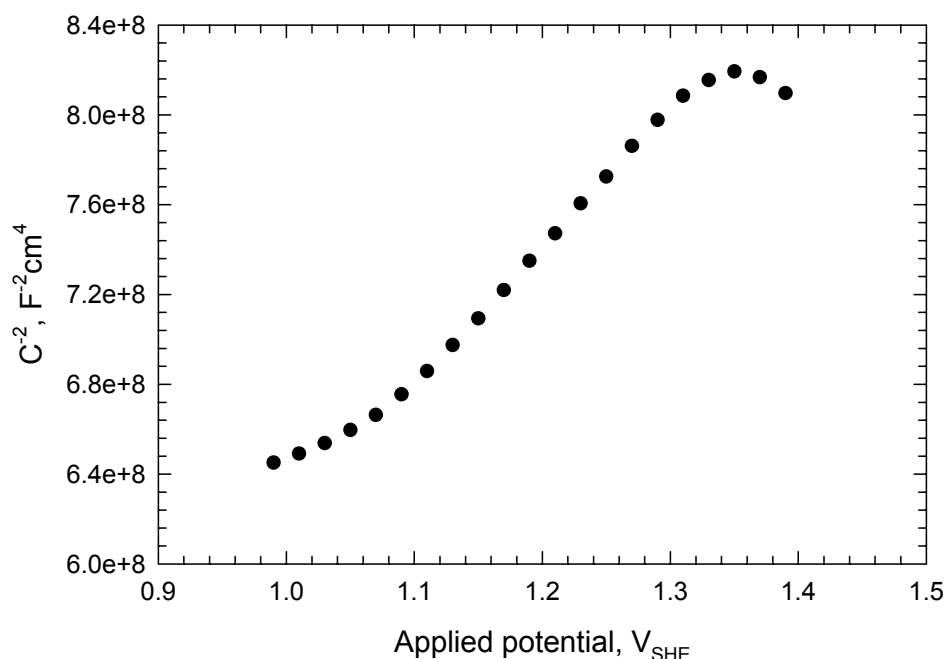


Figure 4-6: Mott-Schottky plot for platinum passivated at a formation potential of $1.39V_{SHE}$ in 0.5M H_2SO_4 solution for 24 hours. The impedance was measured at a frequency 10k Hz while sweeping the potential in the negative direction from the formation potential at a voltage scan rate of 100mV/s.

A typical C^{-2} versus V profile recorded for the passive films formed on Pt in 0.5M H_2SO_4 at a formation voltage of $1.39V_{SHE}$ and at room temperature is presented in Figure 4-6. The profile between $1.0V_{SHE}$ - $1.35V_{SHE}$ is characteristic of n-type

semiconductors. This result shows that the dominant defects in the oxide film over this voltage range are oxygen vacancies and/or platinum interstitials, as invoked in the Point Defect Model (PDM) [7]. Interestingly, the slope of the plot is found to change to a negative value at higher potentials ($E > 1.35V_{\text{SHE}}$), which was initially considered to indicate a change in the electronic character from n-type to p-type. However, as described above, the data shown in Figure 4-6 correspond to a single voltage sweep and hence to a “frozen-in” defect type and concentration, so that a change in the dominant defect from the oxygen vacancy/cation interstitial to the cation vacancy is unlikely. As seen in Figure 4-7, regions of negative slope exist in all of the Mott-Schottky plots, but the potentials for the onset for the negative-slope are different for each case. This is contrary to the expectation that p-type character should be observed only in the formation potential region where cation vacancies become the dominant defects. Stimming and Schultze [20] observed the similar phenomena in studying the capacity of passivated iron electrodes. They explained that, at low potentials, Mott-Schottky type behavior was found indicating that the donor density can be estimated from the linear region, but at high potentials valence band charging in the oxide film, which causes the degeneracy at the surface, contributes to an increase of the capacity. Khan and Schmickler’s [21] theoretical work based on the same experimental results also showed that the surface charge on the metal increases as the potential increases, and that the charge in the valence band starts to contribute to the total capacity at higher potentials, which causes the observed curvature.

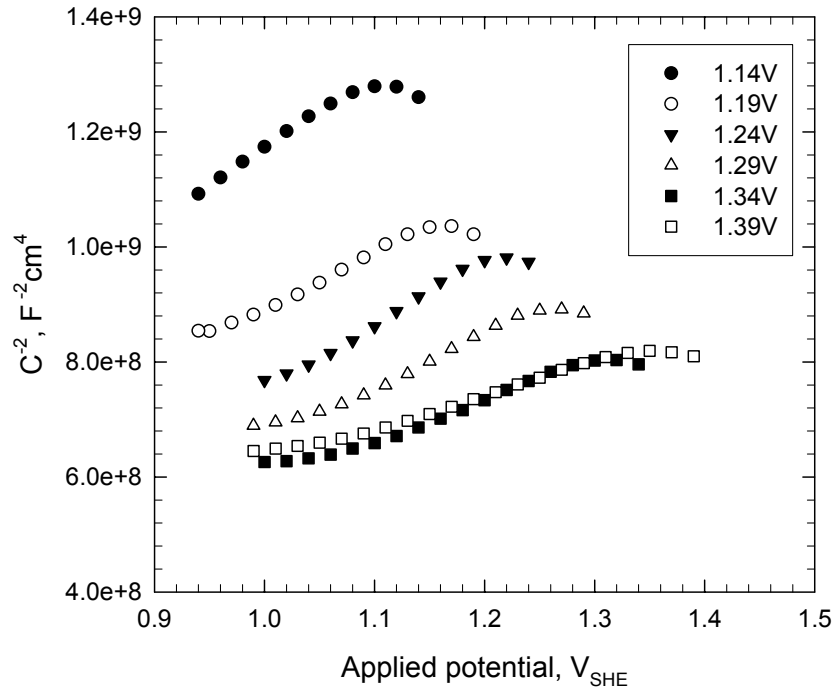


Figure 4-7: Mott-Schottky plots for platinum at different oxide formation potentials in 0.5M H₂SO₄ solution after polarization for 24 hours. The impedance was measured at a frequency 10k Hz while sweeping the potential in the negative direction from the formation potential at a voltage scan rate of 100mV/s.

In terms of classical Mott-Schottky theory, the defect concentration can be calculated from the slope of the Mott-Schottky plot. Here, the slope is taken with neglecting the downward curvature of the plots, which, according to Stimming and Schultze [20], gives approximately the correct donor concentration in the film. Figure 4-8 shows that the donor concentration increases with the formation potential, in which the donor concentrations are calculated from Mott-Schottky plots by using the parameter values obtained from the optimization of the PDM on EIS data with $\hat{\epsilon} = 42.5$ (Table 5-2). A vacancy concentration of the sites on the oxygen sub-lattice of PtO ($4.1 \times 10^{22} / \text{cm}^3$)

expands from 0.087 to 0.164 as the potential is increased from $1.14V_{\text{SHE}}$ to $1.39V_{\text{SHE}}$, respectively. Hence, the highly defective platinum oxide might act like a semimetal at higher potentials, which could play an important role in the oxygen reduction reaction of fuel cell.

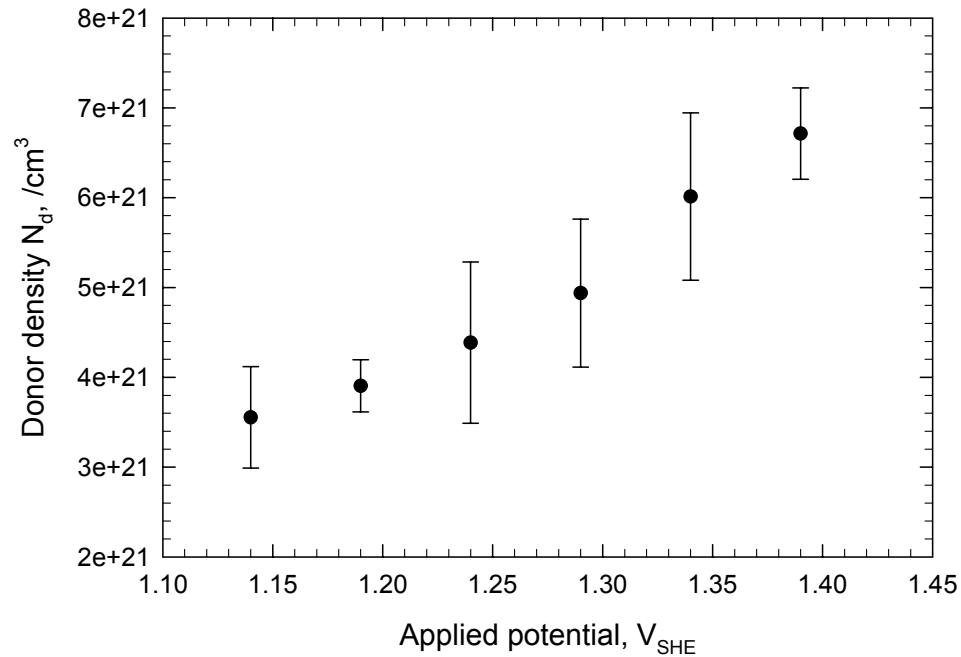


Figure 4-8: Donor density at 20°C calculated from the Mott-Schottky plots as a function of formation potential.

A “conventional” Mott-Schottky plot at 20°C (Figure 4-9) is constructed by plotting C_{ss}^{-2} versus applied potential V , where C_{ss} is the steady state capacitance, against the formation potential of the film, in which the capacitance was measured after polarization for 24 hours and at a frequency of 1k Hz. The slope in this plot is positive,

which is consistent with n-type character of oxidized platinum, and of importance is that the downward curvature at high potentials is no longer observed. The estimated donor density is $2.12 \times 10^{21}/\text{cm}^3$, which is in the range of the donor densities calculated from the transient experimental measurements (Figure 4-8).

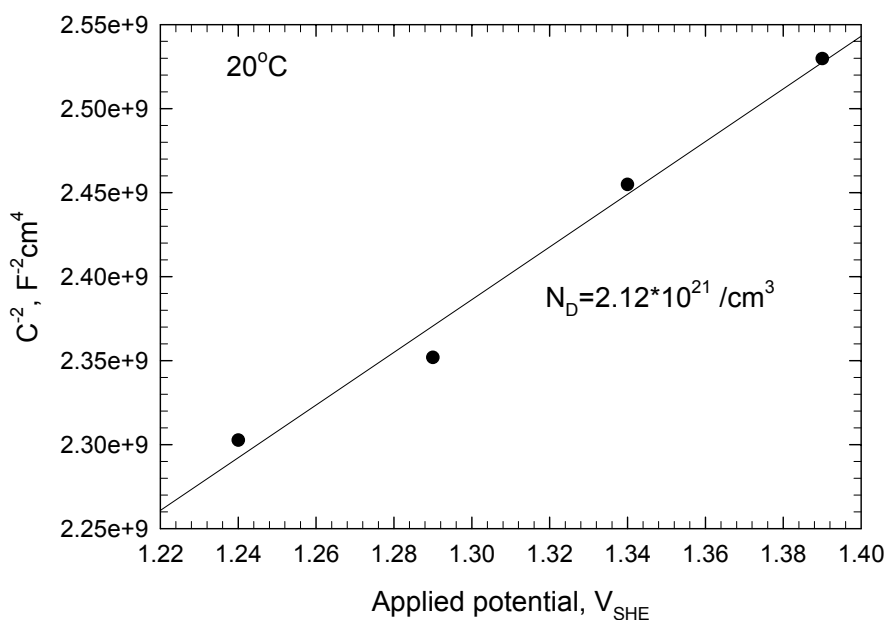


Figure 4-9: Steady-state Mott-Schottky plot for platinum constructed from the capacitance data measured at 1194 Hz in 0.5M H_2SO_4 solution at $T=20^\circ\text{C}$ after polarization for 24 hours at each voltage. Sinusoidal amplitude =10mV (peak-to peak).

As stated by Morrison[22], there are several contributions to the capacity at a semiconductor/solution interface. The measured interfacial capacitance is estimated as follows:

$$C^{-1} = (C_{sc} + C_{ss})^{-1} + C_H^{-1} \quad (4.4)$$

where C_{sc} is the space charge capacitance, C_{ss} is the surface state capacitance, and C_H is the Helmholtz double layer capacitance. In order to simplify the above equation to $C^{-1} = C_{sc}^{-1}$, the classical Mott-Schottky theory made several assumptions, such as absence of surface states and that the double layer capacitance is much greater than the space charge capacitance in the film (barrier layer). However, as has been shown in many studies, including this work, the anodic oxide film formed on platinum in the oxygen reduction region in 0.5M H_2SO_4 solution is only a few monolayers thick. The Debye length for n-type semiconductors is estimated according to

$$L_{Db} = \sqrt{\frac{\hat{\epsilon}\epsilon_0 kT}{q^2 N_D}} \quad (4.5)$$

where $\hat{\epsilon}$ is the dielectric constant of the oxide, ϵ_0 is the vacuum permittivity (8.85×10^{-14} F/cm), k is the Boltzman constant (1.38×10^{-23} J/K), T is the absolute temperature, q is the charge of the electron (1.6×10^{-19} C), N_D is the donor density. Therefore, the debye length for oxidized platinum in 0.5M H_2SO_4 solution is around 2 to 3 angstroms if the value of N_D is taken from Figure 4-9. The debye length is then of the same order as the thickness of the depletion layer, thereby negating the assumption that the dimension is infinite through thickness direction. Thus, the assumption that the

potential approaches the bulk value asymptotically is not valid. Also, slow transfer of the electrons to/from surface states, due to an insufficiently high sweep frequency applied during the experimental measurements of the capacitance, might cause the surface state capacitance C_{ss} not to be negligible compared with C_{sc} , which might then give rise to frequency-dependence of the capacitance in the Mott-Schottky plots (Figure 4-10). Classical Mott-Schottky theory further assumes that the film is doped uniformly. However, Stimming [20] and Wagner [23] found that, in the case of the passive film on iron, the donors are not uniformly doped. The model of Wager includes a Fe^{2+} concentration that decreases with increasing distance from the metal surface. Previous work on zirconium [24] and tungsten [25], in this group, has also shown that the concentration of defects in the oxide film decreases exponentially with distance from the metal/film interface, a result that follows directly from the PDM [7, 26, 27]. Therefore, the defect concentrations in the oxide film on platinum calculated in terms of Mott-Schottky theory should be regarded as being only semi-quantitative or, perhaps, even qualitative in nature. Accordingly, in the present analysis, we will accept the Mott-Schottky analysis as demonstrating that the barrier layer on platinum is an n-type defect semiconductor having a very high defect concentration.

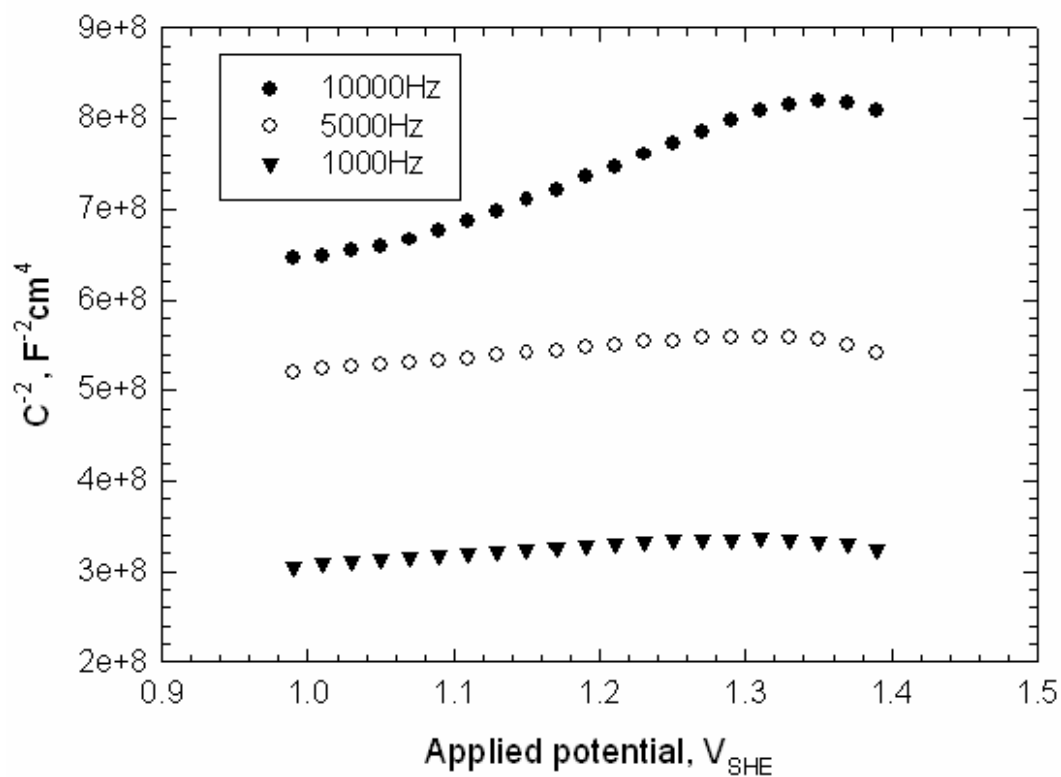
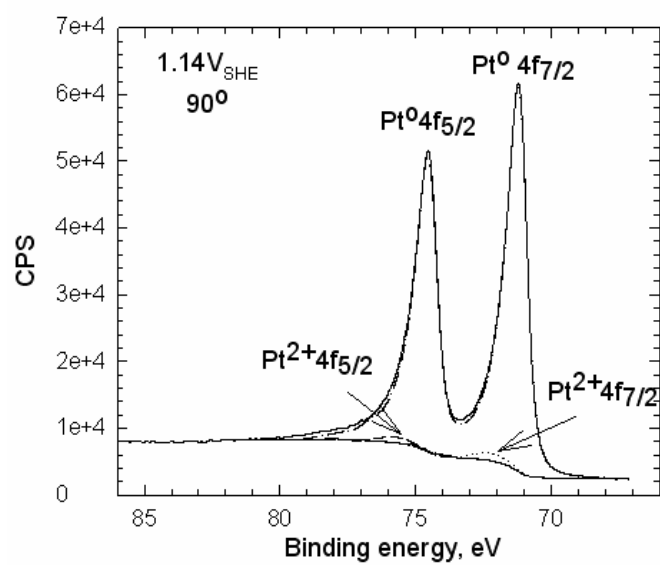
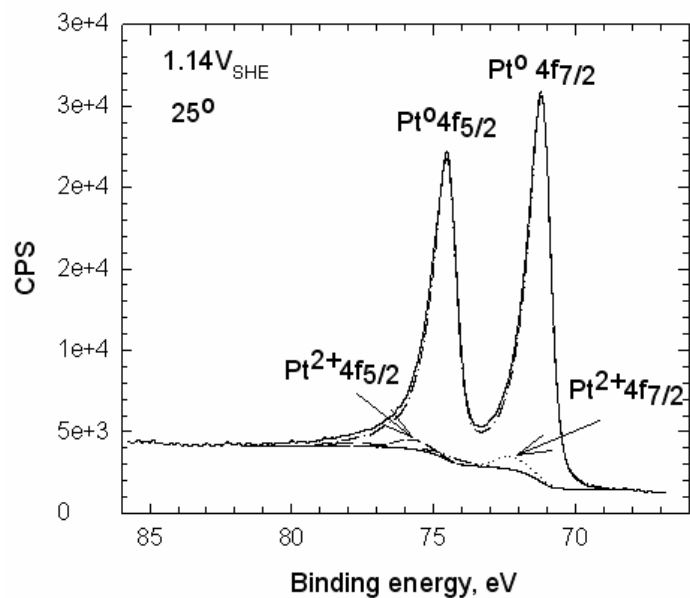
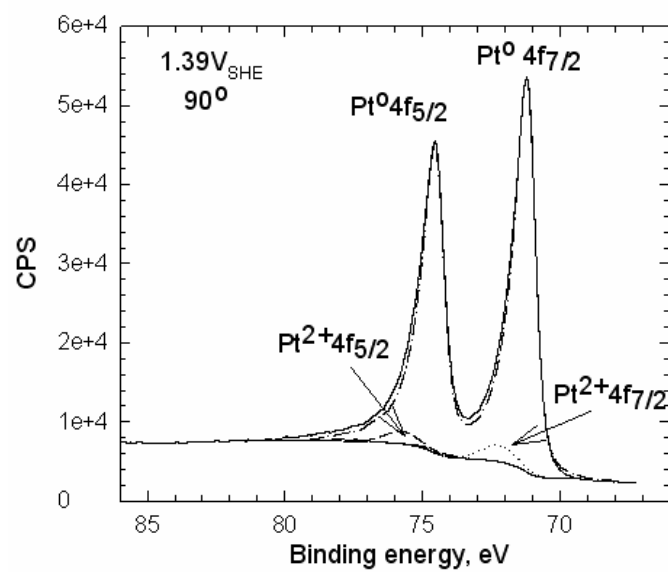
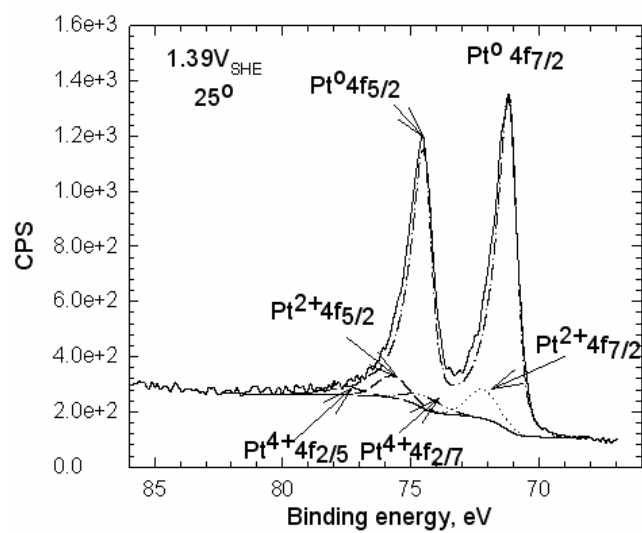


Figure 4-10: Mott-Schottky plots for platinum at 1.39 V_{SHE} in 0.5 M H_2SO_4 solution after polarization for 24 hours as a function of frequency. The impedance was measured at frequencies of 1 kHz, 5 kHz, and 10 kHz, while sweeping the potential in the negative direction from the formation potential at a voltage scan rate of 100 mV/s.

4.4 Compositions of Platinum Oxide Film

As indicated in Figure 4-1, the potential region for the formation of platinum oxide on platinum lies between $1.0V_{SHE}$ - $1.39V_{SHE}$. Film composition was identified using XPS at two angles and comparing films grown at different potentials. XPS survey spectra of the oxide surface detected platinum, oxygen, and carbon. The carbon is attributed to contamination. The platinum 4f spectra of the surface, measured at two takeoff angles (25° and 90°), and the corresponding deconvolutions are shown in Figure 4.10. It is observed that the oxide film formed at a voltage of $1.19V_{SHE}$ contains only Pt(II) peaks. However at the two higher formation potentials, $1.39V_{SHE}$ and $1.44V_{SHE}$, both Pt(II) and Pt(IV) exist in the oxide film.





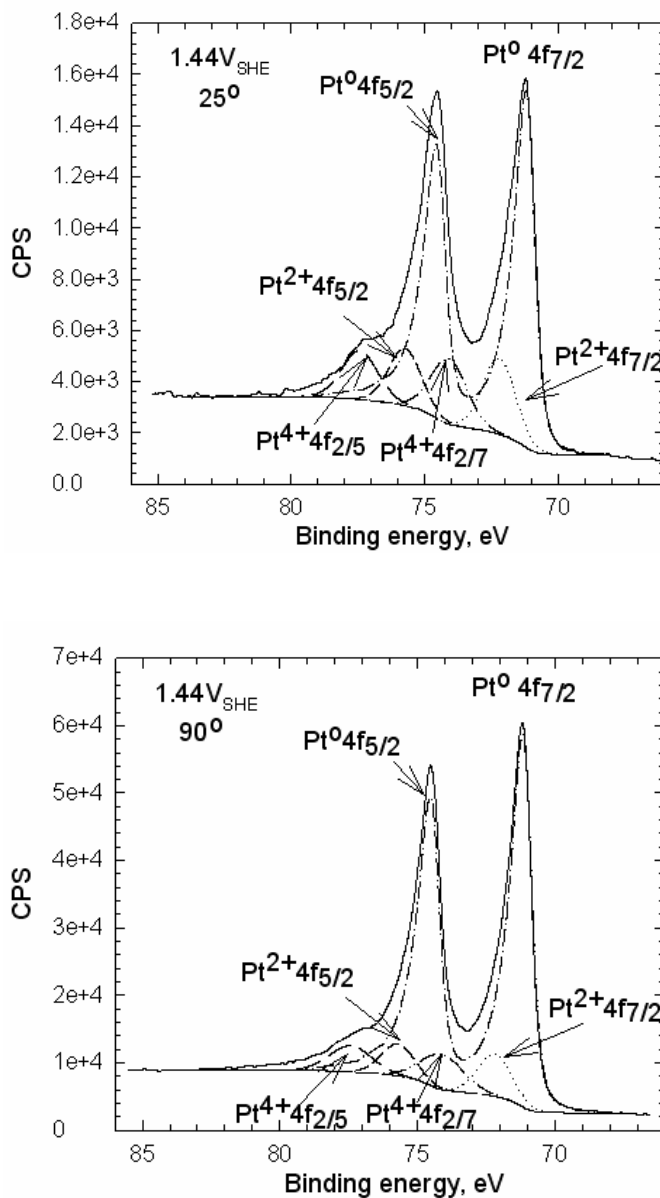


Figure 4-11: ARXPS spectra of the Pt4f regions recorded at two different takeoff angles for Pt surfaces passivated in 0.5M H₂SO₄ for 24 hours at different potentials.

The data presented in Table 4-1 based on Figure 4-11 show that the atomic concentrations of the oxidized platinum species increase with decreasing takeoff angle. Since, at a small takeoff angle, the signal is more surface sensitive, these results show

that the oxide film contains two species [Pt(II) and Pt(IV)] at higher potentials, and that Pt(IV) is located in the outer part of the passive film, while Pt(II) is located in the inner part of the film. As found in most of the previous work [4, 28, 29], using electrochemical methods, the present data suggest that the thin oxide forms over the range of $1.0V_{SHE}$ - $1.39V_{SHE}$ is the barrier layer and mainly contains Pt(II). With an increase in the potential up to $1.39V_{SHE}$, Pt(II) at the outer surface is oxidized to Pt(IV) or Pt(II) ions being ejected from the barrier layer/outer layer interface are oxidized and hydrolyzed to precipitate a Pt(IV) hydroxide phase. In principle, there is no restriction on the thickness of the outer layer, because its formation is not field-driven within the phase. The increase of atomic concentration of these species with increasing formation potential indirectly indicates that the thickness of the oxide film increases with the formation potential.

Table 4-1: Atomic concentrations from Pt4f recorded at two different takeoff (T/O) angles for Pt surfaces passivated in 0.5M H_2SO_4 at the indicated film formation potentials for 24 hours.

| T/O Angle | 90° | 90° | 90° | 25° | 25° | 25° |
|--|---------------|---------------|--------------|---------------|---------------|--------------|
| Polarization Potential/V_{SHE} | Pt(II) | Pt(IV) | Pt(0) | Pt(II) | Pt(IV) | Pt(0) |
| 1.19 | 2.3 | 0 | 97.7 | 3.8 | 0 | 96.2 |
| 1.39 | 4.9 | 0 | 95.1 | 9.2 | 4.6 | 86.2 |
| 1.44 | 10.9 | 11.1 | 78.0 | 17.4 | 16.2 | 66.4 |

4.5 Summary

The work reported here shows that there is nothing remarkable about the anodic oxide film on platinum. Thus, it has a typical bilayer structure with a barrier layer comprising a highly defective oxide and an outer, precipitated layer. The barrier layer can exist in the steady-state, with the steady state thickness varying linearly with the formation voltage, yielding an anodizing constant of approximately 2.5 nm/V, while the steady state passive current is voltage independent within the Pt(II) oxide formation region. The latter is consistent with the n-type electronic character of the film, as predicted by the Point Defect Model (PDM).

References

- [1] S. Shibata, J. Electroanal. Chem., 89 (1977) 37.
- [2] B.E. Conway and G. Jerkiewicz, J. Electroanal. Chem., 339 (1992) 123.
- [3] B.E. Conway, G. Tremiliosi-filho, and G. Jerkiewicz, J. Electroanal. Chem., 297 (1991) 435.
- [4] B.E. Conway, Prog. Surf. Sci., 49 (1995) 331.
- [5] H. Angerstin-Kozłowska, B.E. Conway, and W.B.A. Sharp, J. Electroanal. Chem., 13 (1973) 9.
- [6] D.C. Johnson, D.T. Napp, and S. Brukenstein, Electrochim. Acta, 15 (1970) 1493.
- [7] D.D. Macdonald, J. Electrochem. Soc., 139 (1992) 3434.
- [8] E. Sikora and D.D. Macdonald, Electrochim. Acta, 48 (2002) 69.

- [9] R.D.L. Kronig, J. Opt. Soc. Am., 12 (1926) 547.
- [10] H.A. Kramers, Z. Phys., 30 (1929) 521.
- [11] M. Urquidi-Macdonald, S. Real, and D.D. Macdonald, J. Electrochem. Soc., 133 (1986) 2018.
- [12] D.D. Macdonald and M. Urquidi-Macdonald, J. Electrochem. Soc., 132 (1985) 2316.
- [13] P. Villas and L.D. Calvert, Pearson's Handbook of Crystallographic Data for Intermetallic Phases, ASM International, 1991.
- [14] W.J. Moore Jr. and L. Pauling, J. Am. Chem. Soc., 63 (1941) 1392.
- [15] U. Diebold. In Structure Property Relationships of Oxide Surfaces and Interfaces. Boston, MA: Materials Research Society Symposium-Proceedings, 2000.
- [16] M.A. Henderson, W.S. Epling, C.H.F. Peden, and C.L. Perkins, J. Phys. Chem. B, 107 (2003) 534.
- [17] W. Weiss and W. Ranke, Prog. Surf. Sci., 70 (2002) 1.
- [18] B.-W. Roh and D.D. Macdonald. In 207th Meeting of The Electrochemical Society. Quebec City, Canada, May 2005.
- [19] J. Sikora, E. Sikora, and D.D. Macdonald, Electrochim. Acta, 45 (2000) 1875.
- [20] U. Stimming and J.W. Schultz, Ber. Bunsenges. Phys. Chem., 80 (1976) 1297.
- [21] S.U.M. Khan and W. Schmickler, J. electroanal. Chem., 108 (1980) 329.
- [22] S.R. Morrison, Electrochemistry at Semiconductor and Oxidized Metal Electrodes, Plenum Press, New York and London, 1980.
- [23] C. Wagner, Ber. Bunsenges. Phys. Chem., 77 (1973) 1090.
- [24] A. Goossens, M. Vazquez, and D.D. Macdonald, Electrochim. Acta, 41 (1996) 35.

- [25] D.D. Macdonald, E. Sikora, and J. Sikora, *Electrochim. Acta*, 43 (1998) 2851.
- [26] D.D. Macdonald, A. Sun, N. Priyantha, and P. Jayaweera, *J. Electroanal. Chem.*, 572 (2004) 421.
- [27] D.D. Macdonald, *Pure Appl. Chem.*, 71 (1999) 951.
- [28] S.J. Xia and V.I. Birss, *Electrochim. Acta*, 45 (2000) 3659.
- [29] G. Jerkiewicz, G. Vatankhah, J. Lessard, M.P. Soriaga, and Y.S. Park, *Electrochim. Acta*, 49 (2004) 1451.

Chapter 5

GROWTH MECHANISM OF PLATINUM OXIDE FILM

Capacitance measurements performed in this work indicate that the Pt oxide film grown in the oxide formation region ($1.0 V_{SHE} - 1.39 V_{SHE}$) is a highly doped, n-type defect semiconductor. That the oxide film has a bi-layer structure, where Pt(II) exists in the barrier layer and Pt(IV) resides in the outer layer, is confirmed by the ARXPS studies. Therefore, the experimental results from this work are consistent with the postulates of the PDM [1] for passive films formed on metal surfaces. In addition, the diagnostic criterion derived from the PDM for n-type oxide films, that the logarithm of the steady state current density is independent of formation potential, is also observed experimentally.

Figure 5-1 summarizes the physicochemical processes that are envisioned to occur within the barrier layer of the passive film formed anodically on platinum, according to the PDM. The model applied here is a truncated version of the more general PDM. Since, for an n-type oxide film, the dominant defects in the barrier layer must be oxygen vacancies and/or cation interstitials, the generation and annihilation of cation vacancies are ignored [2].

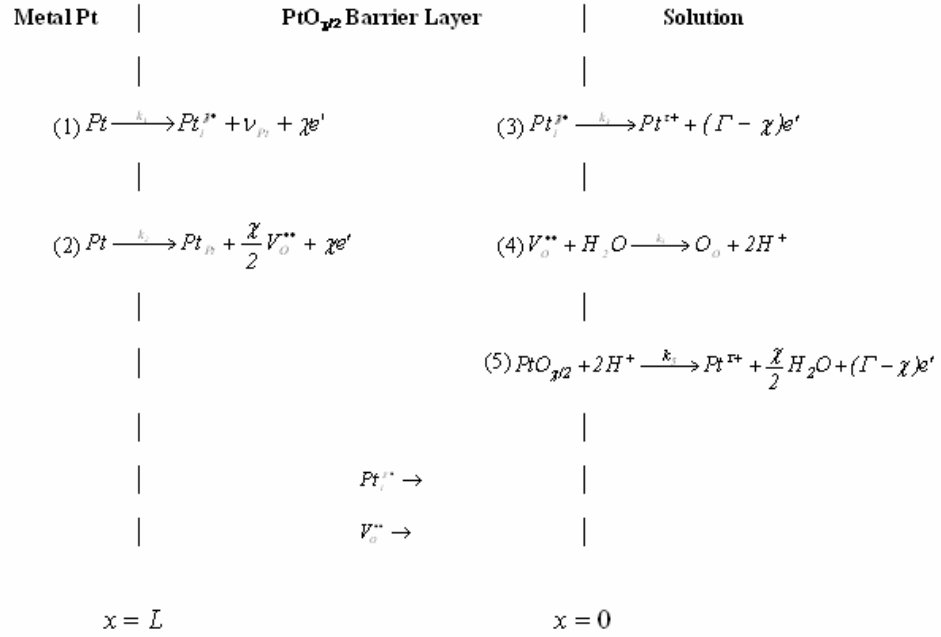


Figure 5-1: Schematic of physicochemical processes that are envisioned to occur within the barrier oxide (PtO_{x/2}) layer on passive platinum, according to the truncated Point Defect Model. $Pt \equiv$ platinum atom; $Pt_i^{x*} \equiv$ interstitial platinum cation; $\nu_{Pt} \equiv$ platinum vacancy in Pt metal substrate; $Pt_{Pt} \equiv$ platinum cation in a normal cation position in the barrier layer; $Pt^{x+} \equiv$ platinum cation in the solution phase (outer layer); $V_O^{**} \equiv$ oxygen vacancy; $O_O \equiv$ oxygen ion in a normal anion site in the barrier layer.

A physico-electrochemical model, based on Figure 5-1, has been developed for the anodic oxide film on Pt for the purpose of interpreting the electrochemical impedance spectroscopy (EIS) data. The model employed is a variant of that previously developed for interpreting EIS data for Alloy 22 [2], and is essentially a truncated form of the general PDM discussed elsewhere [3]. With reference to Figure 5-1, Reaction (1) describes the injection of the metal interstitial, Pt_i^{x*} , into the barrier layer. The platinum

interstitial is transmitted through the barrier layer, primarily under the influence of the electric field, and is then ejected into the solution, as described by Reaction (3). Reaction (2) results in the growth of the barrier layer into the bulk platinum via the generation of oxygen vacancies ($V_O^{\bullet\bullet}$), and Reaction (5) leads to the destruction of the barrier layer by dissolution. Reaction (4) represents the annihilation of the oxygen vacancies at the film/solution interface that are produced by Reaction (2) at the metal/film interface. Note that Reactions (1), (3), and (4) are lattice conservative processes, in that their occurrence does not result in the movement of the corresponding interface with respect to a laboratory frame of reference, while Reactions (2) and (5) are lattice non-conservative processes. A steady state must involve a balance between at least two non-conservative reactions, since only one non-conservative reaction would lead to monotonic growth or thinning of the passive film.

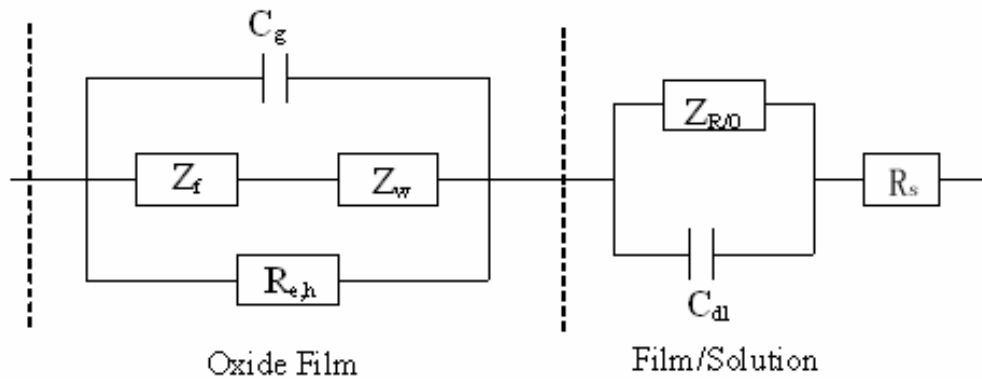


Figure 5-2: Impedance array describing the total impedance of passive platinum.

The electrochemical reactions located at the metal/film or film/solution interfaces thus contribute to the interfacial impedance. In the past treatment of the PDM [1, 2, 4, 5], the impedance due to the ionic and electronic defect transport across the film is assumed to make a much smaller contribution to the overall film impedance than do the interfacial charge transfer processes. However, as Chao, Lin and Macdonald [6] originally presented the PDM, a Warburg-like impedance was expected for the transport of ionic defects through the film. Bojinov et al. [7-9] have also discussed the significant contribution of the transport of both electronic and ionic defects on the film impedance in analogy with the PDM. Accordingly, the current model incorporates the conduction of electronic and ionic defects through the film. The impedance of the oxide film is then represented by the impedance array shown in Figure 5-2 with the total impedance being given as

$$Z_T = \frac{I}{(Z_f + Z_w)^{-1} + R_{e,h}^{-1} + j\omega C_g} + \frac{I}{Z_{R/O}^{-1} + j\omega C_{dl}} + R_s \quad (5.1)$$

where Z_f and Z_w are the impedances due to the interfacial reactions and transport of ionic defects, respectively, as described below. $R_{e,h}$ is the electronic resistance due to the transport of electrons and holes through the film; these terms were considered in the original PDM [6], predating the work of Bojinov et al. [7-9] by about twenty years.¹

¹The Mixed Conduction Model (MCM) proposed by Bojinov et.al [7-9] is essentially identical to the PDM, except that the authors use the high field approximation for describing the electric field and add impedances for the transfer of electrons, holes and ionic defects across the film. However, the latter feature

Since the electrons and holes move rapidly through the film, a pure resistor $R_{e,h}$ is considered to represent the impedance and to be in parallel with the interfacial impedance and the Warburg impedance. $C_g = \hat{\epsilon}\epsilon_0 / L$ [dielectric constant $\hat{\epsilon} = 42.5$ for a passive PtO barrier layer (see later) and vacuum permittivity $\epsilon_0 = 8.85 \times 10^{-14} \text{ F/cm}$] is the geometric capacitance of the film, which is assumed to be in parallel with the interfacial impedance and Warburg impedance. The non-faradaic capacitance of the film is the combination of the geometric and space charge capacitances in parallel, i.e. $C_g + C_{sc}$ [3]. However, the studies of Bockris [10] and Bao [11, 12] on the steady state thickness of the anodic oxide film on platinum show that the film thickness on platinum is 0.2-0.7 nm, which gives values for C_g of 50 $\mu\text{F/cm}^2$ -200 $\mu\text{F/cm}^2$ according to the above expression for C_g . Compared with the values of C_{sc} (20 $\mu\text{F/cm}^2$ -50 $\mu\text{F/cm}^2$, Figure 5.7) from Mott-Schottky plots, the geometric capacitance is thus postulated to dominate the film capacitance. When the solution contains a redox reaction that is capable of accepting charge from the electrode, electron exchange occurs at the film/solution interface at a rate that is governed by the reaction impedance ($Z_{R/O}$). C_{dl} is the double layer capacitance at the film/solution interface. C_{dl} and $Z_{R/O}$ are connected in parallel and both are in series with the film impedance. R_s is the solution resistance between the luggin capillary tip and working electrode surface.

was incorporated in the original PDM [40] and hence does not represent an innovation. Adoption of the high field approximation does not appear to materially affect the predictions of the model.

5.1 Interfacial Impedance Due to the Generation and Annihilation of Defects at the Interfaces and Dissolution of the Film.

The rate of change of barrier layer thickness involves the two lattice non-conservative reactions, resulting in the following expression:

$$\frac{dL}{dt} = -\frac{2\Omega}{\chi} J_O - \Omega k_5 (C_{H^+} / C_{H^+}^0)^n \quad (5.2)$$

where the first term on the right hand side corresponds to the rate of barrier layer generation at the metal/film interface [Reaction (2), Figure 5-1] and the second term corresponds to the rate of dissolution of the barrier layer at the barrier layer/solution interface [Reaction (5), Figure 5-1]. The parameter $\Omega = 14.97 \text{ cm}^3 \text{ mol}^{-1}$ is the molar volume per cation of the barrier layer (PtO), which is calculated according to $\Omega = M / \rho$, where $M = 211.077 \text{ g/mol}$ is the molar weight of PtO and $\rho = 14.1 \text{ g/cm}^3$ is the density of PtO , $\chi = 2$ is the oxidation state of platinum in the barrier layer in the passive state, J_O is the flux of oxygen vacancies within the barrier layer, C_{H^+} is the hydrogen ion concentration in the solution at the film/solution interface (units of mol/l), $C_{H^+}^0$ is the standard state hydrogen ion concentration, defined as being 1.0 mol/l, n is the kinetic order of the film dissolution reaction with respect to C_{H^+} , and k_5 is the rate constant for Reaction (5), Figure 5-1. The inclusion of the standard state for the hydrogen ion concentration ensures that the dimension of k_5 ($\text{mol/cm}^2\text{s}$) is independent of n .

All interfacial reactions that produce or consume electrons contribute to the total current density, which is described as [1, 2, 4, 5]

$$I = F[-\chi J_i^{m/f} - 2J_O^{m/f} - (\Gamma - \chi)J_i^{f/s} + (\Gamma - \chi)k_5(C_{H^+}/C_{H^+}^0)^n] \quad (5.3)$$

in which $F = 96487 \text{ C/equiv}$ is Faraday's constant, and $\Gamma = 2$ is the oxidation state of platinum in solution in the passive range. The fluxes of the point defects in the barrier layer may be written as $J_i = -D_i(\partial C_i / \partial x) - \chi K D_i C_i$ and $J_O = -D_O(\partial C_O / \partial x) - 2K D_O C_O$ for platinum interstitials and oxygen vacancies, respectively, where D and C are the diffusivity and concentration, and subscripts i and O designate platinum interstitials and oxygen vacancies. Additionally, $K = \varepsilon F / RT$, $R = 8.314 \text{ J mol}^{-1} \text{ K}^{-1}$ is the gas constant, T is the Kelvin temperature, and ε is the electric field strength, which is considered to be a constant [1, 2, 4, 5]. The continuity equations for the two defects, $\partial C / \partial t = -\nabla \bullet J$, then become

$$\frac{\partial C_i}{\partial t} = D_i \frac{\partial^2 C_i}{\partial x^2} + \chi D_i K \frac{\partial C_i}{\partial x} \quad (5.4)$$

and

$$\frac{\partial C_O}{\partial t} = D_O \frac{\partial^2 C_O}{\partial x^2} + 2D_O K \frac{\partial C_O}{\partial x} \quad (5.5)$$

These equations are then solved for the initial conditions ($t = 0$) of $C_i(x) = C_i^0(x)$ and $C_o(x) = C_o^0(x)$ and for the boundary conditions ($t > 0$) of: $x = 0$ (the film/solution interface), $J_i(0) = -k_3^0 e^{a_3 V} C_i(0)$ (k_3^0 , cm/s), $J_o(0) = -(\chi/2)k_4^0 e^{a_4 V} C_o(0)$ (k_4^0 , cm/s); at $x = L$ (the metal/film interface), $J_i(L) = -k_1^0 e^{a_1 V} e^{-b_1 L}$ (k_1^0 , mol/cm²s), $J_o(L) = -(\chi/2)k_2^0 e^{a_2 V} e^{-b_2 L}$ (k_2^0 , mol/cm²s). Note that the fluxes of cation interstitials and oxygen vacancies are negative when the species move from the metal/film (m/f) interface to the film/solution (f/s) interface in the coordinate system adopted in Figure 5-1. Combined with the rate constants, the rate of change of the barrier layer thickness [Equation 5.2] and the current density [Equation 5.3] then become

$$\frac{dL}{dt} = \Omega k_2^0 e^{a_2 V} e^{-b_2 L} - \Omega k_5^0 e^{a_5 V} (C_{H^+} / C_{H^+}^0)^n \quad (5.6)$$

and

$$I = F[\chi k_1^0 e^{a_1 V} e^{-b_1 L} + \chi k_2^0 e^{a_2 V} e^{-b_2 L} + (\Gamma - \chi)k_3^0 e^{a_3 V} C_i(0) + (\Gamma - \chi)k_5^0 e^{a_5 V} (C_{H^+} / C_{H^+}^0)^n] \quad (5.7)$$

where C_{H^+} has units of mol/l.

Note that the current density [Equation 5.7] is a function of V , L , and $C_i(0)$.

Accordingly, for any arbitrary changes, δV , δL , and $\delta C_i(0)$, we have

$$\delta I = \left(\frac{\partial I}{\partial V} \right)_{L, C_i(0)} \delta V + \left(\frac{\partial I}{\partial L} \right)_{V, C_i(0)} \delta L + \left(\frac{\partial I}{\partial C_i(0)} \right)_{V, L} \delta C_i(0) \quad (5.8)$$

The variations in V , L , and $C_i(0)$ are sinusoidal in an EIS measurement, so that we write $\delta V = \Delta V e^{j\omega t}$, $\delta L = \Delta L e^{j\omega t}$, and $\delta C_i(0) = \Delta C_i(0) e^{j\omega t}$, where ΔX is the amplitude of the variation in X at a frequency $\omega = 0$. From Equation 5.7, the Faradic admittance is then defined as

$$Y_f = \frac{\delta I}{\delta V} = I^V + I^L \frac{\Delta L}{\Delta V} + I^{C_i(0)} \frac{\Delta C_i(0)}{\Delta V} \quad (5.9)$$

where $I^V = (\partial I / \partial V)_{L, C_i(0)}$, $I^L = (\partial I / \partial L)_{V, C_i(0)}$, and $I^{C_i(0)} = [\partial I / \partial C_i(0)]_{L, V}$. These differentials will be evaluated later from Equation 5.8.

We now return to Equation 5.6 and determine the response of $\partial L / \partial t$ to δV , δL , and $\delta C_i(0)$ by taking the total differentials. Thus, the relaxation in film thickness is

$$d(\delta L) / dt = \Omega k_2^0 a_2 e^{a_2 V} e^{-b_2 L} \delta V - \Omega k_2^0 b_2 e^{a_2 V} e^{-b_2 L} \delta L - \Omega k_5^0 a_5 e^{a_5 V} (C_{H^+} / C_{H^+}^0)^n \delta V \quad (5.10)$$

Considering that $d(\delta L)/dt = j\omega\Delta L e^{j\omega t}$, we obtain

$$j\omega\Delta L e^{j\omega t} = \Omega[k_2^0 a_2 e^{a_2 V} e^{-b_2 L} - k_5^0 a_5 e^{a_5 V} (C_{H^+} / C_{H^+}^0)^n] \Delta V e^{j\omega t} - \Omega k_2^0 b_2 e^{a_2 V} e^{-b_2 L} \Delta L e^{j\omega t} \quad (5.11)$$

which, upon rearrangement, yields

$$\frac{\Delta L}{\Delta V} = \frac{\Omega[k_2^0 a_2 e^{a_2 V} e^{-b_2 L} - k_5^0 a_5 e^{a_5 V} (C_{H^+} / C_{H^+}^0)^n]}{\Omega k_2^0 b_2 e^{a_2 V} e^{-b_2 L} + j\omega} \quad \text{or} \quad \frac{\Delta L}{\Delta V} = \frac{\Phi_2}{1 + j\omega\tau_2} \quad (5.12)$$

where

$$\Phi_2 = \left(\frac{a_2}{b_2} \right) - \left(\frac{k_5^0}{k_2^0} \right) \left(\frac{a_5}{b_2} \right) e^{(a_5 - a_2)V} e^{b_2 L} (C_{H^+} / C_{H^+}^0)^n \quad (5.13)$$

and

$$\tau_2 = \frac{1}{\Omega k_2^0 b_2 e^{a_2 V} e^{-b_2 L}} \quad (5.14)$$

For platinum interstitials, the relaxation for $C_i(0)$ is determined through the mass balance at the film/solution interface $dC_i(0)/dt = -k_3 C_i(0) = -k_3^0 e^{a_3 V} C_i(0)$ (units of k_3^0 are s^{-1}). The total differential is $d(\delta C_i(0))/dt = -k_3^0 [a_3 e^{a_3 V} C_i(0) \delta V + e^{a_3 V} \delta C_i(0)]$. Inserting the sinusoidal variations for δV and $\delta C_i(0)$ therefore yields

$$j\omega \Delta C_i(0) e^{j\omega t} = -k_3^0 a_3 e^{a_3 V} C_i(0) \Delta V e^{j\omega t} - k_3^0 e^{a_3 V} \Delta C_i(0) e^{j\omega t} \quad (5.15)$$

and

$$\Delta C_i(0)(j\omega + k_3^0 e^{a_3 V}) = -k_3^0 a_3 e^{a_3 V} C_i(0) \Delta V \quad (5.16)$$

Therefore,

$$\frac{\Delta C_i(0)}{\Delta V} = \frac{-k_3^0 a_3 e^{a_3 V} C_i(0)}{j\omega + k_3^0 e^{a_3 V}} = -\frac{a_3 C_i(0)}{1 + j\omega \tau_3} \quad (5.17)$$

in which

$$\tau_3 = \frac{1}{k_3^0 e^{a_3 V}} \quad (5.18)$$

The expression for the Faradic admittance is finally derived from Equation 5.9 as

$$Y_f = I^V + I^L \frac{\Phi_2}{1 + j\omega\tau_2} - I^{C_i(0)} \frac{a_3 C_i(0)}{1 + j\omega\tau_3} \quad (5.19)$$

where

$$\begin{aligned} I^V &= \left(\frac{\partial I}{\partial V} \right)_{L, C_i(0)} \\ &= F[a_1 \chi k_1^0 e^{a_1 V} e^{-b_1 L} + a_2 \chi k_2^0 e^{a_2 V} e^{-b_2 L} + a_3 (\Gamma - \chi) k_3^0 e^{a_3 V} C_i(0) + a_5 (\Gamma - \chi) k_5^0 e^{a_5 V} (C_{H^+} / C_{H^+}^0)^n] \end{aligned} \quad (5.20)$$

$$\begin{aligned} I^L &= \left(\frac{\partial I}{\partial L} \right)_{V, C_i(0)} \\ &= F[-b_1 \chi k_1^0 e^{a_1 V} e^{-b_1 L} - b_2 \chi k_2^0 e^{a_2 V} e^{-b_2 L}] = -\chi F[b_1 k_1^0 e^{a_1 V} e^{-b_1 L} + b_2 k_2^0 e^{a_2 V} e^{-b_2 L}] \end{aligned} \quad (5.21)$$

and

$$I^{C_i(0)} = \left(\frac{\partial I}{\partial C_i(0)} \right)_{V,L} = (\Gamma - \chi) F k_3^0 e^{a_3 V} \quad (5.22)$$

In the above expressions, the parameters that appear on the right side are identified with being steady-state quantities.

The parameters, k_1^0 , k_2^0 , k_3^0 , k_4^0 , k_5^0 , in the above equations are functions of solution pH and the standard potential drop across the film/solution interface, $\phi_{f/s}^0$. The

PDM defines $k_1^0 = k_1^{00} e^{-\alpha_1 \beta \chi \gamma pH} e^{-\alpha_1 \chi \gamma \phi_{f/s}^0}$, $k_2^0 = k_2^{00} e^{-\alpha_2 \beta \chi \gamma pH} e^{-\alpha_2 \chi \gamma \phi_{f/s}^0}$,

$k_3^0 = k_3^{00} e^{\alpha_3 \beta \gamma pH} e^{\alpha_3 \gamma \phi_{f/s}^0}$, $k_4^0 = k_4^{00} e^{2\alpha_4 \beta \gamma pH} e^{2\alpha_4 \gamma \phi_{f/s}^0}$, and $k_5^0 = k_5^{00} e^{\alpha_5 \beta (\Gamma - \chi) \gamma pH} e^{\alpha_5 (\Gamma - \chi) \gamma \phi_{f/s}^0}$, in

which α_1 , α_2 , α_3 , α_4 , α_5 are the transfer coefficients, and k_1^{00} , k_2^{00} , k_3^{00} , k_4^{00} , k_5^{00} are

the standard rate constants. The potential drop across the film/solution (f/s) interface is

$\phi_{f/s} = \phi_f - \phi_s = \alpha V + \beta pH + \phi_{f/s}^0$ and that across the metal/film (m/f) interface is

$\phi_{m/f} = \phi_m - \phi_s = (1 - \alpha)V - \varepsilon L - \beta pH - \phi_{f/s}^0$, in which $\alpha = d\phi_{f/s} / dV$ is the dependence of

the potential drop across the barrier layer/solution interface on the applied voltage, V ,

[i.e., α is the polarizability of the barrier layer/outer layer (solution) interface];

$\beta = d\phi_{f/s} / dpH$ is the dependence of the potential drop across the same interface on pH ;

$\phi_{f/s}^0$ is the value of $\phi_{f/s}$ in the standard state ($V = 0$, $pH = 0$); $\gamma = F / RT$;

$K = \varepsilon \gamma = \varepsilon F / RT$, and Table 5-1 lists the rate constants defined in PDM.

Table 5-1: Rate constants $k_i = k_i^0 e^{a_i V} e^{-b_i L}$ for five interfacial reactions in terms of the Point Defect Model.

| Reaction | a_i / V^{-1} | b_i / cm^{-1} | Units of k_i^0 |
|---|--|------------------------|------------------------------------|
| (1) $Pt \xrightarrow{k_1} Pt_i^{\chi\bullet} + v_{Pt} + \chi e'$ | $\alpha_1 (1 - \alpha) \chi \gamma$ | $\alpha_1 \chi K$ | $\text{mol s}^{-1} \text{cm}^{-2}$ |
| (2) $Pt \xrightarrow{k_2} Pt_{Pt} + \frac{\chi}{2} V_o^{\bullet\bullet} + \chi e'$ | $\alpha_2 (1 - \alpha) \chi \gamma$ | $\alpha_2 \chi K$ | $\text{mol s}^{-1} \text{cm}^{-2}$ |
| (3) $Pt_i^{\chi\bullet} \xrightarrow{k_3} Pt^{\Gamma+} + (\Gamma - \chi) e'$ | $\alpha_3 \alpha \Gamma \gamma$ | 0 | cm s^{-1} |
| (4) $V_o^{\bullet\bullet} + H_2O \xrightarrow{k_4} O_o + 2H^+$ | $2\alpha_4 \alpha \gamma$ | 0 | cm s^{-1} |
| (5) $PtO_{\frac{\chi}{2}} + \chi H^+ \xrightarrow{k_5} Pt^{\Gamma+} + \frac{\chi}{2} H_2O + (\Gamma - \chi) e$ | $\alpha_5 \alpha (\Gamma - \chi) \gamma$ | 0 | $\text{mol s}^{-1} \text{cm}^{-2}$ |

5.2 Warburg Impedance Due to Transport of Defects in the Film

When ionic defects (metal interstitials and vacancies, in this case) are generated at the metal/film interface, the transport of the defects through the film to the film/solution interface occurs under the influence of the concentration gradient (diffusion) and the electric field (migration), giving rise to a transport impedance. The Warburg-like impedance function describing the oxygen vacancy transport through the film has been derived by Chao, Lin, and Macdonald [6] in terms of the Nernst-Planck equation:

$$\frac{1}{Z(j\omega)} = \frac{4F^2 D_o}{RT} \left\{ [C_{V_{o^-}}(m/f)]_{dc} (1-\alpha)(K + \sqrt{K^2 + j\omega/D_o}) - A'(\sqrt{K^2 + j\omega/D_o}) \right\} \quad (5.23)$$

where

$$A' = - \frac{[C_{V_{o^-}}(f/s)]_{dc} \alpha + [C_{V_{o^-}}(m/f)]_{dc} (1-\alpha) \exp(KL - \sqrt{K^2 + s/D_o} L)}{\exp(KL) \sinh(\sqrt{K^2 + s/DL})} \quad (5.24)$$

$$[C_{V_{o^-}}(m/f)]_{dc} = \frac{N_V}{\Omega} \exp\left(\frac{2F(1-\alpha)}{RT} V_{dc} - \theta_1\right) \quad (5.25)$$

and

$$[C_{V_{o^-}}(f/s)]_{dc} = \frac{N_V}{\Omega} \exp\left(\theta_2 - \frac{2F\alpha}{RT} V_{dc}\right) \quad (5.26)$$

D_o is diffusion coefficient of the oxygen vacancy, α is the polarizability of the barrier layer/outer layer (solution) interface, F is Faraday's constant, $K = \varepsilon F / RT$, $R = 8.314 \text{ J mol}^{-1} \text{ K}^{-1}$, N_V is Avagadro's number (6.023×10^{23} /mole), Ω is the molar volume of per cation of the barrier layer, θ_1 and θ_2 are constants, and V_{dc} is the d-c component of the external potential. It is important to note that Chao, et al. [6] assumed that the interfacial reactions were at equilibrium, consequently, the model yields the impedance for the transport of defects across the film alone with no contribution to the impedance from the metal/barrier layer and barrier layer/solution interfaces (i.e., the reactions are considered

to be “fast”). Furthermore, transport of metal interstitials across the barrier layer is described by an Equation 5.4 that is identical to that which describes the transport of oxygen vacancies [but with $\chi = 2$, Equation 5.5], so that the same impedance function, Equation 5.23), may be used to represent the impedance due to the transport of interstitials.

Equation 5.23 has the form of a Warburg impedance for a finite thickness diffusion layer. However, at sufficiently high frequencies, where $\omega/D_O \gg K^2$, Equation 5.23 becomes

$$Z_O = \sigma_O \omega^{-1/2} - j \sigma_O \omega^{-1/2} \quad (5.27)$$

Where

$$\sigma_O = RT / F^2 \sqrt{32 D_O} \{ [C_{V_{O^{\cdot}}}(m/f)]_{dc} (1 - \alpha) - A' \} \quad (5.28)$$

or

$$\sigma_O \approx RT / F^2 \sqrt{32 D_O} \{ [C_{V_{O^{\cdot}}}(m/f)]_{dc} (1 - \alpha) \} \quad (5.29)$$

This simple form of the Warburg impedance is used in the current analysis to represent the impedance for the transport of oxygen vacancies across the oxide film on platinum.

As stated by Chao et al. [6], the diffusion coefficient of oxygen vacancies in most metal oxides at room temperature is smaller than 10^{-20} cm²/s. The electric field strength ε in the film is usually around 10^6 V/cm, therefore K is about 3.9×10^7 /cm. The criterion for $\omega \gg D_O K^2$ can then be satisfied whenever $\omega > 10^{-5}$ rad/s, which is satisfied for almost all practical purposes.

Likewise, the Warburg-like impedance for the transport of platinum interstitials through the film can be represented by

$$Z_i = \sigma_i \omega^{-1/2} - j \sigma_i \omega^{-1/2} \quad (5.30)$$

and is in parallel with Z_O . The total impedance due to the ionic transport through the film is therefore defined as

$$Z_w^{-1} = Z_O^{-1} + Z_i^{-1} \quad (5.31)$$

with

$$Z_w = \sigma_w \omega^{-1/2} - j \sigma_w \omega^{-1/2} \quad (5.32)$$

And

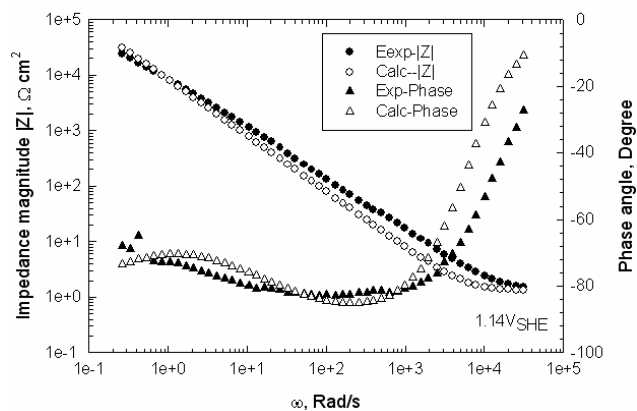
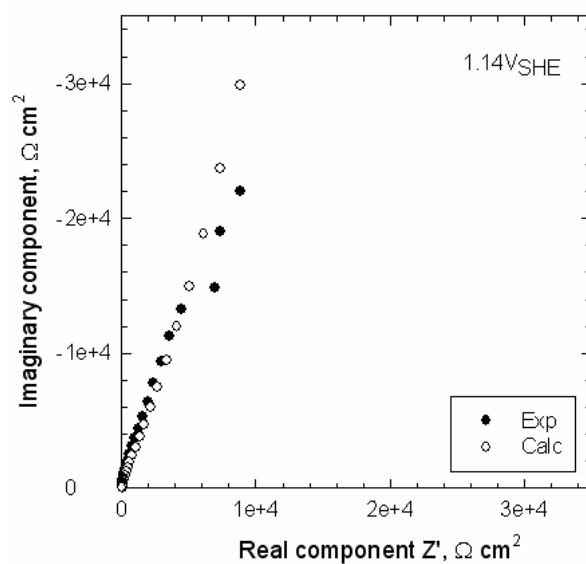
$$\sigma_w = \frac{\sigma_O \sigma_i}{\sigma_O + \sigma_i} \quad (5.33)$$

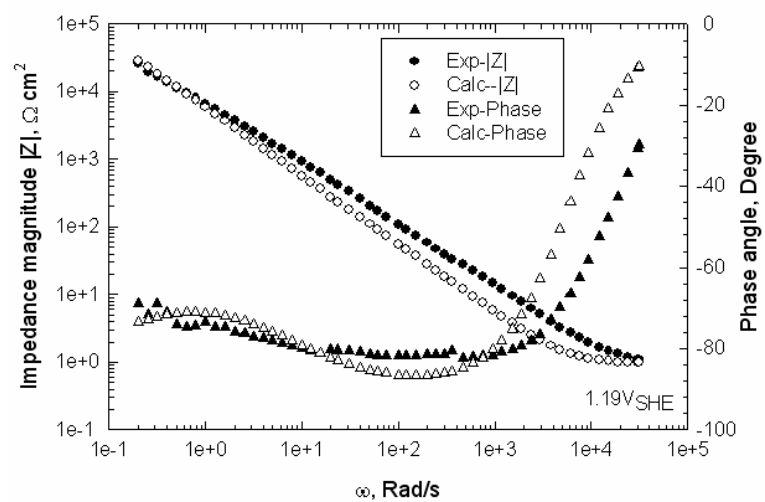
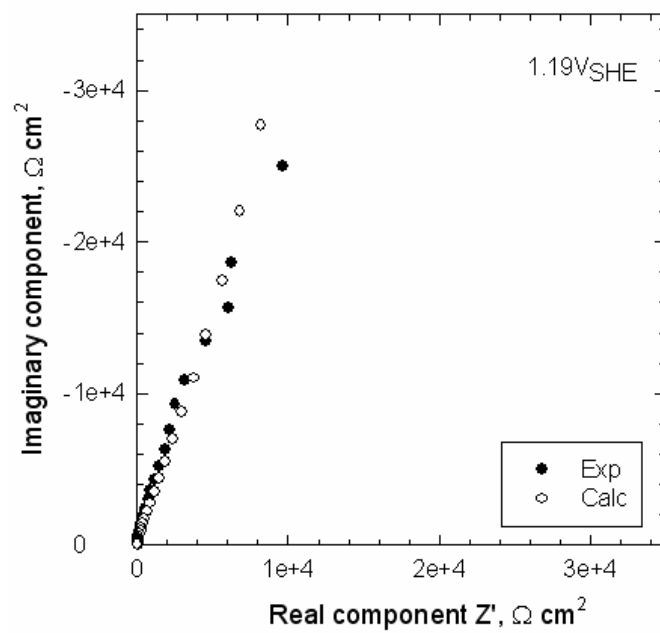
The diffusivity of the principal defect in the film, according to Chao et al. [6], is given by

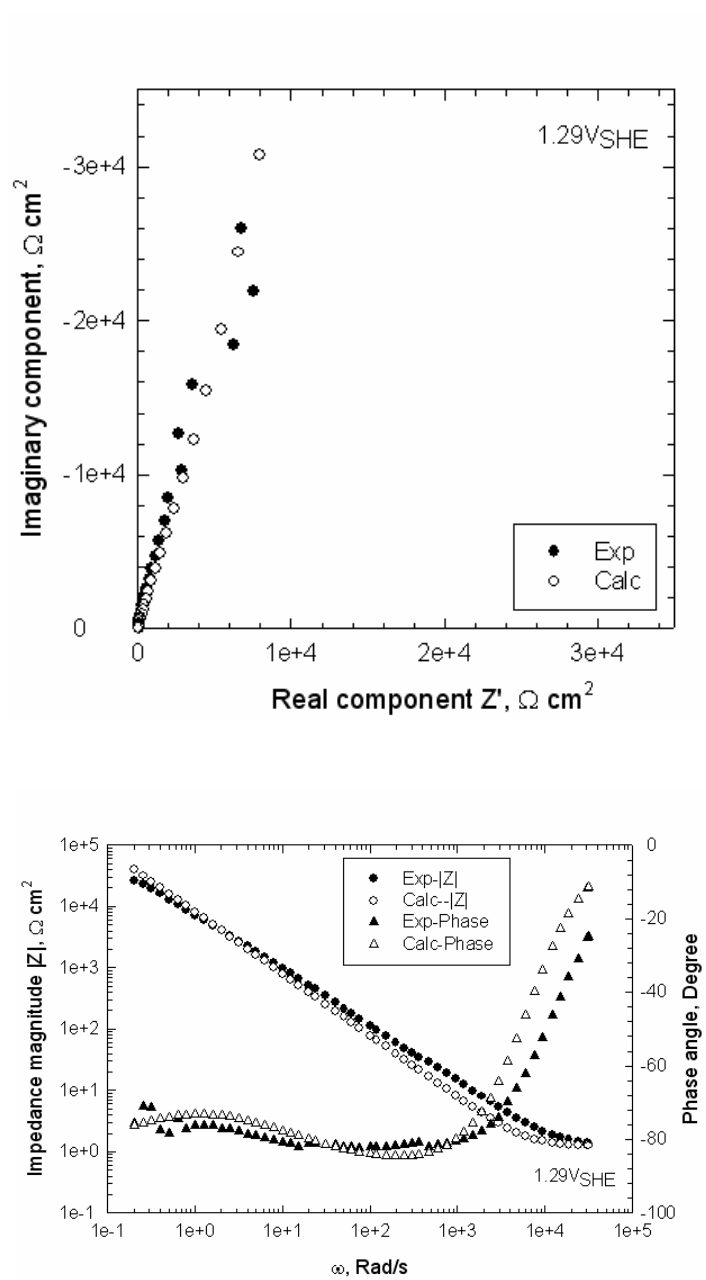
$$D_w = 2(\sigma_w I_{ss} \frac{1-\alpha}{\varepsilon})^2 \quad (5.34)$$

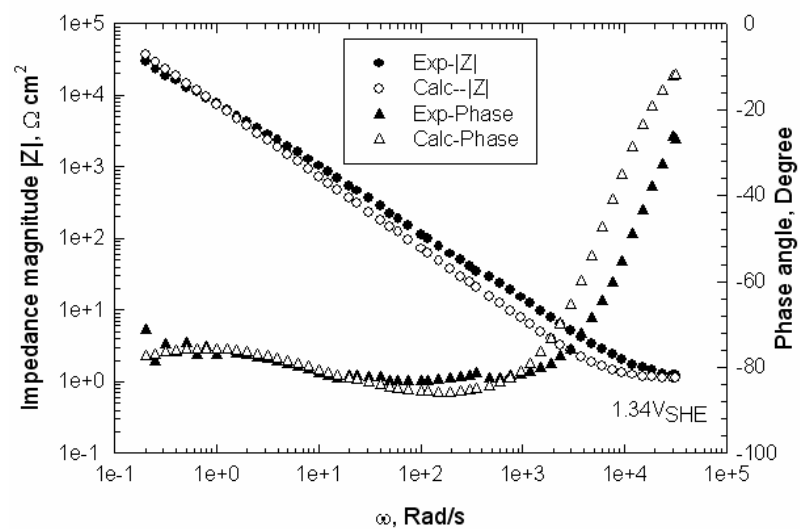
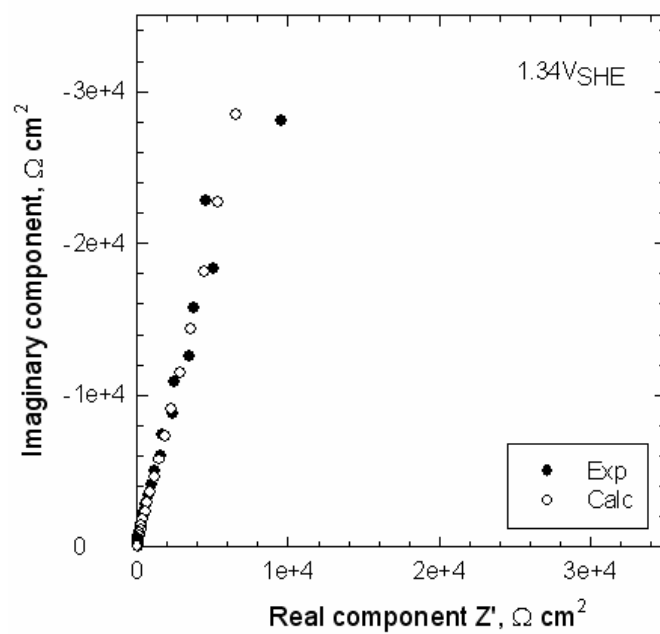
The procedure for optimizing the PDM on experimental impedance data for n-type barrier layers has been described elsewhere [2] and this same procedure is used here for analyzing the passive film on platinum. Optimization was carried out in two stages. In the first stage, all of the parameters except R_s (resistance of the solution between the specimen and the tip of the reference electrode Luggin probe), and n were treated as variables and the optimization procedure yielded values for them. For example, the electronic resistance was found to range from $1.9 \times 10^8 \Omega \bullet \text{cm}^2$ to $2.1 \times 10^8 \Omega \bullet \text{cm}^2$, without any systematic dependence on voltage, corresponding to a lack of redox species in the solution that could accept electronic charge. Likewise, the dependence of the potential drop across barrier layer/outer layer interface on pH , β , was found to vary from -0.011V to -0.013V, while that for $\phi_{f|s}$ in the standard state, $\phi_{f|s}^0$, is -0.009V to -0.013V. In order to reduce the number of variables, we averaged the values obtained in the first stage of the optimization for the electronic resistance, $R_{e,h}$ ($2 \times 10^8 \Omega \bullet \text{cm}^2$), dependence of

potential drop across barrier layer/outer layer interface on pH, β , (-0.01V), and $\phi_{\text{f|s}}$ in the standard state, $\phi_{\text{f|s}}^0$, (-0.01V), and treated these parameters as being constants in the final optimization stage.









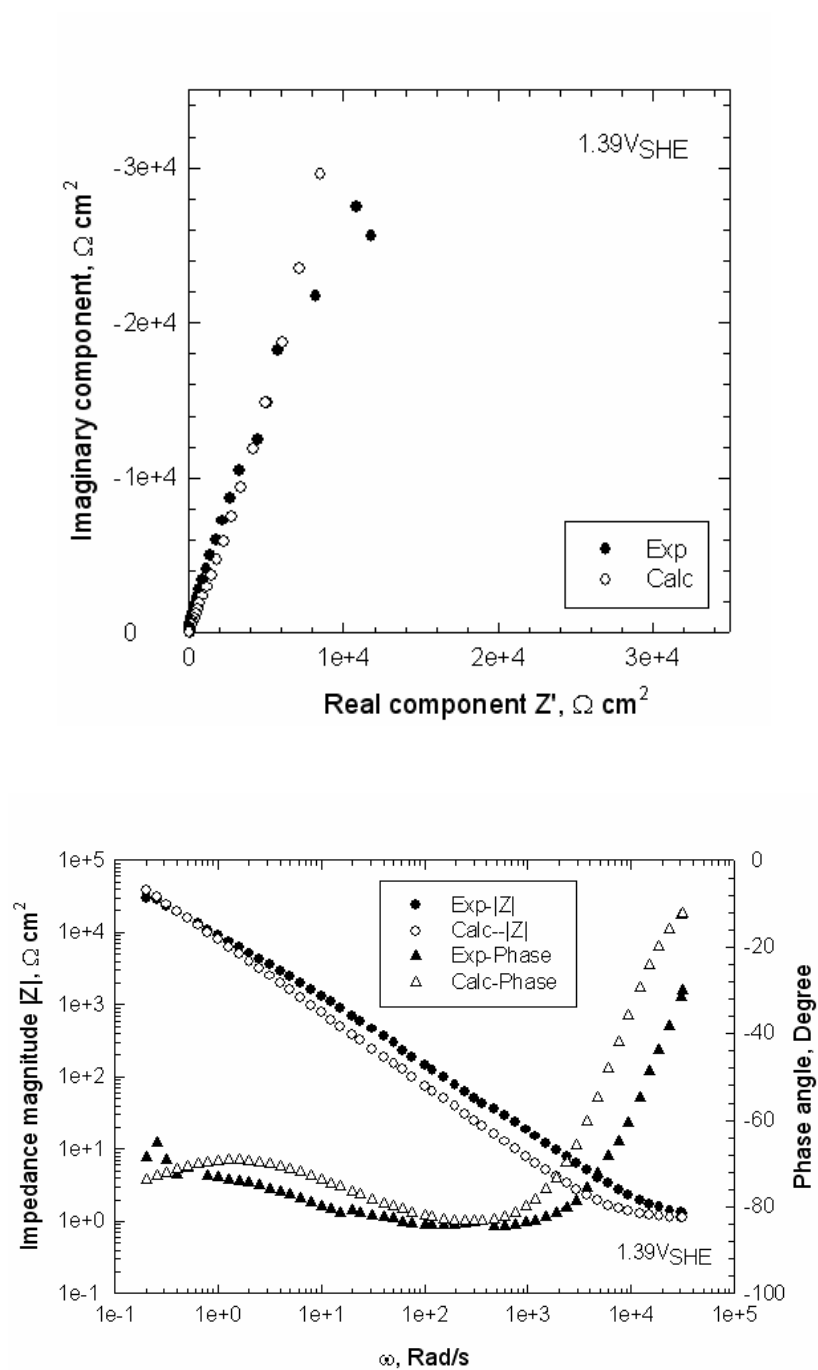


Figure 5-3: Nyquist and Bode plots of impedance data for Pt in 0.5 M H₂SO₄ at applied voltages of 1.19 V_{SHE}, 1.24 V_{SHE}, 1.29 V_{SHE}, 1.34 V_{SHE}, and 1.39 V_{SHE}.

The experimental and calculated impedance data obtained by optimizing the PDM on impedance data measured at different formation potentials are displayed in Figure 5-43. The commercial DataFit software (Version 7.1, www.curvefitting.com) was employed in this work for optimization, in order to obtain the values for the transfer coefficients, α_i , and standard rate constants, k_i^{00} , for the i elementary interfacial reactions, the polarizability of the film/solution interface, α , the electric field strength, ε , and other parameters, as described below. The value for the kinetic order of the dissolution reaction at the film/solution interface with respect to the $[H^+]$ was assumed to be 0.5, due to the fact that we do not have any data upon which the model can be optimized with respect to pH as the independent variable. Values for the fundamental model parameters for passive platinum are presented in Table 5-2. The comparison in Figure 5-43 shows that the correlation between the experimental impedance data and the simulated data is fairly good for the Nyquist plots and Bode plots shown. The parameter values obtained by optimization of the model on impedance data that span the entire passive range are found not to depend on voltage in any systematic manner, which, in itself, is a test of the viability of the model.

Table 5-2: Parameter values from optimization of the Point Defect Model on the experimental impedance data for platinum in deaerated H₂SO₄ (0.5M, pH = 0.2) solution at 20°C as a function of applied potential.

| V_{app} / V_{SHE} | 1.14 | 1.19 | 1.29 | 1.34 | 1.39 | Mean (\pm Standard Deviation) | Origin |
|--|-------|-------|-------|-------|-------|----------------------------------|--|
| $R_s(\Omega \cdot \text{cm}^2)$ Solution resistance | 1.32 | 0.96 | 1.23 | 1.1 | 1.1 | 1.14 ± 0.14 | Assumed from the value of real component of impedance at highest frequency |
| $10^4 C_{dl} (\text{F}/\text{cm}^2)$ Double layer capacitance | 0.8 | 2.0 | 7.0 | 5.0 | 4.0 | 3.76 ± 2.4 | Second stage optim |
| $10^{-8} R_e(\Omega \cdot \text{cm}^2)$ Electronic resistance | 2.0 | 2.0 | 2.0 | 2.0 | 2.0 | 2.0 | First stage optim |
| $10^{-6} \varepsilon (\text{V}/\text{cm})$ Electric field strength | 2.1 | 1.97 | 1.96 | 2.0 | 1.95 | 1.998 ± 0.06 | Second stage optim |
| $\hat{\varepsilon}$ Dielectric constant | 35 | 42.5 | 50 | 42.5 | 42.5 | 42.5 ± 5.3 | Second stage optim |
| $10^{22} k_1^{00} (\text{mol}/\text{cm}^2\text{s})$ Standard rate constant | 5.5 | 5.55 | 6.5 | 5.25 | 5.5 | 5.66 ± 0.48 | Second stage optim |
| $10^{17} k_2^{00} (\text{mol}/\text{cm}^2\text{s})$ Standard rate constant | 5.5 | 10.5 | 12 | 5.1 | 5.08 | 7.64 ± 3.35 | Second stage optim |
| $10^{12} k_5^{00} (\text{mol}/\text{cm}^2 \text{ s})$ Standard rate constant | 3.0 | 4.0 | 1.75 | 3.0 | 1.5 | 2.65 ± 1.03 | Second stage optim |
| α Polarizability of bl/ol interface | 0.5 | 0.5 | 0.505 | 0.5 | 0.5 | 0.50 ± 0.002 | Second stage optim |
| α_1 Transfer coefficient | 0.48 | 0.45 | 0.495 | 0.47 | 0.49 | 0.48 ± 0.02 | Second stage optim |
| α_2 Transfer coefficient | 0.25 | 0.25 | 0.22 | 0.24 | 0.23 | 0.24 ± 0.02 | Second stage optim |
| n Kinetic order of dissolution With $[\text{H}^+]$ | 0.5 | 0.5 | 0.5 | 0.5 | 0.5 | 0.5 | Assumed in both optimization stages |
| $\beta (\text{V})$ Dependence of potential drop across bl/ol interface on pH | -0.01 | -0.01 | -0.01 | -0.01 | -0.01 | -0.01 | First stage optim |
| $\phi_{f s}^0 (\text{V})$ $\phi_{f s}$ in the standard state (V=0, pH=0) | -0.01 | 0.01 | -0.01 | -0.01 | -0.01 | -0.01 | First stage optim |
| $\sigma (\Omega \cdot \text{cm}^2 \cdot \text{s}^{-0.5})$ Warburg coefficient | 3950 | 3925 | 4275 | 3900 | 4000 | 4010 ± 152 | Second stage optim |
| $10^8 L_{ss} (\text{cm})$ Steady state thickness | 1.60 | 4.0 | 5.33 | 5.38 | 7.45 | | Calculated from Equation 5.35 |
| $10^7 I_{ss} (\text{A cm}^{-2})$ Steady state current density | 5.45 | 6.28 | 4.43 | 6.0 | 4.37 | | Calculated from Equation 5.36 |
| $10^{19} D_w (\text{cm}^2/\text{s})$ Diffusivity of principal defect. | 5.25 | 7.83 | 4.58 | 6.84 | 4.02 | 5.70 ± 1.6 | Calculated from Equation 5.34 |

The steady state barrier layer thickness and current density are calculated from the Equation 5.35 parameter values using:

$$L_{ss} = \frac{I}{\varepsilon} [l - \alpha] V - \frac{I}{\alpha_2 \chi K} \ln \left(\frac{k_5^{00}}{k_2^{00} e^{-\alpha_2 \beta \chi \gamma p H} e^{-\alpha_2 \chi \gamma \phi_{f/s}^0}} 10^{(-pH)n} \right) \quad (5.35)$$

and Equation 5.7. However, for, $\chi = \Gamma$, Equation 5.7 simplifies to

$$I_{ss} = \chi F k_1^{00} e^{-\alpha_1 \beta \chi \gamma p H} e^{-\alpha_1 \chi \gamma \phi_{s}^0} e^{\alpha_1 (1-\alpha) \chi \gamma V} e^{-\alpha_1 \chi \varepsilon L_{ss}} + \chi F k_2^{00} e^{-\alpha_2 \chi \beta \gamma p H} e^{-\alpha_2 \chi \gamma \phi_{f/s}^0} e^{\alpha_2 (1-\alpha) \chi \gamma V} e^{-\alpha_2 \chi \varepsilon L_{ss}} \quad (5.36)$$

where, with reference to Figure 5-1, χ is the oxidation state of platinum in the barrier layer (assumed to be 2) and $\gamma = F / RT$. The other parameters are as defined in Table 5-2. As noted in Figure 5-4, the logarithm of the calculated steady state current density, I_{ss} , is independent of the formation potential, as observed experimentally, and which is predicted by the PDM for an n-type semiconductive barrier layer. From Equation 5.36, the total steady state current density consists of the fluxes of the platinum interstitials [Reaction (1), Figure 5-1] and oxygen vacancies [Reaction (2), Figure 5-1] at the metal/film interface if no change in oxidation state of platinum cation upon ejection from the film/solution interface or upon dissolution of the film occurs. The calculated current density due to the oxygen vacancy transfer [second term, Equation 5.36] is then found to

dominate that due to the platinum interstitial transfer [first term, Equation 5.36] at lower potentials, as shown in Figure 5-5. In the past [1, 5], it has proven to be difficult to distinguish whether the n-type defective passive oxide film is cation rich, due to the predominant presence of cation interstitials, or oxygen deficient, due to the predominance of oxygen vacancies. Differentiation might be possible by using glancing X-ray diffraction techniques to ascertain the lattice parameter as a function of distance through the barrier layer, particularly within the region close to the metal/film interface. However, the present work provides a strong theoretical argument for oxygen vacancies being the principal defects in the barrier layer on platinum.

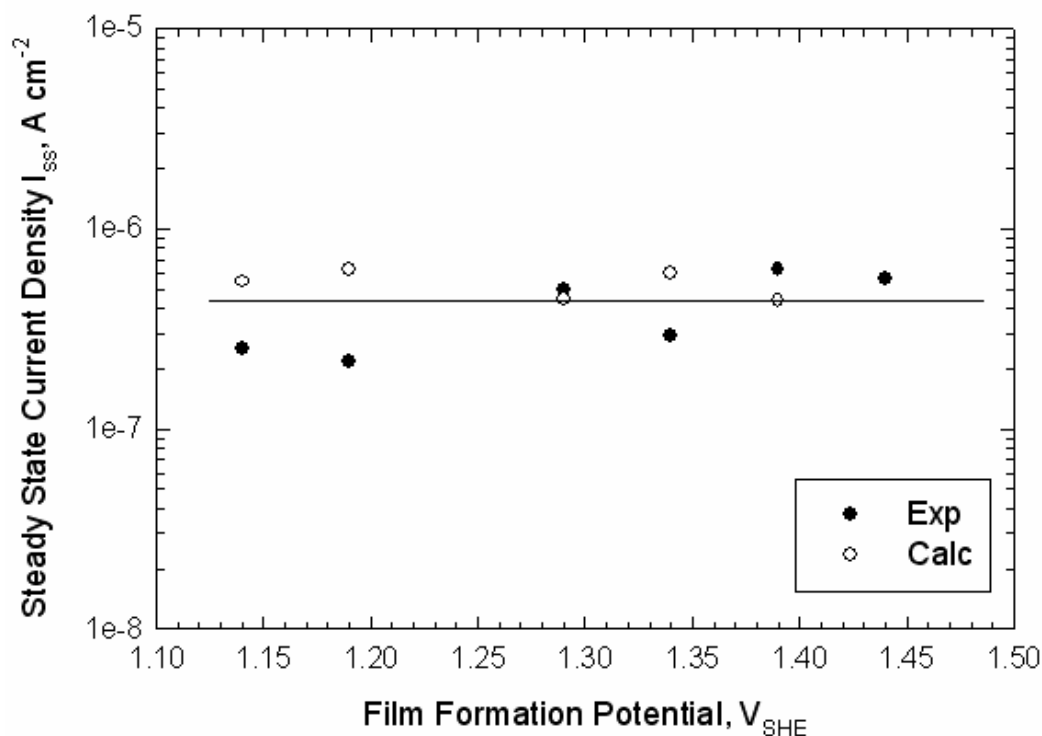


Figure 5-4: Calculated and experimental steady state current density as a function of oxide formation potential. The simulated data were calculated using Equation 5.36 and the mean parameter values summarized in Table 5-2.

The steady state thickness is predicted by the PDM [Equation 5.35] to vary linearly with the formation voltage (Figure 5-6) and this relationship has indeed been found by Bockris et al. [10] and more recently in this laboratory by combining quantum mechanical tunneling theory and redox reaction current measurements with the PDM [11, 12]. The anodizing constant $\partial L_{ss}/\partial V$ from Equation 5.35 is 2.5 nm/V, compared with 2.0 nm/V calculated from the parameter values listed in Table 5-2. This would suggest that the derived L_{ss} values are only semi-quantitative at best, which would not be surprising in light of the fact that they were calculated in the optimization algorithm using the parallel

plate capacitor approximation. The higher value is in excellent agreement with the value of 2.5 nm/V recently determined by Bao and Macdonald [12] for steady state conditions using tunneling current measurements, but it is significantly higher than the 0.95 nm/V obtained by Bockris et al. [10] using ellipsometry. Bao and Macdonald [12] found that the value for the anodizing constant measured under potentiodynamic conditions decreases with increasing voltage sweep rate.

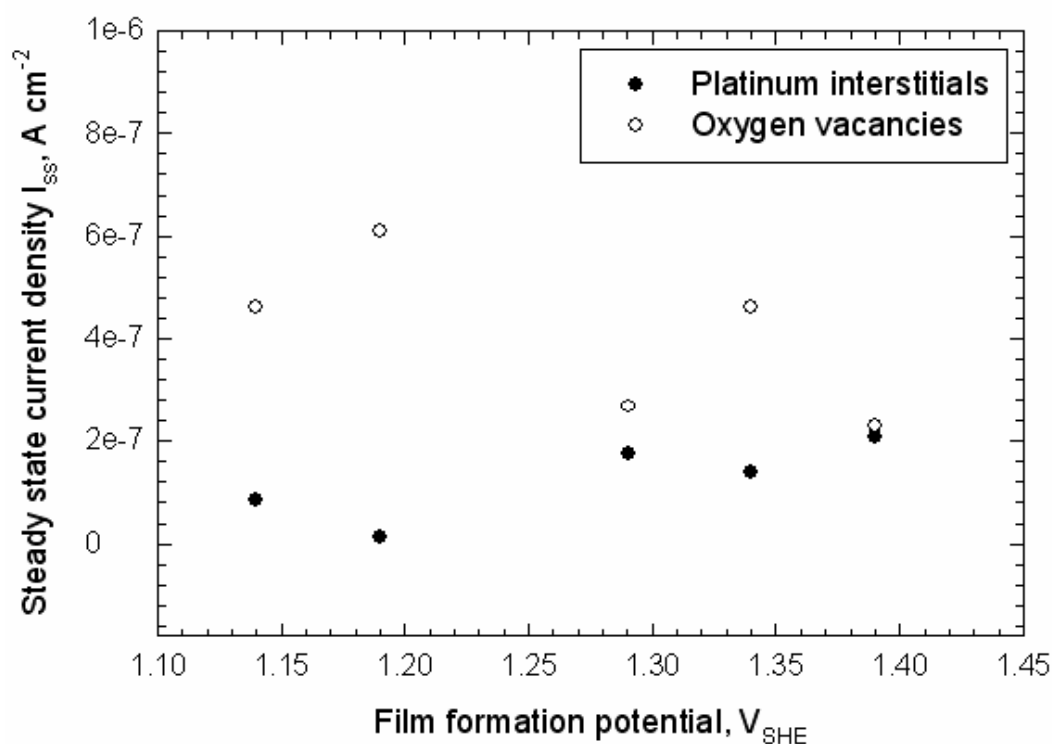


Figure 5-5: Calculated steady state current density due to the movement of platinum interstitials and oxygen vacancies as a function of oxide formation potential. The simulated data were calculated using Equation 5.36 and the mean parameter values summarized in Table 5-2.

Two important issues arise when using the PDM to describe the growth of the anodic oxide films on platinum. The first issue relates to whether the barrier layer is crystalline or amorphous. The second is whether the PDM can explain the growth of an oxide film that is only a few angstroms thick. The degree of crystallinity of an anodic platinum oxide film formed at potentials prior to oxygen evolution remains a subject of controversy, even though the surface structural changes at Pt during oxide film formation and reduction have been extensively investigated [13-17]. STM work coupled with cyclic voltammetry by Itaya et al. [16] indicates that, if a thin oxide film is formed on an electrochemically inactivated surface of single crystal platinum, the structural order of the single crystal surface will be maintained. Ross et al. [13, 14] concluded that the thin oxide on platinum is amorphous because of the lack of reflections in LEED on films formed at 1.7 V_{RHE} . They also attributed the attenuated LEED reflections for films formed between 1.2 V_{RHE} and 1.7 V_{RHE} to the partial oxidation of the surface. However as our XPS results and the work of other researchers show, the oxide film formed at potentials over 1.4 V_{SHE} has two different structures corresponding to the two chemical layers of the oxide film. The hydroxide outer layer [18, 19] usually has a granular and amorphous structure due to the incorporation of water molecules [20]. The lack of crystalline order of the bi-layer, passive film could thus be attributed to the existence of a thick hydroxide outer layer. It is also necessary to point out that LEED, while having high surface sensitivity, is still a diffraction technique and hence only detects long range order. Thus, for barrier oxide films that are only 2 or 3 monolayers thick, and because they probably exist in nano-crystalline domains, LEED might not yield unequivocal information on film crystallinity [21, 22].

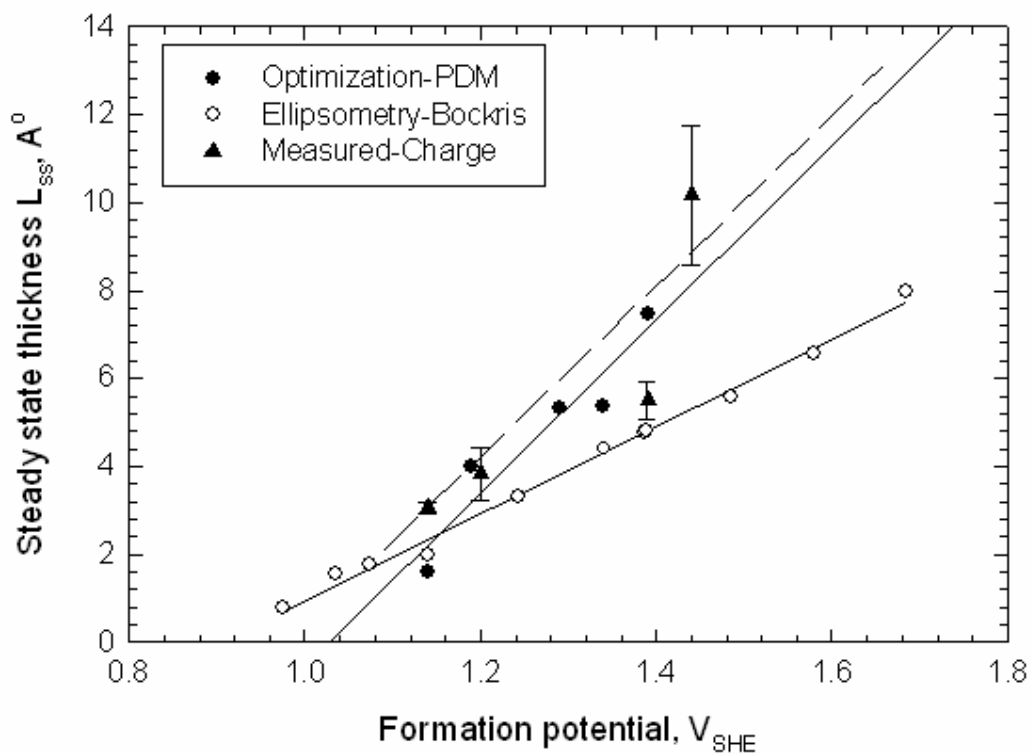


Figure 5-6: Calculated steady state barrier layer thickness from the optimization of the PDM on impedance data compared with the thickness measured by Bockris [10] using ellipsometry and by the present authors using potentiodynamic cathodic reduction at a voltage scan rate -5 mV/s.

Figure 5-1 assumes that platinum interstitials and oxygen vacancies are produced in one monolayer plane at the metal/film interface and are then annihilated at another monolayer plane at the film/solution interface. In principle, no intermediate planes are required. It is known that PtO has a bimolecular tetragonal unit cell with $a = 0.304$ nm and $c = 0.534$ nm (Figure 5-7) [23, 24]. Plane (001) of PtO ($a = 0.304$ nm) has the best match to the (111) plane of metallic platinum ($d_{202} = 0.277$ nm). As suggested by

Conway et al.[25], the polycrystalline platinum surface consists of crystallites having mainly (111) orientation according to the similarity of UPD hydrogen adsorption-desorption profiles in cyclic voltammograms of Pt (poly) and Pt (111). It is thus likely that the oxide film grows with the C axis perpendicular to the metal surface, an orientation of minimal strain, and that the barrier layer exists in nano-crystalline domains. The steady state film thickness calculated from the optimization of the PDM, therefore corresponds to around 2 or 3 monolayers. The present study, therefore, confirms the view that the anodic oxide film formed at platinum grows according to the potential-assisted formation of oxygen vacancies at the metal/film interface and the dissolution of oxide film at the film/solution interface, with these interfaces perhaps being coincident with adjacent planes. With regard to the applicability of the PDM, the minimum thickness for which the necessary structural conditions exist for the application of the model is possibly as small as one monolayer (Figure 5-7) or 0.134 nm.

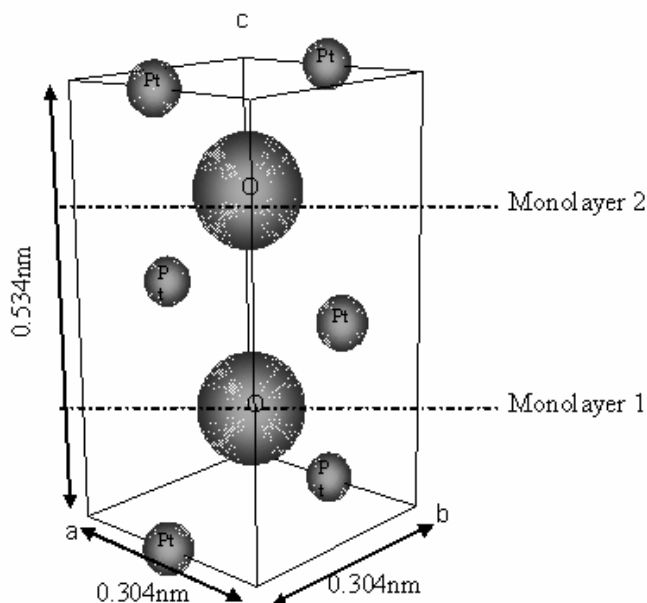


Figure 5-7: Unit cell of PtO with $a = b = 0.304\text{nm}$ and $c = 0.534\text{nm}$. It is proposed that the barrier layer comprises the unit cell in nano-crystalline domains with the c-axis perpendicular to the metal surface.

As noted previously, the place exchange model (PEM) has been applied by Conway [26] and Jerkiewicz, et. al.[27] to describe the growth of the first two monolayers of oxide on platinum. The PEM can account for the logarithmic growth law in time, but it does not account for the existence of steady states in the current or film thickness, as noted above. It is also difficult, however, to accept this model as representing physical reality, since it is based upon the unlikely occurrence of cooperative rotation of MO dipoles over macroscopic dimensions. Such a process would seem to be unlikely on entropic grounds.

Optimization of the PDM on the experimental impedance data yields a defect diffusivity of $(5.7 \pm 1.6) \times 10^{-19} \text{ cm}^2/\text{s}$. Assuming that the principal defect is the oxygen vacancy, as indicated by the steady state current density, this value is considered to be eminently reasonable, even though we could not find any data in the literature with which it could be compared. This number is likely to be high, however, when compared with values for single crystals, because it presumably includes grain boundary diffusion, recognizing that the barrier layer is most likely nano-crystalline in structure.

5.3 Summary

Platinum joins a long list of other metals, such as Ni [28], W [29] and Alloy 22 [2, 4], whose anodic oxide behavior has been successfully interpreted in terms of the PDM. With regard to the catalytic activity of Pt for redox reactions at high potentials, including the oxygen electrode reaction, a major factor in determining the exchange current density and the Tafel constant is the thickness of the barrier layer. In the case of platinum, the barrier layer is very thin, resulting in higher values for redox reaction exchange current densities, and lower Tafel constants, than for other metals having thicker barrier layers, thereby facilitating charge transfer across the film by quantum mechanical tunneling. However, other factors may also be critical in determining the catalytic activity of platinum (and other metals), including the electronic structure [30] and the presence of defects in the oxide surface that may act as catalytic reaction sites.

References

- [1] D.D. Macdonald, *Pure Appl. Chem.*, 71 (1999) 951.
- [2] D.D. Macdonald, A. Sun, N. Priyantha, and P. Jayaweera, *J. Electroanal. Chem.*, 572 (2004) 421.
- [3] D.D. Macdonald and A. Sun, *Electrochim Acta*, 51 (2006) 1767
- [4] N. Priyantha, P. Jayaweera, D.D. Macdonald, and A. Sun, *J. Electroanal. Chem.*, 572 (2004) 409.
- [5] D.D. Macdonald, *J. Electrochem. Soc.*, 139 (1992) 3434.
- [6] C.Y. Chao, L.F. Lin, and D.D. Macdonald, *J. Electrochem. Soc.*, 129 (1982) 1874.
- [7] I. Betova, M. Bojinov, P. Kinnunen, P. Pohjanne, and T. Saario, *Electrochim. Acta*, 47 (2002) 3335.
- [8] M. Bojinov, S. Cattarin, M. Musiani, and B. Tribollet, *Electrochim. Acta*, 48 (2003) 4107.
- [9] M. Bojinov, G. Fabricius, T. Laitinen, K. Makela, T. Saario, and G. Sundholm, *Electrochim. Acta*, 45 (2000) 2029.
- [10] A.K.N. Reddy, M.A. Genshaw, and J.O.M. Bockris, *J. Chem. Phys.*, 48 (1968) 671.
- [11] M.N. Kamrun, J. Bao, and D.D. Macdonald, *Corros. Sci.*, Special Issue Commemorating the Development of Tafel's Law, 47 (2005) 3111.
- [12] J. Bao and D.D. Macdonald. In *Proceedings of the Symposium on Electrocatalysis, 207th Meeting of The Electrochemical Society. Quebec City, Canada: Electrochemical Society, May 2005.*

- [13] F.T. Wagner and P.N. Ross Jr., *Surf. Sci.*, 160 (1985) 305.
- [14] F.T. Wagner and P.N. Ross Jr., *J. Electroanal. Chem.*, 150 (1983) 141.
- [15] Z. Nagy and H. You, *Electrochim. Acta*, 47 (2002) 3037.
- [16] K. Itaya, S. Sugawara, K. Sashikata, and N. Furuya, *J. Vac. Sci. Technol. a*, 8 (1990) 515.
- [17] F. Di Quarto, S. Piazza, C. Sunseri, M. Yang, and S.-M. Cai, *Electrochim. Acta*, 41 (1996) 2511.
- [18] V.I. Birss, M. Chang, and J. Segal, *J. Electroanal. Chem.*, 355 (1993) 181.
- [19] S.J. Xia and V.I. Birss, *Electrochim. Acta*, 44 (1998) 467.
- [20] J. Kunze, V. Maurice, L.H. Klein, H.-H. Strehblow, and P. Marcus, *Corr. Sci.*, 46 (2004) 245.
- [21] G. Tremiliosi-Filho, G. Jerkiewicz, and B.E. Conway, *Langmuir*, 8 (1992) 658.
- [22] H. Angerstein-Kozlowka, B.E. Conway, B. Barnett, and J. Mozota, *J. Electroanal. Chem.*, 100 (1979) 417.
- [23] W.J. Moore Jr. and L. Pauling, *J. Am. Chem. Soc.*, 63 (1941) 1392.
- [24] P. Villas and L.D. Calvert, *Pearson's Handbook of Crystallographic Data for Intermetallic Phases*, ASM International, 1991.
- [25] B.E. Conway and G. Jerkiewicz, *J. Electroanal. Chem.*, 339 (1992) 123.
- [26] B.E. Conway, B. Barnett, H. Angerstein-Kozłowska, and B.V. Tilak, *J. Chem. Phys.*, 93 (1990) 8361.
- [27] G. Jerkiewicz, G. Vatankhah, J. Lessard, M.P. Soriaga, and Y.S. Park, *Electrochim. Acta*, 49 (2004) 1451.
- [28] E. Sikora and D.D. Macdonald, *Electrochim. Acta*, 48 (2002) 69.

- [29] J. Sikora, E. Sikora, and D.D. Macdonald, *Electrochim. Acta*, 45 (2000) 1875.
- [30] T. Toda, H. Igarashi, and M. Watanabe, *J. Electrochem. Soc.*, 145 (1998) 4185.

Chapter 6

pH DEPENDENCE IN ALKALINE SOLUTIONS

6.1 Electrochemical Properties

Cyclic voltammograms (Figure 6-1) were first recorded in 0.01M, 0.1M, and 1M KOH solutions at a scan rate 100mV/s. Similar to the voltammograms measured in acidic solutions, the cyclic voltammograms obtained in alkaline solutions of different pH show also three regions: the hydrogen adsorption and desorption region at lower potentials ($-0.8V_{SHE}$ - $-0.4V_{SHE}$); the double layer capacitance region at intermediate potentials ($-0.4V_{SHE}$ - $-0.2V_{SHE}$); and the formation and reduction of platinum oxide(s) region at higher potentials ($-0.2V_{SHE}$ - $1.0V_{SHE}$). The passive (oxide formation) potential region in Figure 6-1 is observed to shift in the negative direction with increasing pH, as expected from the Pourbaix diagram, and the film formation potentiodynamic current density increases with increasing pH, as does the steady state current density, a finding that is predicted by the PDM [1].

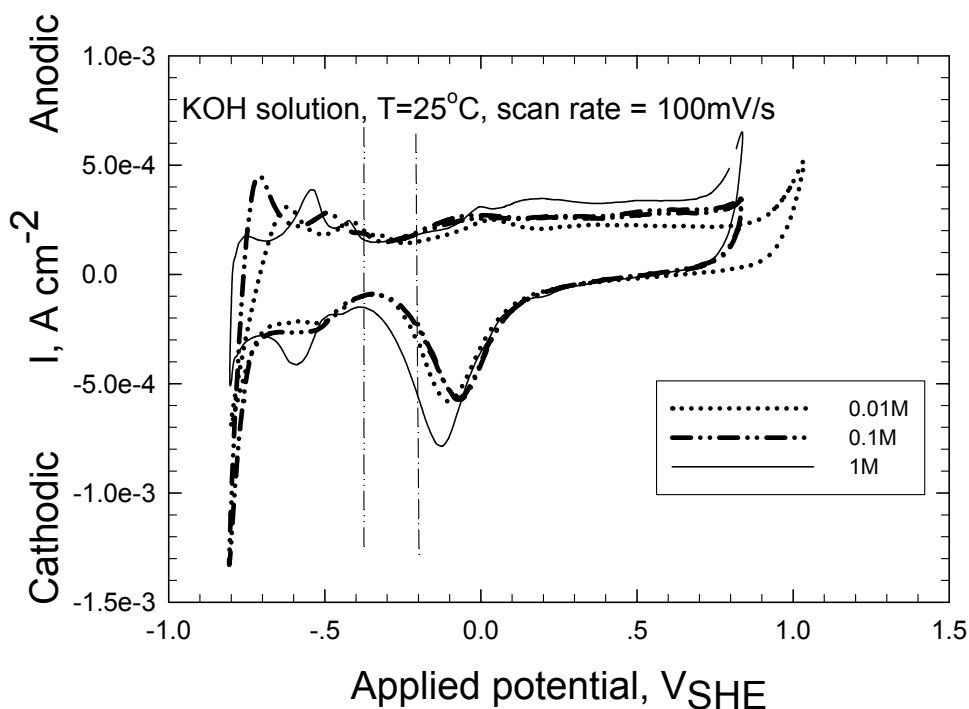


Figure 6-1: Cyclic voltammograms of platinum in KOH solutions with 0.01M, 0.1M, and 1M.

In Figure 6-2, Figure 6-3, and Figure 6-4, Mott-Schottky plots obtained from experiments in alkaline solutions display positive slopes, which are characteristic of n-type semiconductors [2]. The capacitance measurements in acid solution (Chapter 4) also show that the anodic film on platinum is n-type in electronic character although a small region of negative slope exists in the Mott-Schottky plots at high potentials. The Mott-Schottky studies therefore show that the dominant defects in the oxide films formed anodically on platinum in both alkaline and acid solutions are oxygen vacancies and/or platinum interstitials, as postulated in the Point Defect Model (PDM) [3]. The regions of negative slope in Mott-Schottky plots observed for high potentials in acidic solutions are not detected for the films formed in alkaline solutions. There is, however, a tendency

toward a change in slope as indicated for the data recording during the highest formation potential. In this regard, it is important to note that the Mott-Schottky plots presented in Figure 6-2, Figure 6-3, Figure 6-4 and, are “unconventional”, in that the film was grown at the formation potential for a period of 24h and then the potential was swept in the negative direction at a sweep rate of 100mV/s while simultaneously measuring the capacitance at 1kHz. This procedure was adopted, in order to “freeze-in” the defect concentration and the film thickness, so as to comply more closely with Mott-Schottky theory. The origin of the tendency toward a negative slope (and hence toward p-type character) at high potentials is controversial. This tendency may indicate that cation vacancies become the dominant defect or it may arise from anion adsorption or some other process.

Nonlinearity and frequency dependence (Figure 6-5) of the plots are also observed in alkaline solutions as are in acid solution. In Chapters 2 and 4, we have discussed that Mott-Schottky analysis is applied to study the electrochemical interface system based on a few assumptions, such as the absence of surface states and that the double layer capacitance is much greater than the space charge capacitance in the film (barrier layer) [4]. If these assumptions are not valid in the electrochemical interface system, then nonlinearity and frequency dependence may manifest in the results.

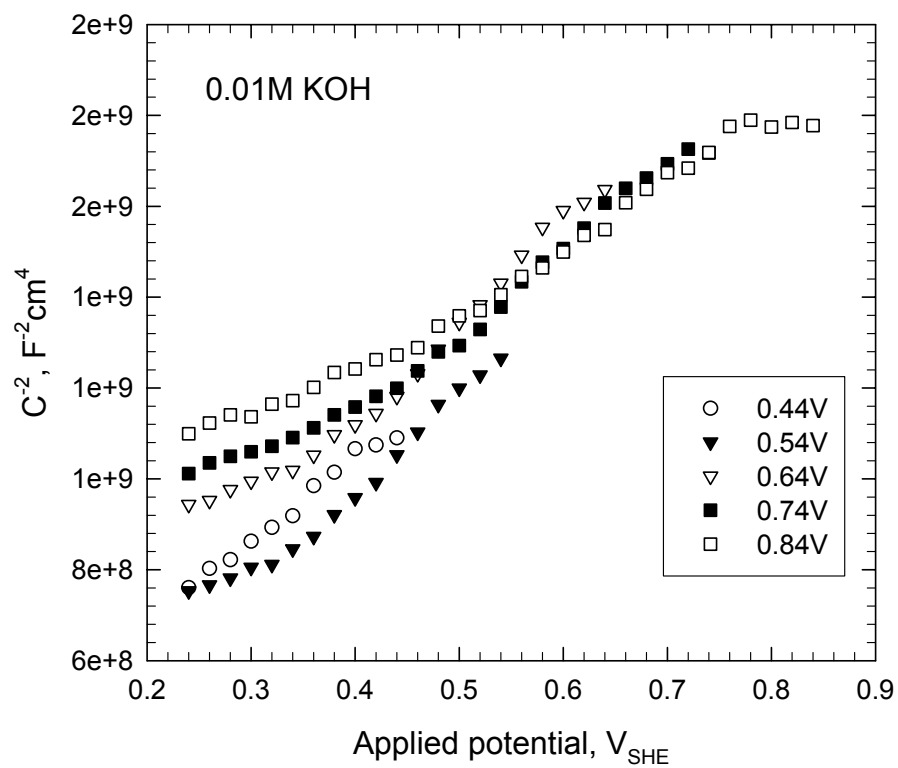


Figure 6-2: Mott-Schottky plots of platinum oxide film formed in 0.01M KOH solution as a function of film formation potential.

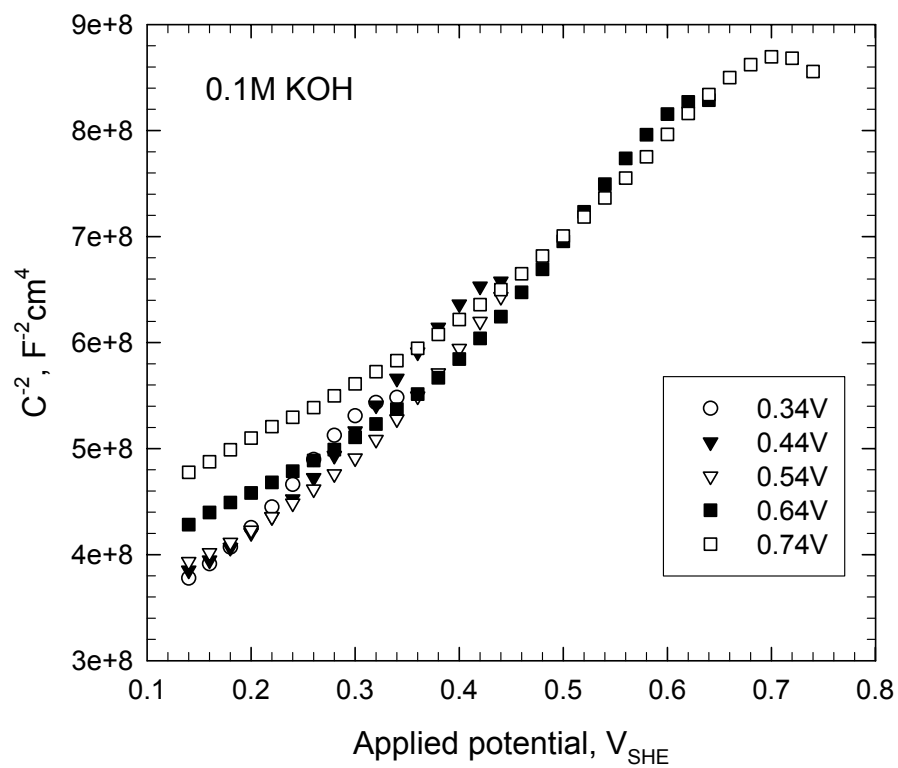


Figure 6-3: Mott-Schottky plots of platinum oxide film formed in 0.1M KOH solution as a function of film formation potential.

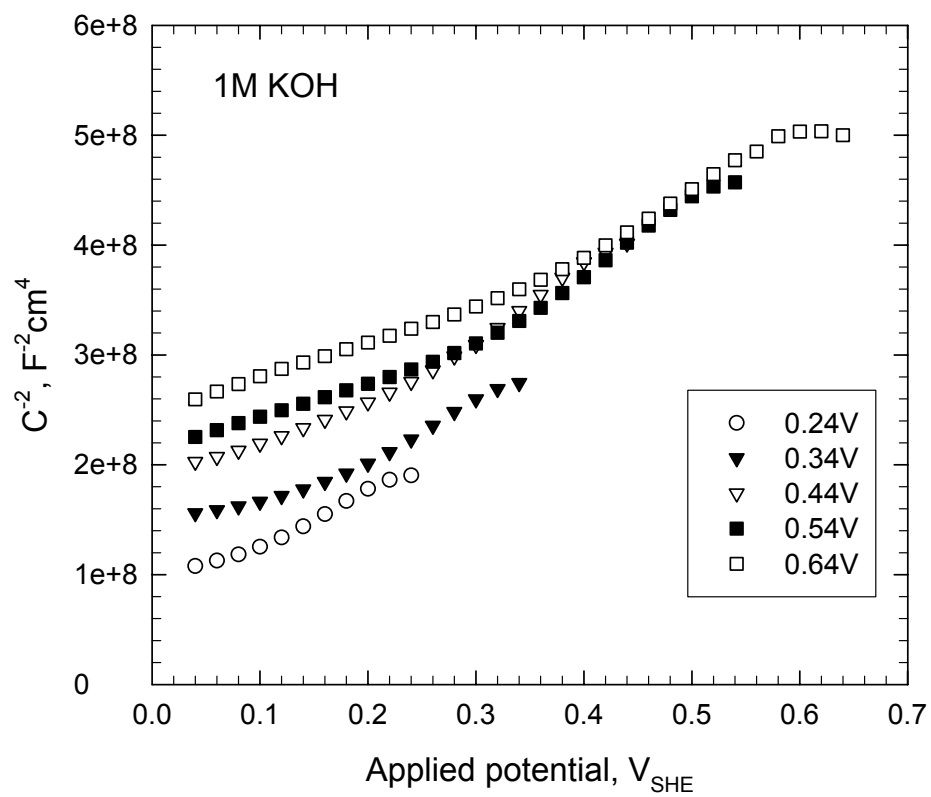


Figure 6-4: Mott-Schottky plots of platinum oxide film formed in 1M KOH solution as a function of film formation potential.

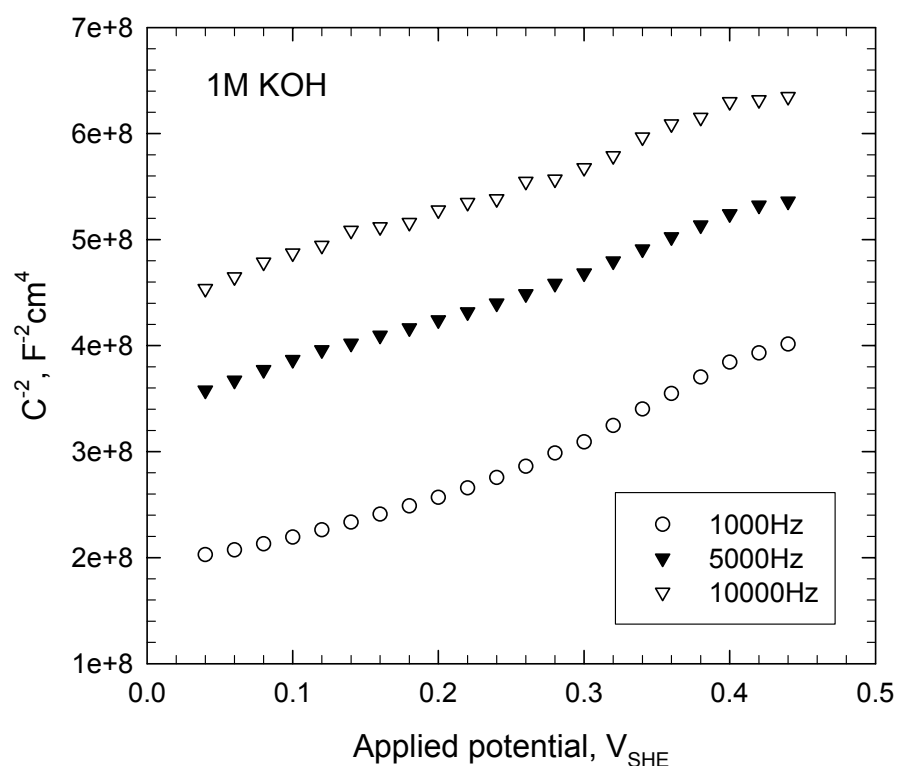


Figure 6-5: Mott-Schottky plots of platinum oxide film formed at potential $0.44V_{SHE}$ in 1M KOH solution as a function of sweep frequencies.

Figure 6-6 shows that as pH increases the slopes of the plots of the oxide film formed at same voltage decreases. This indicates that donor concentrations increase with the pH. The defect concentration is calculated from the slope of the Mott-Schottky plot according to Equation Error! Not a valid link. by using the parameter values obtained from the optimization of the PDM on EIS data with $\hat{\epsilon} = 42.5$ (Table 5-2). By calculating the fraction of vacancy concentration of the sites on the oxygen sub-lattice of PtO as a function of pH, one observes that the oxide film becomes more and more degenerate as

pH increases in alkaline solution. However the maximum fraction (0.193) of vacancy concentration at pH= 14 in alkaline solution is only a little greater than the maximum fraction value (0.164) obtained in acid solution. It is thus apparent that although the oxide film formed on platinum in both acid and alkaline solutions is highly defective and degenerate, the semiconductive character is still the major electrical characteristic of the oxide film on platinum. The exponential increase of defect concentration with the formation potential at each pH (Figure 6-7) is also observed as is in acid solution (Figure Error! Not a valid link.).

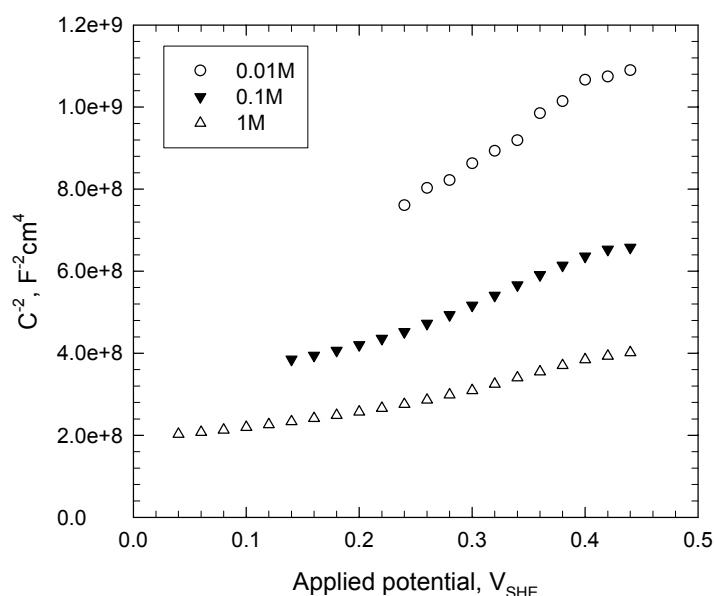


Figure 6-6: Mott-Schottky plots of platinum at oxide formation potential $0.44V_{SHE}$ as a function of pH, sweep rate is 100mV/s.

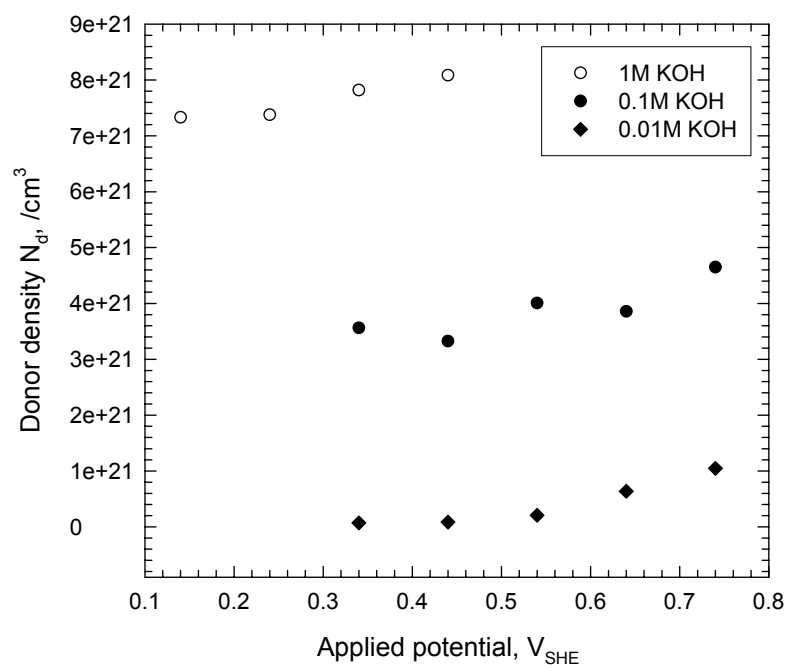


Figure 6-7: Donor concentrations of oxide films calculated according to Mott-Schottky method as function of pH.

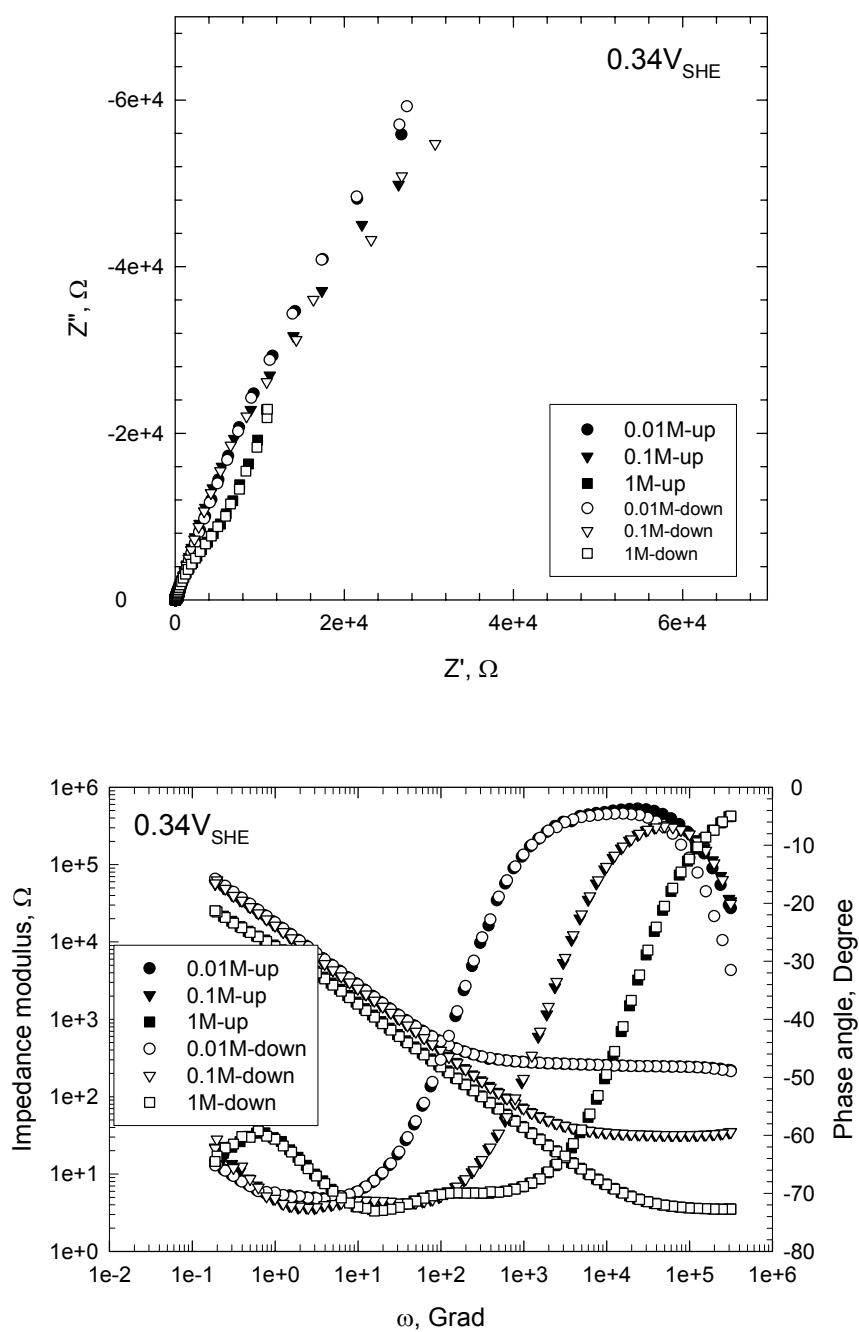


Figure 6-8: Electrochemical impedance spectroscopy data of platinum oxide film in KOH solution of 0.01M, 0.1M, and 1M.

Specimens, which were pre-oxidized for 24 hours at various constant potentials in order to reach the steady state, were measured to obtain the electrochemical impedance spectroscopy data at three pH values. A set of results are shown in Figure 6-8. It can be seen that with the increase of pH, the magnitude of the impedance decreases. The good agreement of both Nyquist and Bode plots is observed when the frequency was scanned (stepped) from low to high frequency and then immediately scanned in the reverse direction. The stability of the system during EIS measurement is thus demonstrated and it is established that the system conforms to the constraints of Linear Systems Theory (LST).

Steady state is typically defined as being a state of a system in which the conditions do not change with time. Accordingly, a true steady state during film growth arises only from a balance between the rate of film growth and the rate of film dissolution [5]. Transient experiments were designed to examine whether the anodic film grown on platinum attains a true steady state. In Figure 6-9, the changes of film thickness is plotted as a function of time as the potential is stepped from a higher value to a lower value in the passive potential region. At each potential, the system is allowed to evolve by holding the potential constant for 24h. The formation potentials were selected from Figure 6-1 to be in the passive potential range. These were chosen so that the electroreduction of the passive film at the metal/film interface can not be responsible for film thinning upon stepping the passive potential from a high to a low value. The film thickness was then determined from the imaginary component of the electrochemical

impedance measured at a fixed frequency of 1kHz. It is noted from Figure 6-9, that the film thicknesses immediately decreases after stepping the potential in the negative direction for all three pH values but, then, after a few seconds, the thickness increases until a new steady state thickness is attained. Of particular importance is that the film thickness decreases as the formation potential decreases. As we have summarized in the previous paper [2], the rate laws of the HFM, PEM, and NGM except the PDM predict that the oxide film will grow to infinite thickness instead of reaching steady state within finite time. This growth is predicted regardless of whether ΔV is positive or negative, and irrespective of the magnitude of the step in voltage.

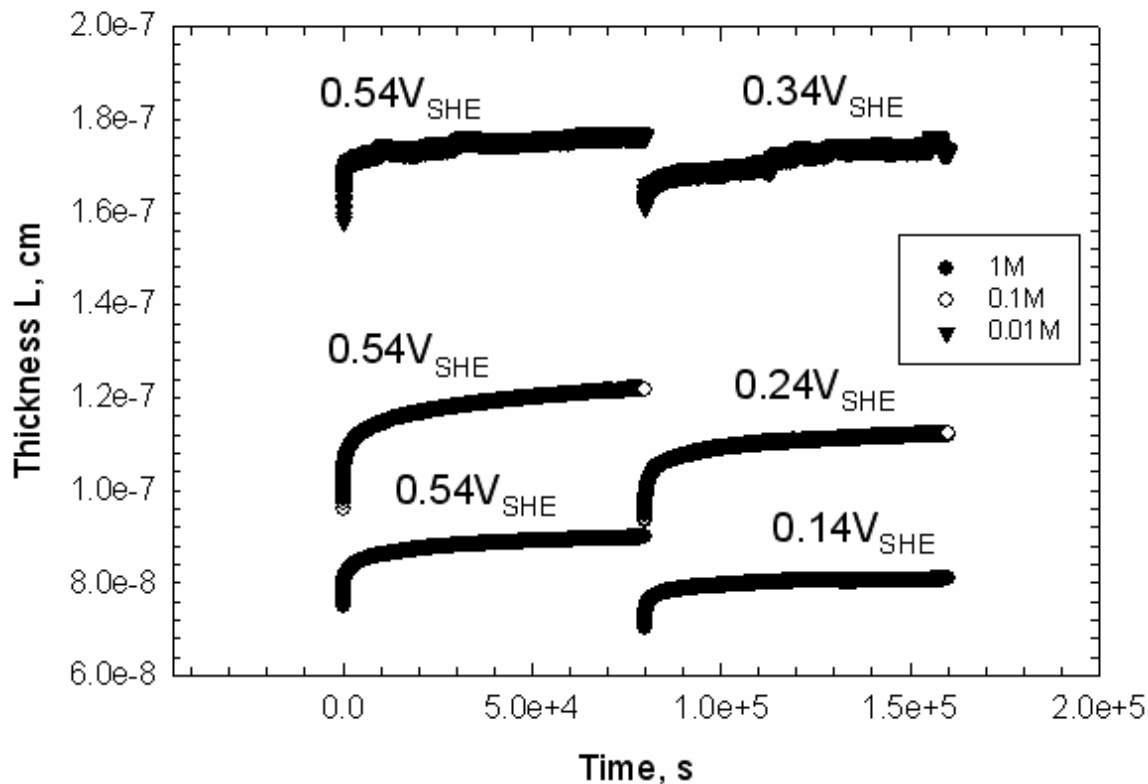


Figure 6-9: Experimental results for the reduction in thickness of the passive film on

platinum as a function of pH upon stepping the potential from the high to low values.

In this regard, it is apparent that these predictions are contrary to the results in Figure 6-9. The PDM explains this behavior by noting that, when the potential is stepped in the negative direction, the rate of the film formation becomes smaller than the rate of dissolution and, accordingly, the film thickness decreases until the steady state for the reduced potential at constant pH is reached [5].

6.2 Diagnostic Criteria of the PDM

The steady state of the passive film has been extensively studied and explained according to the PDM, in which the dominant defects are cation vacancies, anion vacancies, and cation interstitials. The analytical relationships between the steady state film thickness, the passive current, the applied potential, and the solution pH give rise to the diagnostic criteria. These analytical diagnostic criteria predict that the passive films on nickel [7] and tungsten [5] are p-type and n-type, respectively. This has been demonstrated by capacitance measurements analyzed according to Mott-Schottky theory.

As indicated above, the general Point Defect Model (Figure 6-10) postulates that the point defects present in the barrier layer are cation vacancies, cation interstitials and oxygen vacancies as designated by the Kroger-Vink notation [8]. The diagnostic criteria are predicted from the dependencies of L_{ss} and $\ln I_{ss}$ on the formation potential and pH. The criteria depend on whether or not a change in the oxidation state occurs upon

ejection of a cation from the barrier layer at the barrier layer/solution (outer later) interface during dissolution of the film.

With reference to Figure 6-10, the change in the film thickness with time is described in terms of the two lattice non-conservative reactions, as follows [9]:

$$\frac{dL}{dt} = -\frac{2\Omega}{\chi} J_o - \Omega k_7 \left(C_{H^+} / C_{H^+}^0 \right)^n \quad (6.1)$$

in which Ω is the mole volume per cation of the barrier layer ($MO_{\chi/2}$), χ is the oxidation state of the cation in the barrier layer, Γ is the oxidation state of the cation in the outer layer/solution, J_o is the flux for oxygen vacancies within the barrier layer from the m/bl interface, where they are generated, to the bl/ol interface where they are annihilated, C_{H^+} is the hydrogen ion concentration in the solution at the bl/ol interface, $C_{H^+}^0$ is the standard state hydrogen ion concentration, defined as being 1.0 mol/l, n is the kinetic order of the film dissolution reaction with respect to C_{H^+} , and k_7 is the rate constant for Reaction (7), Figure 6-10. Table 6-1 and Table 6-2 display the rate constants for the seven interfacial reactions; in these expressions, α is the polarizability of the bl/ol interface (i.e., dependence of the potential drop across the interface on the applied potential), β is the dependence of the potential drop at the bl/ol interface on pH, $\gamma = F/RT$, and α_j and k_j^0 are the transfer coefficient and the standard rate constant, respectively, for the j^{th} reaction shown in Figure 6-10.

Table 6-1: Rate constants $k_i = k_i^0 e^{a_i V} e^{-b_i L}$ for the interfacial defect generation and annihilation reactions employed in the Point Defect Model.

| Reaction | a_i (V^{-1}) | b_i (cm^{-1}) | Units of k_i^0 |
|---|---------------------------------------|------------------------|----------------------|
| (1) $m + V_M^{\chi'} \xrightarrow{k_1} M_M + v_m + \chi e'$ | $\alpha_1(1-\alpha)\chi\gamma$ | $\alpha_1\chi K$ | $\frac{l}{s}$ |
| (2) $m \xrightarrow{k_2} M_i^{\chi+} + v_m + \chi e'$ | $\alpha_2(1-\alpha)\chi\gamma$ | $\alpha_2\chi K$ | $\frac{mol}{cm^2 s}$ |
| (3) $m \xrightarrow{k_3} M_M + \frac{\chi}{2} V_{\ddot{O}} + \chi e'$ | $\alpha_3(1-\alpha)\chi\gamma$ | $\alpha_3\chi K$ | $\frac{mol}{cm^2 s}$ |
| (4) $M_M \xrightarrow{k_4} M^{\Gamma+} + (\Gamma - \chi)e'$ | $\alpha_4\alpha\Gamma\gamma$ | 0 | $\frac{mol}{cm^2 s}$ |
| (5) $M_i^{\chi+} \xrightarrow{k_5} M^{\Gamma+} + (\Gamma - \chi)e'$ | $\alpha_5\alpha\Gamma\gamma$ | 0 | $\frac{cm}{s}$ |
| (6) $V_{\ddot{O}} + H_2O \xrightarrow{k_6} O_O + 2H^+$ | $2\alpha_6\alpha\gamma$ | 0 | $\frac{cm}{s}$ |
| (7) $MO_{\chi/2} + \chi H^+ \xrightarrow{k_7} M^{\Gamma+} + \frac{\chi}{2} H_2O + (\Gamma - \chi)e'$ | $\alpha_7\alpha(\Gamma - \chi)\gamma$ | 0 | $\frac{mol}{cm^2 s}$ |

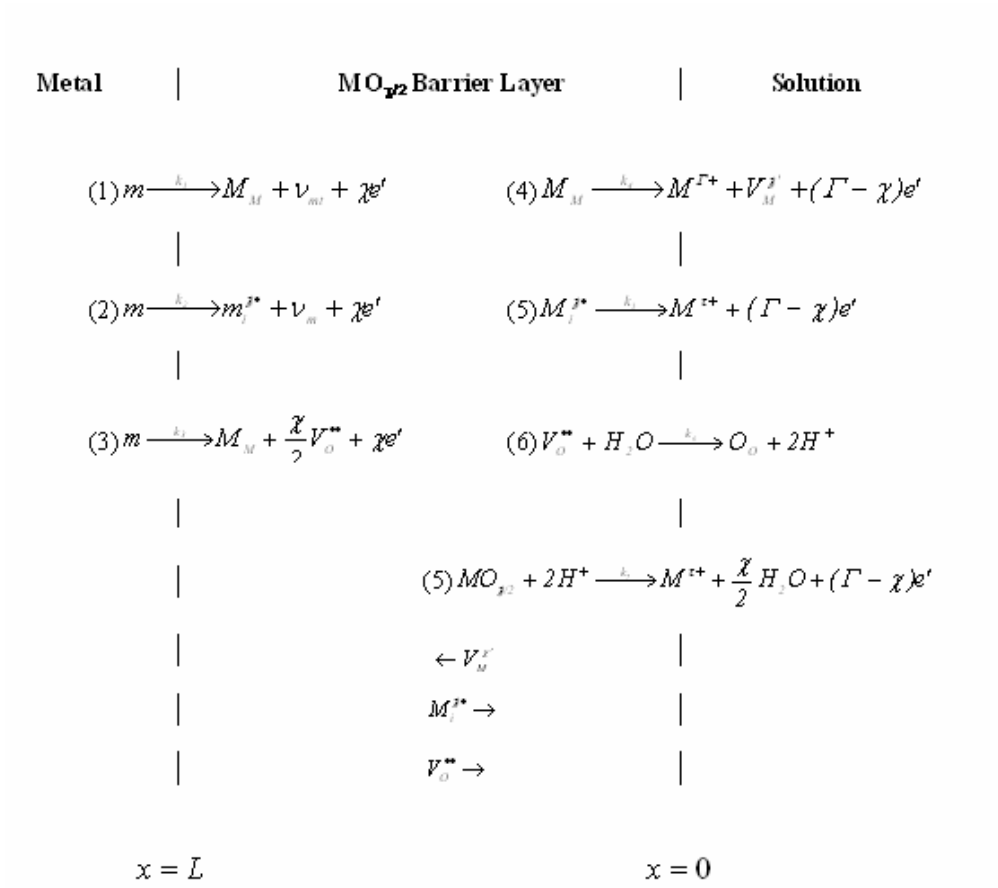


Figure 6-10: Schematic of physicochemical processes that are envisioned to occur within the barrier oxide (MO_{x/2}) layer on passive metal, according to the Point Defect Model. $m \equiv$ metal atom; $V_M^{r'}$ \equiv cation vacancy; M_i^{j*} \equiv interstitial cation; $\nu_m \equiv$ metal vacancy in metal substrate; $M_M \equiv$ metal cation in a normal cation position in the barrier layer; $M^{r+} \equiv$ metal cation in the solution phase (outer layer); V_O^{**} \equiv oxygen vacancy; $O_O \equiv$ oxygen ion in a normal anion site in the barrier layer.

Table 6-2: Definition of the standard rate constants for the interfacial defect generation and annihilation reactions employed in the Point Defect Model.

| Reaction | k_i^0 |
|---|---|
| (1) $m + V_M^{\chi'} \xrightarrow{k_1} M_M + v_m + \chi e'$ | $k_1^{00} e^{-\alpha_1 \beta \chi \gamma p H} e^{-\alpha_1 \chi \gamma \phi_{f/s}^0}$ |
| (2) $m \xrightarrow{k_2} M_i^{\chi+} + v_m + \chi e'$ | $k_2^{00} e^{-\alpha_2 \beta \chi \gamma p H} e^{-\alpha_2 \chi \gamma \phi_{f/s}^0}$ |
| (3) $m \xrightarrow{k_3} M_M + \frac{\chi}{2} V_{\ddot{O}} + \chi e'$ | $k_3^{00} e^{-\alpha_3 \beta \chi \gamma p H} e^{-\alpha_3 \chi \gamma \phi_{f/s}^0}$ |
| (4) $M_M \xrightarrow{k_4} M^{\Gamma+} + (\Gamma - \chi) e'$ | $k_4^{00} e^{\alpha_4 \beta \Gamma \gamma p H} e^{\alpha_4 \Gamma \gamma \phi_{f/s}^0}$ |
| (5) $M_i^{\chi+} \xrightarrow{k_5} M^{\Gamma+} + (\Gamma - \chi) e'$ | $k_5^{00} e^{\alpha_5 \beta \Gamma \gamma p H} e^{\alpha_5 \Gamma \gamma \phi_{f/s}^0}$ |
| (6) $V_{\ddot{O}} + H_2O \xrightarrow{k_6} O_O + 2H^+$ | $k_6^{00} e^{\alpha_6 \beta \Gamma \gamma p H} e^{\alpha_6 \Gamma \gamma \phi_{f/s}^0}$ |
| (7) $MO_{\chi/2} + \chi H^+ \xrightarrow{k_7} M^{\Gamma+} + \frac{\chi}{2} H_2O + (\Gamma - \chi) e'$ | $k_7^{00} e^{\alpha_7 (\Gamma - \chi) \beta \gamma p H} e^{\alpha_7 (\Gamma - \chi) \gamma \phi_{f/s}^0}$ |

All interfacial reactions that result in a change in oxidation state contribute to the total current density, which is written as

$$I = F [\chi J_c^{m/f} + (\Gamma - \chi) J_c^{f/s} - \chi J_i^{m/f} - (\Gamma - \chi) J_i^{f/s} - 2 J_o^{m/f} + (\Gamma - \chi) k_7 (C_{H^+} / C_H^0)^n] \quad (6.2)$$

in which $F = 96487 C/mol$ is Faraday's constant, subscripts C , i , and O designate cation vacancies, cation interstitials, and oxygen vacancies, respectively, and superscripts m/f and f/s signify the metal/barrier layer (film) and barrier layer/outer layer (solution) interfaces. Note that in the coordinate system adopted in Figure 6-10, the fluxes of metal interstitials and oxygen vacancies are negative, while the flux of cation vacancies is positive.

Under steady state conditions, $dL/dt = 0$ and $J_c^{m/f} = J_c^{f/s} = J_c$, $J_i^{m/f} = J_i^{f/s} = J_i$, and $J_o^{m/f} = J_o^{f/s} = J_o = (\chi/2)k_7(C_{H^+}/C_{H^+}^0)^n$. These relationships yield the steady state thickness of the barrier layer and the passive current density as

$$L_{ss} = \frac{1}{\varepsilon} \left[l - \alpha - \frac{\alpha\alpha_7}{\alpha_3} \left(\frac{\Gamma}{\chi} - l \right) \right] V + \frac{1}{\varepsilon} \left\{ \frac{2.303n}{\alpha_3\chi\gamma} - \beta \left[\frac{\alpha_7}{\alpha_3} \left(\frac{\Gamma}{\chi} - l \right) + l \right] \right\} pH + \frac{1}{\alpha_3\chi K} \ln \left(\frac{k_3^0}{k_7^0} \right) + \frac{6.909n}{\alpha_3\chi\gamma\varepsilon} - \frac{\Phi_{f/s}^0}{\varepsilon} \left[\frac{\alpha_7}{\alpha_3} \left(\frac{\Gamma}{\chi} - l \right) + l \right] \quad (6.3)$$

and

$$I_{ss} = IF \left[k_2^{00} e^{-\alpha_2\beta\chi\gamma pH} e^{-\alpha_2\chi\gamma\Phi_{f/s}^0} e^{\alpha_2(1-\alpha)\chi\gamma V} e^{-\alpha_2\chi\gamma L_{ss}} + k_4^{00} e^{\alpha_4\beta\Gamma pH} e^{\alpha_4\Gamma\gamma\Phi_{f/s}^0} e^{\alpha_4\alpha\Gamma\gamma V} + k_3^{00} e^{-\alpha_3\beta\chi\gamma pH} e^{-\alpha_3\chi\gamma\Phi_{f/s}^0} e^{\alpha_3(1-\alpha)\chi\gamma V} e^{-\alpha_3\chi\gamma L_{ss}} \right] \quad (6.4)$$

respectively.

As noted from Equation 6.3, the steady state thickness is a linear function of the film formation potential and solution pH. It is also predicted in Equation 6.4 that the steady state current density contains three components corresponding to the movement of cation vacancies, metal interstitials and oxygen vacancies through the film. Cation vacancies are electron donors, thereby doping the barrier layer p-type, whereas oxygen

vacancies and metal interstitials are electron donors, resulting in n-type doping. Thus, three limiting cases can be identified:

- 1) Cation vacancy-conducting films (p-type), where

$$I_{ss} = IF \left[k_4^{00} e^{\alpha_4 \beta \Gamma \gamma p H} e^{\alpha_4 \Gamma \gamma \Phi_{f/z}^0} e^{\alpha_4 \alpha \Gamma \gamma \mathcal{V}} \right] \quad (6.5)$$

Therefore,

$$\partial \ln I_{ss} / \partial V = \alpha_4 \alpha \Gamma \gamma \quad (6.6)$$

$$\partial \ln I_{ss} / \partial p H = \alpha_4 \beta \Gamma \gamma \quad (6.7)$$

- 2) metal interstitials-conducting films (n-type) with

$$I_{ss} = IF \left[k_2^{00} e^{-\alpha_2 \beta \chi \gamma p H} e^{-\alpha_2 \chi \gamma \Phi_{f/z}^0} e^{\alpha_2 (1-\alpha) \chi \gamma \mathcal{V}} e^{-\alpha_2 \chi \varepsilon \gamma L_{ss}} \right] \quad (6.8)$$

Therefore,

$$\begin{aligned} \partial \ln I_{ss} / \partial V &= \alpha_2 (1-\alpha) \chi \gamma - \alpha_2 \chi \varepsilon \gamma \left(\partial L_{ss} / \partial V \right) \\ &= \alpha_2 \alpha_7 \alpha (\Gamma - \chi) \gamma / \alpha_3 \end{aligned} \quad (6.9)$$

$$\begin{aligned}
\frac{\partial \ln I_{ss}}{\partial pH} &= -\alpha_2 \beta \chi \gamma - \alpha_2 \chi \gamma \varepsilon \left(\frac{\partial L_{ss}}{\partial pH} \right) \\
&= 2.303n - \beta \gamma \alpha_7 (\Gamma - \chi) - \beta \chi \gamma (\alpha_2 + \alpha_3)
\end{aligned} \tag{6.10}$$

3) oxygen vacancies-conducting films (n-type) with

$$I_{ss} = IF \left[k_3^{00} e^{-\alpha_3 \beta \chi \gamma pH} e^{-\alpha_3 \chi \gamma \Phi_{f/s}^0} e^{\alpha_3 (1-\alpha) \chi \gamma V} e^{-\alpha_3 \chi \gamma L_{ss}} \right] \tag{6.11}$$

Therefore,

$$\begin{aligned}
\frac{\partial \ln I_{ss}}{\partial V} &= \alpha_3 (1-\alpha) \chi \gamma - \alpha_3 \chi \gamma \varepsilon \left(\frac{\partial L_{ss}}{\partial V} \right) \\
&= \alpha_7 \alpha \gamma (\Gamma - \chi)
\end{aligned} \tag{6.12}$$

$$\begin{aligned}
\frac{\partial \ln I_{ss}}{\partial pH} &= -\alpha_3 \beta \chi \gamma - \alpha_3 \chi \gamma \varepsilon \left(\frac{\partial L_{ss}}{\partial pH} \right) \\
&= \alpha_3 \beta \gamma (1 - \chi) - 2.303n
\end{aligned} \tag{6.13}$$

The predicted dependencies of L_{ss} and $\ln I_{ss}$ on the formation potential and pH give rise to the diagnostic criteria. For those cases where no change in oxidation state upon

ejection of a cation from the barrier layer ($\Gamma = \chi$) or upon dissolution of the film occurs, the diagnostic functions are summarized in Table 6-3.

Table 6-3: Diagnostic criteria for determining the conductive nature of the barrier layer ($\Gamma = \chi$).

| Criterion | Cation vacancies conducting (p-type) | Metal interstitials conducting (n-type) | Oxygen vacancies conducting (n-type) |
|--|--|--|--|
| $\left(\frac{\partial \ln I_{ss}}{\partial V} \right)_{pH}$ | $\alpha_4 \alpha \Gamma \gamma$ | 0 | 0 |
| $\left(\frac{\partial L_{ss}}{\partial V} \right)_{pH}$ | $\frac{1}{\varepsilon} [l - \alpha]$ | $\frac{1}{\varepsilon} [l - \alpha]$ | $\frac{1}{\varepsilon} [l - \alpha]$ |
| $\left(\frac{\partial \ln I_{ss}}{\partial pH} \right)_V$ | $\alpha_4 \beta \Gamma \gamma$ | $2.303n - \beta \chi \gamma (\alpha_2 + \alpha_3)$ | $\alpha_3 \beta \gamma (l - \chi) - 2.303n$ |
| $\left(\frac{\partial L_{ss}}{\partial pH} \right)_V$ | $\frac{1}{\varepsilon} \left\{ \frac{2.303n}{\alpha_3 \chi \gamma} - \beta \right\}$ | $\frac{1}{\varepsilon} \left\{ \frac{2.303n}{\alpha_3 \chi \gamma} - \beta \right\}$ | $\frac{1}{\varepsilon} \left\{ \frac{2.303n}{\alpha_3 \chi \gamma} - \beta \right\}$ |

Plots of $\ln(I_{ss})$ against potential for platinum in KOH solutions (pH 12-14) are shown in Figure 6-11. As predicted by the PDM, the logarithm of steady state current density is independent of applied voltage prior to the oxygen evolution region or perhaps prior to the region where Pt (II) is oxidized to Pt (IV). This behavior is consistent with the prediction of the PDM on n-type oxide (Table 6-3). It is also noted that the current density obtained by a step-wise increase in the potential after each 24 hours potentiostatic period is in good agreement with the current density obtained during a reverse scan. This demonstrates steady-state behavior for the system.

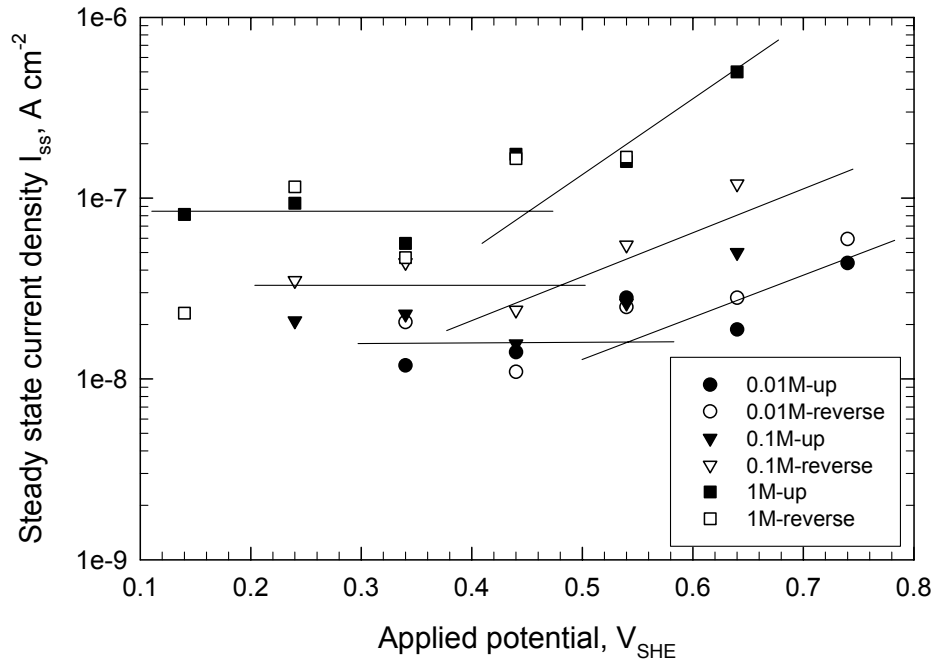


Figure 6-11: Dependence of the steady state current density on applied potential and pH.

Furthermore, the steady state thickness shown in Figure 6-12 was calculated from specific capacitance data. In order to analyze the EIS data, it was assumed that the oxide is the dielectric of a parallel plate capacitor with a leaky, parallel resistance. It is observed that the film thickness increases linearly with the formation potential, and the slope is independent of pH, within the experimental uncertainty. According to the diagnostic criteria of the PDM, this slope does not depend on pH, and equals $(1 - \alpha) / \varepsilon$. The polarizability of the barrier layer/solution interface, α , can have values between 0

and 1, with other work [1] indicating that for very thin films, the value lies toward the upper extreme of this range. Taking $\alpha = 0.8$ and $\varepsilon = 2 \times 10^6 \text{V/cm}$ from a previous study [2], we have $\partial \ln(L_{ss})/\partial V = 1.0 \text{nm/V}$ for all pH ranges, which is in satisfactory agreement with the experimental value of 0.92 nm/V (Figure 6-12). Alternatively, the electric field strength for passive metals having very thin passive films lies between $2 \times 10^6 \text{V/cm}$ and $5 \times 10^6 \text{V/cm}$, which after assuming $\alpha = 0.5$ yields $\partial \ln(L_{ss})/\partial V = 2.5 \text{nm/V}$ and 1.0nm/V , respectively. This is also in reasonable agreement with experiment. As we have discussed elsewhere [2], due to the difficulty in measuring values for fundamental parameters in the PDM, these estimates must be viewed as being only semi-quantitative until the optimization of the PDM on high quality electrochemical impedance data can be completed. This work is now underway. In this regard, the value of $\partial \ln(L_{ss})/\partial V$ and the value of the steady-state current, I_{ss} , provide important constraints on the optimization process. It is also noteworthy that a pH dependence of $\partial V/\partial L$ of the platinum oxide film formed in alkaline solutions was observed by Damjanovic et al. [10, 11] using galvanostatic measurements, which is contrary to our experimental result (Figure 6-12). However, no dependence of $\partial V/\partial L$ in acid solution [12, 13] was reported. Damjanovic et al. [14] stated that only if the rate determining step occurs at the film/solution interface, the observed pH dependence in alkaline solution and independence in acid solution could be accounted for in terms of the HFM model. They have also questioned if the change in the charge distribution within the oxide film affects the field in the double layer and consequently the rate of oxide growth, if a process at the oxide film/solution interface is the rate determining step. However, we further note that,

while the acid solution used by Damjanovic et al [14] was purged with argon, the alkaline solution was purged with oxygen. Accordingly, the oxygen reduction reaction presumably occurred on the platinum surface, with the result that the electrochemical response was not determined by the oxide film alone. Finally, under galvanostatic conditions, it is difficult to accept that a steady state may have been achieved, in which case the diagnostic criteria given in Table 6-3 for potentiostatic conditions do not apply.

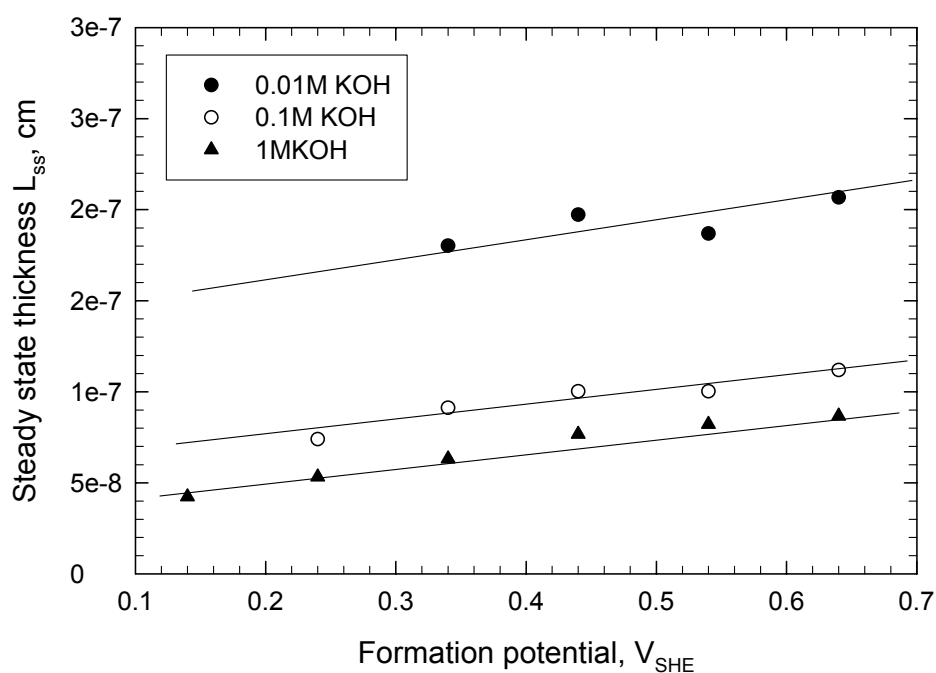


Figure 6-12: Dependence of steady state thickness of the platinum oxide film as a function of applied voltage and pH. The film thickness is obtained from capacitance by assuming that the oxide is the dielectric of a parallel plate capacitor with a leak resistance in analyzing EIS data measured at each formation potential.

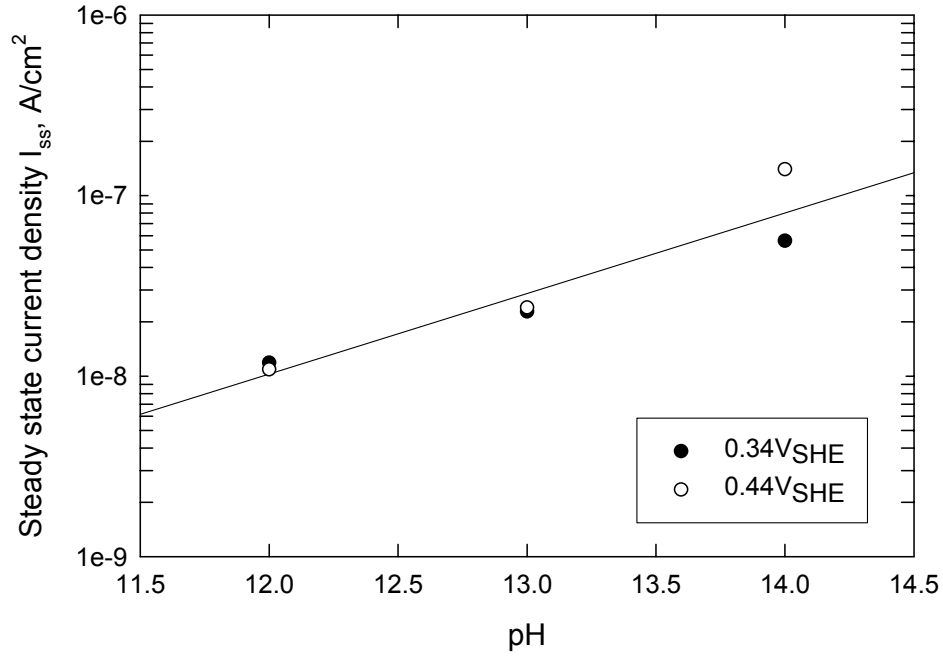


Figure 6-13: Dependence of the steady state current on pH for platinum in KOH solution.

As shown in Figure 6-11, the steady state current does not depend on the applied voltage prior to oxygen evolution for any of the pH values investigated. A plot of the steady state current versus pH is shown in Figure 6-13. Here, we plot the current density measured at 0.34 and 0.44V_{SHE} for three pH values, since only these two applied voltages are in the passive potential range prior to oxygen evolution. It is noted from Figure 6-13 that the logarithm of the steady state current density linearly increases with the pH, and the slope is equal to 0.58. From Table 6-3, we may then calculate $[\partial \ln(I_{ss}) / \partial pH]_V$. Note that the dominant defects in an n-type oxide could be either oxygen vacancies or

metal interstitials, or both, and that the diagnostic criteria are the same for these two defects (Table 6-3). As we have stated elsewhere [2], this renders difficult differentiation between the oxygen vacancy and the cation interstitial being the dominant defect in an oxide on the basis of electrochemical studies alone (Table 6-3). However, recent work in this laboratory suggests that these cases may be differentiated by optimization of the PDM on high quality electrochemical impedance data through examination of the values for the rate constants obtained. The fact that $[\partial \ln(I_{ss}) / \partial pH]_V$ is independent of pH (Figure 6-13) is consistent with the diagnostic criteria listed in Table 6-3 and it is evident that this quantity, too, may become an important constraint in optimization.

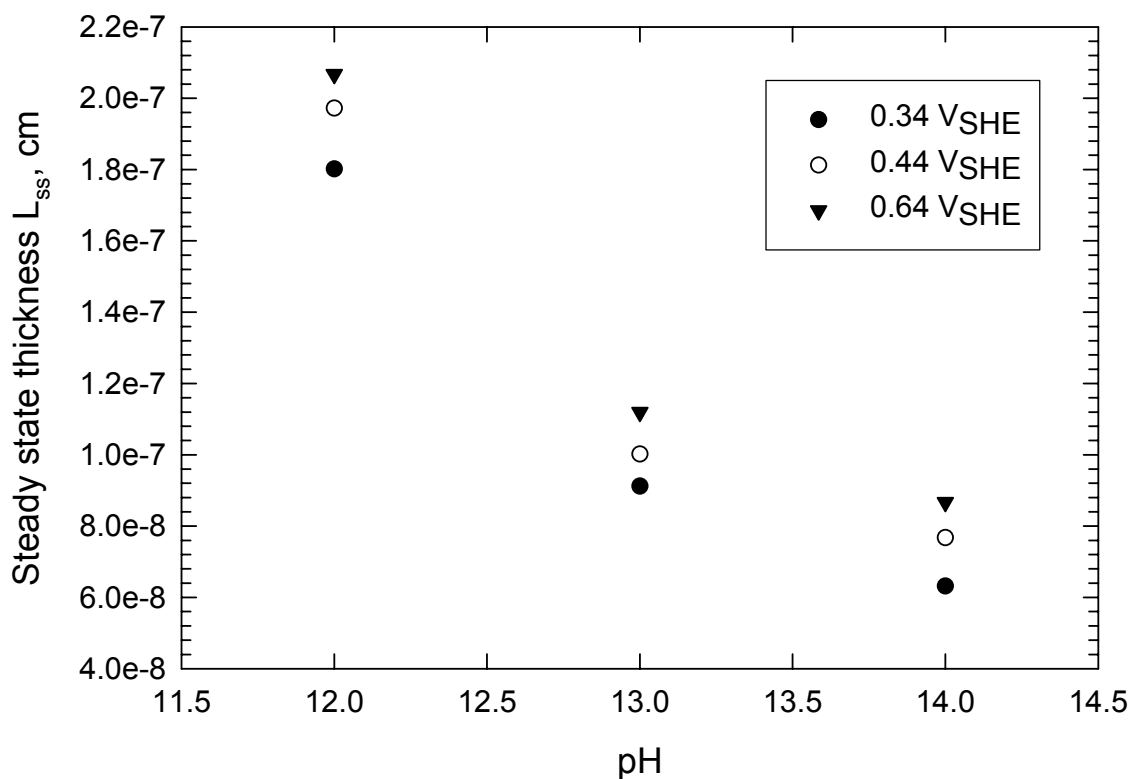


Figure 6-14: Dependence of the steady state thickness on pH for platinum oxide.

Finally, the steady state thickness is plotted against pH at three passive potentials in Figure 6-14. A linear relationship between steady state thickness and pH is observed, and the steady state thickness decreases with pH. The slope of the plot is also found to be independent of applied potentials and to equal -5.9×10^{-8} cm/pH. This linear relationship is also consistent with the prediction of the PDM (Table 6-3).

6.3 Optimization of the PDM on EIS Data as a Function of pH

As we have stated above, since the model uses elementary reactions to describe film growth, most of the parameters involved, such as the rate constants, transfer coefficients, and so forth, cannot be obtained by direct experimental measurement. An unequivocal set of model parameters will therefore not be easily obtained when the number of unknowns is greater than the number of observables. By determining the dependencies of L_{ss} and I_{ss} on the applied voltage and pH from the independent experiments, one is able to place more constraints on the optimization of the PDM on EIS data in alkaline solutions. One can also more accurately describe the kinetic nature of the processes that generate and annihilate vacancies at the interfaces. Here, we employ the truncated version of the PDM, for n-type oxide as described in Chapter 5, to interpret the experimental EIS data in alkaline solutions varying concentration with the diagnostic criteria (Table 6-3) as the constraints.

The procedure for optimizing the PDM on experimental impedance data for n-type barrier layers has been described in Chapter 5 and this same procedure is used here. Optimization was also carried out in two stages. In the first stage, all of the parameters

except R_s (resistance of the solution between the specimen and the tip of the reference electrode Luggin probe), were treated as variables. The optimization procedure yielded estimated values for these variables.

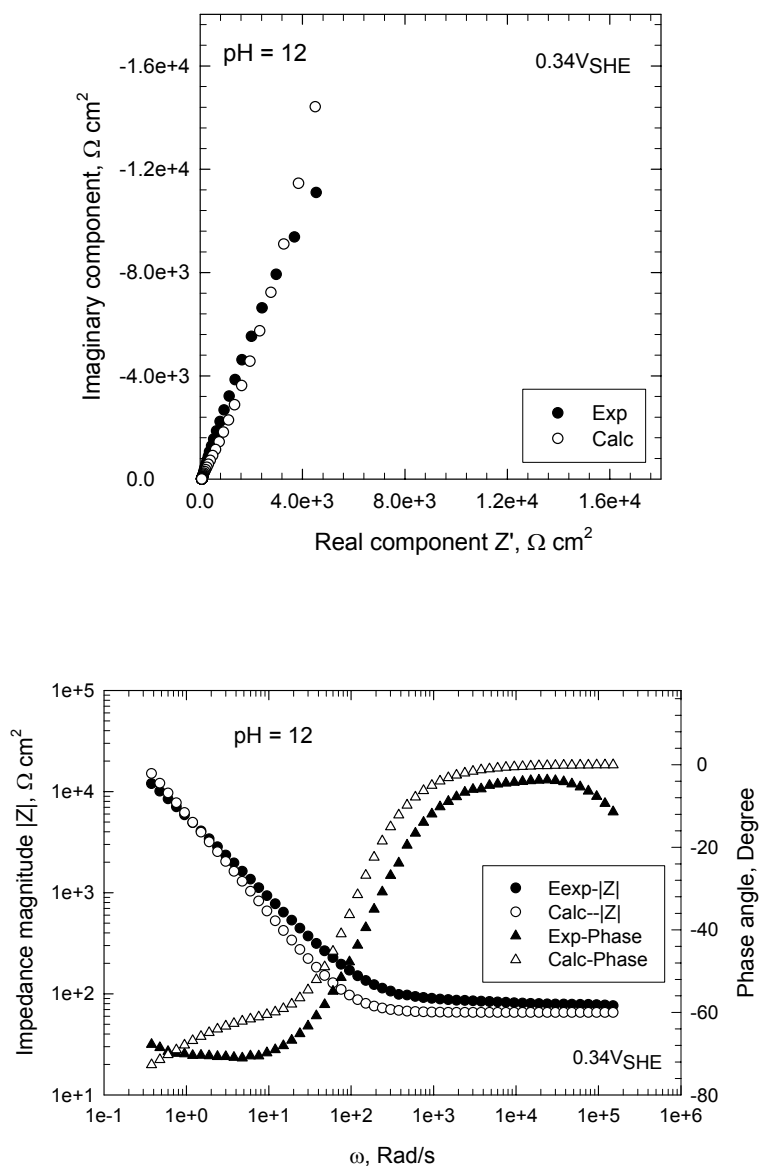


Figure 6-15: Nyquist and Bode plots of impedance data for Pt in 0.01M KOH at applied voltages of 0.34 V_{SHE}.

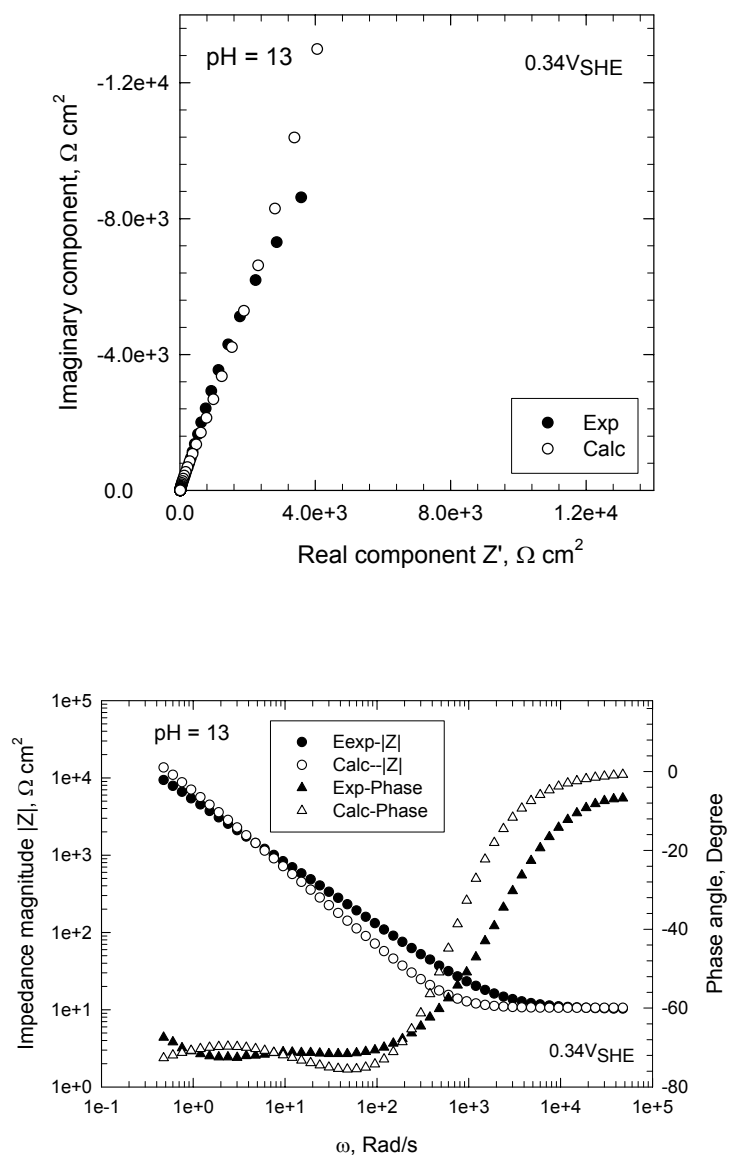


Figure 6-16: Nyquist and Bode plots of impedance data for Pt in 0.1M KOH at applied voltages of $0.34 V_{\text{SHE}}$.

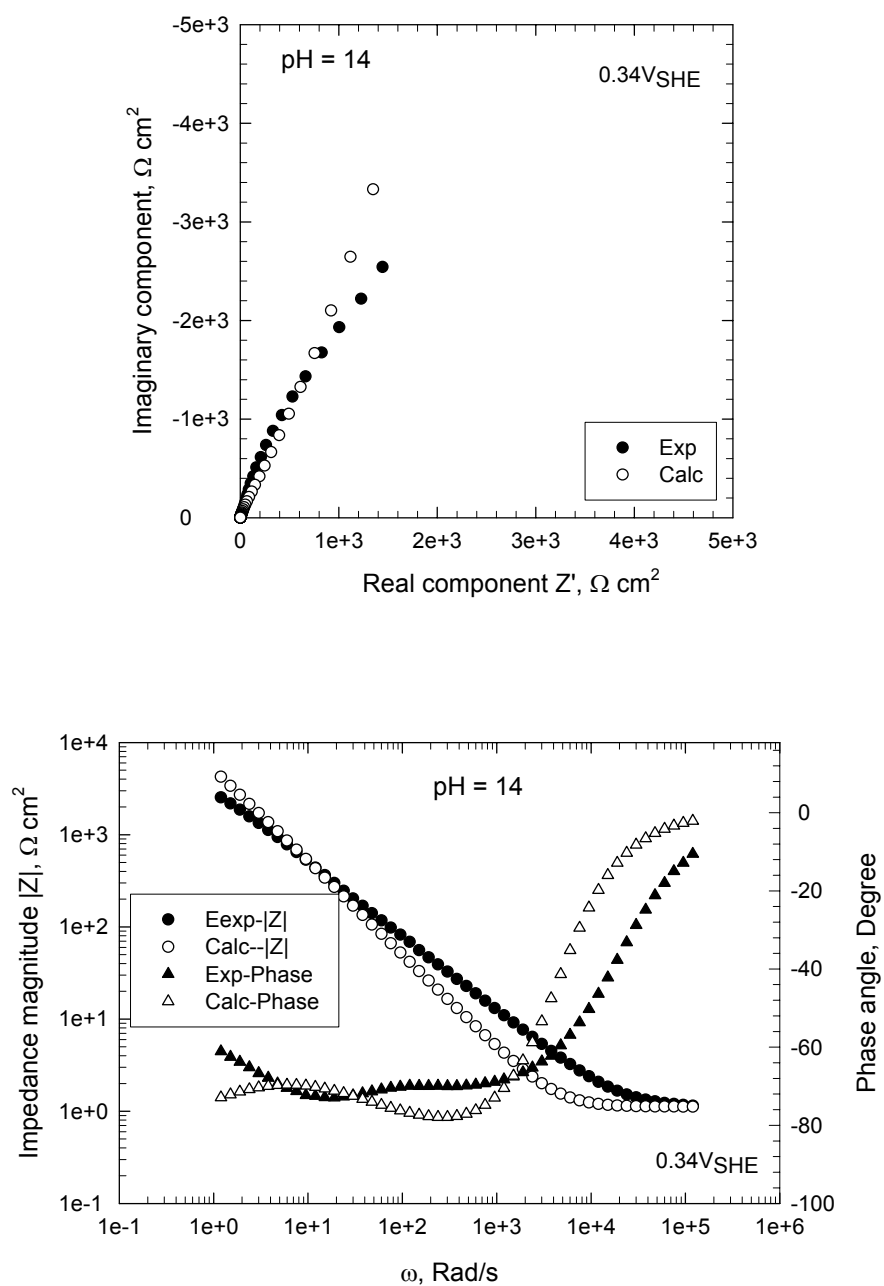
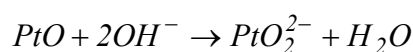


Figure 6-17: Nyquist and Bode plots of impedance data for Pt in 1M KOH at applied voltages of $0.34 \text{ V}_{\text{SHE}}$.

The calculated impedance data obtained by optimizing the PDM using impedance data measured at a constant formation potential and various pH values are displayed in Figure 6-15 - Figure 6-17. The commercial DataFit software (Version 7.1, www.curvefitting.com) was also employed in this work for optimization, in order to obtain the values for the transfer coefficients, α_i , and standard rate constants, k_i^{00} , for the i elementary interfacial reactions, the polarizability of the film/solution interface, α , the electric field strength, ε , and other parameters, as described below. It is also very interesting to note that the kinetic order of the dissolution reaction at the barrier layer/solution interface with respect to the (H^+) is negative, according to the experimentally-determined dependencies of L_{ss} and I_{ss} on pH. Since the dissolution reaction occurs in alkaline solution, the sign of the kinetic order is accounted for by assuming that the barrier layer dissolves to form platinate species is thus possible to be produced in the solution. The reaction (7) in Figure 6-10 in alkaline solutions could then be expressed as follows;



or possibly



The first reaction would account for the passive state, in which the oxidation state of the cation in the barrier layer is identical to that in solution (PtO_2^{2-}). The second reaction, in which a change in oxidation state occurs upon dissolution (not included in the diagnostic criteria listed in Table 6-3), may account for the Tafel behavior observed at higher potentials (Figure 6-11). However, the same Tafel behavior may be accounted for

by oxygen evolution, so that a major task in future work will be to differentiate between these two possibilities. Equation 5.2 is accordingly written as

$$\begin{aligned}\frac{dL}{dt} &= -\frac{2\Omega}{\chi} J_O - \Omega k_5 \left(C_{OH^-} / C_{OH^-}^0 \right)^{n'} \\ &= -\frac{2\Omega}{\chi} J_O - \Omega k_5 \left(K_w^{n'} \left(C_{H^+} / C_{H^+}^0 \right)^{-n'} \right) \\ &= -\frac{2\Omega}{\chi} J_O - \Omega k_5 \left(K_w^{-n} \left(C_{H^+} / C_{H^+}^0 \right)^n \right)\end{aligned}$$

where K_w is the equilibrium constant for H_2O , n' is the kinetic order of the dissolution reaction at the film/solution interface with respect to $[OH^-]$, which is positive, and n is the kinetic order of the dissolution reaction at the film/solution interface with respect to $[H^+]$. The experimental results indicate that n is negative in alkaline solutions.

Values for the fundamental model parameters for passive platinum are presented in Table 6-4. The comparison in Figure 6-15 - Figure 6-17 show that the correlation between the experimental impedance data and the simulated data is acceptable for the Nyquist plots and Bode plots shown. The parameter values obtained by optimization of the model on impedance data that span the pH range are found not to depend on pH in any systematic manner. This, in itself, is also a test of the viability of the model. The value for the kinetic order of the dissolution reaction at the film/solution interface with respect to $[H^+]$ is found to be -0.2, which is consistent with the experimental results. Thus the platinate is formed during the dissolution reaction of the oxide film in alkaline solutions. The defect diffusivities calculated from the optimization is shown to increase with the pH, which implies that the defects transport faster at higher pH.

Table 6-4: Parameter values from optimization of the Point Defect Model on the experimental impedance data for platinum formed at $0.34V_{SHE}$ in deaerated KOH solutions at $20^{\circ}C$ as a function of pH.

| V_{app} / V_{SHE} | 12 | 13 | 14 | Mean (\pm Standard Deviation) | Origin |
|--|---------|---------|---------|----------------------------------|--|
| $R_s(\Omega \cdot cm^2)$ Solution resistance | 65.35 | 10.55 | 1.12 | | Assumed from the value of real component of impedance at highest frequency |
| $10^5 C_{dl} (F/cm^2)$ Double layer capacitance | 8 | 8 | 8 | 8.3 ± 0.4 | Second stage optim |
| $10^8 R_e(\Omega \cdot cm^2)$ Electronic resistance | 2.05 | 2.05 | 2.05 | 2.05 | First stage optim |
| $10^{-6} \varepsilon (V/cm)$ Electric field strength | 3 | 3 | 3 | 3 | First stage optim |
| $\hat{\varepsilon}$ Dielectric constant | 45 | 45 | 45 | 45 | First stage optim |
| $10^{19} k_1^{00} (mol/cm^2 s)$ Standard rate constant | 1 | 1 | 1 | 1 | First stage optim |
| $10^{13} k_2^{00} (mol/cm^2 s)$ Standard rate constant | 1.08 | 0.59 | 0.84 | 8.38 ± 1.71 | Second stage optim |
| $10^{16} k_5^{00} (mol/cm^2 s)$ Standard rate constant | 4 | 4 | 4 | 4 | First stage optim |
| α Polarizability of bl/ol interface | 0.725 | 0.725 | 0.725 | 0.725 | First stage optim |
| α_1 Transfer coefficient | 0.375 | 0.535 | 0.455 | 0.45 ± 0.06 | Second stage optim |
| α_2 Transfer coefficient | 0.022 | 0.029 | 0.025 | 0.025 ± 0.003 | Second stage optim |
| n Kinetic order of dissolution With $[H^+]$ | -0.2065 | -0.2068 | -0.2066 | -0.21 | Second stage optim |
| $\beta (V)$ Dependence of potential drop across bl/ol interface on pH | -0.04 | -0.04 | -0.04 | -0.04 | First stage optim |
| $10^3 \phi_{f s}^0 (V)$ $\phi_{f s}$ in the standard state ($V=0, pH=0$) | -5.5 | -1 | -3.25 | -3.25 ± 1.6 | Second stage optim |
| $10^{-5} \sigma (\Omega \cdot cm^2 s^{-0.5})$ Warburg coefficient | 1.12 | 1.03 | 1.07 | 1.07 ± 0.03 | Second stage optim |
| $10^8 L_{ss} (cm)$ Steady state thickness | 17.2 | 10.0 | 4.7 | | Calculated from Equation 5.35 |
| $10^8 J_{ss} (A cm^{-2})$ Steady state current density | 2.32 | 3.29 | 5.49 | | Calculated from Equation 5.36 |
| $10^{19} D_w (cm^2/s)$ Diffusivity of principal defect. | 1.14 | 1.9 | 2.23 | | Calculated from Equation 5.34 |

As noted in Figure 6-18, the logarithm of the calculated steady state current density, I_{ss} , increases with the formation potential. The slopes of both experimental and calculated current in Figure 6-18 shows very little difference. As we have stated above, we chose the dependency of logarithmic I_{ss} on pH for dominant defect species as oxygen vacancies of the n-type oxide film as the constraint during the simulation. This was selected because the optimization results in acid solution indicates that the dominant defects in platinum oxide film are oxygen vacancies. However, the contribution of platinum interstitials transport to the total current is also found in Figure 6-19, although it is not dominant. This might cause the deviation of the slope of the calculated current in Figure 6-18. Equation 5.36 in Chapter 5, the total steady state current density, consists of the fluxes of the platinum interstitials [Reaction (1), Figure 5.1] and oxygen vacancies [Reaction (2), Figure 5.1] at the metal/film interface if there is no change in oxidation state of the platinum cation upon ejection from the film/solution interface or upon dissolution of the film. The calculated current density due to the oxygen vacancy transfer [second term, Equation 5.36] is then also found to dominate due to the platinum interstitial transfer [first term, Equation 5.36] at different pH, as shown in Figure 6-19. Likewise, the present work provides a strong theoretical argument that oxygen vacancies are the principal defects in the barrier layer on platinum formed in alkaline solutions.

The steady state thickness is found experimentally to decrease linearly with the pH and this relationship is also obtained from the optimization of the PDM on EIS data (Figure 6-20). The slopes of $\partial L_{ss}/\partial pH$ of both experimental and simulation results are in good agreement.

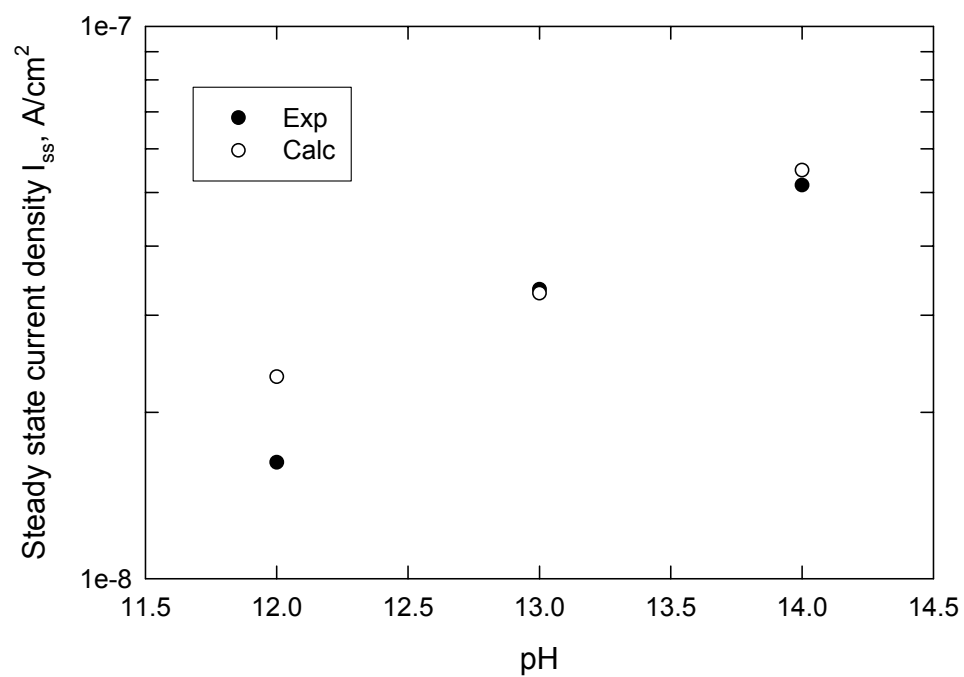


Figure 6-18: Dependence of steady state current on pH for platinum in KOH solution.

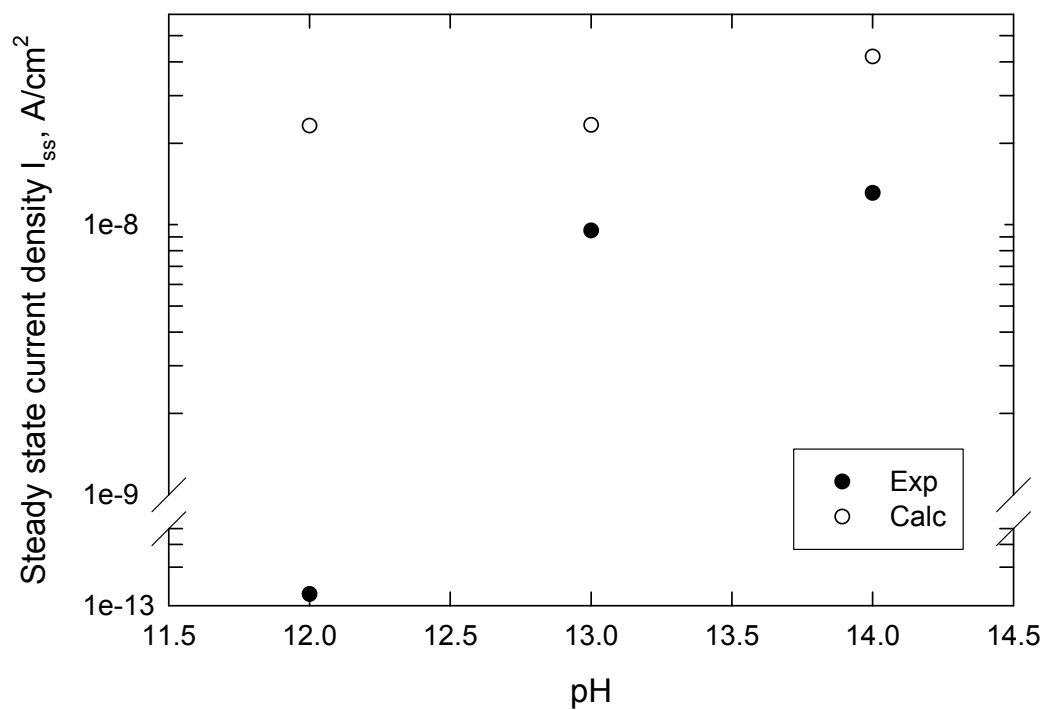


Figure 6-19: Dependence of steady state current due to the transport of platinum interstitials and oxygen vacancies, respectively, on pH for Pt in KOH solutions.

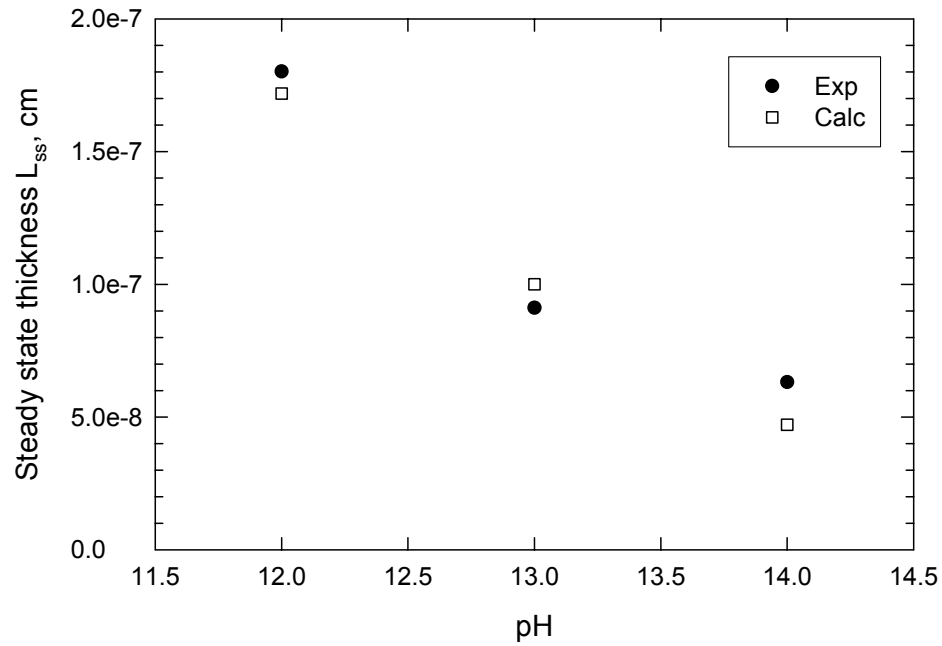


Figure 6-20: Dependence of steady state thickness on pH for platinum in KOH solution.

6.4 Summary

The present experiments and analysis show that there is no distinction between the properties and growth of the anodic oxide film on platinum formed in either acid or alkaline solutions. The experimental data show that the oxide film is a highly defective n-type oxide and has a bi-layer structure. The experimental data confirm the existence of steady-state conditions in the current and film thickness. Diagnostic criteria derived from the PDM account for the experimentally-determined dependencies of the steady state passive current and film thickness on voltage and pH in the passive region. The kinetic order for dissolution of the barrier layer with respect to the hydrogen ion concentration is

found to be negative. This indicates that the film may dissolve to form platinate Pt(II) or Pt(IV) species. The experimentally established diagnostic criteria derived from the PDM are employed as constraints in the optimization of the PDM on EIS data.

References

- [1] D.D. Macdonald, *Pure Appl. Chem.*, 71, (1999) 951.
- [2] A. Sun, J. Franc, and D.D. Macdonald, *J. Electrochem. Soc.*, In press, (2006)
- [3] N. Priyantha, P. Jayaweera, D.D. Macdonald, and A. Sun, *Journal of Electroanalytical Chemistry*, 572, (2004) 409.
- [4] S.R. Morrison, *Electrochemistry at Semiconductor and Oxidized Metal Electrodes*, Plenum Press, New York and London, 1980.
- [5] D.D. Macdonald, E. Sikora, and J. Sikora, *Electrochimica Acta*, 43, (1998) 2851.
- [6] D.D. Macdonald, M.A. Rifaie, and G.R. Engelhardt, *Journal of Electrochemical Society*, 148, (2001) B343.
- [7] D.D. Macdonald, S.R. Biaggio, and H. Song, *J. Electroanal. Chem.*, 139, (1992) 170.
- [8] D.D. Macdonald and A. Sun, *Electrochimica Acta*, 51, (2006) 1767.
- [9] D.D. Macdonald, A. Sun, N. Priyantha, and P. Jayaweera, *Journal of Electroanalytical Chemistry*, 572, (2004) 421.

- [10] A. Damjanovic, L.S.R. Yeh, and J.F. Wolf, J. Electrochem. Soc., 129, (1982) 55.
- [11] A. Damjanovic, L.S.R. Yeh, and J.F. Wolf, J. Electrochem. Soc., 126, (1979) C150.
- [12] A. Damjanovic and L.S.R. Yeh, J. Electrochem. Soc., 125, (1978) C124.
- [13] A. Damjanovic, A.T. Ward, B. Ulrick, and M. Ojea, J. Electrochem. Soc., 122, (1975) 471.
- [14] A. Damjanovic, L.S.R. Yeh, and J.F. Wolf, J. Electrochem. Soc., 127, (1980) 1945.

Chapter 7

CONCLUSIONS AND FUTURE WORK

7.1 Conclusions

The properties of, and the growth mechanism for the oxide film formed anodically on platinum in acid and alkaline solutions have been investigated using electrochemical transient (cyclic voltammetry) and steady state (potentiostatic polarization and EIS) electrochemical methods as well as Angle-Resolved X-ray Photoelectron Spectroscopy (ARXPS). The principal findings of this study are as follows:

1. The formation of the anodic oxide film on platinum is readily characterized by cyclic voltammetry, as described in many previous studies.
2. Angle-Resolved XPS studies on oxide film in acid solution show that the anodic oxide film on platinum has a bilayer structure, comprising a highly defective, n-type Pt(II) barrier oxide layer adjacent to the metal and, at sufficiently high voltages, a precipitated Pt(IV) outer layer.
3. Mott-Schottky analysis of the interfacial capacitance measured at high frequency in acid solution reveals a high defect (donor) concentration, as high as 0.164 of the combined cation interstitial and anion sublattice sites in the film, assuming one cation interstitial site per cation sublattice site.

4. An n type semiconductive character of oxide formed in both acid and alkaline solution is found by capacitance measurements. The negative slopes of Mott-Schottky plots observed for each formation potential in acid solution are not found in alkaline solution, which could be due to the anion adsorption to the surface in acid solution that results in the increase of surface charge at the interface.
5. The steady state thickness of the barrier layer in acid solution is very small, corresponding to no more than two tetragonal unit cells at a voltage of 1.4 V_{SHE}.
6. The thickness of the barrier layer varies linearly with the formation voltage and the steady state current density is independent of potential in both acid and alkaline solutions, both of which are consistent with the diagnostic criteria obtained from the Point Defect Model (PDM) for the formation of an n-type barrier oxide layer.
7. The linear dependencies of the steady state current and thickness on pH are also observed from the experiments in alkaline solutions. The value for the kinetic order of the dissolution reaction at the film/solution interface with respect to the $[H^+]$ is then shown to be negative, which suggests that the palatinate (PtO₂)²⁻ might be produced during the dissolution of oxide film in alkaline solutions.
8. Diagnostic Criteria are derived for the PDM with cation vacancies, metal interstitials, and oxygen vacancies as the doping defects in the film. These predictions are in good agreement with the experimental results.
9. The existence of a finite, steady-state thickness of the barrier oxide layer implies that dissolution of the barrier layer occurs and hence the dynamics of

film growth are inconsistent with the rate laws of the Place Exchange Mechanism (PEM) and the High Field Model (HFM). The experimental findings are consistent with the prediction of the PDM, which postulates that the properties of the barrier layer can be described in terms of the generation and annihilation of point defects (oxygen vacancies and cation interstitials) at the metal/barrier layer and barrier layer/outer layer (solution) interfaces, and with film growth occurring at the metal/film interface and dissolution taking place at the film (barrier layer)/solution interface.

10. Optimization of the PDM on electrochemical impedance spectroscopy (EIS) data for the passive state yields a set of model (including kinetic) parameter values that can be used to predict both the steady state and the transient film thickness and current. By comparing the calculated steady state current density with experimentally-measured values, we conclude that the principal defect in the barrier layer is the oxygen vacancy.
11. On the basis of structural and epitaxial factors, we postulate that the barrier oxide layer, comprising oxygen-deficient and possibly metal-rich $Pt_{1+x}O_{1-y}$, grows in nano-crystalline domains with the C axis of the bimolecular tetragonal unit cell ($a = 0.304\text{nm}$ and $c = 0.534\text{nm}$) being oriented perpendicular to the metal surface; this being the orientation of minimal strain.
12. We judge that there is nothing remarkable about the anodic passive film on platinum, except perhaps that it is very thin. In terms of the structure and electronic properties of the film, platinum joins many other metals whose passive films are successfully accounted for by the Point Defect Model.

7.2 Future Work

The future work following this dissertation should be mainly focused on a few aspects.

1. Further characterization of solid state properties of the oxide film on platinum by using photoelectrochemical method.

Mott-Schottky analysis as the most popular electrochemical method for determining the charge distribution in the passive film has been employed in this dissertation. However, as we have stated in the previous chapter, the classical Mott-Schottky method made a lot of assumptions in order to be applied to interpret the electrochemically formed oxide film and the band structure of the film could not be obtained from the capacitance measurements. In order to more accurately describe the solid states of the film on platinum, the photoelectrochemical method should be applied to study the film, the band gap energies and the flatband potential are then be able to be determined.

2. *in-situ* electrochemical ellipsometry experiments should be performed for the film formed in alkaline solutions. Ellipsometry is particularly attractive for probing the properties of the passive films with the non-destructivity, extreme sensitivity to minute interfacial effects and application to surface films having a thickness as small as monoatomic to as large as several microns. The thickness and the dielectric properties of the film can be deduced by the analysis of the ellipsometry parameters.

3. The compositions of the oxide films on platinum formed in alkaline solutions should be determined by XPS. Our XPS results show that the outer layer is only formed at higher potential in acid solution. However, in alkaline solution, the thicker film is usually formed at each formation potential, which has been demonstrated by our experimental results. It has been known that in alkaline solution, the OH^- is easily involved in the film formation and could result in the formation of outer layer of the film. Therefore, XPS needs to be employed to detect the film structure and the composition for the film formed in alkaline solution in order to describe the properties of the film formed on platinum.
4. Optimization of the PDM on EIS data in alkaline solution should be further performed as a function of potential with the diagnostic criteria as the constraints in order to more accurately describe the kinetics of film growth on platinum.

Appendix A**An Electrochemical Impedance Study of Alloy-22 in NaCl Brine at Elevated
Temperature: II. Reaction Mechanism Analysis****Digby D. Macdonald¹ and Adan Sun****Center for Electrochemical Science and Technology****Pennsylvania State University****University Park, PA 16802****and****Namal Priyantha and Palitha Jayaweera****Materials Research Laboratory****SRI International****Menlo Park, CA 94025**

¹ Corresponding author, e-mail: macdonald@matse.psu.edu.

Abstract

Development of deterministic models for predicting the accumulation of corrosion damage to High Level Nuclear Waste (HLNW) canisters requires the acquisition of values for various model parameters. In the present work, we describe the extraction of values for various parameters in the Point Defect Model (PDM) for the growth of passive films on Alloy-22, from electrochemical impedance data for this alloy measured in saturated $NaCl$ brine (6.2 m) at 80 $^{\circ}C$, as described in Part I. The barrier layer of the passive film on Alloy-22 in the passive region ($V < 0.6 V_{she}$) is postulated to be defective chromic oxide ($Cr_{2+x}O_{3-y}$) with n -type electronic character. The data suggest that the barrier layer is cation rich ($x > y$) with cation interstitials being the principal defect, but it is not possible to exclude oxygen vacancies, unequivocally, as being the principal defect. If the barrier layer is cation rich, the phase is estimated to have the composition $Cr_{2.028}O_3$ close to the metal/film interface, whereas if it is oxygen deficient the stoichiometry is estimated to be $Cr_2O_{2.981}$ at the same location. The thickness of the barrier layer in the passive region is found to increase linearly with voltage while the passive current density is constant. In the transpassive range ($V > 0.6 V_{she}$), the passive film is found to be a p -type semi conductor, and the thickness of the barrier layer decreases, while log of the passive current increases, with increasing applied potential. These observations are consistent with the predictions of the PDM for passive films on metals and alloys, including the transition from the passive to the transpassive states, which is predicted to coincide with a change in oxidation state of the chromium species

being ejected from the barrier layer from $Cr(III)$ to $Cr(VI)$ and with the oxidative dissolution of the film. The principal defect in the barrier layer in the transpassive state appears to be the $Cr(III)$ cation vacancy, which is generated by the oxidative ejection of cations from the barrier layer. Optimization of the PDM on the impedance data has yielded a set of parameter values for the passive state that can be used in deterministic models for predicting the accumulation of general corrosion damage to Alloy-22 in HLNW repositories.

Key Words: Electrochemical Impedance Spectroscopy, Alloy-22, passivity, high level nuclear waste.

Introduction

As noted elsewhere [1,2], the disposal of High Level Nuclear Waste (HLNW) represents one of the greatest challenges to face humankind, because the horizon over which safe disposal must be assured is twice as far into the future (10,000 years) as recorded human history is in the past. The principal threat to the integrity of the Alloy-22 canisters that are scheduled to contain the waste in the Yucca Mountain, Nevada repository is corrosion, but our empirical experience with the corrosion of Alloy-22 under all conditions is less than two decades or no more than about two thousandths of the design lifetime. Our empirical experience with the corrosion of Alloy-22 under

conditions that are relevant to HLNW disposal is no more than about a fifth of that time (a fraction of 0.0004 of the design life). Thus, empirical methods alone are unlikely to provide the required accuracy of prediction to assure the public of safe disposal and, hence, an alternative strategy must be developed [1]. The strategy that is being developed by the authors of the present work for predicting the accumulation of general [1] and localized [2] corrosion damage to HLNW canisters is determinism, and one such model, the General Corrosion Model (GCM) [1], has been used by one of the authors (DDM) for predicting the accumulation of general corrosion damage to Alloy-22 in Yucca Mountain-type repositories. However, previous predictions using the GCM essentially employed “guesstimates” of values for various parameters and hence the predictions are not expected to accurately simulate what might actually occur in service. The purpose of the present paper is to extract values for various parameters in the GCM by optimization of the Point Defect Model (PDM) [3], which is a component of the GCM, on Electrochemical Impedance Spectroscopic (EIS) data for Alloy-22 in saturated NaCl brine (6.2 *m*), *pH* = 3, at 80 °C that are presented in Part I. We chose EIS as the tool for extracting parameter values, because of its well recognized utility for identifying reaction mechanisms and because it is readily combined with reaction models in optimization procedures to extract desired parameter values [3-8].

As noted in Part I [4], the interpretation of impedance data is normally done at two levels; the formulation of “equivalent electrical circuits (EECs)” [5] and identification of reaction models (mechanisms) [5-11]. The first essentially simulates the electrical properties of the system with little pretense of providing mechanistic or physico-electrochemical information. While the EECs are useful for identifying various

relaxations and for calculating the associated time constants (see Part I), they are not capable of yielding the information that we seek from this study; namely kinetic data for the reactions involved in the system. It is for this reason that we employ a reaction mechanism in the form of the Point Defect Model (PDM) [3], in order to interpret impedance data for Alloy-22 in prototypical HLNW environments.

Point Defect Model

Figure A.1 summarizes the physicochemical processes that are envisioned to occur within the barrier layer of the passive film formed on the Alloy-22, according to the PDM [3]. In this model, which is a truncated version of the more general PDM that also includes the generation and annihilation of cation vacancies [3], it is assumed that the barrier layer on Alloy-22 is a defective chromic oxide of the form $Cr_{2+x}O_{3-y}$. The defect formula indicates that the barrier layer is either cation rich ($x > y$), due to the predominant presence of cation interstitials, or oxygen deficient ($y > x$), due to the predominant presence of oxygen vacancies. In any event, the barrier layer is *n*-type in electronic character, which is consistent with the proposed defect structure (see later). While it has proven to be difficult, if not impossible, to distinguish between the cation rich and oxygen deficient possibilities, the present work suggests that this might be

possible by using glancing X-ray diffraction techniques to ascertain the density of the barrier layer, particularly within the region close to the metal/film interface.

Reaction (1) describes the injection of the metal interstitial, Cr_i^{z+} , into the barrier layer. The chromium interstitial is then transmitted through the barrier layer and ejected into the solution, as described by Reaction (3). Reaction (2) results in the growth of the barrier layer into the bulk Alloy-22 via the generation of oxygen vacancies ($V_o^{\bullet\bullet}$), and Reaction (5) leads to the destruction of the barrier layer by dissolution. Reaction (4) represents the annihilation of oxygen vacancies at the film/solution interface, which are produced by Reaction (2) at the metal/film interface. Note that Reactions (1), (3), and (4) are lattice conservative processes, in that their occurrence does not result in the movement of the corresponding interface with respect to a laboratory frame of reference, while Reactions (2) and (5) are lattice non-conservative processes [3]. A steady state must involve a balance between at least two non-conservative reactions, since only one non-conservative reaction would lead to monotonic growth or thinning of the passive film. Considering our findings that the dominant defects in the barrier layer on Alloy-22 within the passive state must be oxygen vacancies or chromium interstitials, with the latter being most likely, the reactions regarding the consumption (at the metal/film interface) and production (at the film/solution interface) of chromium (III) vacancies are not included in the impedance model. However, as discussed later in this paper, cation vacancies appear to be the dominant defect in the transpassive state.

The rate of change of barrier layer thickness involves two lattice non-conservative reactions, as follows:

$$\frac{dL}{dt} = -\frac{2\Omega}{\chi} J_o - \Omega k_5 C_{H^+}^n \quad (\text{A.1})$$

where the first term on the right hand side corresponds to barrier layer generation at the alloy/film interface [Reaction (2), Figure A.1] and the second term corresponds to the dissolution of the barrier layer at the barrier layer/solution interface. The parameter $\Omega = 14.59 \text{ cm}^3 \text{ mol}^{-1}$ is the molar volume per cation of the barrier layer, $\chi = 3$ is the oxidation state of chromium in the barrier layer in the passive state, J_o is the flux of oxygen vacancies within the barrier layer, C_{H^+} is the hydrogen ion concentration in the solution at the film/solution interface, n is the kinetic order of the film dissolution reaction with respect to C_{H^+} , and k_5 is the rate constant for Reaction (5), Figure A.1. Table 1 displays the functional forms of the rate constants for the five interfacial reactions identified in Figure A.1; the definition of standard rate constants will be given later in this section.

All interfacial reactions that produce or consume electrons contribute to the total current density, which is described as

$$I = F[-\chi J_i^{m/f} - 2J_o^{m/f} - (\Gamma - \chi)J_i^{f/s} + (\Gamma - \chi)k_5 C_{H^+}^n] \quad (\text{A.2})$$

in which $F = 96487 \text{ C/equiv}$ is Faraday's constant, and $\Gamma = 3$ is the oxidation state of chromium in solution in the passive range. At sufficiently high potentials, chromium

may enter the solution in the +6 state (as chromate, CrO_4^{2-}), either by ejection of cation interstitials (Reaction 3, Figure A.1) or by barrier layer dissolution (Reaction 5, Figure A.1), or both. In that case, $\Gamma = 6$.

The fluxes of the point defects in the barrier layer may be written as $J_i = -D_i(\partial C_i / \partial x) - \chi K D_i C_i$ and $J_o = -D_o(\partial C_o / \partial x) - 2K D_o C_o$ for chromium interstitials and oxygen vacancies, respectively, where D and C are the diffusivity and concentration, and subscripts i and o designate chromium interstitials and oxygen vacancies. Additionally, $K = \varepsilon F / RT$, $R = 8.314 \text{ J.mol}^{-1} \text{ K}^{-1}$ is the gas constant, T is the absolute temperature, and ε is the electric field strength, which is considered to be a constant, according to the PDM [3]. The continuity equations $\partial C / \partial t = -\nabla J$ then become

$$\frac{\partial C_i}{\partial t} = D_i \frac{\partial^2 C_i}{\partial x^2} + \chi D_i K \frac{\partial C_i}{\partial x} \quad (\text{A.3})$$

and

$$\frac{\partial C_o}{\partial t} = D_o \frac{\partial^2 C_o}{\partial x^2} + 2D_o K \frac{\partial C_o}{\partial x} \quad (\text{A.4})$$

These equations are then solved for the initial conditions ($t = 0$) of $C_i(x) = C_i^0(x)$ and $C_o(x) = C_o^0(x)$ and for the boundary conditions ($t > 0$) of: $x = 0$ (the film/solution interface), $J_i(0) = -k_3^0 e^{a_3 V} C_i(0)$ (k_3^0 , cm/s), $J_o(0) = -(\chi/2) k_4^0 e^{a_4 V} C_o(0)$ (k_4^0 , cm/s); at $x = L$ (the metal/film interface), $J_i(L) = -k_1^0 e^{a_1 V} e^{-b_1 L}$ (k_1^0 , mol/s/cm^2),

$J_o(L) = -(\chi/2)k_2^0 e^{a_2 V} e^{-b_2 L} (k_2^0, mol/s/cm^2)$. Note that the fluxes of cation interstitials and oxygen vacancies are negative when the species move from the metal/film (m/f) interface to the film/solution (f/s) interface in the coordinate system adopted in Figure A.1.

Combined with the rate constants shown in Table 1, the rate of change of the barrier layer thickness [Equation (A.1)] and the current density [Equation (A.2)] then become

$$\frac{dL}{dt} = -\Omega k_2^0 e^{a_2 V} e^{-b_2 L} - \Omega k_3^0 e^{a_3 V} C_{H^+}^n \quad (A.5)$$

and

$$I = F[\chi k_1^0 e^{a_1 V} e^{-b_1 L} + \chi k_2^0 e^{a_2 V} e^{-b_2 L} + (\Gamma - \chi)k_3^0 e^{a_3 V} C_i(0) + (\Gamma - \chi)k_5^0 e^{a_5 V} C_{H^+}^n] \quad (A.6)$$

where C_{H^+} has units of mol/cm^3 .

Note that the current density [Equation (A.6)] is a function of V , L , and $C_i(0)$.

Accordingly, for any arbitrary changes δV , δL , and $\delta C_i(0)$ we have

$$\delta I = \left(\frac{\partial I}{\partial V} \right)_{L, C_i(0)} \delta V + \left(\frac{\partial I}{\partial L} \right)_{V, C_i(0)} \delta L + \left(\frac{\partial I}{\partial C_i(0)} \right)_{V, L} \delta C_i(0) \quad (A.7)$$

The variations in V , L , and $C_i(0)$ are sinusoidal in an EIS measurement, so that we

write $\delta V = \Delta V e^{j\omega t}$, $\delta L = \Delta L e^{j\omega t}$, and $\delta C_i(0) = \Delta C_i(0) e^{j\omega t}$; note that ΔX is the amplitude

of the variation in X at a frequency $\omega = 0$. From Equation (A.7), the Faradic admittance is then defined as

$$Y_f = \frac{\delta I}{\delta V} = I^V + I^L \frac{\Delta L}{\Delta V} + I^{C_i(0)} \frac{\Delta C_i(0)}{\Delta V} \quad (\text{A.8})$$

where $I^V = (\partial I / \partial V)_{L, C_i(0)}$, $I^L = (\partial I / \partial L)_{V, C_i(0)}$, and $I^{C_i(0)} = (\partial I / \partial C_i(0))_{L, V}$. These differentials will be evaluated later from Equation (A.6).

We now return to Equation (A.5) and determine the response of $\partial L / \partial t$ to δV , δL , and $\delta C_i(0)$ by taking the total differential. Thus, for the relaxation in film thickness:

$d(\delta L) / dt = \Omega k_2^0 a_2 e^{a_2 V} e^{-b_2 L} \delta V - \Omega k_2^0 b_2 e^{a_2 V} e^{-b_2 L} \delta L - \Omega k_5^0 a_5 e^{a_5 V} C_{H^+}^n \delta V$. Considering that

$d(\delta L) / dt = j\omega \Delta L e^{j\omega t}$, we obtain

$$j\omega \Delta L e^{j\omega t} = \Omega(k_2^0 a_2 e^{a_2 V} e^{-b_2 L} - k_5^0 a_5 e^{a_5 V} C_{H^+}^n) \Delta V e^{j\omega t} - \Omega k_2^0 b_2 e^{a_2 V} e^{-b_2 L} \Delta L e^{j\omega t} \quad (\text{A.10})$$

which upon rearrangement yields

$$\frac{\Delta L}{\Delta V} = \frac{\Omega(k_2^0 a_2 e^{a_2 V} e^{-b_2 L} - k_5^0 a_5 e^{a_5 V} C_{H^+}^n)}{\Omega k_2^0 b_2 e^{a_2 V} e^{-b_2 L} + j\omega} \quad \text{or} \quad \frac{\Delta L}{\Delta V} = \frac{\Phi_2}{1 + j\omega \tau_2} \quad (\text{A.11})$$

where

$$\Phi_2 = \left(\frac{a_2}{b_2} \right) - \left(\frac{k_5^0}{k_2^0} \right) \left(\frac{a_5}{b_2} \right) e^{(a_5 - a_2)V} e^{b_2 L} C_{H^+}^n \quad (\text{A.11})$$

and

$$\tau_2 = \frac{1}{\Omega k_2^0 b_2 e^{a_2 V} e^{-b_2 L}} \quad (\text{A.12})$$

For chromium interstitials, the relaxation for $C_i(0)$ is determined through the mass balance at the film/solution interface $dC_i(0)/dt = -k'_3 C_i(0) = -k_3'^0 e^{a_3 V} C_i(0)$ (units of $k_3'^0$ are s^{-1}). The total differential is $d(\delta C_i(0))/dt = -k_3'^0 [a_3 e^{a_3 V} C_i(0) \delta V + e^{a_3 V} \delta C_i(0)]$.

Inserting the sinusoidal variations for δV and $\delta C_i(0)$ therefore yields

$$j\omega \Delta C_i(0) e^{j\omega t} = -k_3'^0 a_3 e^{a_3 V} C_i(0) \Delta V e^{j\omega t} - k_3'^0 e^{a_3 V} \Delta C_i(0) e^{j\omega t} \quad (\text{A.13})$$

and

$$\Delta C_i(0) (j\omega + k_3'^0 e^{a_3 V}) = -k_3'^0 a_3 e^{a_3 V} C_i(0) \Delta V. \quad (\text{A.14})$$

Therefore,

$$\frac{\Delta C_i(0)}{\Delta V} = \frac{-k_3'^0 a_3 e^{a_3 V} C_i(0)}{j\omega + k_3'^0 e^{a_3 V}} = -\frac{a_3 C_i(0)}{1 + j\omega \tau_3} \quad (\text{A.15})$$

in which

$$\tau_3 = \frac{1}{k_3^0 e^{a_3 V}} \quad (\text{A.16})$$

The expression for the Faradaic admittance is finally derived from Equation (A.8) as

$$Y_f = I^V + I^L \frac{\Phi_2}{1 + j\omega\tau_2} - I^{C_i(0)} \frac{a_3 C_i(0)}{1 + j\omega\tau_3} + j\omega C \quad (\text{A.17})$$

in which the parallel geometric capacitance $C = \hat{\varepsilon}\varepsilon_0 / L$ [dielectric constant $\hat{\varepsilon} = 30$ for a passive Cr_2O_3 barrier layer (see later) and vacuum permittivity $\varepsilon_0 = 8.85 \times 10^{-14} \text{ F/cm}$] is taken into consideration, and

$$\begin{aligned} I^V &= \left(\frac{\partial I}{\partial V} \right)_{L, C_i(0)} \\ &= F[a_1 \chi k_1^0 e^{a_1 V} e^{-b_1 L} + a_2 \chi k_2^0 e^{a_2 V} e^{-b_2 L} + a_3 (\Gamma - \chi) k_3^0 e^{a_3 V} C_i(0) + a_5 (\Gamma - \chi) k_5^0 e^{a_5 V} C_{H^+}^n] \end{aligned} \quad (\text{A.18})$$

$$\begin{aligned} I^L &= \left(\frac{\partial I}{\partial L} \right)_{V, C_i(0)} \\ &= F[-b_1 \chi k_1^0 e^{a_1 V} e^{-b_1 L} - b_2 \chi k_2^0 e^{a_2 V} e^{-b_2 L}] = -\chi F[b_1 k_1^0 e^{a_1 V} e^{-b_1 L} + b_2 k_2^0 e^{a_2 V} e^{-b_2 L}] \end{aligned} \quad (\text{A.19})$$

$$I^{C_i(0)} = \left(\frac{\partial I}{\partial C_i(0)} \right)_{V, L} = (\Gamma - \chi) F k_3^0 e^{a_3 V} \quad (\text{A.20})$$

In the above expressions, the parameters that appear on the right side (L and $C_i(0)$) are identified with the steady-state quantities. At steady state, Equation (A.3) and (A.4) become

$$\frac{\partial^2 C_i}{\partial x^2} + \chi K \frac{\partial C_i}{\partial x} = 0 \quad (\text{A.21})$$

$$\frac{\partial^2 C_o}{\partial x^2} + 2K \frac{\partial C_o}{\partial x} = 0 \quad (\text{A.22})$$

the solutions for which are

$$C_i(x) = A_i e^{-\chi K x} + B_i \quad (\text{A.23})$$

$$C_o(x) = A_o e^{-2Kx} + B_o \quad (\text{A.24})$$

The expressions for the fluxes therefore become

$$J_i = -\chi K D_i B_i \quad (\text{A.25})$$

$$J_o = -2K D_o B_o \quad (\text{A.26})$$

From the boundary conditions, the coefficients are obtained as

$$B_i = \frac{k_1^0 e^{a_1 V} e^{-b_1 L}}{\chi K D_i} \quad (\text{A.27})$$

and

$$B_o = \frac{(\chi/2) k_2^0 e^{a_2 V} e^{-b_2 L}}{2 K D_o} \quad (\text{A.28})$$

Because the fluxes for a given species at two interfaces are equal at steady state:

$-k_3^0 e^{a_3 V} C_i(0) = -k_1^0 e^{a_1 V} e^{-b_1 L}$ and $-(\chi/2) k_4^0 e^{a_4 V} C_o(0) = -(\chi/2) k_2^0 e^{a_2 V} e^{-b_2 L}$, the steady-state concentrations for chromium interstitials and oxygen vacancies at the film/solution interface are

$$C_i(0) = \left(\frac{k_1^0}{k_3^0} \right) e^{(a_1 - a_3)V} e^{-b_1 L} \quad (\text{A.29})$$

$$C_o(0) = \left(\frac{k_2^0}{k_4^0} \right) e^{(a_2 - a_4)V} e^{-b_2 L} \quad (\text{A.30})$$

In the case of steady state, Equation (A.1) becomes

$$J_o(L) = -(\chi/2) k_5 C_{H^+}^n \quad (\text{A.31})$$

and from Equations (A.26) and (A.28)

$$-(\chi/2)k_5C_{H^+}^n = -2KD_o \left(\frac{(\chi/2)k_2^0 e^{a_2V} e^{-b_2L}}{2KD_o} \right) \quad (A.32)$$

Therefore, the steady-state barrier layer thickness is

$$L_{ss} = \left(\frac{a_2 - a_5}{b_2} \right) V - \frac{1}{b_2} \ln \left[\left(\frac{k_5^0}{k_2^0} \right) C_{H^+}^n \right] \quad (A.33)$$

The parameters, k_1^0 , k_2^0 , k_3^0 , $k_3'^0$, k_4^0 , k_5^0 , in the above equations and Table 1 are a function of solution pH and are not the standard rate constants for the interfacial reactions, since the PDM defines $k_1^0 = k_1^{00} e^{-\alpha_1 \beta \chi \gamma pH} e^{-\alpha_1 \chi \gamma \phi_{f/s}^0}$, $k_2^0 = k_2^{00} e^{-\alpha_2 \beta \chi \gamma pH} e^{-\alpha_2 \chi \gamma \phi_{f/s}^0}$, $k_3^0 = k_3^{00} e^{\alpha_3 \beta \chi \gamma pH} e^{\alpha_3 \Gamma \gamma \phi_{f/s}^0}$, $k_3'^0 = k_3'^{00} e^{\alpha_3 \beta \chi \gamma pH} e^{\alpha_3 \Gamma \gamma \phi_{f/s}^0}$, $k_4^0 = k_4^{00} e^{2\alpha_4 \beta \gamma pH} e^{2\alpha_4 \gamma \phi_{f/s}^0}$, and $k_5^0 = k_5^{00} e^{\alpha_5 \beta (\Gamma - \chi) \gamma pH} e^{\alpha_5 (\Gamma - \chi) \gamma \phi_{f/s}^0}$, in which α_1 , α_2 , α_3 , α_4 , α_5 are the transfer coefficients, and k_1^{00} , k_2^{00} , k_3^{00} , $k_3'^{00}$, k_4^{00} , k_5^{00} are the standard rate constants. The potential drop across the film/solution (f/s) interface is $\phi_{f/s} = \phi_f - \phi_s = \alpha V + \beta pH + \phi_{f/s}^0$ and that across the metal/film (m/f) interface is $\phi_{m/f} = \phi_m - \phi_s = (1 - \alpha)V - \varepsilon L - \beta pH - \phi_{f/s}^0$, in which $\alpha = d\phi_{f/s} / dV$ is the dependence of the potential drop across the barrier layer/solution interface on the applied voltage, V , [i.e., α is the polarizability of the barrier layer/outer layer (solution) interface];

$\beta = d\phi_{f/s} / dpH$ is the dependence of the potential drop across the same interface on pH ; $\phi_{f/s}^0$ is the value of $\phi_{f/s}$ in the standard state; $\gamma = F / RT$; and $K = \varepsilon\gamma = \varepsilon F / RT$.

Results and Discussion

Mott-Schottky Analysis

The Mott-Schottky relation for an n -type semi conductor is commonly written in the form

$$\frac{1}{C^2} = \frac{2}{\hat{\varepsilon}\varepsilon_0 e N_D} \left(V - V_{fb} - \frac{kT}{e} \right) \quad (\text{A.34})$$

where $\hat{\varepsilon}$ is the dielectric constant of the film, ε_0 is the vacuum permittivity (8.85×10^{-14} F/cm), e is the electronic charge (1.60×10^{-19} C), V is the applied voltage, V_{fb} is the “flat band” potential, N_D is the donor density, and kT/e has a value of about 0.025 V at ambient temperature. This expression is strictly valid only if the space charge capacitance due to the existence of a depletion region within the barrier layer dominates the interphasial capacitance, an issue that is explored further below. Thus, a plot of $1/C^2$ versus V is predicted to be linear with a slope of $2/\hat{\varepsilon}\varepsilon_0 e N_D$, from which the donor density may be

derived, provided the dielectric constant is known. A comparable expression exists for a *p*-type semi conductor, namely

$$\frac{1}{C^2} = \frac{-2}{\hat{\epsilon}\epsilon_0 e N_A} \left(V - V_{fb} - \frac{kT}{e} \right) \quad (\text{A.35})$$

where N_A is the acceptor concentration. In this case, a plot of $1/C^2$ versus V will yield a straight line of slope $-2/\hat{\epsilon}\epsilon_0 e N_A$.

The Mott-Schottky plot shown in Figure A.2, which was constructed from capacitance data measured at 5 kHz, displays two, clearly defined linear regions. That at lower potentials is characteristic of an *n*-type semi conductor, which in turn is consistent with the dominant defects in the film being chromium interstitials and/or oxygen vacancies, as postulated earlier in this paper. The calculated donor density is $6.7 \times 10^{20}/\text{cm}^3$, which is typical of passive films on other metals and alloys (e.g., Ni, stainless steels, W, and Fe) [12-14]. At high voltages, the electronic character of the film changes dramatically and assumes a *p*-type character having an acceptor density that is only slightly lower (by a factor of about 2) than the donor density in the passive region. The most likely explanation for the change in electronic character is the generation of cation vacancies (electronic acceptors and hence *p*-type dopants) at the film/solution interface through the oxidative ejection of cations from the film, a process that can be represented as



We also note, again, that the film undergoes a sharp decrease in thickness over the same voltage range at which the electronic character changes (Figure A.5, see later) and this issue is explored further below.

As noted above, the donor concentration in the passive state, as calculated from the slope of the Mott-Schottky plot, assuming a dielectric constant of 30, is $6.7 \times 10^{20} \text{ cm}^{-3}$. Assuming that the barrier layer is cation rich (due to the presence of cation interstitials), the formula for the barrier layer can be represented as $\text{Cr}_{2.028}\text{O}_3$, where the degree of cation non-stoichiometry is 1.4 %, assuming a molar volume per cation of 14.59 cm^3 . Since the interstitials are (presumably) concentrated in the barrier layer close to the metal/film interface, one would expect the unit cell dimension to be slightly larger at the *m/f* interface than in the outer reaches of the film. On the other hand, if the barrier layer is oxygen deficient, the formula becomes $\text{Cr}_2\text{O}_{2.981}$. In this case, the unit cell dimension close to the *m/f* interface should be slightly lower than that for the stoichiometric oxide. These predictions could be checked by glancing angle X-ray diffraction techniques, but the facilities for doing this were not available to the authors of this paper. If successful, glancing angle X-ray diffraction techniques might provide the first known means of differentiating between cation rich and oxygen deficient barrier oxide layers. Finally, from an electronic viewpoint, the barrier layer is best represented as a *metal- n^+ -i-solution* structure, in which the region close to the metal/film interface is degenerately doped, such that the Fermi level moves above the conduction band (i.e., to higher electron energies).

Optimization of the PDM on Impedance Data

Typical experimental impedance spectra for the passive state on Alloy-22 are shown in Figure A.3, in the form of Nyquist plots, in which the imaginary component of the impedance is plotted against the real component for decreasing frequencies. Also plotted in these figures are impedance data calculated from the model described above, after optimization of the PDM on the experimental data to derive values for the various model parameters. The DataFit software (Version 7.1, www.curvefitting.com) was employed in this work for optimization, in order to obtain values for the transfer coefficients, α_i , and standard rate constants, k_i^{00} , for the i elementary interfacial reactions, the polarizability of the film/solution interface, α , the electric field strength (ϵ), and other parameters as described below. The values for the kinetic order of the dissolution reaction at the film/solution interface with respect to the $[H^+]$, and for β and $\phi_{f/s}^0$ were assumed. The assumption of values for n and β is the result of the fact that we do not have any data upon which the model can be optimized with respect to pH as the independent variable.

Optimization was carried out in two stages. In the first stage, all of the parameters except R_s (resistance of the solution between the specimen and the tip of the reference electrode Luggin probe), n , β and $\phi_{f/s}^0$ were treated as variables and the optimization procedure yielded values for them. For example, the dielectric constant was found to range from 26 to 34, without any systematic dependence on voltage, except that the two largest values of 34 were found at the highest voltages. On the other hand,

Moffat and Latanision [15], in their study of passive chromium, found that the dielectric constant of the Cr_2O_3 passive film increased systematically with increasing voltage when calculated from the XPS-derived thickness using the parallel plate capacitor expression. Likewise, the value for the electric field strength was found to vary from 0.9×10^6 V/cm to 1.9×10^6 V/cm, while that for α ranged from 0.69 to 0.71.

In order to reduce the number of variables, we averaged the values obtained in the first stage of the optimization for the dielectric constant (30), electric field strength (1.4×10^6 V/cm), and α (0.7), and treated these parameters as being constants in the final optimization stage. In performing the optimization, we also assumed that the geometric capacitance of the oxide film (C_g) and the double layer capacitance on the solution side of the film/solution interface (C_{dl}) are connected in series and are in parallel with the Faradaic impedance due to the charge transfer reactions at the interfaces. Both C_g and C_{dl} were initially treated as variables, but the choosing of a dielectric constant in the second stage of the optimization essentially fixed the geometric capacitance (C_g) to a value that is consistent with the film thickness (i.e., $C_g = \epsilon\epsilon_0 / L_{ss}$). Values for the fundamental model parameters for passive Alloy-22 in saturated NaCl brine at 80 °C, $pH = 3$, are presented in Table A.2 and comparisons between the experimental and simulated impedance data are displayed in Figure A.2.

The correlation between experimental impedance data and simulated data is acceptable for the Nyquist plots shown, in most cases, and is similar to that reported in other studies [8-11]. Thus, the impedance model based on the PDM provides a reasonable account of the experimental data, although other models may be equally

successful. In any event, the parameter values obtained by optimization of the model on impedance data that span the entire passive range are found not to depend on voltage in any systematic manner, which, in itself, is a test of the viability of the model. The parameter values have been averaged to yield a single set for passive Alloy-22 (shown in Table A.2, last column). However, in closing, we note that the phase angle Bode plot (not shown) displays significant differences between the experimental and simulated data, especially in the higher frequency range where the impedance is very low. A possible reason is that the phase angle, defined as $\theta = \tan^{-1}(-Z''/Z')$, is a very sensitive function of Z' and Z'' , so that a slight deviation in Z' or Z'' give rise to a large fluctuation in θ .

Steady State Barrier Layer Thickness and Current

The steady state barrier layer thickness and current density were calculated using the “parallel plate” capacitor formula [Equation (A.37)]

$$L_{ss} = \hat{\epsilon}\epsilon_0 / C_g \quad (\text{A.37})$$

and Equation (A.38)

$$I_{ss} = \Gamma F \left[k_1^o e^{a_1 V} e^{-b_1 L_{ss}} e^{c_1 pH} + (1 - \chi / \Gamma) k_5^o e^{a_5 V} e^{c_5 pH} (C_{H^+})^n \right] \quad (\text{A.38})$$

respectively, where C_g (F/cm^2) is the geometric capacitance of the barrier layer and the other parameters are as previously defined. In calculating the steady state thickness of the barrier layer, we assume that the geometric capacitance can be estimated from the imaginary component of the interfacial impedance at very high frequencies. While this is commonly done in studies of this type, we note that an inconsistency arises between Mott-Schottky (M-S) analysis and the film thickness calculation. Thus, assuming that the geometric and space charge capacitances are in parallel and this combination is in series with the double layer capacitance and the faradaic impedance, we see that the total non-faradaic capacitance of the interface is given by $(C_g + C_{sc})^{-1} + C_{dl}^{-1}$. Assuming further that the double layer capacitance is large compared with the space charge capacitance and the geometric capacitance, the non-faradaic capacitance of the interface reduces to $C_g + C_{sc}$. Thus, in performing Mott-Schottky analysis it is assumed that the space charge capacitance dominates, but for calculating the thickness the geometric capacitance is postulated that the geometric capacitance dominates the interfacial capacitance (that is, C_g and C_{sc} are assumed to dominate simultaneously!). Notwithstanding this inconsistency, interfacial capacitance data are used extensively for determining dopant concentration from M-S analysis and for calculating thickness. Both yield reasonable values for the calculated quantities. Pending future resolution of this inconsistency, we have elected to continue, in this paper, the common practice of using high frequency capacitance data to calculate both film thickness and dopant concentration.. Finally, the dielectric constant used in calculating the barrier layer thickness is obtained by the optimization procedure and is listed in Table A.2.

The steady-state current/voltage correlation is divided into two regions; that for $V < 0.6 V_{she}$ in which the current is independent of voltage and that for higher potentials where the current is found to be an increasing function of voltage. This is precisely as is predicted by the Point Defect Model [3], which yields the steady state current in the form of Equation (A.38) for an n-type barrier layer, if we note that in the low potential region, where the current is constant, $\chi = \Gamma (= 3)$, while at higher potentials $\chi (= 3) < \Gamma (= 6)$. Noting that $a_1 = \alpha_1(1 - \alpha)\chi\gamma$, $b_1 = \alpha_1\chi K$, and $a_5 = \alpha_5\alpha(\Gamma - \chi)\gamma$ (Table A.1), we see that the exponent

$$a_1V - b_1L_{ss} = \exp\left[\frac{\alpha_1\alpha_5\alpha}{\alpha_2}(\Gamma - \chi)\gamma V\right] \quad (\text{A.39})$$

in Equation (A.33) is one, so that the current from the transmission of interstitials across the barrier layer is a constant (independent of V), provided that $\Gamma = \chi$. Under these same conditions (passive state and $\Gamma = \chi$), the current due to film dissolution is zero [see Equation (A.38)], so that the passive current is a constant, as observed. On the other hand, in the high potential region, where $\Gamma > \chi$, both terms on the right side of Equation (A.38) become exponentially increasing functions of V . Furthermore, as shown by the Mott-Schottky analysis in this paper, the electronic nature of the transpassive state is p-type, corresponding to the dominant defect being the cation vacancy, as discussed earlier. The current due to transmission of cation vacancies is predicted to be also an exponential function of voltage, in which case the transpassive current density takes the form

$$I_{ss} = be^{a_c V} \quad (\text{A.40})$$

where a_c is the exponent for cation vacancies. A full discussion of the theory for the transpassive state has been given elsewhere [1,16] and is beyond the present paper. Importantly, Equation (A.40) predicts that the current follows Tafel's law as

$$\ln(I_{ss}) = \ln(b) + a_c V \quad (\text{A.41})$$

as observed in Figure A.4. A least squares fit of Equation (A.41) to the data contained in the figure for voltages greater than 0.58 V_{she} yields $a_c = 5.7 \pm 1.0 \text{ V}^{-1}$.

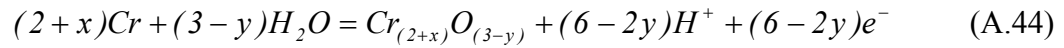
According to the Point Defect Model [3], the steady state thickness of the barrier oxide layer is given by

$$L_{ss} = \frac{1}{\varepsilon} \left[1 - \alpha - \frac{\alpha \alpha_s}{\alpha_2} \left(\frac{\Gamma}{\chi} - 1 \right) \right] V + \frac{1}{\varepsilon} \left[\frac{2.303n}{\alpha_2 \chi \gamma} - \beta - \frac{\alpha_s \beta (\Gamma - \chi)}{\alpha_2 \chi} \right] pH + \frac{1}{\alpha_2 \chi K} \ln \left(\frac{k_2^o}{k_5^o} \right) \quad (\text{A.42})$$

where, with reference to Figure A.1, Γ is the oxidation state of Cr in solution (3 or 6), χ is the oxidation state of chromium in the barrier layer (assumed to be 3), and the other parameters are as previously defined. As proposed elsewhere [3], Equation (A.42) can be written in a compact form as

$$L_{ss} = \frac{1}{\varepsilon} \left[1 - \alpha - \frac{\alpha \alpha_s}{\alpha_2} \left(\frac{\Gamma}{\chi} - 1 \right) \right] (V - E_{bl}^e) \quad (\text{A.43})$$

where E_{bl}^e is the equilibrium potential for the barrier layer formation reaction. This reaction may be written as



which accounts for the possibilities that the barrier layer is cation rich or oxygen deficient, or both. Because of the lack of data on the thermodynamic properties of defective *Cr(III)* oxides, it is not possible to calculate E_{bl}^e in an *a priori* manner. However, in previous work (e.g., that for the formation of the passive film on Zn [3,12]), E_{bl}^e has been found to equal the equilibrium potential for the formation of the stoichiometric oxide (ZnO). Inspection of Figure A.5 shows that the voltage of zero thickness for the barrier layer is $-0.556 V_{she}$ compared with $-0.789 V_{she}$ calculated for the formation of stoichiometric Cr_2O_3 at 80 °C under the prevailing conditions. This difference suggests that the defective barrier layer on Alloy-22 (see below) is considerably less stable thermodynamically than is the stoichiometric oxide. On the other hand, it may be argued that the thickness data plotted in Figure A.5 contain a systematic error, because of the use of the parallel plate capacitor expression or because of the use of an inappropriate value for the dielectric constant. If this were the case, the thickness versus voltage correlation for potentials lower than $0.6 V_{she}$ should be displaced upward

by 0.37 nm, in order for the potential of zero thickness to agree with the calculated equilibrium voltage for Cr_2O_3/Cr . Indeed, as previously noted [3], such a procedure may be used to internally calibrate passive film thickness measurements.

Finally, for the passive range, we note that a least squares fit of the derived L_{ss} [Equation (A.37)] on voltage yields an anodizing constant of $\partial L_{ss} / \partial V = 1.6 \text{ nm/V}$ compared with 2.1 nm/V calculated from Equation (A.43) using the values of α and ε listed in Table A.2. The latter value is characteristic of passive films for a large number of systems, which display $\partial L_{ss} / \partial V$ values ranging from 1.9 to 2.4 nm/V. This would suggest that the derived L_{ss} values are only semi-quantitative at best, which would not be surprising in light of the fact that they were calculated in the optimization algorithm using the parallel plate capacitor approximation. However, we note that Moffat and Latanision [15], using *ex situ* XPS measurements of passive film thickness on chromium in 1 M H_2SO_4 , found an anodizing constant of 1.5 nm/V, which is in good agreement with the value obtained in this study for passive Alloy-22

From Equation (A.42) or (A.43) we see that if, at some voltage, the oxidation state of the metal species being ejected from the barrier layer increases (e.g., from 3 to 6, in the case of a Cr_2O_3 barrier layer), the steady state thickness of the barrier layer is predicted to undergo a concomitant decrease with increasing voltage ($\partial L_{ss} / \partial V = -4.37 \text{ nm/V}$, as determined by a least squares fit of the thickness data shown in Figure A.4). This explanation of the existence of the transpassive state was presented previously [1,16] and it appears to be a general phenomenon; that is, the transpassive state is induced by the oxidative emission of cations from, *and* by the oxidative

dissolution of, the barrier later, with the latter resulting in a decrease in the barrier layer thickness as the voltage is increased [see Equation (A.41), with $\Gamma > \chi$]. The oxidative emission of cations accounts for the change in electronic type (n-type to p-type, in the case of Alloy-22) and both cation emission and oxidative dissolution account for the sharp increase in the current as the potential is made more positive [cf. Equation (A.38) with $\Gamma > \chi$].

Summary and Conclusions

Development of deterministic models for predicting the accumulation of corrosion damage to High Level Nuclear Waste (HLNW) canisters requires the acquisition of values for various model parameters. In the present work, we describe the extraction of values for various parameters in the Point Defect Model (PDM) for the growth of passive films on Alloy-22 from electrochemical impedance data for this alloy measured in saturated NaCl brine (6.2 m, $pH = 3$) at 80 °C, as described in Part I. The principal findings of this study are as follows:

- The passive film on Alloy-22 in the passive region ($V < 0.6 V_{she}$) is postulated to be defective chromic oxide and is found to be *n*-type in electronic character. Current evidence suggests that it is cation rich with cation interstitials being the

principal defect, but it is not possible to exclude, unequivocally, oxygen vacancies as being the dominant defect; in any event, oxygen vacancies are always present in the barrier layer at a level that is commensurate with the rate of growth of the barrier layer into the substrate alloy.

- If the barrier layer is cation rich, the phase is estimated to have the composition $Cr_{2.028}O_3$ close to the metal/film interface, whereas if it is oxygen deficient the stoichiometry is estimated to be $Cr_2O_{2.981}$ at the same location.
- The thickness of the barrier layer in the passive region is found to increase linearly with voltage, while the passive current density is constant.
- In the transpassive range ($V > 0.6 V_{she}$), the passive film is found to be a *p*-type semi conductor, possibly due to the generation of cation vacancies via the oxidative ejection of $Cr(VI)$ species from the barrier layer, thereby generating excess cation vacancies. The thickness of the barrier layer is found to decrease with voltage, while \log (passive current density) increases linearly with the applied voltage.
- Optimization of the PDM on the impedance data for the passive state has yielded a set of parameter values that can be used in deterministic models for predicting the accumulation of general corrosion damage on Alloy-22 in contact with saturated NaCl brine at 80 °C..

The experimental observations summarized above are consistent with the predictions of the PDM for passive films on metals and alloys, including that for the transition from the passive to the transpassive states.

References

1. D. D. Macdonald, "The Holy Grail: Deterministic Prediction of Corrosion Damage Thousands of Years into the Future", in Prediction of Long Term Corrosion Behaviour in Nuclear Waste Systems (Ed. D. Ferron and D. D. Macdonald), Europ. Corros. Fed. Publ. No. 36, p. 75 (2003).
2. D. D. Macdonald, G. R. Engelhardt, P. Jayaweera, N. Priyantha, and A. Davydov, "The Deterministic Prediction of Localized Corrosion Damage to Alloy-22 HLNW Canisters", in Prediction of Long Term Corrosion Behaviour in Nuclear Waste Systems (Ed. D. Ferron and D. D. Macdonald), Europ. Corros. Fed. Publ. No. 36, p. 103 (2003).
3. D. D. Macdonald, Pure Appl. Chem., **71**, 951 (1999).
4. N. Priyantha, P. Jayaweera, D. D. Macdonald, and A. Sun, "An Electrochemical Impedance Study of Alloy-22 in NaCl Brine at Elevated Temperature: I. Measurement of the Impedance", J. Electroanal. Chem., preceding paper (2004).
5. J. R. Macdonald, Impedance Spectroscopy, Wiley, N.Y., 1987.
6. D. D. Macdonald, D. D. and M.C.H. McKubre. "Impedance Measurements in Electrochemical Systems". Chapter 2 in Modern Aspects of Electrochemistry. 14: 61(1982). Edited by J. O'M. Bockris, B. E. Conway, and Ralph E. White. Plenum Press, NY.

7. C. Gabrielli, "Identification of Electrochemical Processes by Frequency Response Analysis", Technical Report Number 004/83, Solartron Instruments, Farnborough, UK, 1980.
8. D. D. Macdonald, S. Real, S. I. Smedley and M. Urquidi-Macdonald. *J. Electrochem. Soc.*, **135**, 2410 (1988).
9. D. D. Macdonald, D. D. and S. I. Smedley, *Electrochim. Acta*, **35**, 1949 (1990).
10. I. Betova, M. Bojinov, T. Latinen, K. Makela, P. Pohjanne, and T. Saario, *Corros. Sci.*, **44**, 2675 (2002).
11. I. Betova, M. Bojinov, and T. Tzvetkoff, *Electrochim. Acta*, **49**, 2295 (2004).
12. K. Ismail, E. Sikora, and D. D. Macdonald, *J. Electrochem. Soc.*, **145**, 3141 (1998).
13. E. Sikora and D. D. Macdonald, *J. Electrochem. Soc.*, **147**, 4087 (2000).
14. J. Liu and D. D. Macdonald, *J. Electrochem. Soc.*, **148**, B425 (2001).
15. T. P. Moffat and R. M. Latanision, *J. Electrochem. Soc.*, **139**, 1869 (1992).
16. D. D. Macdonald, "Theory of the Transpassive State", H. H. Uhlig Award Address, The Electrochemical Society Fall Meeting, San Francisco, CA, September 2 – 7, 2001.

Acknowledgments

The authors gratefully acknowledge the measurement of the data used in this work by SRI International under Department of Energy, Nuclear Energy Research Initiative, Contract No. DE-FG03-99SG21884. DDM gratefully acknowledges partial support of this work by DOE's Yucca Mountain Project under Subcontract A20257JG1S via Innovation Design Technology Inc.

Tables

Table A.1. Rate constants $k_i = k_i^0 e^{a_i V} e^{-b_i L}$ for five interfacial reactions in terms of the Point Defect Model.

| Reaction | a_i (V^{-1}) | b_i (cm^{-1}) | Units of k_i^0 |
|---|---------------------------------------|------------------------|--------------------------------|
| (1) $Cr \xrightarrow{k_2} Cr_i^{\chi+} + v_{Cr} + \chi e'$ | $\alpha_1(1-\alpha)\chi\gamma$ | $\alpha_1\chi K$ | $\frac{mol}{cm^2 s}$ |
| (2) $Cr \xrightarrow{k_3} Cr_{Cr} + \frac{\chi}{2} V_{\ddot{O}} + \chi e'$ | $\alpha_2(1-\alpha)\chi\gamma$ | $\alpha_2\chi K$ | $\frac{mol}{cm^2 s}$ |
| (3) $Cr_i^{\chi+} \xrightarrow{k_5} Cr^{\Gamma+} + (\Gamma - \chi)e'$ | $\alpha_3\alpha\Gamma\gamma$ | 0 | $\frac{cm}{s}$ |
| (4) $V_{\ddot{O}} + H_2O \xrightarrow{k_6} O_O + 2H^+$ | $2\alpha_4\alpha\gamma$ | 0 | $\frac{cm}{s}$ |
| (5) $CrO_{\chi/2} + \chi H^+ \xrightarrow{k_7} Cr^{\Gamma+} + \frac{\chi}{2} H_2O + (\Gamma - \chi)e'$ | $\alpha_5\alpha(\Gamma - \chi)\gamma$ | 0 | $\frac{mol^{0.4}}{cm^{0.2} s}$ |

Table A.2. Parameter values from optimization of the Point Defect Model on the experimental impedance data for Alloy-22 in deaerated, saturated NaCl (6.2 m, $pH = 3$) solution at 80 °C as a function of applied potential.

| V vs.SHE | -0.002 | 0.098 | 0.198 | 0.398 | 0.498 | 0.598 |
|------------------------|----------|----------|----------|----------|----------|----------|
| R_s | 0.1 | 0.1 | 0.1 | 0.1 | 0.1 | 0.1 |
| C_{dl} | 3.36E-05 | 3.59E-05 | 3.11E-05 | 3.66E-05 | 4.28E-05 | 3.92E-05 |
| ε | 1.4E6 | 1.4E6 | 1.4E6 | 1.4E6 | 1.4E6 | 1.4E6 |
| ε^{\wedge} | 30 | 30 | 30 | 30 | 30 | 30 |
| k_{100} | 1.66E-13 | 9.15E-14 | 1.22E-13 | 1.17E-13 | 1.24E-13 | 1.12E-13 |
| k_{200} | 5.44E-15 | 5.79E-15 | 6.69E-15 | 5.07E-15 | 5.51E-15 | 4.90E-15 |
| k_{500} | 1.14E-09 | 1.91E-09 | 1.29E-09 | 1.35E-09 | 1.60E-09 | 1.63E-09 |
| α | 0.7 | 0.7 | 0.7 | 0.7 | 0.7 | 0.7 |
| α_1 | 0.213 | 0.186 | 0.154 | 0.118 | 0.112 | 0.102 |
| α_2 | 0.185 | 0.191 | 0.120 | 0.126 | 0.123 | 0.121 |
| n | 0.6 | 0.6 | 0.6 | 0.6 | 0.6 | 0.6 |
| β | -0.005 | -0.005 | -0.005 | -0.005 | -0.005 | -0.005 |
| ϕ^0 | -0.1 | -0.1 | -0.1 | -0.1 | -0.1 | -0.1 |
| Ω | 14.59 | 14.59 | 14.59 | 14.59 | 14.59 | 14.59 |
| $L_{ss}(cm)$ | 8.64E-08 | 9.63E-08 | 1.3E-07 | 1.42E-07 | 1.68E-07 | 1.83E-07 |
| $I_{ss}(A/cm^2)$ | 4.33E-08 | 3.36E-08 | 3.33E-08 | 5.33E-08 | 5.18E-08 | 8.82E-08 |

| | Mean (\pm Standard Deviation) | Origin |
|------------------------|-------------------------------------|---|
| R_s | 0.1 | Assumed |
| C_{dl} | (3.65 \pm 0.38)E-05 | Second stage optim. |
| ε | 1.4E6 | First stage optim. |
| ε^{\wedge} | 30 | First stage optim. |
| k_{100} | (1.22 \pm 0.22)E-13 | Second stage optim. |
| k_{200} | (5.57 \pm 0.58)E-15 | Second stage optim. |
| k_{500} | (1.49 \pm 0.26)E-09 | Second stage optim. |
| α | 0.7 | First stage optim. |
| α_1 | 0.148 \pm 0.041 | Second stage optim. |
| α_2 | 0.144 \pm 0.031 | Second stage optim. |
| n | 0.6 | First stage optim. |
| β | -0.005 | Assumed |
| ϕ^0 | -0.1 | First stage optim. |
| Ω | 14.59 | Calculated for Cr ₂ O ₃ |

List of Figures

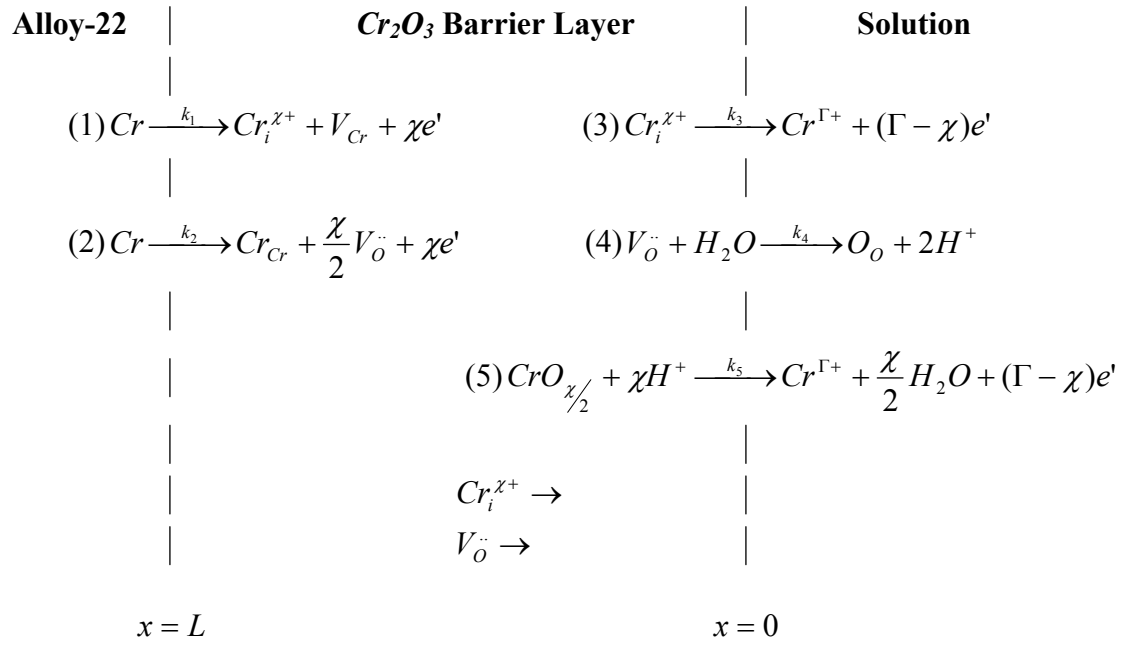
Figure A.1. Schematic of physicochemical processes that are envisioned to occur within the barrier oxide (Cr_2O_3) layer on passive Alloy-22, according to the truncated Point Defect Model. $Cr \equiv$ chromium atom; $Cr_i^{z+} \equiv$ interstitial chromium cation; $V_{Cr} \equiv$ chromium vacancy in the C-22; $Cr_{Cr} \equiv$ chromium cation in a normal cation position; $Cr^{\Gamma+} \equiv$ chromium cation in the solution phase; $V_O^{\cdot\cdot} \equiv$ oxygen vacancy; $O_O \equiv$ oxygen ion in an anion site.

Figure A.2. Mott-Schottky plot for passive C-22 in saturated NaCl (6.2 m) at 80 °C, pH = 3. Note the specific capacitance was measured in the ascending and descending voltage directions. Note further that the barrier layer in the passive state is *n*-type in electronic character, but at high potentials in the transpassive state the film becomes *p*-type in character.

Figure A.3. Nyquist impedance diagrams for Alloy-22 in deaerated, saturated NaCl (6.2 m, pH = 3) solution at 80 °C and as a function of potential in the passive state, showing a comparison between the experimental and simulated data.

Figure A.4. Plot of steady state current versus voltage for Alloy-22 in saturated NaCl (6.2 m, pH = 3) at 80 °C, as determined experimentally at ascending and descending voltages and as calculated from the optimized parameters listed in Table A.2.

Figure A.5. Plot of steady-state barrier layer thickness versus voltage for Alloy-22 in saturated NaCl (6.2 m, $pH = 3$) at 80 °C, as determined from the measured capacitance using the parallel plate condenser model.

**Figure A.1.**

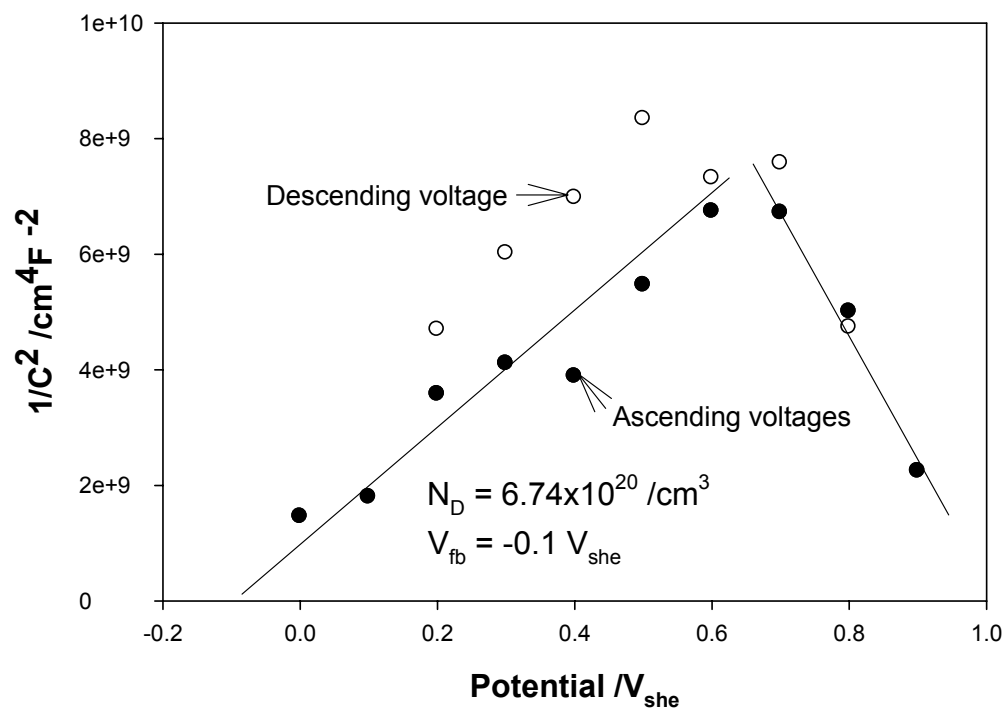
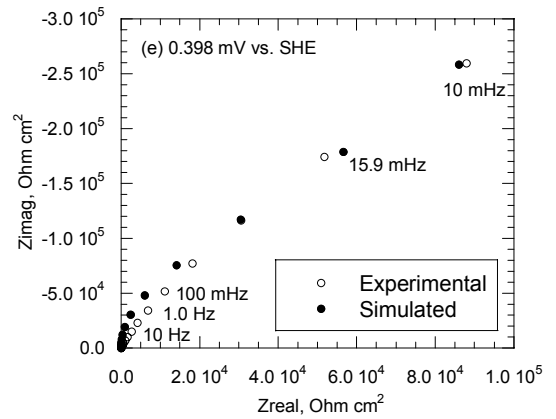
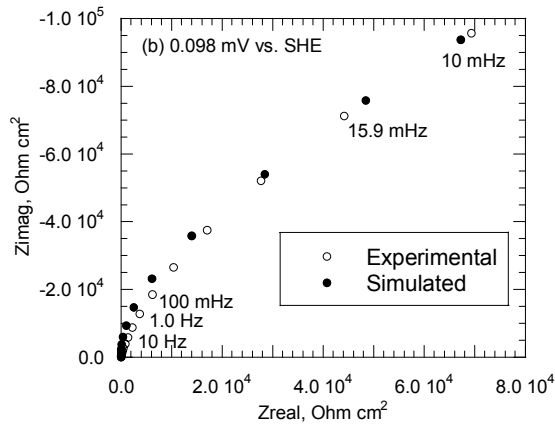
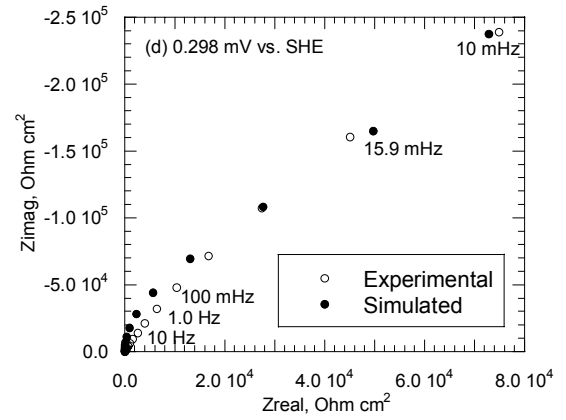
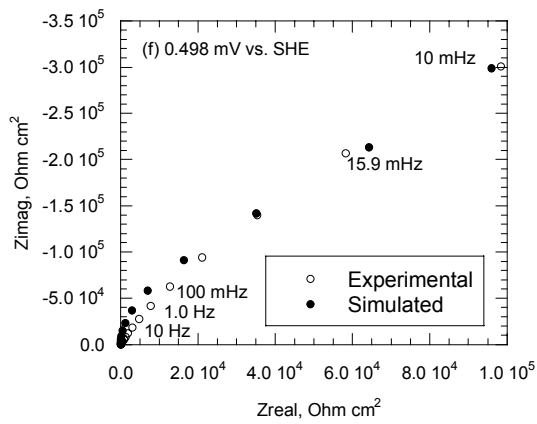
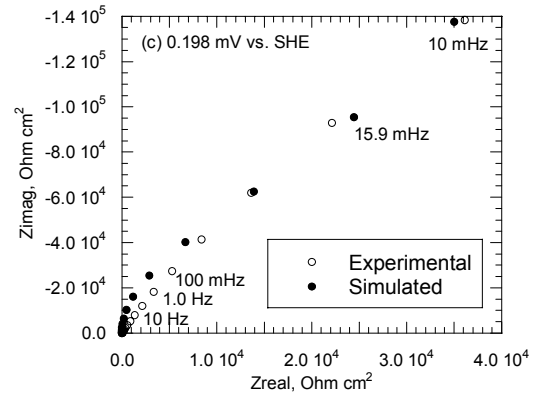
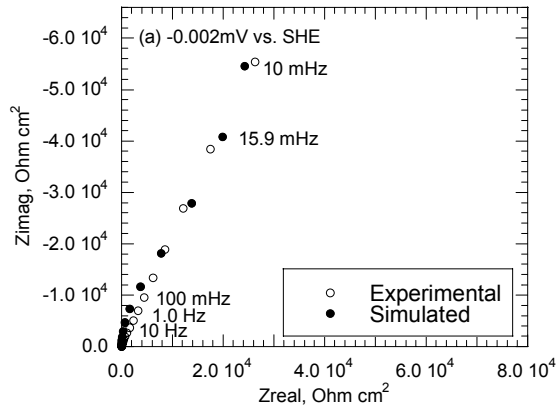
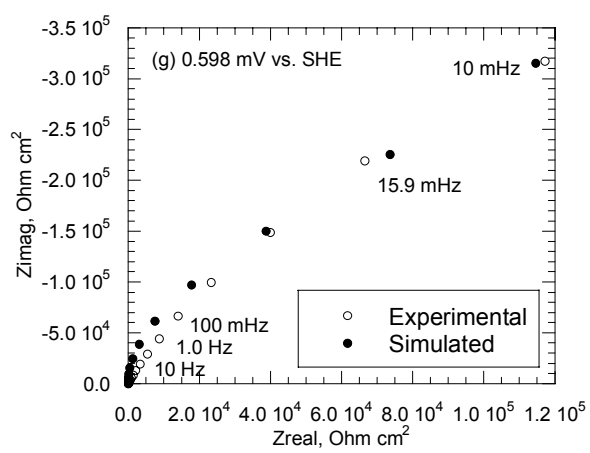


Figure A.2.



**Figure A.3.**

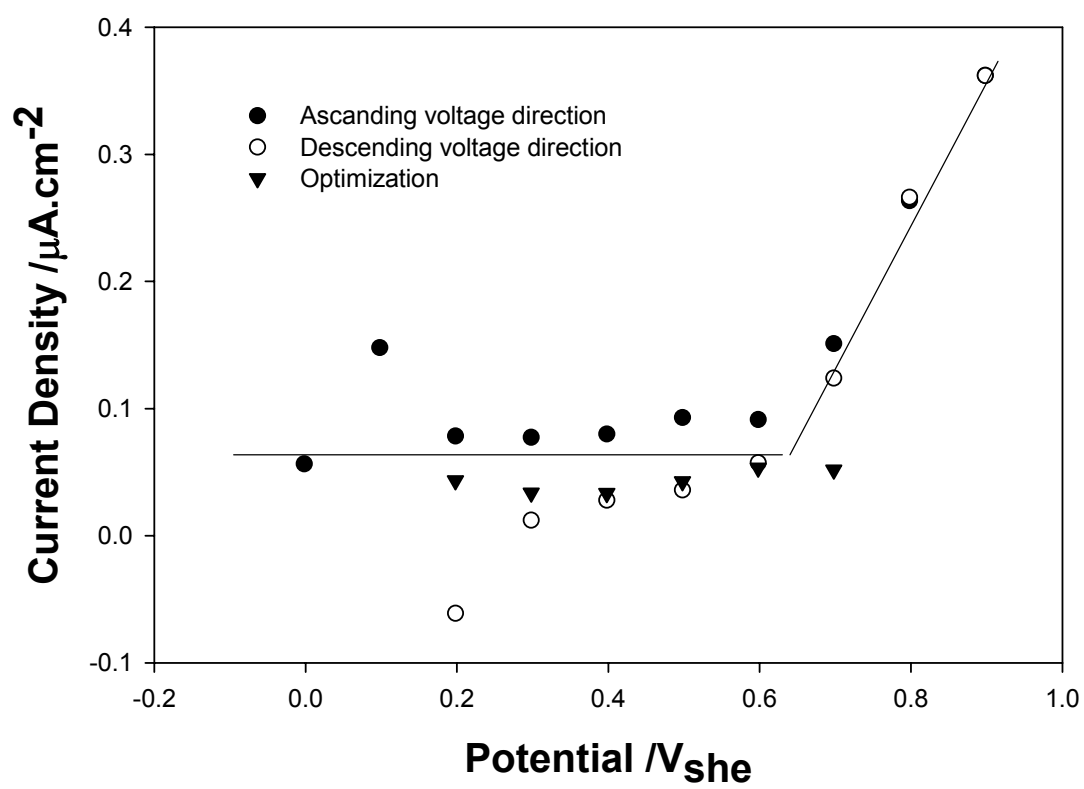


Figure A.4.

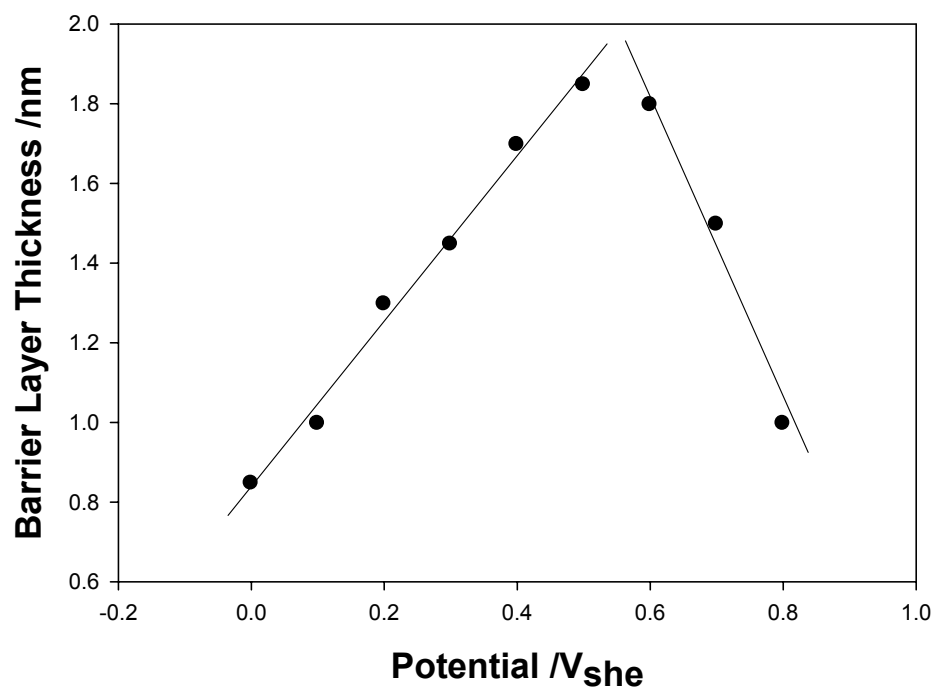


Figure A.5.

Appendix B

General Corrosion of Alloy 22: Experimental Determination of Model Parameters from Electrochemical Impedance Spectroscopy Data

L. Glen McMillion, Adan Sun, Digby D. Macdonald and D.A. Jones

Abstract

Models used to predict general corrosion of Alloy 22 for High Level Nuclear Waste (HLNW) containers must be deterministic, relying upon time-invariant natural laws, because of long time scales. Such models for corrosion damage accumulation prediction require experimental data to determine model parameters. Electrochemical Impedance Spectroscopy (EIS) data were collected in deaerated 4 M NaCl, pH 6 solutions at 30° and 60° C. “Steady state” passive current density and EIS data were measured under potentiostatic conditions at several steps over the passive potential range for Alloy 22. Fresh electrolyte was continuously flowed through test cells allowing test specimens to remain undisturbed for up to six weeks during data collection. Optimization of the Point Defect Model (PDM) for growth and breakdown of passive films on the impedance data has yielded parameters that can be used for predicting general corrosion damage to Alloy 22 in HLNW repositories.

I. INTRODUCTION

The regulatory life of the proposed Yucca Mountain High Level Nuclear Waste (HLNW) repository is 10,000 years. During this time the primary engineered barrier that is to prevent release of radioactive material into the environment is proposed to be a corrosion-resistant material (CRM) outer shell covering the Waste Package (WP) container. The current selection for the CRM is Alloy 22 (UNS N06022), a Ni-Cr-Mo-W-Fe alloy. Alloy 22 forms a defective chromic oxide passive film which results in excellent corrosion resistance under oxidizing conditions; the presence of molybdenum in Alloy 22 results in corrosion resistance in reducing environments.

Yucca Mountain is composed of fractured volcanic tuff and rhyolite. The fractured nature of the mountain results in the air in the repository drifts being in equilibrium with the external atmospheric pressure. Considering the different ground waters present (well water, perched water, pore water), the conditions are such that relatively concentrated aerated brine solutions of near-neutral to basic pH and a wide range of ionic compositions may be present on the WP containers resulting in a variety of corrosive environments[1].

Because of the need to isolate high-level nuclear waste for up to 10,000 years, and the very low corrosion rates of Alloy 22 and other candidate CRM's, WP container integrity in the face of general and localized corrosion must be assured on the basis of model predictions as well as direct measurement of corrosion rates. Because Alloy 22 and other CRM's display extremely low corrosion rates, empirical measurement of corrosion rates by weight loss may be subject to large experimental uncertainty because

of relatively short test periods. For example, one two-year test found the corrosion rate of Alloy 22 to be 0.01 micron per year [1]. These models should be deterministic, relying upon time- and space-invariant natural laws in order to yield accurate predictions over the very long time scale of the regulatory life of the repository. To accurately predict corrosion of all kinds DOE has developed the General Corrosion Model (GCM), which will be used as part of the regulatory task of designing the WP container and drip shield. As part of the General Corrosion Model (GCM) for overall corrosion performance prediction modeling, the Point Defect Model (PDM) of passive film growth and breakdown on metals, developed by D.D. Macdonald [2,3], may be used to model anodic processes.

II. POINT DEFECT MODEL

The PDM describes passive film processes using fundamental chemical reactions and physicochemical properties of the metal-film-solution interface. Reaction rate constants and other model parameters are determined from experimental data by optimizing the data on the PDM using a nonlinear least squares curve fit. Experimental data required for the derivation of PDM parameters are electrochemical impedance spectroscopy (EIS) data and the applied potential, temperature, chloride concentration, and pH under which the data were collected.

Five physicochemical processes occurring within the barrier layer (passive film), which form the basis of the PDM for Alloy 22, are summarized in Figure B.1. It is assumed that the barrier layer is a defective chromic oxide of the form $\text{Cr}_{2+x}\text{O}_{3-y}$ and having the stoichiometric formula Cr_2O_3 . The barrier layer is an n-type semiconductor [4] and the defect formula indicates it is either cation-rich due to cation interstitials, or oxygen deficient due to the presence of oxygen vacancies, or both.

In Figure 1, Reaction 1 describes the injection of chromium cation interstitials into the barrier layer. Reaction 3 describes transmission of chromium interstitials through the barrier layer and their subsequent ejection into the solution. Reaction 2 describes growth of the barrier layer into the bulk Alloy 22 by generation of oxygen vacancies and chromium cations in normal lattice positions. Reaction 4 describes consumption of oxygen vacancies at the solution/barrier interface, and Reaction 5 describes destruction of the barrier layer by dissolution.

The oxidation state of chromium in the barrier layer is $\chi = 3$ and the oxidation state of chromium ions in solution is $\Gamma = 3$. Cr is chromium metal atom, $\text{Cr}_i^{\chi+}$ is interstitial chromium ion, Cr_{Cr} is chromium ion in normal lattice position, $\text{Cr}^{\Gamma+}$ is chromium ion in solution, V_{Cr} is chromium vacancy, V_{o} is oxygen vacancy.

Reactions 1, 3, and 4 are lattice-conservative in that they do not result in movement of the barrier layer interface with respect to the laboratory reference frame. Reactions 2 and 5 are lattice non-conservative and result in growth or thinning of the barrier layer; rate of change of the barrier layer thickness is described in terms of the two lattice non-conservative reactions, as follows [4]:

$$\frac{dL}{dt} = -\frac{2\Omega}{\chi} J_o - \Omega k_5 C_{H^+}^n \quad (\text{B.1})$$

in which Ω is the molar volume per cation of the barrier layer ($CrO_{\chi/2}$), $\chi=3$ is the oxidation state of the cation in the barrier layer, $\Gamma=3$ is the oxidation state of the cation in the outer layer/solution, J_o is the flux for oxygen vacancies within the barrier layer from the metal/barrier layer interface, where they are generated, to the barrier layer/solution interface where they are annihilated, C_{H^+} is the hydrogen ion concentration in the solution at the barrier layer/solution interface, n is the kinetic order of the film dissolution reaction with respect to C_{H^+} , and k_5 is the rate constant for Reaction (5), Figure 1.

All interfacial reactions that produce or consume electrons contribute to the total current density, which is described as

$$j = F[-\chi J_i^{m|f} - 2J_o^{m|f} - (\Gamma - \chi)J_i^{f|s} + (\Gamma - \chi)k_5 c_{H^+}^n] \quad (\text{B.2})$$

in which $F = 96487 \text{ C mol}^{-1}$ is Faraday's constant, and $\Gamma=3$ is the oxidation state of chromium in solution in the passive range. Tables 1 and 2 display the rate constants for the five interfacial reactions; in these expressions, The potential drop across the barrier layer/solution (f|s) interface is $\phi_{f|s} = \phi_f - \phi_s = \alpha V + \beta pH + \phi_{f|s}^0$ and that across the metal/barrier layer (m|f) interface is $\phi_{m|f} = \phi_m - \phi_s = (1 - \alpha)V - \varepsilon L - \beta pH - \phi_{f|s}^0$, in which $\alpha = d\phi_{f|s} / dV$ is the dependence of the potential drop across the barrier layer/solution interface on the applied voltage, V , (i.e., α is the polarizability of the

barrier layer|solution interface); $\beta = d\phi_{f|s} / dpH$ is the dependence of the potential drop across the same interface on pH; $\phi_{f|s}^0$ is the value of $\phi_{f|s}$ in the standard state; $\gamma = F / RT$; and $K = \varepsilon\gamma = \varepsilon F / RT$, and α_j and k_j^0 are the transfer coefficient and the standard rate constant, respectively, for the j^{th} reaction shown in Figure 1.

As Macdonald et al [4] stated that the fluxes of oxygen vacancies and cation interstitials within the barrier layer from the metal/barrier layer interface, may be written as

$$J_o(L) = -(\chi/2)k_2^0 e^{a_2 V} e^{-b_2 L} \quad (k_2^0, \text{mol s}^{-1} \text{cm}^{-2}) \quad (\text{B.3})$$

$$J_i(L) = -k_1^0 e^{a_1 V} e^{-b_1 L} \quad (k_1^0, \text{mol s}^{-1} \text{cm}^{-2}) \quad (\text{B.4})$$

$$J_i(0) = -k_3^0 e^{a_3 V} c_i(0) \quad (k_3^0, \text{cm/s}) \quad (\text{B.5})$$

where L the interface in the metal/barrier layer.

Combined with the rate constants shown in Table B.1, the rate of change of the barrier layer thickness (Equation (B.1)) and the current density (Equation (B.2)) then become

$$\frac{dL}{dt} = \Omega k_2^0 e^{a_2 V} e^{-b_2 L} - \Omega k_5^0 e^{a_5 V} c_{H^+}^n \quad (\text{B.6})$$

$$j = F[\chi k_1^0 e^{a_1 V} e^{-b_1 L} + \chi k_2^0 e^{a_2 V} e^{-b_2 L} + (\Gamma - \chi)k_3^0 e^{a_3 V} c_i(0) + (\Gamma - \chi)k_5^0 e^{a_5 V} c_{H^+}^n] \quad (\text{B.7})$$

Note that the current density (Equation (B.6)) is a function of V , L , and $c_i(0)$.

Accordingly, for any arbitrary changes δV , δL , and $\delta c_i(0)$ we have

$$\delta j = \left(\frac{\partial j}{\partial V} \right)_{L, c_i(0)} \delta V + \left(\frac{\partial j}{\partial L} \right)_{V, c_i(0)} \delta L + \left(\frac{\partial j}{\partial c_i(0)} \right)_{V, L} \delta c_i(0) \quad (\text{B.8})$$

The variations in V , L , and $c_i(0)$ are sinusoidal in an EIS measurement, so that we write $\delta V = \Delta V e^{j\omega t}$, $\delta L = \Delta L e^{j\omega t}$, and $\delta c_i(0) = \Delta c_i(0) e^{j\omega t}$; note that ΔX is the amplitude of the variation in X at a frequency $\omega = 0$. From Equation (B.7), the Faradic admittance is then defined as

$$Y_f = \frac{\delta j}{\delta V} = j^V + j^L \frac{\Delta L}{\Delta V} + j^{c_i(0)} \frac{\Delta c_i(0)}{\Delta V} \quad (\text{B.9})$$

where $j^V = (\partial j / \partial V)_{L, c_i(0)}$, $j^L = (\partial j / \partial L)_{V, c_i(0)}$, and $j^{c_i(0)} = (\partial j / \partial c_i(0))_{V, L}$.

Details of the derivation of the expression for the impedance of a passive interface are given elsewhere [4].

III. EXPERIMENTAL

A. Quality Assurance

All experimental work reported here was performed under control of the University and Community College System of Nevada (UCCSN) Quality Assurance Program, which is approved by the U.S. Department of Energy Office of Civilian Radioactive Waste Management (OCRWM) Yucca Mountain Project (YMP).

B. Materials

Specimens used for electrochemical testing were cut from Hastelloy C-22 plate stock obtained from Haynes International. The plate stock is from heat number 2277-1-3148 and was found to conform to the requirements of ASTM B 575 99a for Alloy N06022. All specimens used in this work were in the as-received, mill annealed condition; no further heat treatment was performed.

The Alloy 22 working electrode specimens are ½-inch diameter by 10 mm long right cylinders mounted in epoxy. The specimens are mounted so that only one flat circular face of 1.267 cm² area is exposed to the electrolyte and the rest of the surface area is covered by epoxy. Electrical connection to the working electrode is a 12 AWG copper wire threaded into the opposite flat circular face. The copper wire is protected from the electrolyte by a ¼-inch O.D. x 8-inch long glass tube, the end of which is also embedded in the epoxy cast to protect the threaded joint from electrolyte. The specimen is mounted such that when installed in the test cell the exposed face is vertically oriented.

Specimens used for anodic cyclic polarization measurements were wet-polished with 240 grit followed by 600 grit SiC paper according to ASTM standard methods [5,6]. Specimens used for passive current density and EIS measurements were polished to a 0.05 µm mirror finish. The sequence used was to wet polish using 240 grit, 400 grit and 600 grit SiC papers followed by polishing on a lapping wheel using 1 µm, 0.3 µm and 0.05 µm Al₂O₃ aqueous suspensions followed by 20 minutes in an ultrasonic cleaning

bath. All specimens were wet-polished and not allowed to dry at any time between beginning the polishing process and being mounted in the test cell.

Electrolyte was prepared using deionized water of 12 M Ω /cm resistivity, A.C.S. Reagent Grade chemicals, Class A volumetric flasks and pipettes conforming to ASTM standards [7], and an NIST-traceable calibrated balance.

Electrolyte was 4 molar sodium chloride buffered to pH 6 using a sodium acetate/acetic acid buffer system. The buffer system was a 40:1 molar ratio of sodium acetate to acetic acid. The total acetate concentration was 6.83×10^{-3} molar.

C. Apparatus and Instrumentation

Because Alloy 22 displays nanoampere-level passive current densities and because these tests are designed to run continuously for times up to 2,000 hours, a number of special features have been incorporated into the experimental apparatus to increase accuracy of the experimental data.

Fresh electrolyte was continuously flowed through the test cells to prevent accumulation of corrosion reaction products and to prevent changes in electrolyte pH and chemical composition from occurring during the course of the tests. Electrolyte was discarded after one pass through the system.

Each test cell is constructed with the Alloy 22 working electrode (WE) and a platinum counter electrode (CE) housed in separate compartments separated by an ultra fine (0.9-1.4 μm) porous ceramic frit. This allows electrolytic conductivity between the

electrodes but largely prevents chemical species produced at the counter electrode from moving to the working electrode where they could be electrochemically oxidized resulting in an error in the measured passive current density. The risk of species migrating from counter electrode to working electrode is further reduced by providing independent electrolyte inlets and outlets to the counter electrode and working electrode compartments. Flow rates and electrode compartment volumes are such that the residence time for electrolyte in the counter electrode compartment is about 60 minutes (30 mL volume with 0.5 mL/min flow rate) and residence time in the working electrode compartment is about 300 minutes (1440 mL volume with 4 mL/min flow rate).

Figure B.2 is a schematic of the test cell. The cell is constructed of a 2 L reaction flask with a Teflon top that has been machined to accommodate nylon compression fittings with Viton O-rings to seal all of the penetrations. Not shown in the schematic is the glass thermowell and thermocouple and the fitting for the working electrode compartment vapor condenser.

The reference electrodes (RE) are Ag/AgCl with 4M KCl filling solution. Data presented in this work are as potential versus Ag/AgCl/4M KCl with the reference element at the test temperature and have not been corrected to the Standard Hydrogen Electrode (SHE) scale. Reference electrode elements were made by thermal decomposition of silver oxide/silver chlorate paste on silver wire after Ives and Janz [8]. The Ag/AgCl reference electrode is placed inside a Luggin probe tube which is positioned so the reference element is inside the test cell at the same temperature as the working electrode. This eliminates the salt bridge and attendant errors associated with correcting potential to account for the salt bridge and thermal gradient. Dimensions of

the Luggin probe tip are 4 mm O.D. by 2 mm I.D. The tip is placed 4 mm from the working electrode face. Examination of working electrode faces after cyclic polarization measurements show minimal shadowing due to the Luggin probe.

The counter electrode (CE) is a 25 mm x 25 mm platinum foil sheet connected to the potentiostat with a platinum wire, which is spot welded to the foil.

Dissolved oxygen is removed from the electrolyte by purging with ultra-high purity (UHP) nitrogen gas. The electrolyte flow system incorporates three vessels in series; a 30 gallon pumped feed tank, a 10 liter gravity feed tank, and the test cells; all three vessels are purged with UHP nitrogen.

The entire system is constructed of materials that were selected to minimize oxygen diffusion into the system through component walls. Nitrogen delivery tubing and metering components are copper metal, glass, and FluoroEthylene Polymer (FEP)-lined Tygon tubing. Copper metal acts as an oxygen scavenger and is impermeable to oxygen diffusion. FEP-lined Tygon tubing is used only for connections in the N₂ delivery system. These materials virtually eliminate oxygen diffusion into the N₂ system through tubing runs. The electrolyte flow system is constructed from FEP tubing, FEP-lined Tygon[®] tubing, glass, and High-Density Polyethylene (HDPE). These materials have the lowest oxygen permeability of all commercially available tubing and vessel materials that meet chemical compatibility requirements.

Electrolyte flow is by gravity to prevent pressure waves caused by metering pumps from disrupting the boundary layer of electrolyte in contact with the Alloy 22 specimen. Boundary layer disruption affects mass transport between the passive film and the bulk electrolyte and so affects the kinetics of passive film processes.

Electrolyte flow through the cell is maintained by pressurizing the inside of the cell to 14 inches of water (0.5 psi). Pressurization is accomplished by placing the nitrogen outlet in a graduated cylinder under a 14-inch column of water. Nitrogen gas and electrolyte flows are controlled with needle valves and monitored with rotameters to ensure long-term stability of flow rates.

Test cell temperature is maintained by immersion in digitally-controlled oil baths; temperature control is ± 0.2 Celsius degrees. Temperature inside the test cells was measured using a glass thermowell immersed in the center of the test cell and National Institute of Standards and Testing (NIST)-traceable calibrated J-type thermocouples and an appropriate thermocouple thermometer.

Allihn-type vapor condensers were used to minimize concentration effects due to water vapor loss. Each counter electrode compartment has a 300 mm condenser while each working electrode compartment has a 400 mm condenser. A longer condenser is required for the working electrode compartment because the nitrogen flow rate is higher.

PC-based programmable potentiostats were used. Four identical potentiostats were available to the project. Accuracy of the data was ensured by checking the calibration of the potentiostats using NIST-traceable electrical resistors and a NIST-traceable calibrated multimeter.

D. Procedures

Open circuit potential (OCP), potentiodynamic anodic cyclic polarization, Electrochemical Impedance Spectroscopy (EIS), passive current density (i_p), and passive current density transients in response to step changes in applied potential were measured.

Open circuit potential and anodic cyclic polarization were measured first to determine the potential range over which Alloy 22 displays passivity for the electrolyte and temperature specific to each test. For each OCP/cyclic polarization test a specimen freshly polished to 600 grit, which had not been allowed to dry since polishing, was mounted in the test cell in room-temperature, aerated electrolyte. Deaeration with UHP N_2 was begun immediately and continued for one hour at room temperature after which the oil immersion bath was turned on to the desired temperature set point. N_2 flow rates were 150 mL/min for the working electrode compartment and 15 mL/min for the counter electrode compartment. Electrolyte flow rates were 4 mL/min for the working electrode compartment and 0.5 mL/min for the counter electrode compartment.

Open circuit potential was measured for between 12 and 18 hours. Once OCP was determined to be stable and within the expected range (which indicates a properly prepared specimen) the cyclic polarization measurement was performed according to ASTM standards [5,6]. Measurements were begun at open circuit potential and potential was scanned in the anodic direction at 0.1667 mV/sec to a maximum current of 6 mA, where the scan direction was reversed without changing the scan rate. The cyclic polarization results were evaluated to determine the passive potential range for Alloy 22 under the given conditions.

EIS/passive current density tests were performed as follows: A specimen freshly polished to 0.05 μm Al_2O_3 and cleaned ultrasonically, which was not allowed to dry, was mounted in the test cell, which was assembled as described above, and collection of OCP was begun. After the desired operating temperature had been reached and OCP was determined to be satisfactory, the specimen was anodically polarized to the potential corresponding to the low (cathodic) end of the passive region (-250mV at 60°C and -200mV at 30°C) as shown by the anodic polarization curve. Potentiostatic passive current density was collected at a sample rate of one data point every 10 seconds. Passive current density was observed until it was judged that a quasi-steady-state had been reached. Two EIS scans over the range 10 kHz to 10 mHz were then run back-to-back, the first in the high frequency to low frequency direction and the second in the low frequency to high frequency direction. Ten measurements per decade in frequency were taken.

Potential was then stepped 100 mV in the anodic direction while measuring the resulting current transient with a 0.1 second sampling rate. The system was allowed the same length of time as previously to come to steady state and EIS data were measured again as before. This process was then repeated in 100 mV steps. The intention of this work was to cover the entire passive range in 100 mV steps, however, the onset of stable crevice corrosion at the Alloy 22-epoxy interface of the mounted specimens prevented the entire test from being completed.

E. EIS and Validity of Results

In order for EIS data to be valid the system must conform to the following requirements of linear systems theory. The system must be stable, i.e., passive current must be at steady state; the current response to an applied alternating voltage must be linear; and the system response must be causal and finite valued. The conditions of causality and finite valued response are assumed to be valid. Linear response is ensured by limiting the amplitude of the applied alternating voltage signal to 10 mV. Steady state is determined by observing the passive current versus time over a period of many hours until the rate of change is judged to be insignificant over the approximately 45 minutes required to run two EIS scans which are compared to check for hysteresis; significant hysteresis indicates the system is not at steady state. To check for hysteresis, two impedance scans are performed sequentially, the first scan in the high-frequency to low-frequency direction and the second scan in the low-frequency to high-frequency direction. For this work, the frequency range was 10 kHz to 10 mHz. Validity of EIS results is also verified by applying the Kramers-Kronig transforms [9].

IV. EXPERIMENTAL RESULTS and DISCUSSION

Electrochemical Impedance Spectroscopy (EIS) data were collected for Alloy 22 in deaerated 4 molar sodium chloride solution buffered to pH 6 with sodium acetate /acetic acid at temperatures of 30°C and 60°C.

The data shown in Figures 3 and 4 were collected to check the validity of the EIS results by comparing two back-to-back impedance scans to check for hysteresis; hysteresis would indicate the system was not at steady state over the time required to collect the data. Figure B.3 shows the Nyquist plot for back-to-back scans performed after the specimen had been held potentiostatically at -250 mV vs. Ag/AgCl for 113 hours at 60.5°C . In the Nyquist plot the frequency used to collect each data point is not shown; the highest impedance values correspond to the lowest frequency with impedance decreasing with increasing frequency. This is seen explicitly on the Bode plot shown in Figure B.4. Note that impedance is reported in ohms and has not been corrected to $\text{ohm}\cdot\text{cm}^2$ by multiplying by the 1.267 cm^2 area of the test specimen. These figures show no hysteresis. In fact, the data for these scans are so close as to be virtually indistinguishable.

After it was determined that 113 hours of potentiostatic conditioning at 60.5°C allowed the system to come to a sufficiently steady state to collect valid EIS data, the effect of time at a specific potential was investigated. The Nyquist plot and Bode plot shown in Figure B.5 and 6, respectively, present impedance and phase shift versus time data for a specimen held at -200 mV vs. Ag/AgCl at 30°C . EIS scans were run at 71, 214, and 352 hours and it is seen that impedance increases with increasing time. For each data set back-to-back scans were performed and checked for hysteresis, which was absent in all cases. The magnitude of change seen between 71 and 214 hours and between 214 and 352 hours is about the same (4%) indicating a constant rate of change. This indicates that although the quasi-steady state attained after 71 hours is sufficiently stable to

generate valid EIS data a true steady state had not been attained even after 352 hours. No further attempt was made to establish how long it takes to reach a true steady state.

The effect of potential on impedance is shown in Figures 7, 8, 9, and 10 for two different specimens at 60° C. Nyquist plots are shown in Figures 7 and 9 while the corresponding Bode plots are shown in Figures 8 and 10. Figures 7 and 8 show EIS results for a specimen with 14 nA/cm² passive current density and Figures 9 and 10 show EIS results for a specimen with passive current density of 62 nA/cm². In both cases, impedance increases with increasing anodic potential. It is also seen that impedance is dependent upon passive current density; impedance increases with decreasing passive current density. Also note the 62 nA/cm² test (Figures 9 and 10) shows an unusual feature in the low frequency region between 0.1 Hz to 0.01 Hz; the phase shift plot has upturned tails, which are more pronounced with increasing potential, and there are corresponding discontinuities in the slopes of the impedance versus frequency plots, which can be seen in the Bode and Nyquist plots. Similar behavior is seen in Figures 5 and 6 (time dependence of impedance at 30° C), but the upturned tails and impedance slope discontinuities are on the high frequency end (1,000 Hz to 10,000 Hz).

V. IMPEDANCE DATA ANALYSIS

The commercial DataFit software (version 7.1) is employed in this work for the optimization of PDM on impedance data in order to get the kinetic parameters for the

elementary reactions in Figure 1. The experimental and calculated impedance data from the optimization of PDM at 30°C and 60°C are plotted in the form of Nyquist plot (Figure B.11-12). The correlation between experimental impedance data and the calculated data is quite good for the Nyquist plots shown. Thus, the impedance model based on the PDM provides a reasonable account of the experimental data. However, we note that the phase angle Bode plot (not shown) displays significant differences between the experimental and simulated data, especially in the higher frequency range where the impedance is very low. A possible reason is that the phase angle, defined as $\theta = \tan^{-1}(-Z''/Z')$, is a very sensitive function of Z' and Z'' , so that a slight deviation in Z' or Z'' give rise to a large fluctuation in θ .

The kinetic model parameters for Alloy-22 in deaerated 4 molar NaCl solution (pH=6) at 30°C and 60°C are presented in Table B.3. From Figure 1 and Equation (B.1) or (6) we see that reaction 5 describes the destruction of the barrier layer oxide film and k_5^{00} is standard rate constant for reaction 5 and is independent of the potential, thickness and pH value. Thus from the comparison of the kinetic parameters at 30°C and 60°C in Table B.3, k_5^{00} is predicted to increase with the temperature; that is, the dissolution of chromium oxide increases as the temperature increases. Most importantly, it is noted in Figure 1 that the rate of loss of the metal is due to penetration of the film into the metal (Reaction 2) and the rate of flow of the metal through the film as interstitials (Reaction 1). Therefore, the corrosion rate of Alloy-22 could be calculated from Equation (B.10)

$$r = V_m (k_1 + k_2) \quad (\text{B.10})$$

where r is the corrosion rate in cm/s, V_m is the atomic volume of the metal chromium in cm³/mol, k_1 and k_2 are the rate constants for Reactions 1 and 2 in the PDM in mol/cm²s. Substituting the expressions for k_1 and k_2 from Table B.1 and 2, Equation (B.10) becomes

$$r = V_m (k_1^{00} e^{-\alpha_1 \beta \chi \gamma p H} e^{-\alpha_1 \chi \gamma \phi_f^0 / s} e^{\alpha_1 (1-\alpha) \chi \gamma} e^{-\alpha_1 \chi k L} + k_2^{00} e^{-\alpha_2 \beta \chi \gamma p H} e^{-\alpha_2 \chi \gamma \phi_f^0 / s} e^{\alpha_2 (1-\alpha) \chi \gamma} e^{-\alpha_2 \chi K L}) \quad (\text{B.11})$$

where the thickness L can be calculated in terms of parallel plate capacitor theory with $L = \hat{\epsilon} \epsilon_0 / C$, V_m is 7.23 mol/cm³. Thus the corrosion rate of Alloy-22 in deaerated 4 molar NaCl solution (pH=6) at 30°C and 60°C can be calculated in terms of Equation (B.11) using the parameter values listed in Table B.3. The calculated corrosion rate for both 30°C and 60°C is 0.05 $\mu\text{m}/\text{year}$ and 0.09 $\mu\text{m}/\text{year}$, respectively. The corrosion rate is predicted to increase with the temperature. The value of this corrosion rate can be compared with the long-term experimental observations [10], which show the corrosion rate to be of the order of 0.01-0.02 $\mu\text{m}/\text{year}$. If we translate the corrosion rate into a corrosion loss, that will be 0.5 to 0.9 mm over the 10,000-year lifetime of the repository. Therefore, general corrosion may not represent a threat to canister integrity.

VI. SUMMARY and CONCLUSIONS

Deterministic modeling is required to accurately predict performance of Alloy 22 or other corrosion resistant materials into the far future required for high level nuclear waste disposal sites. The Point Defect Model, developed by D.D. Macdonald is one such model. This model has been validated for Alloy 22 by collection of high-accuracy Electrochemical Impedance Spectroscopy experimental data, extracting model parameters by a multivariate curve fitting method, and comparing calculated with experimental impedance spectra. A good correlation between calculated and experimental data is seen verifying the validity of the Point Defect Model for passive films on Alloy 22. The corrosion rate of Alloy 22 at different temperature is calculated in terms of the model parameters from the optimization of PDM on impedance data. The corrosion loss of Alloy 22 is in the range that long-term experiments reported.

VII. REFERENCES

1. G. M. Gordon: Corrosion, 2002, vol. 58, pp. 811-825.
2. Digby D. Macdonald: J. Electrochem. Soc., 1992, vol. 139, pp. 3434-3449.
3. C.Y. Chao, L.F. Lin, and D.D. Macdonald: J. Electrochem. Soc., 1981, vol. 128, pp. 1187-1198.
4. Digby D. Macdonald, Adan Sun, Namal Priyantha, and Palitha Jayaweera: J. Electroanal. Chem., In Press, 2004.

5. ASTM G 61 – 86 (Reapproved 1998), Standard Test Method for Conducting Cyclic Potentiodynamic Polarization Measurements for Localized Corrosion Susceptibility of Iron-, Nickel, or Cobalt-Based Alloys.
6. ASTM G5-94 (Reapproved 1999), Standard Reference Test Method for Making Potentiostatic and Potentiodynamic Anodic Polarization Measurements.
7. ASTM E542-01, Standard Practice for Calibration of Laboratory Volumetric Apparatus.
8. David J.G. Ives and George J. Janz, eds.: Reference Electrodes Theory and Practice, 1st ed., Academic Press, New York and London, 1961, pp. 207-209.
9. John R. Scully, David C. Silverman, and Martin W. Kendig, eds.: Electrochemical Impedance: Analysis and Interpretation, ASTM, Philadelphia, PA, 1993, pp. 115-170.
10. Namal Priyantha, Palitha Jayaweera, Digby D. Macdonald, and Adan Sun: J. Electroanal. Chem., In Press, 2004.

VIII. ACKNOWLEDGEMENTS

The authors gratefully acknowledge the sponsorship of the U.S. Department of Energy Office of Civilian Radioactive Waste Management through DOE/UCCSN Cooperative Agreement DE-FC28-98NV12081.

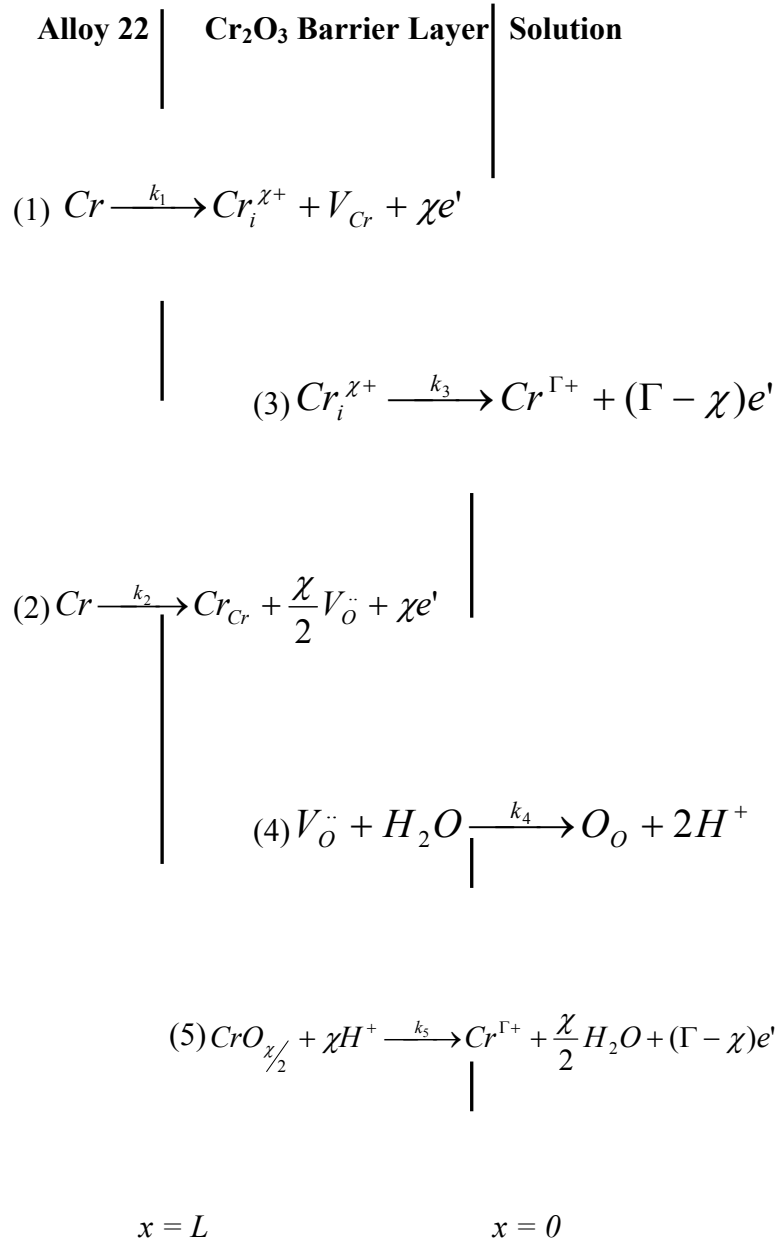


Figure B.1. Reactions for the PDM on Alloy 22

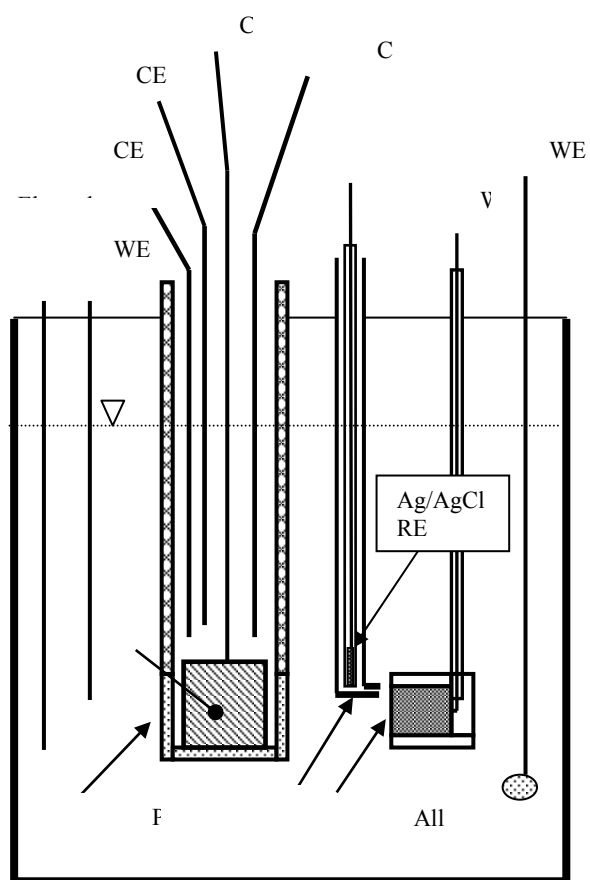


Figure B.2. Schematic of Test

**Nyquist Plot, C-22, pH 6, 4M NaCl, 113 hr. at
-250 mV vs. Ag/AgCl at 60.5°C
Passive Current Density 14 nA/cm²**

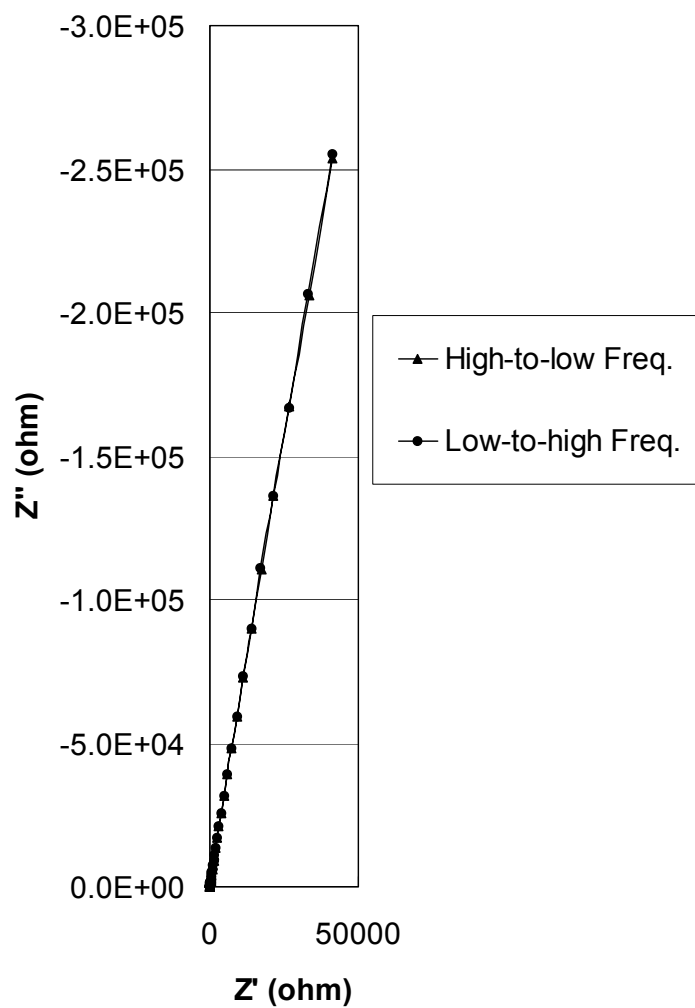


Figure B.3. Nyquist plot showing absence of hysteresis in EIS data after the specimen was held for 113 hr. potentiostatically at -250 mV vs. Ag/AgCl at 60.5°C . Note that only one curve is easily discernible because forward and reverse scans overlap.

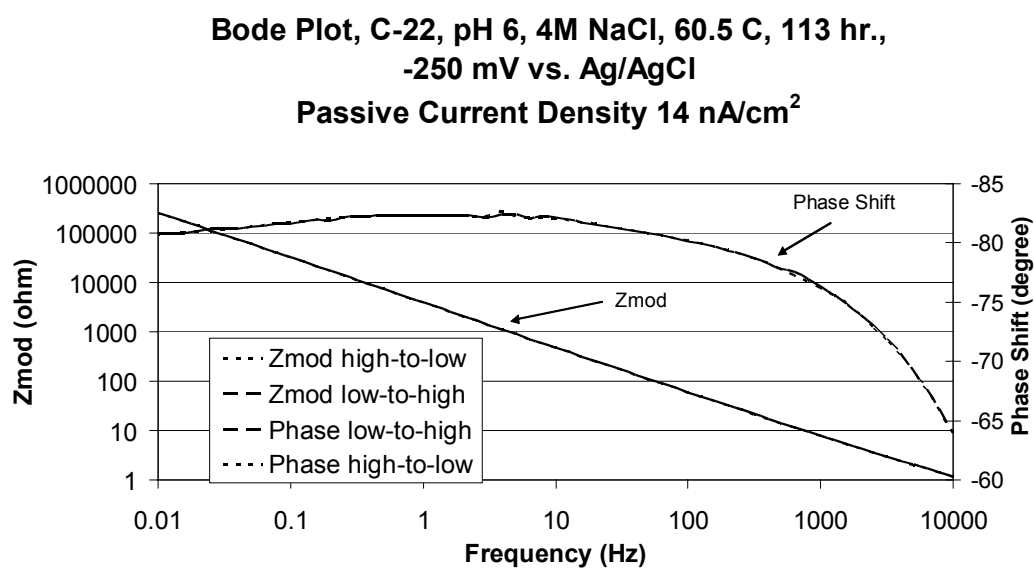


Figure B.4. Bode plot showing absence of hysteresis in EIS data after the specimen was held for 113 hr. potentiostatically at -250 mV vs. Ag/AgCl at 60.5°C . Note that only one curve is discernible for impedance and phase shift because forward and reverse scans overlap.

Nyquist Plot, Alloy 22, Z vs. Time
-200 mV vs. Ag/AgCl at 30°C, pH 6, 4M NaCl

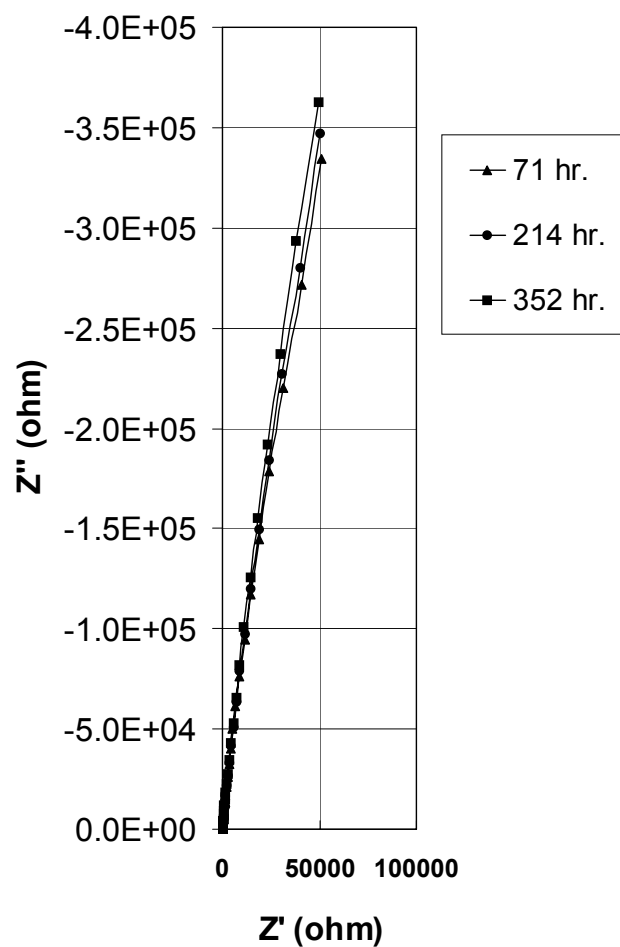


Figure B.5. Nyquist plot showing time dependence of impedance for a specimen held potentiostatically at -200 mV vs. Ag/AgCl at 30° C.

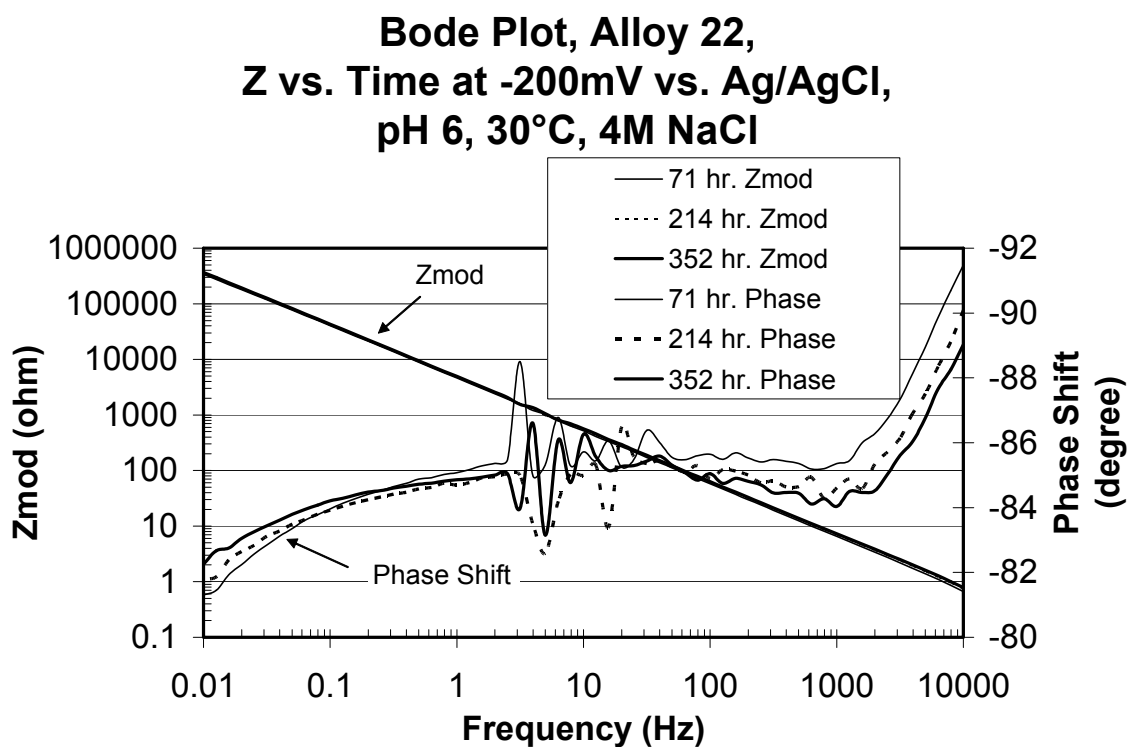


Figure B.6. Bode plot showing time dependence of impedance and phase shift for a specimen held potentiostatically at -200 mV vs. Ag/AgCl at 30°C .

**Nyquist Plot, Alloy 22, -250mV to -50mV vs.
Ag/AgCl at 60°C, pH 6, 4M NaCl,
Passive $I = 14 \text{ nA/cm}^2$**

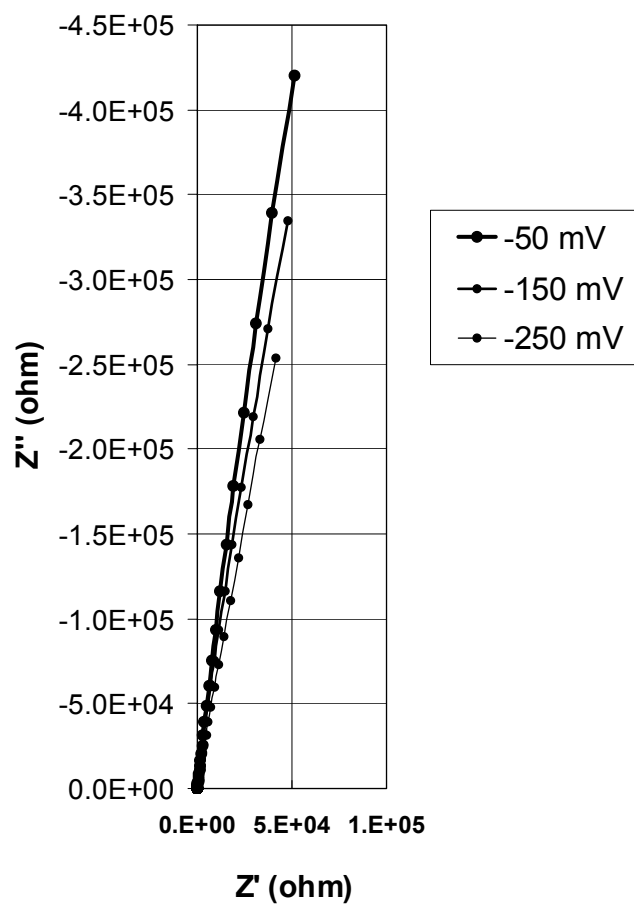


Figure B.7. Nyquist plot for potential dependence of impedance for a specimen with 14 nA/cm^2 passive current density.

**Bode Plot, Alloy 22, 60C,
-250 mV to -50 mV vs. Ag/AgCl, pH 6, 4M NaCl
Passive $I = 14 \text{ nA/cm}^2$,**

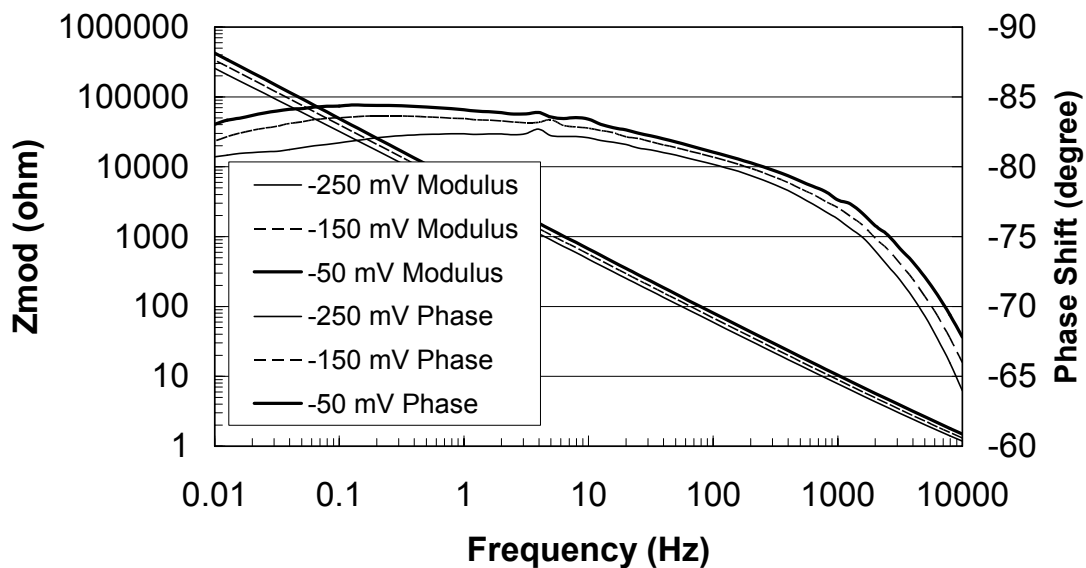


Figure B.8. Bode plot for potential dependence of impedance and phase shift for a specimen with 14 nA/cm^2 passive current density.

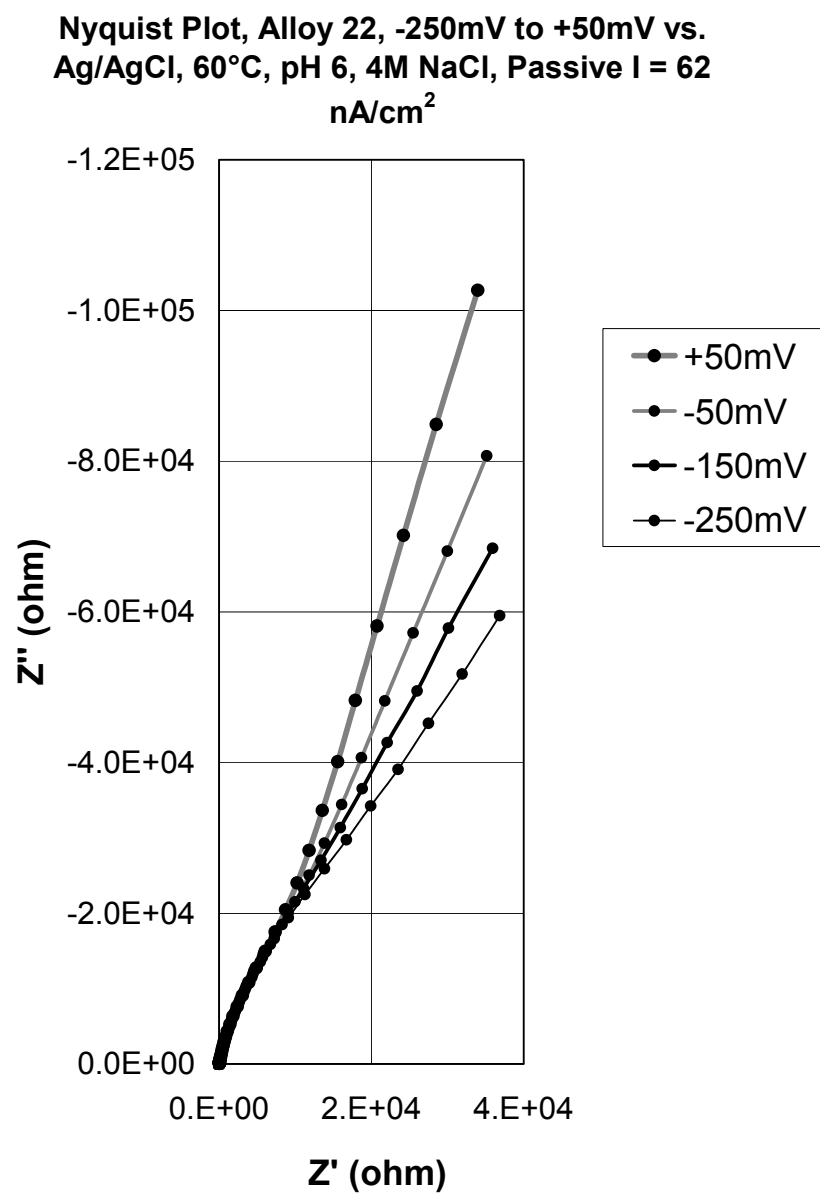


Figure B.9. Nyquist plot for potential dependence of impedance for a specimen with 62 nA/cm² passive current density.

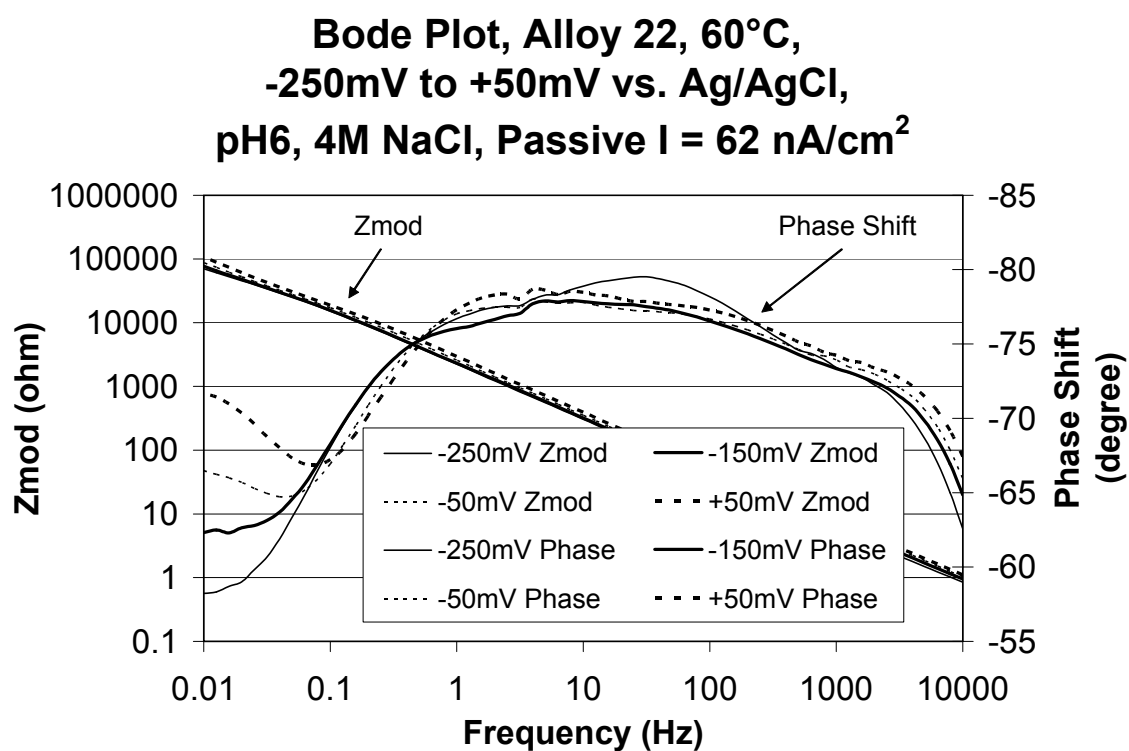


Figure B.10. Bode plot for potential dependence of impedance and phase shift for a specimen with 62 nA/cm² passive current density.

Alloy 22 Impedance, Measured & Calculated,
-200mV Ag/AgCl, pH 6, 4M NaCl, 30C

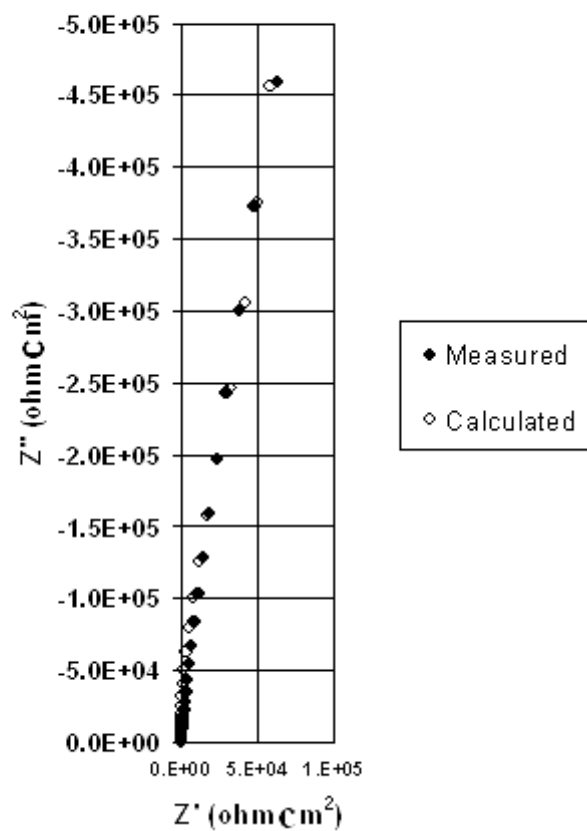


Figure B.11. Nyquist plot comparing measured and calculated impedance for -200 mV vs. Ag/AgCl at 30° C in deaerated pH 6, 4 molar NaCl electrolyte.

**Alloy 22 Impedance, Measured & Calculated,
14 nA/cm², -250mV Ag/AgCl, pH 6, 4M NaCl,
60 C**

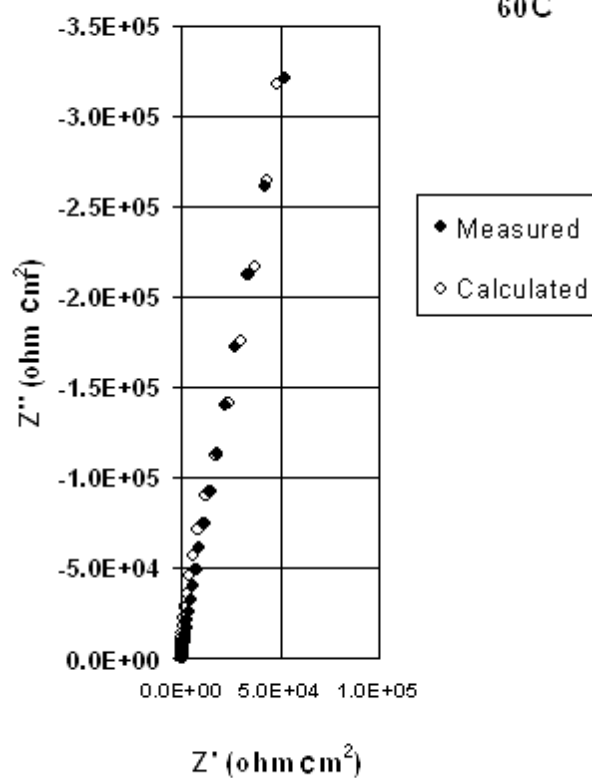


Figure B.12. Nyquist plot comparing measured and calculated impedance for -250 mV vs. Ag/AgCl at 60° C showing 14 nA/cm² passive current density in deaerated pH 6, 4 molar NaCl electrolyte.

Table B.1. Rate constants $k_i = k_i^0 e^{a_i V} e^{-b_i L}$ for the interfacial defect generation and annihilation reactions employed in the Point Defect Model.

| Reaction | a_i (V^{-1}) | b_i (cm^{-1}) | Units of k_i^0 |
|--|---------------------------------------|------------------------|--------------------------------|
| (1) $Cr \xrightarrow{k_1} Cr_i^{\chi+} + v_{Cr} + \chi e'$ | $\alpha_1(1 - \alpha)\chi\gamma$ | $\alpha_1\chi K$ | $\frac{mol}{cm^2 s}$ |
| (2) $Cr \xrightarrow{k_2} Cr_{Cr} + \frac{\chi}{2} V_o^{\cdot\cdot} + \chi e'$ | $\alpha_2(1 - \alpha)\chi\gamma$ | $\alpha_2\chi K$ | $\frac{mol}{cm^2 s}$ |
| (3) $Cr_i^{\chi+} \xrightarrow{k_3} Cr^{\Gamma+} + (\Gamma - \chi)e'$ | $\alpha_3\alpha\Gamma\gamma$ | 0 | $\frac{cm}{s}$ |
| (4) $V_o^{\cdot\cdot} + H_2O \xrightarrow{k_4} O_o + 2H^+$ | $2\alpha_4\alpha\gamma$ | 0 | $\frac{cm}{s}$ |
| (5) $CrO_{\chi/2} + \chi H^+ \xrightarrow{k_5} Cr^{\Gamma+} + \frac{\chi}{2} H_2O + (\Gamma - \chi)e'$ | $\alpha_5\alpha(\Gamma - \chi)\gamma$ | 0 | $\frac{mol^{0.5}}{cm^{0.5} s}$ |

Table B.2. Definition of the standard rate constants for the interfacial defect generation and annihilation reactions employed in the Point Defect Model.

| Reaction | k_i^0 |
|--|---|
| (1) $Cr \xrightarrow{k_1} Cr_i^{\chi+} + v_{Cr} + \chi e'$ | $k_1^{00} e^{-\alpha_1 \beta \chi \gamma p H} e^{-\alpha_1 \chi \gamma \phi_{f/s}^0}$ |
| (2) $Cr \xrightarrow{k_2} Cr_{Cr} + \frac{\chi}{2} V_o^{\cdot\cdot} + \chi e'$ | $k_2^{00} e^{-\alpha_2 \beta \chi \gamma p H} e^{-\alpha_2 \chi \gamma \phi_{f/s}^0}$ |
| (3) $Cr_i^{\chi+} \xrightarrow{k_3} Cr^{\Gamma+} + (\Gamma - \chi) e'$ | $k_3^{00} e^{\alpha_3 \beta \Gamma \gamma p H} e^{\alpha_3 \Gamma \gamma \phi_{f/s}^0}$ |
| (4) $V_o^{\cdot\cdot} + H_2O \xrightarrow{k_4} O_o + 2H^+$ | $k_4^{00} e^{\alpha_4 \beta \Gamma \gamma p H} e^{\alpha_4 \Gamma \gamma \phi_{f/s}^0}$ |
| (5) $CrO_{\chi/2} + \chi H^+ \xrightarrow{k_5} Cr^{\Gamma+} + \frac{\chi}{2} H_2O + (\Gamma - \chi) e'$ | $k_5^{00} e^{\alpha_5 (\Gamma - \chi) \beta \gamma p H} e^{\alpha_5 (\Gamma - \chi) \gamma \phi_{f/s}^0}$ |

Table B.3. Parameter values used in the optimization of PDM on the impedance of Alloy-22 in deaerated pH 6, 4 molar NaCl.

| E_{app} / mV vs. Ag/AgCl | -200/30°C | -250/60°C | Dimensions |
|---|-----------|-----------|--|
| R_s (Solution resistance) | 0.5 | 0.003 | ohms |
| $\tilde{\epsilon}_1$ ϵ (Electric field strength) | 1.15 | 1.2 | V/cm |
| $\hat{\epsilon}$ (Dielectric constant) | 21 | 22 | |
| $10^{14} k_1^{00}$ | 4.17 | 5.97 | mol/cm ² .s |
| $10^{15} k_2^{00}$ | 1.34 | 9.14 | (mol/cm ² .s) |
| $10^9 k_5^{00}$ | 1.81 | 837 | (mol ^{0.5} /cm ^{0.5} .s) |
| | 0.50 | 0.44 | |
| α_1 | 0.38 | 0.26 | |
| α | 0.31 | 0.30 | |
| n | 0.5 | 0.5 | |
| β | -0.0037 | -0.0045 | V |
| $\phi_{f s}^0$ | -0.042 | -0.047 | V |

VITA

Adan Sun

Adan Sun was born on November 09, 1974 in Fuxin, China. She graduated from Liaoning Normal University with her bachelor's degree in 1996. She earned her master's degree in Dalian University of Technology in 1999. She came to Pennsylvania State University to start her Ph.D study in 2001.